Segmentation of the Left Atrium and Pulmonary Veins from Contrast-Enhanced MR Images

Rashed Karim

A dissertation submitted in partial fulfilment
of the requirements for the degree of
Doctor of Philosophy
of
Imperial College London

September 2009
Department of Computing
Imperial College London

Abstract

Atrial fibrillation is an important cardiovascular disease causing cardiac malfunction. The left atrium and pulmonary veins are the structures most affected. Radio-frequency catheter ablation has now become a standard procedure for correcting atrial fibrillation. The procedure is minimally invasive and pre-planning the procedure is essential. It is normally required to image the atrium. Segmentation of the left atrium and pulmonary veins from medical images is an important problem and a necessary step for further analysing the left atrium.

This dissertation describes techniques for segmenting the left atrium from MR angiography images. It also describes methods for extracting sub-atrial structures of the atrium such as the central atrial body and pulmonary veins. As pulmonary veins of the left atrium have complex vessel networks, the centrelines of these vessels are extracted allowing for better visualisation and compact representation. Furthermore, the dissertation describes a framework for analysing the atrium. The pulmonary drainage trees are reconstructed using graph structures. Important atrial characteristics relevant to catheter ablation procedures are quantified. These include atrial anatomy and ostial diameters.

The methods described in the dissertation are evaluated on real patient datasets and compared against manual approaches. A comparative study of the proposed left atrium segmentation algorithm with an existing approach showed that the proposed approach yields better segmentations. Furthermore, results show that the proposed techniques for pulmonary drainage reconstruction correctly compute and classify atrial anatomy in the majority of cases. The computation of ostial diameters also show close agreement with gold-standard measurements. A series of studies performed to investigate the effect of user parameters on the quality of segmentation and measurements obtained show reproducibility of results. It is envisaged that the methods proposed will improve the efficacy of catheter ablation by providing useful and accurate atrial characteristics and information.

To the One and Only ...

Acknowledgements

I would like to thank my supervisor Prof. Daniel Rueckert for his guidance, support and encouragement through my years at Imperial College. I consider myself extremely fortunate to have worked under his supervision. I am also very grateful to him for undertaking the behemoth task of proof-reading this thesis and several of my previous manuscripts. Throughout this PhD, it was his vision, motivation and invaluable input that has brought me to this phase. I would also like to thank my co-supervisor Prof. Duncan Gillies for his support and mentorship.

I am also thankful to Dr. Raad Mohiaddin of the Royal Brompton Hospital for his invaluable input and Peter Drivas for his assistance in acquiring the cardiac MR images. Many thanks to Dr. Louisa Malcolme-Lawes and Dr. Prapa Kanagaratnam of the St. Mary's Hospital London for their collaboration and input. I would also like to express my gratitude to colleagues and friends of the VIP group for their support over the course of my research.

Sincere thanks to Prof. Majid Mirmehdi, Prof. Nasir M. Rajpoot and Dr. Peter Cashman for agreeing to be my examiners.

I cannot express in words the magnitude of support my parents Hussain Ahmed and Mehar Nigar have provided me to pursue my goals. Without their encouragement and love this thesis could not have materialized. I am also very grateful to Shabbir Ahmed, Fatima Hussain, Ayman Hussain and the *late* Tofail Ahmed for providing me with immense support and encouragement. Thanks also to Q. N. Faruque and Ruhi Zerina Faruque for being so patient, supportive and loving. Finally, I am indebted to my loving wife, Tasmia, for providing me with infinite encouragement and support. Without her support, I would find it very difficult to accomplish this work.

Contents

List of Tables

List of Figures

Abbreviations

AAM	Active appearance model
ASM	Active shape model
AV	Atrioventricular
CT	Computed tomography
CVD	Cardiovascular diseases
DT	Distance transform
ECG	Electrocardiography
EM	Expectation-Maximization
FD	First bifurcation distance
GDT	Geometric deformable template
GUI	Graphical user interface
HU	Hounsfeld units
ICP	Iterative closest point
IRTK	Image registration toolkit
ITK	Insight toolkit
LV	Left ventricle
MDCT	Multi-detector computed tomography
MIP	Maximum intensity projection
MRA	Magnetic resonance angiography
MRI	Magnetic resonance imaging
MSCT	Multi-slice computed tomography
PCA	Principal components analysis

RF	Radio-frequency
RFCA	Radio-frequency catheter ablation
RV	Right ventricle
SA	Sinoatrial
TOF	Time-of-flight
VTK	Visualisation toolkit

Notations

I	Image
κ	Curvature
∇	Gradient operator
$*$	Convolution operator
F	Force field
∇^2	Laplacian operator
E	Edge magnitude
H	Hessian matrix
σ	The width of the Gaussian kernel
$\mathcal{E}$	Diffusion tensor
ξ	Distance transform
$\mathcal{Y}$	Separating surface between adjacent Voronoi cells
$D(\cdot)$	Size of a Voronoi cell
$\bigcap$	Intersection
$\bigcup$	Union
$\setminus$	Set-theoretic difference
$\subset$	Subset
$\in$	Set member-of
$\notin$	Set not member-of
ϕ	n-dimensional function
λ	Eigenvalue
$\mathcal{V}$	Vesselness filter response

Π	Geometric plane
θ	Angle
$\mathbb{R}$	Set of real numbers
$N(\cdot)$	Neighbourhood set of points of a voxel lattice
$\mathcal{N}$	Normal distribution
Ω	Ostial boundary

Chapter 1

Introduction

Cardiovascular diseases (CVD) and related illnesses is an important cause of death in the developing world [144]. CVD is on a sharp rise in developing countries. The early diagnosis and treatment of CVD is crucial in reducing mortality and improving the quality of life of people suffering from such illnesses. The human heart is a complex organ requiring novel cardiac imaging and analysis techniques for diagnosis and detection of CVD. This chapter presents the motivation for this thesis, an overview of the structure of the thesis and its main contributions.

1.1 Motivation

Atrial Fibrillation is a condition related to abnormal electrical activity in the atrium. In the famous Framingham heart study, it was found that 12% of the adults studied had developed atrial fibrillation [12]. Atrial fibrillation was also associated with a 1.5- to 1.9-fold mortality risk with a high incidence of stroke. Census based projections estimate that by the year 2050, 12-15 million people in the United States will be affected by atrial fibrillation [92, 118]. Atrial fibrillation primarily involves the left atrium and pulmonary veins of the heart. Its genesis and maintenance is not very well understood, but a competing theory suggests it is caused by abnormal tissues within pulmonary veins firing erratic impulses resulting in fibrillating atria.

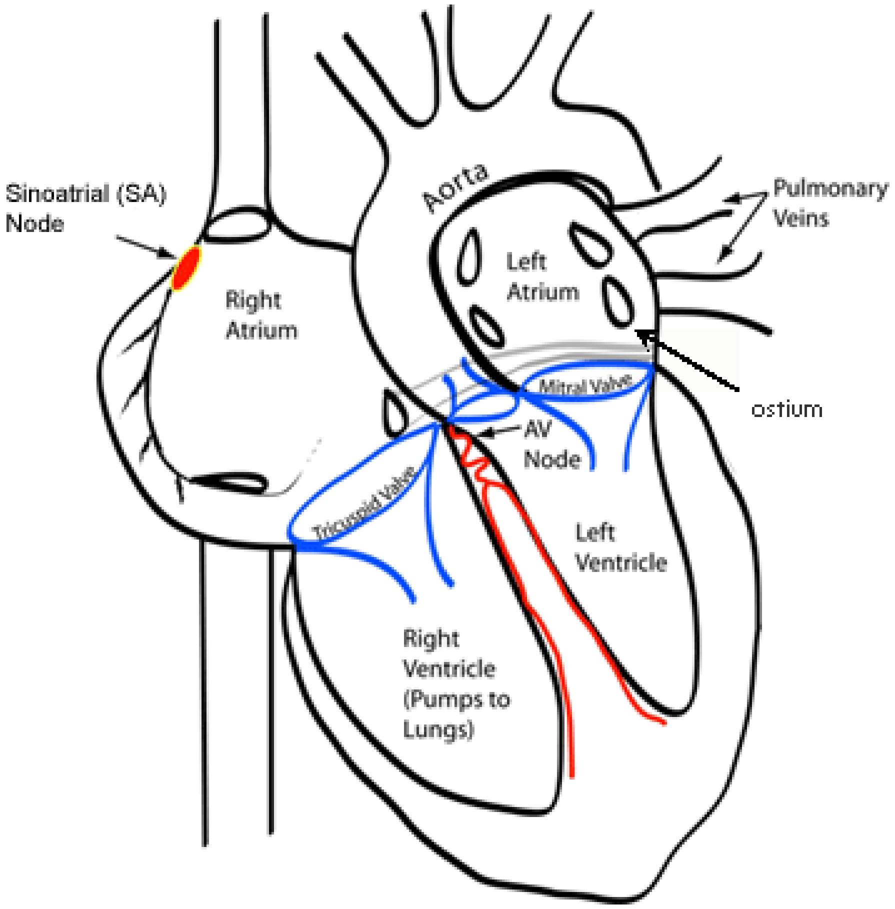

Figure 1.1: Figure showing the four main chambers of the heart, including important cardiac structures. Figure adapted from Medtrees.com

Minimally invasive procedures for correcting atrial fibrillation are now becoming increasingly popular, especially as alternate treatment methods are either invasive or do not have a permanent cure [172]. Radio-frequency catheter ablation (RFCA) is an important and common atrial fibrillation correction procedure. Other procedures include cryoablation [98] and the Cox-Maze [34]. In the RFCA procedure, the heart is accessed through a vein in the groin region known as the femoral vein. Catheters with high radio-frequency energy at the tip destroy tissue regions of the left atrium, selected on the basis of the tissue's activation times during atrial contraction. These tissue regions normally conduct the erratic impulses in the left atrium. In addition, tissue regions around each pulmonary vein to the left atrium are also destroyed. The patient's atria are brought to normal rhythm after successful ablation.

Over the years, success rates for RFCA have improved and complications have decreased [172]. The procedure currently involves careful pre-planning prior to the ablation step. This is partly

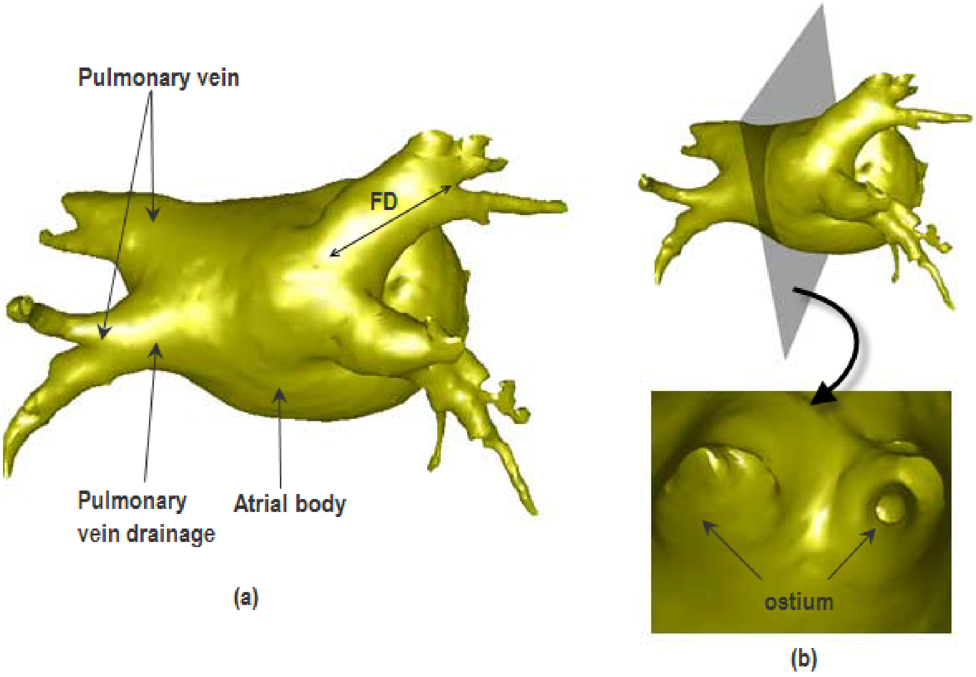

(a)

(b)

Figure 1.2: (a) Image of a segmented left atrium with its structures labelled. The first bifurcation distance (FD) is the distance measured from the ostium to the first bifurcation in the pulmonary vein. (b) The opening of each pulmonary vein also known as the ostium as seen projected on the cutting plane.

due to the intricacies of the procedure and the complex nature of left atrial anatomy. In a recent study, it was found that the left atrial anatomy varied substantially across patient subjects [109]. It is now understood that obtaining detailed characteristics and anatomy of the patient's left atrium can achieve a more efficient and successful ablation and prevent potential complications [176]. These characteristics include ostial diameters, first bifurcation distances and atrial body volume (see Fig. 1.2). With recent advances in cardiac imaging, it is now possible to non-invasively image the left atrium and study its anatomy. These modalities include magnetic resonance angiography (MRA) and multi-detector computed tomography (MDCT). They now both provide increasingly greater resolution images of the left atrium and pulmonary veins.

In a typical image of the left atrium, the pulmonary artery and ascending aorta come in the field of view and hinder the identification of the left atrium (see Fig. 1.1). This obstruction makes it difficult to visualise the left atrium even in three-dimensional surface reconstruction images. Segmentation of the left atrium to remove surrounding structures is a useful step prior to its visualisation and examination. The left atrial anatomy is known to be highly complex and variable. Manual segmentation of the left atrium not only becomes a laborious task but is also prone to errors. Moreover, with increasing resolution of images the task of manual delineation becomes impractical. Segmentation using automated techniques is thus non-trivial and essential for studying the left atrium prior to RFCA procedures.

Automated techniques for the segmentation of the left atrium and pulmonary veins not only provide better visualisations but also enable further analysis of the structures. In RFCA, it is important to extract accurate characteristics of the atrium such as the ostial diameters. Obtaining these manually is challenging and often suffers from inter-observer variabilities. The ostium is at the junction where the pulmonary vein meets the atrium. If the exact locations of pulmonary veins can be pre-computed, it is possible to compute the location and diameters for the ostium. Furthermore, atrial anatomy is reported using first bifurcation distances of pulmonary vein trees. If the exact first bifurcation distances can be computed from identified trees, the anatomy can be reported with greater confidence.

With higher resolution cardiac images becoming increasingly available, it is envisaged that automated techniques for segmenting and analysing the left atrium and pulmonary veins will play an increasingly important role in improving the accuracy and success rates of RFCA procedures.

1.2 Contributions

The main contributions of this thesis are as follows:

- **Segmentation of the left atrium from contrast-enhanced MRA**: Identification of the left atrium from contrast-enhanced MRA images is an important segmentation problem. The thesis develops a method to extract the left atrium from contrast-enhanced MRA images. The method uses a combination of classical and modern approaches for making segmentation more robust. It also proposes a threshold-based region-growing for extracting the left atrial blood pool. Furthermore, an interactive method to correct for over-segmentations is also proposed. The entire method is fast and robust.

- **Segmentation of atrial body and the pulmonary veins**: To perform further analysis on the left atrium, it is important to segment and locate the sub-atrial structures of the left atrium namely, the central atrial body and the pulmonary veins. A method to segment the atrial body from left atrium images is proposed. Furthermore, a method for extracting centrelines of pulmonary veins draining into the left atrium is also proposed. Together these techniques build an important framework for extracting patient-specific information about the atrial anatomy.

- **Computation of drainage locations and pulmonary vein trees**: Several important characteristics of the left atrium relating to RFCA procedures can be extracted from the network configurations of pulmonary vein trees draining into the left atrium. These include locations of ostia, first bifurcation distances and atrial anatomy. A method to locate pulmonary vein drainages to the left atrium is proposed. A method to compute and construct the pulmonary vein drainage networks from centrelines is presented. A method to represent this network as a graph structure is also proposed.

- **Quantification of ostia and atrial anatomy**: Accurate information relating to the left atrium's characteristics is necessary for making RFCA procedures more efficient and reducing complications. A method to semi-automatically locate ostial positions is proposed. Furthermore, a method to compute ostial diameters is also proposed. Atrial anatomy is quantified in terms of the number of drainage, drainage network configuration and first bifurcation distances. A method to compute these characteristic features from the sub-atrial structure framework and pulmonary vessel drainage trees is proposed. The proposed methods are fast and robust.

1.3 Thesis overview

The thesis outline is as follows:

Chapter 2 presents the relevant clinical and imaging background for this thesis. It presents a brief overview of the characteristics of the human cardiovascular system relevant to the thesis. The main aspects of atrial fibrillation are also discussed. We also review the main atrial fibrillation corrective procedures currently available. The role of atrial anatomy in RFCA is also discussed, including the current pre-procedural imaging techniques used. The chapter also presents an overview of the most commonly used cardiac imaging techniques.

Chapter 3 presents the relevant technical background for this thesis. It gives an overview of image segmentation methods. At the end of each segmentation technique, it reviews the existing literature for cardiac segmentation related applications of the technique. Furthermore, the chapter also includes a review of vessel segmentation techniques.

Chapter 4 describes the left atrium segmentation algorithm. Detailed descriptions of the necessary pre-processing steps are given. The region-split-and-merge approach is next described using a Voronoi formulation of the Euclidean distance transform (DT) space. Finally, a technique to exclude over-segmented regions is described.

Chapter 5 describes the segmentation methods for the atrial body and pulmonary veins. The level set framework for segmenting atrial body is presented. A level set framework for segmenting atrial body is presented. The chapter provides a description of the proposed method for extracting pulmonary vein centrelines. Furthermore, a method for modelling and visualising centrelines using cubic B-spline curves is also presented.

Chapter 6 lays out the techniques for reconstructing and representing vessel trees using graph structures. It also presents the methods proposed for identifying and classifying atrial anatomy. Furthermore, methods to compute ostial diameters using two different techniques are presented. Techniques for making the ellipse-fitting process more robust is also discussed.

Chatper 7 presents details of the experiments carried out to evaluate the proposed methods. It presents a description of the results obtained. Furthermore, it provides a discussion of the results and discusses any limitations found in the studies. The methods evaluated and presented in this chapter are as follows:

- Left atrium segmentation.
- Pulmonary vein centreline evaluation.
- Evaluation of ostial diameters.
- Evaluation of pulmonary vessel tree and atrial anatomy: This includes separate evaluations of drainage quantification and first bifurcation distances.

Chapter 8 concludes this thesis with a discussion of the methodologies used and the primary contributions. Furthermore, it describes general limitations of the proposed techniques. A summary of possible future work is presented. Fig. 1.3 gives a high-level overview of the proposed approaches in the form of a flow diagram.

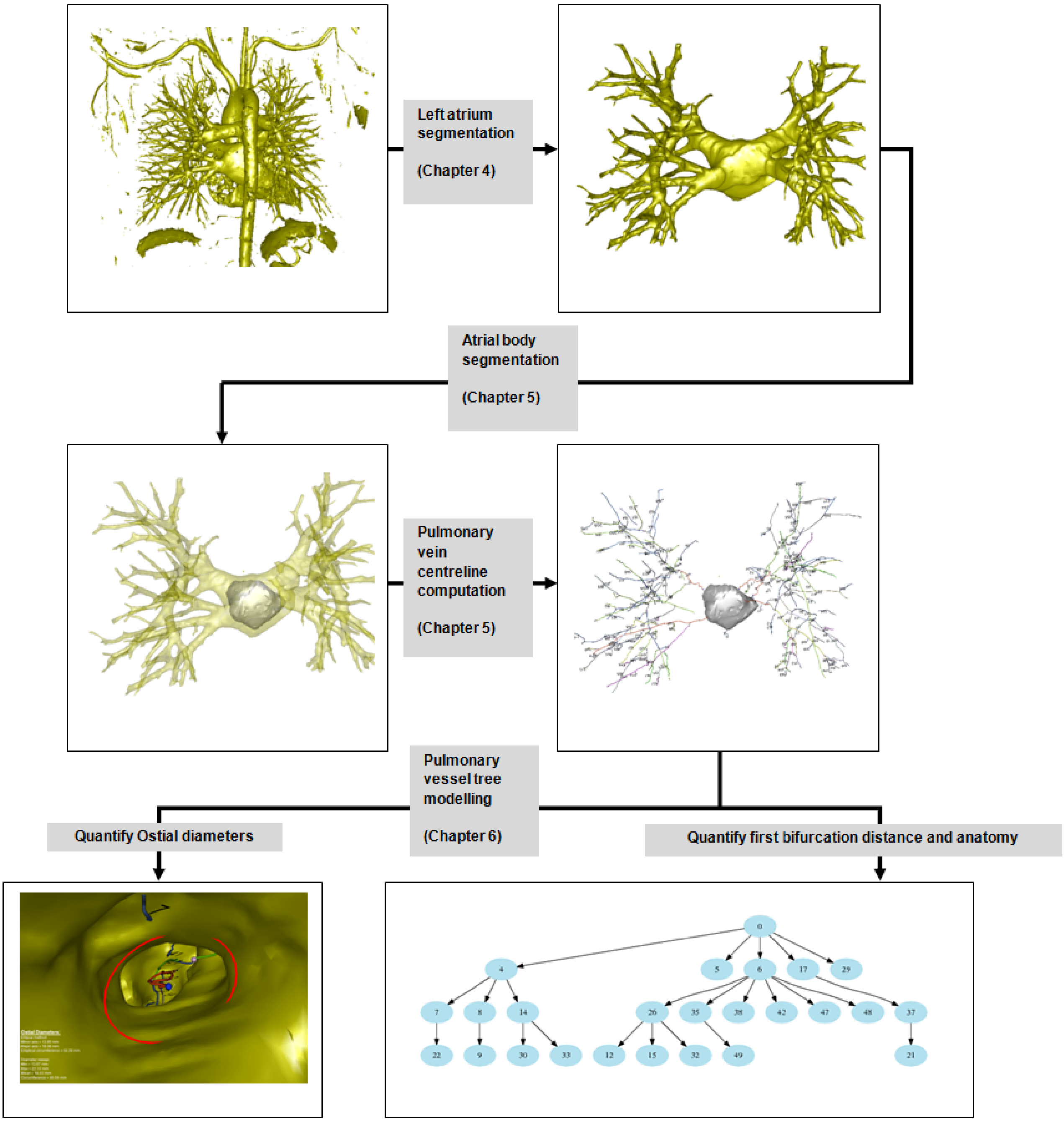

Figure 1.3: A high-level overview of the proposed techniques in this thesis with image visualisations obtained at each step.

Chapter 2

Clinical background: Atrial fibrillation

Atrial fibrillation is a condition resulting in cardiac malfunction. The areas affected most are the left atrium and pulmonary veins. Corrective procedures for atrial fibrillation have been available since the past decade. Currently, there has been a growing clinical interest in the area of minimally invasive procedures. Atrial fibrillation can now be successfully treated using minimally invasive catheter ablation. This targets the left atrium and pulmonary veins. Imaging the left atrium and pulmonary vein prior to the procedure is essential. Advances in cardiovascular imaging have made it possible to acquire high resolution images of the left atrium and pulmonary veins. Using imaging, clinicians are interested in extracting information on the characteristics of the left atrium that is useful for planning the treatment.

2.1 The cardiovascular system

The human heart has four chambers. The upper two chambers are called the left and right atria and the lower chambers are called the left and right ventricles (see Fig. 1.1 on page 6). Blood is constantly pumped into and out of the heart. The heart accomplishes this through regular beating. A single beat is also often termed a cardiac cycle, which comprises all events that occur between the beginning of one beat and the beginning of the next. In a single cardiac cycle, blood enters and leaves the four chambers in a systematic manner. The blood entering the heart to the left and the right sides is distinctly different. To the right, de-oxygenated blood from the body enters the heart via the veins and to the left oxygenated blood from the lungs enters the heart.

The atria and ventricles have different functions. Atria receive blood from various parts of the body and the ventricles deliver this blood to the organs including the lungs. In addition, the right and the left sides have very specific roles. The right atrium receives de-oxygenated blood and pumps it to the right ventricle which in-turn pumps it to the lungs. The left atrium receives a fresh supply of oxygenated blood and pumps it into the left ventricle which in-turn pumps it to the aorta.

A major network of vessels carry blood into and out of the heart's chambers. The pulmonary veins carry the oxygen-rich blood from the lungs to the left atrium. The aorta then channels this blood from the left ventricle to the rest of the body's organs. To the right side, the superior vena cava brings de-oxygenated blood from the rest of the body to the right atrium. The pulmonary artery carries this blood from the right ventricle to the lungs for oxygenation. These illustrate the heart's primary function in the human body: It is responsible for pumping and circulating blood through various organs by repeated and rhythmic contractions.

2.1.1 Mechanisms of the heart beat

The beating of the heart is caused by the contraction of some specialised cardiac muscles called the *Myocardium*. These muscles are very different from other muscular tissues in the body, such that they can contract and also conduct electrical impulses. This is only possible since unlike other muscles they are composed of very specialised cells. Although all of the heart's muscle cells are capable of producing the electrical impulses, a very specific portion of the heart is responsible for initiating these electrical impulses. This part is called the sinoatrial (SA) node which is a group of cells located near the wall of the atrium (see Fig. 1.1 on page 6). The cells produce cell-membrane contractions. Since all the cells are interconnected, this activation is conducted across all neighbouring cells.

The electrical activation of cells surrounding the atria causes them to first contract. As the impulses travel down to the base of the heart, the ventricles contract and the atria can relax. This critical delay between the atrial and ventricular contraction times allows blood from the atria to fill up the ventricles before being pumped out. Such a delay is only possible since the atria and ventricles are electrically disconnected at all but one point called the atrioventricular (AV) node (see Fig. 1.1 on page 6). The AV node, which has a limited impulse-carrying capacity, is the only channel through which the impulses can travel to the ventricles preventing the atria and ventricles from contracting at the same time.

This systematic propagation of impulses causes the atria and ventricles to contract and relax resulting in a heart beat. In a resting healthy adult, the SA node normally cause the heart to beat at about 70 beats per minute (bpm). This rate increases with physical activity. The maximum heart rate during exercise varies in adults with age and fitness. An age-predicted formula commonly used is $\mathrm{HR}_{max} = 220 - age$, although its validity is not yet established [169]. The heart rate usually does not exceed 220 bpm in adults.

2.2 Atrial fibrillation

Atrial fibrillation is a condition caused by a disruption of the normal sinus rhythm described in the previous section. Random electrical impulses are fired from dysfunctional locations other than the SA node interrupting the normal rhythm. It primarily affects the atria as they respond to these random impulses by contracting. As a consequence, atrial contraction rates are random and can become abnormally high in patients with atrial fibrillation. Contraction rates of 400-600 bpm have been reported [124]. However, the AV node plays a very important role by filtering most of these abnormal impulses. As a result, the ventricles continue to pump at the normal rate. Nevertheless, this abnormal fibrillation of the atria reduces the effectiveness in pumping blood efficiently to the ventricles. This inefficient pumping results in pooling of blood in the atria. This can cause blood to clot and severe consequences such as a heart attack or stroke become highly likely.

The two main theories on the genesis of atrial fibrillation are *Automaticity* and *Re-entry*. Initially, automaticity was thought to cause atrial fibrillation. However, over the past 50 years, re-entry has been the dominant conceptual mechanism model of atrial fibrillation strongly influenced by work of Moe and co-workers [119, 124]. Most researchers agree that a unifying theory of its mechanism is still lacking and is very much an active area of research [123]. However, it is clear that the onset and maintenance of sustained atrial fibrillation, irrespective of the underlying mechanism, requires both a trigger (i.e. automaticity) and an atrial substrate that is capable of maintaining re-entry [123]. Atrial fibrillation is thus caused and maintained by automaticity and re-entry and both these mechanisms are not mutually exclusive. We discuss both phenomena in some detail.

2.2.1 Re-entry

Moe and co-workers [119] first postulated that atrial fibrillation is caused due to a phenomenon known as re-entry. This was later confirmed by mapping atrial activation in animal and human hearts [180]. In a healthy human heart, an impulse will originate at the SA node and move from one end of the heart to the other end before dying out. These impulses are conducted through heart muscle cells. Normally, the impulses will pass through quickly only allowing the cells to respond once for each impulse. However, if conductance is abnormally slow in some areas the impulses are not able to conduct as desired. Part of the impulse or wave will arrive late and is potentially treated as a new impulse by the cells. The cells respond a second time for the same impulse resulting in a re-entry. These responses manifest into the re-entrant wavelets seen in Fig. 2.1(B). Depending on the timing, this can produce a sustained abnormal rhythm leading to atrial fibrillation.

Atrial substrates are believed to cause re-entrant wavelets. These substrates are mostly structural changes of the atria that are known to hinder impulse conduction. The most apparent substrate to cause re-entry is *Fibrosis*. It is a condition in which the fibre orientations of the atria are altered. These can potentially create zones of conduction delay [123]. Fibrotic changes have mostly been found to occur in an aging heart [65].

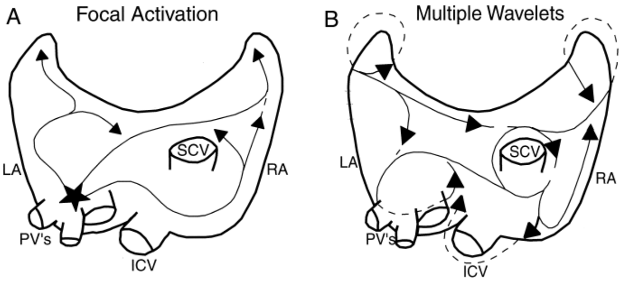

Figure 2.1: A. Activation paths in automaticity. The firing focus (marked by the star) often lies in regions of pulmonary veins. B. Activation paths in re-entry. Random re-entrant wavelets caused by slow-moving and thus fractionation of impulses. Labels: LA - left atrium, PV- pulmonary vein, SCV - superior vena cava, ICV - inferior vena cava and RA - right atrium. Image taken from [114]

2.2.2 Automaticity

The SA node acts as a pacemaker. It is solely responsible for generating electrical impulses to activate the cardiac cells. This pacemaker ability is however present in every heart muscle cell. In normal circumstances, these cells do not fire their own impulse. However, it has been found that cells can abnormally start firing their own impulses destroying the sinus rhythm [156]. These abnormal regions exhibit automaticity and are also known as *ectopic foci*. Patients may have one or more such focal points. The presence of ectopic focal activity does not always result in atrial fibrillation. It may cause a single premature beat now and then. But, if the ectopic focus fires more often than the SA node, it can produce a sustained abnormal rhythm leading to atrial fibrillation.

It is established that ectopic focal points occur mostly in the vicinity of pulmonary vein ostia and frequently in the superior pulmonary veins [68, 59, 26]. It is also hypothesised that areas derived from the embryonic cardiac conduction system may contribute to the arrhythmogenic (i.e. arrhythmia inducing) substrate in adult hearts [72]. Myocardial sleeves are part of the embryonic cardiac system and will normally extend into the pulmonary veins in adults. Such locations have thus been primary targets of suspicion in diagnosing and treating patients with atrial fibrillation. This is one of the reasons why pulmonary veins play an important role in the diagnosis and treatment of atrial fibrillation.

2.3 Atrial fibrillation treatment

The aim of atrial fibrillation treatment procedures is to put the heart back into its normal sinus rhythm. Over the past 50 years, understanding of the mechanism of atrial fibrillation has evolved and so has its treatment. The following sections provide a discussion of the most common procedures available for treatment available.

2.3.1 Pharmacological treatment

One of the first methods introduced for correcting atrial fibrillation was by using so-called *anti-arrhythmic* drugs. These drugs control the rhythm by altering the electrical properties of the heart. Although these drugs were not specifically developed for atrial fibrillation, they were found initially to be effective in bringing the patient back into sinus rhythm. Many of the drugs have been found to have several indirect side-effects such as lethal congenital disorders if given in pregnancy [107]. It is now established that, ironically, the effects of these drugs can themselves lead to life threatening rhythm disorders and increase mortality in atrial fibrillation patients [124]. For a detailed discussion on drug therapy in atrial fibrillation, see [39].

2.3.2 The Cox-Maze procedure

Surgical procedures have been investigated widely by researchers. Re-entry is known to be caused by fibrotic changes in the atrium. Cox and co-workers [34] devised the Cox-Maze surgical procedure that creates a series of incisions arranged in a maze-like pattern in the atria. Incisions are created over the entire atrium and are thus very effective in blocking re-entry. The procedure requires *open-chest* surgery and is complex. There is also a substantial risk of serious post-surgical complications such as cerebrovascular accidents, cardiac tamponade and loss of atrial rhythm. Despite these risks, researchers have reported high success rates ($\sim 90\%$) in restoring rhythm and correcting atrial fibrillation using the Cox-Maze [154]. This procedure evolved into the Cox-Maze III procedure which remained the gold-standard for treating atrial fibrillation for many years [138].

Over the past decade, atrial fibrillation treatment has changed, influenced by the work of Jais et al. [68]. They showed that atrial fibrillation was caused due to rapidly firing foci (i.e. automaticity) located close to the pulmonary veins. Once these ectopic focal points can be located, using radio-frequency energy, the firing focus points are electrically disconnected from the rest of the heart. The procedure is less invasive and quicker than the traditional Cox-Maze. Nevertheless, the Cox-Maze remains an option for patients who require open-chest surgery for other reasons.

2.3.3 Radio-frequency catheter ablation

Radio-frequency Catheter Ablation (RFCA) has now become the treatment of choice for correcting atrial fibrillation [88]. Different ablative techniques have been developed with varying clinical efficacy and safety. These are focal ablation within pulmonary veins, segmental ablation and circumferential ablation [108, 127, 132]. We restrict our discussion to circumferential ablation, which is now a common and effective RFCA technique [132, 60]. In this procedure, the conduction pathway of an ectopic focus is blocked by creating circular lesions (see Fig. 2.2). Lesions are made by burning tissue, the process also known as ablation. These lesions are made frequently around pulmonary veins. In cases where the patient is diagnosed with chronic atrial fibrillation, it may be preferable to have Cox-Maze type lesions. Ablation destroys a tissue's electrical conductance properties and is performed using a catheter probe that can deliver high radio-frequency energy at its tip thereby burning the tissue. RFCA procedures have conventionally been performed under fluoroscopic guidance with the use of a manually steered catheter. More recently, *robotic* approaches involving a remotely-controlled robotic catheter have improved the accuracy and efficacy of these procedures.

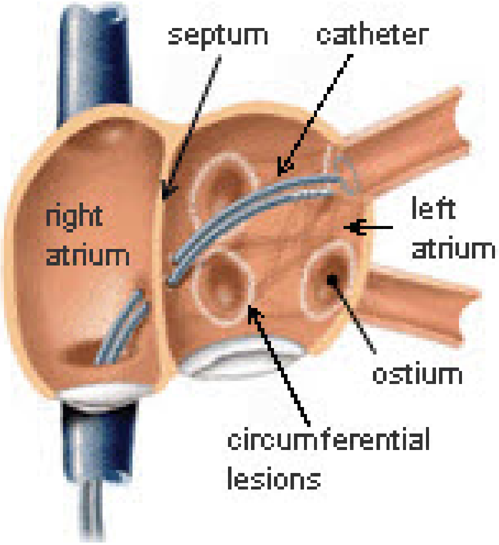

Figure 2.2: Circumferential ablation technique for correction atrial fibrillation. The catheter accesses the left atrium through the septum. Circular lesions are created around each pulmonary vein ostium. Image adopted from [146]

Imaging in catheter ablation

Treatment planning prior to ablation procedure is necessary. This will mostly involve identifying the atrial anatomy and selecting ablation points. Conventionally, fluoroscopy and eletrocardiograms (ECG) have been used to analyze atrial anatomy. By injecting contrast material into the left atrium its anatomy is visualised. However, this is incapable of providing accurate 3D anatomical information. It is now well established that the use of MRA and multi-detector row CT provides far superior 3D anatomical detail [81]. The use of *electroanatomical* maps [132] coupled with MRA/CT have also gained wide popularity. With a roaming catheter, 3D electroanatomical maps are constructed that display the spatial distribution of electrical activity in reference to an ECG. Other maps such as voltage and activation maps are also acquired. It is also now possible to integrate these maps with MRA/CT scans whereby areas of abnormal activity can be spatially located [100]. Once these points are located, circular lesions can be planned and mapped.

The procedure can begin after the left atrial anatomy has been studied carefully and ablation points have been mapped and located. The catheter accesses the left atrium through the femoral vein, into the right atrium and through the septum (see Fig. 2.2). Once inside the left atrium,

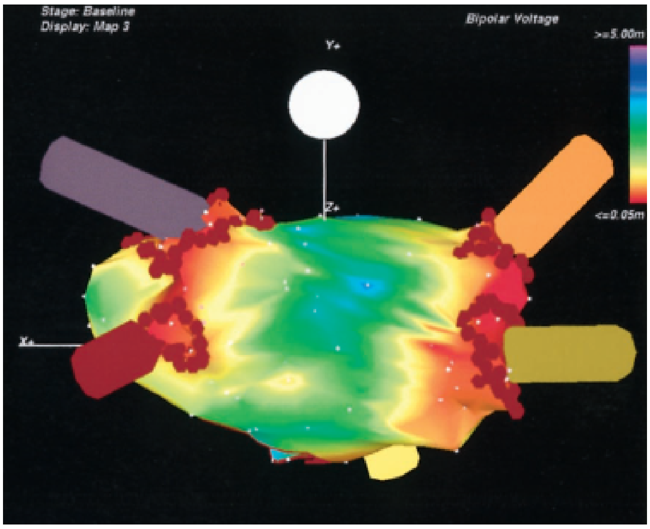

Figure 2.3: Figure showing a post-ablation voltage map used in assessing the success of an RFCA procedure. Note the circumferential ablation path as indicated by the red circles. Adapted from Pappone et al. [133]

it can access pulmonary veins from within the atrium. It can be guided using a combination of various techniques. Fluoroscopy produces real-time images of the catheter's position in relation to the atrium. In some systems, catheters have position sensors which automatically register it with a 3D/4D heart model [192]. Most catheters also have pressure sensors coupled with a force feedback at the controller's end.

Robotic catheters

Conventional catheters can be difficult to manoeuvre, especially around tortuous vessel segments. This has given way to so-called robotic approaches, where catheter navigation is remotely controlled. We briefly describe two different kinds of remote navigation that are marketed by two different companies. The first is the Sensei$^{\text{TM}}$ robotic arm developed by Hansen Medical Inc. [75]. It is an electromechanical master/slave system that can remotely control a steerable guide catheter. The catheter is controlled using a Novint falcon-like joystick [5]. The joystick allows movement in all three dimensions and provides a high-fidelity three-dimensional force feedback. The catheter can be viewed in real-time in a fluoroscopic view on the physician's workstation, with an added superimposed icon/model of the catheter. The catheter can also sense pressure at its tips, sending continuous feedback to the physician's workstation. A notable feature of the system is its extensive reachability and flexibility. A second remote navigation system is marketed by Biosense Webster. It uses the CARTO$^{\text{TM}}$ mapping and navigation system coupled with the Stereotaxis Niobe Magnetic Navigation System. The catheter tip is steered using the influence of an external magnetic field. Ernst et al. [45] report on initial experience and success with the procedure.

The efficacy of robotic approaches remains an area of debate amongst electrophysiologists. Success rates of 85-90% have been reported [145]. However, some clinicians have also reported higher complication rates of around 19%, which is more than the typical averages for manual procedures (4-5%) [122]. The complications associated with RFCA are similar to those associated with any cardiac catheterisation process [81]. These include endocardial charring, pulmonary vein dissection and atrial or pulmonary vein perforation [188].

2.3.4 Associated post-ablation conditions

Post-procedural conditions can include thinning of the pulmonary vein, also commonly known as pulmonary vein *stenosis*. This is more prevalent in cases where ablation is performed close to the ostium [190]. A different type of condition is recurrent atrial fibrillation and is a common post-procedural condition in RFCA [121]. Patients complain of recurring episodes of atrial fibrillation, weeks after the procedure. The primary cause of this are ectopic focal points that go undetected and hence un-ablated. They may also be sometimes caused due to the recovery of the pulmonary vein conduction pathways [121]. As a precautionary measure, some clinicians prefer to do pulmonary vein isolations where a pulmonary vein is completely isolated and disconnected. If all pulmonary veins are detected and ablated, recurrence of atrial fibrillation can be significantly reduced. This emphasises the importance of having good knowledge of the underlying anatomy prior to RFCA procedures. For an investigational study on the after-effects of RFCA, see [132].

2.4 The left atrium in atrial fibrillation

The left atrium is central to our study. With RFCA now becoming the most commonly preferred and effective atrial fibrillation correcting procedure, we discuss some aspects of left atrial anatomy in relation to RFCA procedures.

2.4.1 Left atrial anatomy

The anatomy of the left atrium is highly complex. The modal anatomy, found in approximately 70% of the general population [53], consists of four pulmonary veins, two superior and two inferior that drain into the left atrium from both the right and left sides. These pulmonary veins branch out into various other peripheral vessels as can be seen in Fig. 2.6. The venoatrial junctions are also known as pulmonary vein drainages. At the mouth of the opening of the drainage is the *ostium.* The central structure is being referred to as the *atrial body* in rest of the thesis. Thus the distinction from the left atrium, which we refer to include both the pulmonary vein and the atrial body. Please refer to Fig. 1.2 on page 7 for a labelled atrial anatomy.

The anatomy of the left atrium is known to vary significantly between patient subjects. Along with the shape of the atrial body, the number and orientation of the pulmonary vein drainages are known to vary significantly. Marom et al. [109] reported in a study conducted on 200 patients in which 10 different variations were located to the right side, and 4 different variations to the left side. See Fig. 2.4 and Fig. 2.5 for the different variations. A simple classification system to describe the different anatomies has been proposed. A three-letter word is used to describe each anatomy to the left or right side of the atrium. The first letter is either 'R' or 'L' indicating whether it is to the left or right, the second letter specifies the number of drainages and the last letter gives the variation. For example, R4a indicates four pulmonary veins to the right side and the *a* refers to the specific variation within this class. Studies have also reported variations of the left atrial body size [1, 140]. The size seems to vary with the human body's surface area and gender. There is also some degree of variability on the size and diameter of pulmonary veins that drain into the left atrium. These variations show how every patient case

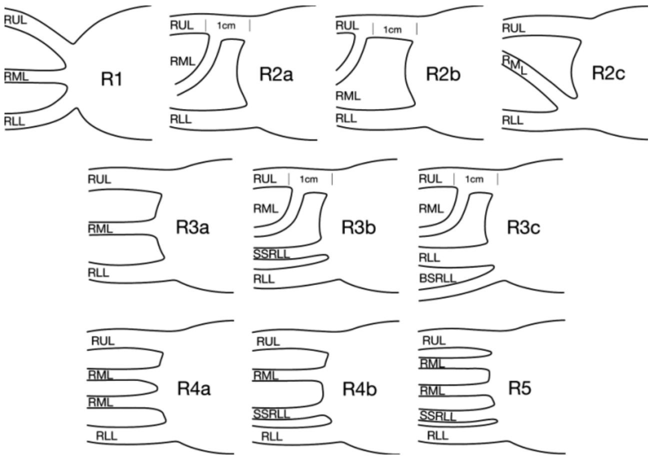

Figure 2.4: Figure showing the variations to the right side of the atrium from a study conducted on 200 patients. Abbreviations: RUL - right upper lobe, RML - right middle lobe, RLL - right lower lobe, SRLL - superior segment right lower lobe. Adapted from Marom et al. [109]

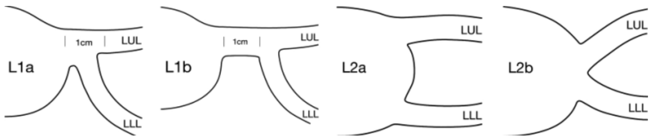

Figure 2.5: Figure showing the variations to the left side of the atrium from a study conducted on 200 patients. Abbreviations: LLL - left lower lobe, LUL - left upper lobe. Adapted from Marom et al. [109]

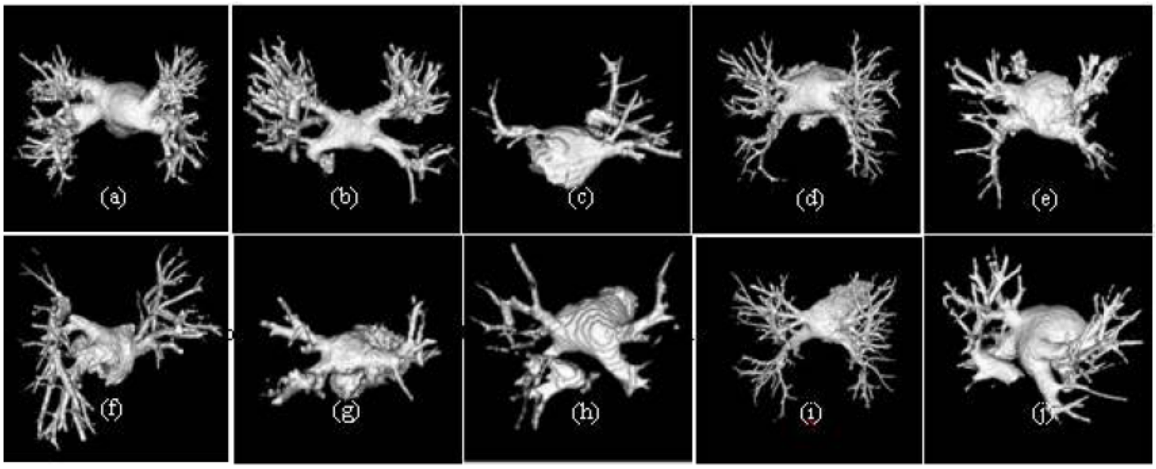

Figure 2.6: Surface reconstructions of the left atrium from contrast-enhanced MR images. Note the variations between different patient subjects

can be unique making careful examination of the anatomy essential prior to any procedure.

2.4.2 Pulmonary vein ostium

Left atrial pulmonary veins have been closely studied because of their relevance to atrial fibrillation and RFCA. Several studies on pulmonary vein ostia can be found (see [186, 187, 42]). The ostium's diameter and shape is of particular interest. This is for two important reasons:

- Determinant of post-ablation stenosis.
- Determinant of the catheter size.

The ostial diameters are measured prior to and after ablation. Such measurements can be used to assess the degree of stenosis. Variations in diameter size have also been studied [155]. There is intra-subject variability: the superior pulmonary vein ostia are significantly larger than the inferior pulmonary vein ostia. In addition, inter-subject variability has also been reported (see Table 2.1).

Mean Ostium Diameters	
Right superior	19.8 mm
Left superior	19.2 mm
Right inferior	16 mm
Left inferior	17.3 mm

Table 2.1: This table shows the mean pulmonary vein ostium diameters on a study based on 42 patients in Scharf et al. [155]

2.5 Pre-procedural planning for ablation procedures

Regardless of the atrial fibrillation procedure, planning the procedure prior to execution is an important and essential step. Careful planning can greatly increase the success of the procedure and reduce post-procedural complications. The planning process primarily involves studying the left atrial anatomy and selecting ablation points. With the advancement of medical imaging over the past decade, atrial fibrillation treatment planning has greatly evolved. The trend is towards improving accuracy of pre-procedural measurements and increasing the detail to which anatomical assessments can be made. More recently, there has been a growing interest in the integration of data from various image sources [163, 79].

2.5.1 Pre-procedural imaging of the left atrium and pulmonary veins

Different imaging modalities have been used for assessment of the left atrial anatomy. The use of conventional angiography has been reported in several past studies for obtaining atrial anatomy. The disadvantages are that it exposes the patient to long doses of x-ray radiation. It also does not give a true three-dimensional view, obscuring vessels due to their overlaps. Vessel overlaps are common in pulmonary vein networks. A different technique used is intracardiac echocardiography, which provides real-time imaging of the pulmonary veins [187]. Although it is useful for guiding a catheter during RFCA, it is not effective for visualising the left atrium and pulmonary vein relationship. These two imaging modalities have also shown some discrepancies in the ostial diameters they measure. These are generally measured using digital callipers [155]. Conventional angiography overestimated while echocardiography underestimated diameters in a reported study [187].

Spatial resolution has been greatly improved by imaging the pulmonary veins using CT, multi-detector row CT (MDCT) and MR angiography imaging techniques. These techniques provide accurate information about the atrial anatomy and have low inter/intra-observer variability. In addition to this, a three dimensional view can be acquired, allowing visualisation of not only the inferior and superior veins but also the anterior and posterior walls of the veins. Surface reconstructions are also possible, by combining information from all three planes (transverse, sagittal and coronal). Views through the volume generated using maximum intensity projections (MIP) can also be obtained. Such views make anatomies relatively easier to assess than with conventional angiography. Furthermore, these imaging modalities have increasingly been used to provide real-time stereotactic (i.e. precise positioning in three dimensional space) catheter guidance during RFCA [41] albeit with the use of real-time catheter information from fluoroscopy. Fluoroscopy remains a commonly used modality for acquiring intra-procedural real-time images.

CT and MDCT scanning is fast requiring a single breath hold and can be completed within 20 seconds. In contrast, MR angiography has much longer scan times. A major disadvantage of CT and MDCT scans is that they expose patients to considerable amounts of radiation: 3.1 - 4.1 mSv. Such doses are likely to cause fatal-radiation induced cancer every 1,240 - 1,640 scans [74]. Furthermore, MDCT can miss important information if contrast material is not used. Thus, 100 ml of nephrotoxic Iodine contrast is normally injected prior to MDCT scans [21]. Despite these risks, some institutions use MDCT in pre-planning RFCA for its quick acquisition times and high resolution images [37]. MR Angiography remains a non-invasive technique for imaging patients prior to RFCA [44]. For a detailed discussion on imaging modalities used in atrial fibrillation, see Maksimović et al. [99].

2.5.2 Pre-procedural measurements

Pre-procedural measurements improve the accuracy of the RFCA procedure and help to avoid post-ablation complications. We list in this section the various different measurements that are taken prior to these procedures (see [99, 37]). Since procedural protocols vary between institutions, measurements listed are not part of every protocol.

- Pulmonary vein diameter size: A determinant of catheter size and post-ablation stenosis. Small diameters (< 10 mm) have high stenosis potential and are best avoided unless they show strong evidence of ectopic focus. It is also important to note that ostial diameters decrease by 32.5% in atrial systole [28]. Thus measurements must be taken and compared within the same phase.

- Left atrial dimension and volume: Dimensions such as mean longitudinal diameter and transverse dimensions are measured. The transverse diameter is defined as the distance between the midpoint of the right- and left-sided pulmonary veins using an oblique axial image. The anteroposterior and longitudinal diameters are measured at the midpoint of the transverse diameter using an oblique axial and a sagittal image [90].

- Examination of anatomy: To find any extra pulmonary veins, especially the right middle pulmonary veins [37]. Also searches for any major anomalies.
- Pulmonary vein trunk length: Distance between ostium and first bifurcation is measured [37]. This distance previously indicated how far from the ostium, ablation could be performed. Ablation is now preferred close to ostia.
- Spatial separation distances of pulmonary veins.
- Amount of fatty tissue between posterior left atrial wall and the oesophagus: These fatty tissues can insulate the oesophagus from thermal injury. In some patients this layer may be absent in certain regions [87].

2.6 Post-ablation management

To monitor any complications arising from ablation, it is now standard procedure to follow-up patients who have undergone an RFCA procedure. For a discussion on complications, see [37].

Imaging after ablation is performed on the pulmonary veins to monitor possible dynamics of pulmonary vein stenosis due to its high incidence rates (30-40%). A Pulmonary vein diameter reduction of more than 50% after 3 months usually indicates potential progressive high-grade stenosis [141]. The left atrial volume is also monitored. In patients with successfully restored sinus rhythm, the left atrial size decreases, although atrial size reduction is also associated with late recurrence of atrial fibrillation [132]. Other remote complications such as pulmonary vein thrombosis and occlusive disease are visible on CT/MRA scans. These cases are very rare and one study reports none in more than 300 cases conducted over a period of three years [37].

2.7 Imaging of the cardiovascular system

Imaging of the left atrium forms an integral part of an RFCA procedure. It is a convenient way of extracting anatomical information of the left atrium and pulmonary veins. In this section, we briefly review the main imaging modalities used for imaging the cardiovascular system. A broader review of cardiac imaging techniques can be found in Webb [177] and Suetens [165].

2.7.1 X-ray

X-ray imaging is a very common and popular technique in medical imaging. X-rays are part of the electromagnetic spectrum, comprised of photons with very high energy. It interacts with tissues in different ways such that different tissues absorb X-rays differently. X-ray imaging produces 2D images of 3D objects. In X-ray imaging of the heart, a radiographic contrast agent is injected into the patient using a catheter This technique is also more commonly known as angiography or angiogram. The catheter is advanced either percutaneously or using the femoral vessels, or by surgical cut-down using the antecubital vessels. X-ray imaging of the heart chambers and vessels reveal the anatomy. Usually a digital subtraction technique is employed. An image taken prior to injecting the contrast is subtracted from the contrast-enhanced image. The result shows only the blood vessels which carry the contrast agent (see Fig. 2.7).

Figure 2.7: A coronary angiogram showing the coronary arteries in an x-ray image

2.7.2 Echocardiography

Ultrasound is often preferred as an inexpensive, quick and non-invasive means of imaging the human body. Ultrasound of the cardiac chambers is also known as Echocardiography. 2D Ultrasound scanners are usually portable and scans can be made at the bedside. The technique relies on sound waves reflected from body tissues much like a sonar. Unlike X-ray imaging, the patient is not exposed to harmful radiations. However, a drawback of echocardiography imaging is the its inability to provide detailed anatomical information. The two main types of echocardiography techniques are as follows:

1. Conventional echocardiography - measures the intensity of the reflected wave along with the time taken for the wave to return to the transducer. The measured signal is produced in an image form.
2. Doppler imaging - Measures the shift in frequency and wavelength of the reflected wave. This determines the velocity of moving tissues based on the doppler effect. A doppler image is reconstructed from tissue velocities.

2.7.3 X-ray computed tomography

X-ray computed tomography or CT is an imaging modality that produces cross-sectional images representing the X-ray attenuation properties of the body. Using a thin X-ray beam, a set of lines are scanned covering an entire field of view (see Fig. 2.8). This is done using either the parallel-beam geometry (Fig. 2.8(a)), or by using a fan-beam geometry (Fig. 2.8(b)). The process is repeated for a large number of angles (Fig. 2.8(c) and (d)) producing attenuation measurements for all possible angles and distances from the centre. These measurements are combined and the actual attenuation at each point on the scanned slice can be reconstructed.

Intensities in CT images are usually expressed in Hounsfield units (HU). This system of units is a linear transformation from the original linear attenuation coefficient measurements into one where air, water and bone are assigned -1000 HU, 0 HU and 1000 HU [165]. Gray level

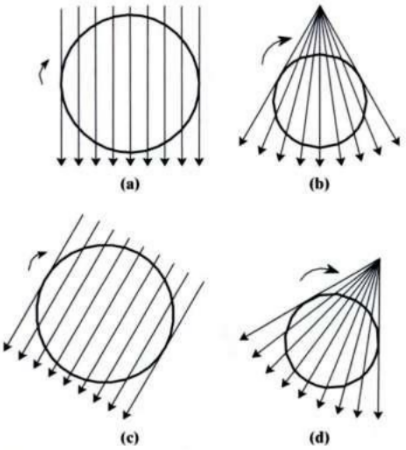

Figure 2.8: The basic scanning procedures in CT. Adapted from Seutens [165]

transformations are applied to such a dynamic range of scales, producing the reconstructed gray level image.

CT provides images which have a high spatial resolution and a comparable short acquisition time. There is also a good contrast between bone and soft-tissues. However, the contrast between different types of soft-tissues can be poor and this is overcome by using contrast agents. CT is preferred to MRI for patients with cardiac pacemakers. Due to its short acquisition times, it is also suitable for patients who may feel claustrophobic inside MRI scanners. A major disadvantage of CT is the relatively high exposure dose of X-ray radiation.

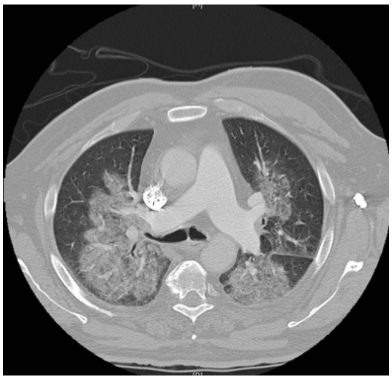

Figure 2.9: A CT scan of the chest

In cardiac imaging, CT is commonly used for imaging the arteries. Ultrafast CT is used for measuring the amount of calcium deposits in coronary arteries [3]. It is also possible to acquire multi-slice images using multi-slice CT (MSCT) and multi-detector helical CT (MDCT) scanners. These are now commonly used for assessing cardiac structure and morphology. They also assist in planning complex invasive procedures such as RFCA [37]. Vessel diameter is an important pre- and post-ablation measurement for the detection of stenosis. It has been shown that although MDCT has good overall sensitivity in detecting vessel stenosis, this sensitivity decreases with an increasing heart rate [54]. An abnormally high atrial contraction rate is a common condition for patients suffering from atrial fibrillation. This leaves a large window of error for stenosis measurements taken with MDCT. A comprehensive study on left atrial anatomy and pulmonary veins using MDCT can be found in [159].

2.7.4 Magnetic resonance imaging

MRI plays an increasingly important role in the imaging of the cardiovascular system. It provides much greater contrast between the different soft tissues than CT imaging. MRI uses strong magnetic fields to produce maps of atomic nuclei. The most commonly imaged nucleus is hydrogen. Hydrogen atoms are present in abundance in the human body. They can be found in water and fat molecules.

The orbital motion of electrons around a hydrogen nucleus give its atom a magnetic moment, allowing it to interact with external magnetic fields as any magnet. During MR image acquisition, the subject is placed inside the bore of a superconducting magnet. The image acquisition involves an initial sequence of exciting radio frequency (RF) pulses and a recording of the emitted signal. The amplitude of the signal is used to generate maps showing the anatomy of the heart. In MRI, it is possible to acquire images in both 3D and 4D.

MRI is commonly preferred as a non-invasive means of imaging the cardiac chambers. The energy of RF photons is much lower than that of x-rays, making it a safer imaging technique. MR images also have medium to high resolution and can be obtained for any desired location and plane. However, the quality of MR images can be affected by some factors:

- Artifacts due to cardiac motion: Constant cardiac contraction and relaxation can cause artifacts resulting in loss of contrast and blurring. A technique known as ECG-gating can be employed to synchronise imaging with the cardiac cycle.

- Artifacts due to respiratory motion: Slices acquired in different breath-holds are displaced and smeared due to the breathing motion of the patient. This can be avoided with the use of fast breath-held or respiratory-triggered acquisitions.
- Artifacts caused due to blood flow: In gradient-echo images, due to blood flow, the imaging plane is constantly replaced by a fresh bolus of non-magnetised blood. The blood excited by the RF-pulse exits the plane before the magnetic resonance signal is acquired. This results in a high signal from each bolus flowing through.
- The partial volume effect: A voxel can contain one or more tissue types. The signal intensity depends on the proportion of each tissue type present in the voxel. This results in blurred image borders between the tissue types.

To avoid the above described artifacts several methods have emerged. A discussion of these methods is beyond the scope of this thesis. See Seutens [165] for further details.

2.7.5 Magnetic resonance angiography

MRA is important to our study for assessing the pulmonary vein anatomy. In MRA, vasculature structures can be studied by exploiting the high magnetic resonance signal of flowing blood. Using a variety of techniques, almost all the signal from static tissues can be suppressed. The three main techniques for clinical MRA are Time-of-Flight (TOF), phase-contrast and contrast-enhanced Gadolinium imaging.

TOF techniques rely on blood-flow related enhancement and do not use exogenous contrast-material. In TOF, the flow-related enhancement is maximised and background tissue is suppressed. Background suppression can be achieved since TOF is a gradient-echo technique; thus exposure to repeated excitation pulses in rapid succession saturates most tissues in an imaging plane. In this way stationary tissues are saturated. Flowing blood, without having experienced any excitation pulse, enters the imaging plane fully magnetised. This enables it to generate a high signal following RF pulses. This results in bright signals in vessels with flowing blood and suppressed dark stationary tissues. Using a Maximum Intensity Projection (MIP), the vessels can be visualised easily.

In phase-contrast MRI, phase data is used to reconstruct either velocity-encoded flow quantification, as described previously, or else MRA images. The reconstruction methods differ for both these applications. For phase contrast MRA, images show the velocity of voxels computed for the flowing blood. They are very sensitive to slow flow and this enables good background suppression. The velocity is computed by combining the net effect of the velocity in each of the three directions (x, y and z). For flow quantification, velocity-encoded images are generated using phase differences which are computed by subtracting the phase shifts generated by flow-encoded and flow-compensated acquisitions. The signal intensity is proportional to the velocity of the blood moving through or within the slice plane. For further details, see Lee and Helmers [83].

Contrast-enhanced MRA employs exogenous agents such as Gadolinium to provide vascular contrast. A bolus of Gadolinium is injected intravenously into the patient and this alters the T_1 and T_2 relaxation times of the blood. After passage through the venous circulation, right heart, pulmonary circulation, and the left heart, the bolus fills the arteries of interest. To achieve high-quality images, the contamination of gadolinium in the arteries must be enough to cause a sufficient T_1 shortening which produces a high-signal in the images. Gadolinium-enhanced MRA can be performed with most MR scanners. They can produce high-spatial resolution images with a broad anatomic coverage.

Artifacts in contrast-enhanced MRA images are not uncommon and the following is a list of their main sources (see [113] for further details):

- Artifacts caused by turbulence and bolus diffusion.
- **Artifacts from physiological motion**: This can be due to cardiac motion and respiration.
- **Ringing artifact**: Caused due to the suboptimal timing of the contrast arrival to the targeted area.

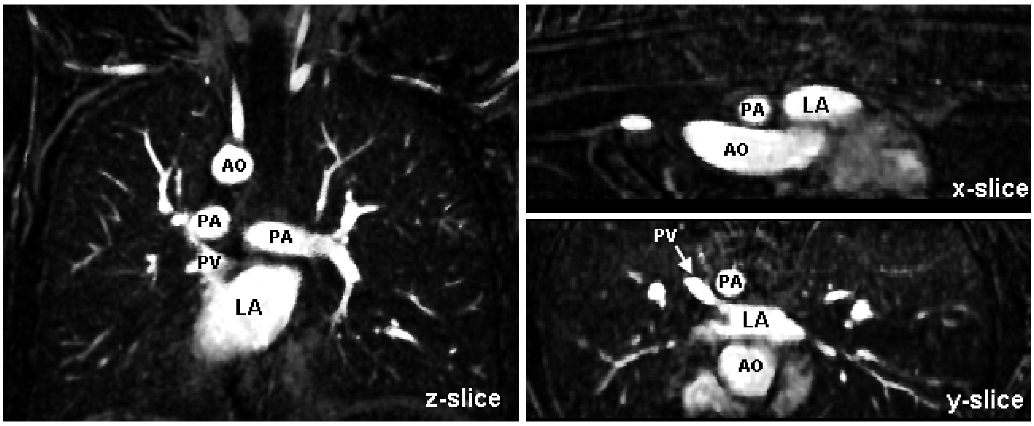

Patient-1

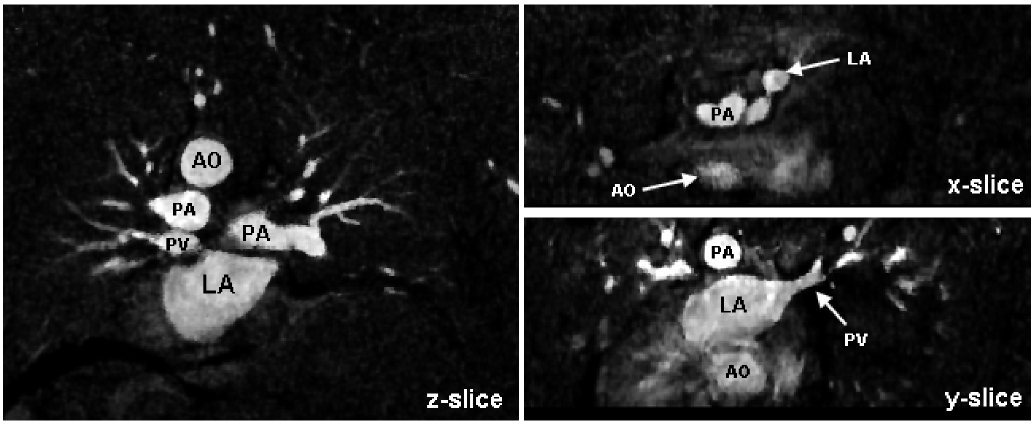

Patient-2

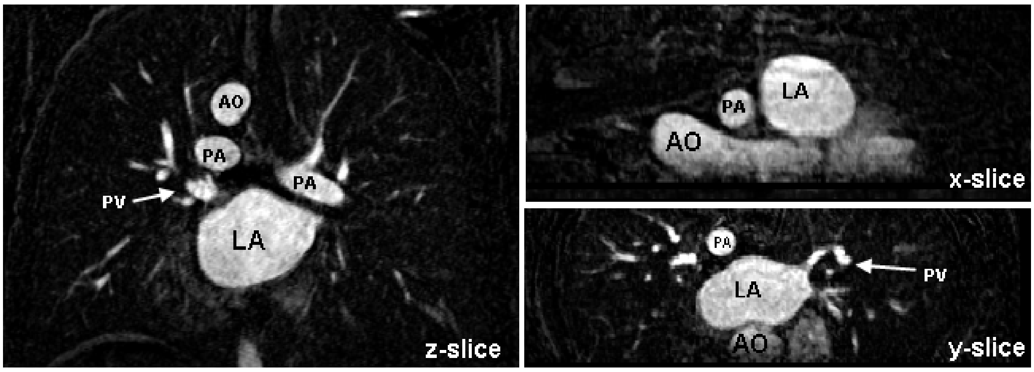

Patient-3

Figure 2.10: Contrast enahnced MR angiography image of the left atrium of three patients with each slice (X,Y and Z) shown. These images can be found in Table 4.1 (pg. 66) as image 27 (top figure), image 30 (middle figure) and image 32 (bottom figure). Labelled structures: LA - left atrium, PA - pulmonary artery, PV - pulmonary vein and AO - aorta.

- **Spatial aliasing**: Caused due to wrap-around in images.
- **Artifacts from mis-registration**: Caused after subtraction of post- from pre-contrast, if the patient moves between the two acquisitions.

The contrasting-agents used in contrast-enhanced MRA are non-toxic and safe. They are a good alternative to the conventional Iodine-based contrast agents used in CT angiography, especially in patients who are allergic to such agents, diabetic patients, or patients who have pre-existing renal disease [83]. The left atrium is commonly imaged using contrast-enhanced MR angiography. The Gadolinium contaminated blood pool in the atrium and the pulmonary veins reveals the anatomy. This is the approach adopted in all our image acquisitions. See Fig. 2.10 for examples of acquired images.

Chapter 3

Technical background: Image segmentation

The advent of cardiac imaging techniques has improved the diagnosis and planning of cardiac malfunction. It is now possible to provide high spatial resolution 3D and 4D images of the heart. Currently, modern imaging technologies include CT and MRI. Both these modalities generate large volumes of images. The clinician is faced with the task of analysing these images before a diagnosis can be made or a treatment can be planned. Image processing is a branch of computer science that deals primarily with the extraction of relevant and interesting features in images. Automated cardiac image processing techniques can summarise relevant information for the clinician, saving time and money for patients and health institutions. A first step for many automated analysis is image segmentation. Image segmentation algorithms play a vital role in cardiac image analysis and its applications. This chapter provides an overview of methods for computer-assisted or computer-automated segmentation of structures from cardiac images. It also presents an overview of vessel segmentation methods.

3.1 Image segmentation

Image segmentation is the process of partitioning an image into regions that are homogeneous with respect to one or more characteristics or features [23, 15]. Consider the domain of the image which is given by I, then the segmentation problem is to determine the disjoint subsets $S_k \subset I$ whose union is the entire domain I:

$$I = \bigcup_{k=1}^{n} S_k \tag{3.1}$$

where $S_k \cap S_j = \emptyset$ for $k \neq j$. In medical images, a segmentation method ideally finds those sets that correspond to anatomical structures or regions of interest. We discuss classical and modern methods of segmentation applied to medical imaging. Several reviews on general segmentation methods [61, 131] and medical image segmentation [148, 25, 15, 166, 29, 6, 136] can be found in the literature.

3.2 Classical methods

The simplest of the classical methods available for segmentation is thresholding. A tissue class is identified by a range of intensities. These ranges are found by partitioning the pixel intensity histogram for each tissue class. Segmentation using thresholding can be difficult to achieve if tissue classes have similar intensities, or if the background pixels have similar intensities to one or more tissue classes (see Fig. 3.1). Some well known automated thresholding techniques include the mode method [139] and the Otsu method [130]. In cardiac imaging, Fernando et al. [46] applied local thresholding methods in X-ray cardiac angiograms. Weng et al. [181] proposed an extension of the thresholding algorithm for segmenting the left and right ventricles from 3D gradient-echo MR and CT images. The algorithm can only approximately locate ventricle borders. Moreover, the algorithm is tested on healthy subjects only.

Edge detection is a commonly used technique in segmentation. An edge is indicated by the rate of change of intensity or gradient near a given pixel. Several methods exist for finding intensity

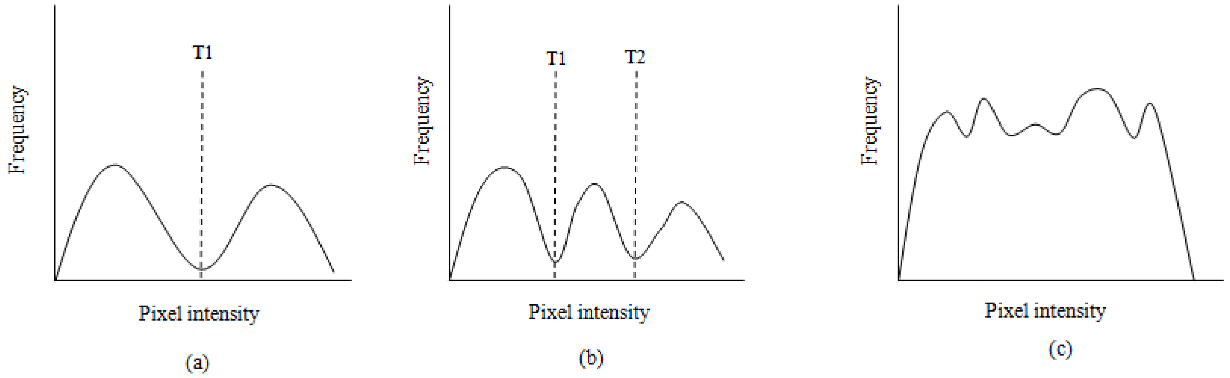

Figure 3.1: The histogram in (a) can be partitioned with a single global threshold value T1 and the image is segmented into the distinct classes. The histogram in (b) is relatively harder to segment as it requires determining the two global thresholds T1 and T2. It is impossible to partition the histogram in (c) using global thresholding.

gradients (see [171]). The magnitude of the intensity gradient is thresholded, allowing strong edges to be distinguished from weak ones. In cardiac images, it is rare to find clear and distinct edges around structures of interest. Edge detection algorithms with enhanced capabilities have been proposed for segmenting cardiac structures of interest. Waiter et al. [175] used a semi-automated edge-detection scheme for segmenting the endo- and epi-cardial borders of the left ventricle in short axis cine-MRI scans. The semi-automated approach begins with the user interactively placing circles to estimate the epi- and endo-cardial borders. The region between the two circles defines a search space for locating edges. The search is performed radially at 2° intervals yielding 180 different points on the circular region. These points give an approximated boundary, which are later polynomially-fitted allowing the missing or mis-represented regions of the border to be interpolated. The result is a smooth epi/endo-cardial border of the left ventricle. The method relies heavily on the correct placement of circles by the user.

Region growing [2] is a segmentation technique for finding group of connected pixels with intensity homogeneity. This remains an attractive method for medical image segmentation as the result of region growing is always a connected region. In medical images, most structures of interest are well connected. Various region growing methods have been proposed for segmenting structures of interest in medical images. Bankman et al. [10] proposed the use of a multi-seed region growing technique for detecting micro-calcifications in mammograms. This approach has also been used for segmenting blood vessels in angiographic images [110]. A major drawback of these approaches is that growing regions easily leak into neighbouring structures. This is common in cardiac images as adjacent structures often have some degree of intensity homogeneity.

Another classical approach is watershed segmentation. Segmentation is achieved with a *watershed transform* of the image (see [147]). It is an intuitive approach where an image can be imagined as a topographic surface. Fig. 3.2 illustrates the watershed transform. The watershed transform is known to have some drawbacks when applied to medical images. These include over-segmentation, sensitivity to noise, poor detection of thin or low signal-to-noise ratio structures [56]. Preprocessing procedures have been proposed to improve the effectiveness of watershed transforms in various procedures. Cristoforetti et al. [36] applies it to left atrium segmentation from multi-detector CT images. After a preliminary filtering step involving anisotropic diffusion [134], the intensity gradient magnitude is computed. The watershed regions are determined using manually selected seeds in each of the six chosen tissue classes (cardiac chambers, pulmonary vein, artery and aorta). These regions are bounded by high gradient magnitude pixels. One of these regions is the left atrium. Furthermore, Grau et al. [56] improve the watershed transform for segmenting medical images by introducing prior information. The algorithm was validated on knee cartilage and brain grey-matter segmentations. Huang et al. [66] proposed a modification of the watershed transform for extracting contours

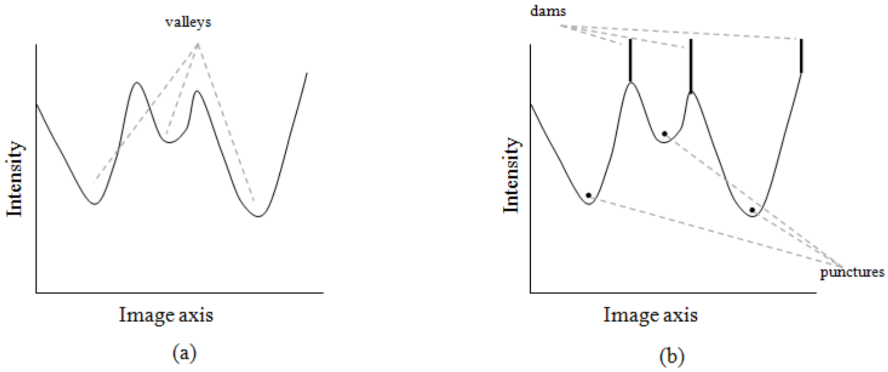

Figure 3.2: The watershed concept: (a) A 1D image defined as a topographic relief with bright pixels as mountain-tops and dark pixels as valleys. (b) Markers selected by an operator are viewed as punctures in the surface of valleys. Water levels rise from punctures and dams prevent mixing of water from adjacent valleys. The dam walls define the watershed transform of the image.

of breast tumors from ultrasound images. For 3D cardiac volumetric images, the watershed transform has also been applied for segmenting the left ventricle chamber [64].

John and Rahn [69] apply a technique similar to the watershed transform for segmenting left atrium from CT angiogaphy and MRA images. The blood pool in the heart chambers is contrast-enhanced in these images. It is assumed that chambers can be separated by making cuts at narrowings of the blood pool. The medial axis transform is applied to these images, treating volumetric objects as a union of balls (see Fig. 3.3). The algorithmic formulation of making cuts at narrowings is achieved using a distance transformation of the binary blood pool, followed by a watershed-like transform of the distance transformation image. The algorithm is fast requiring minimal user interaction. The method relies heavily on the existence of narrowings between heart chambers. In images that require smoothing, such narrowings can be dilated, making it impossible to compute the right cuts. Furthermore, manual thresholding is used to obtain the binary blood pool. This can easily introduce false narrowings within the binary blood pool.

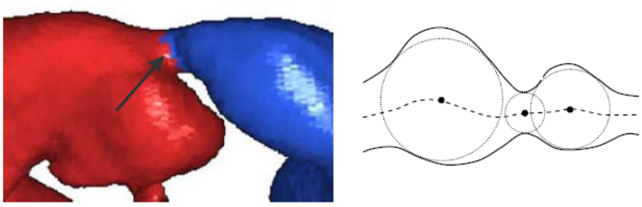

Figure 3.3: A narrowing and possible cut between heart chambers as indicated by the arrow (left image). The medial axis (dashed line) of a two-dimensional object with the medial balls (right image). Image adopted from [69]

3.3 Model-based segmentation techniques

Unlike the classical approaches, model-based segmentation techniques incorporate *a-priori* information about the object to be segmented. This is useful in cardiac images where most objects of interest are expected to have some variation across different subjects. A good survey of cardiac modelling techniques can be found in [49]. We discuss common model-based approaches: Deformable and statistical shape models.

3.3.1 Deformable models

Deformable models are curves or surfaces that are allowed to deform in the presence of external and internal forces. Various deformable models have been proposed and these range from a simple closed curve [76] to more complicated models such as super-quadrics [170]. We classify deformable models into two categories. These are the classical energy minimising model and shape-constrained surface models. Other variants of deformable models also exist. A survey of deformable models is found in [112].

Energy-minimising deformable models

These are energy minimising deformable models that are governed by a pre-defined energy function. The energy function usually contains terms involving the internal energy of the model itself and the external energy from the image. The objective is to find an equilibrium between these two energy terms. Active contours or *Snakes* are the simplest kind of deformable models. See [76, 9] for further details on active contours.

Cardiac structures in MR images pose several challenges to the classical energy minimising snake. Turbulent blood flow in some areas can cause spurious edges affecting the edge potential function. Also, the similarity in image texture within cardiac and neighbouring muscles can make contour deformation excessive. This has necessitated the development of a new generation of active contour models: One such is the stochastic active contour model [137] which integrates modern curve evolution theory (i.e. level set methods) and statistical modelling. In this model, an energy functional is defined which combines stochastic region-based and edge-based information with shape priors of the heart and local properties of the contour. The algorithm is validated on the left ventricle boundary. A different variation of active contours which does not require an edge-dependent functional has also been proposed [24]. Here an energy functional term that depends on the object and background's intensities is minimised.

Most active contours require good initialisations. In most cases, the initial contour is preferably placed inside the object of interest to obtain good results. Also, in the absence of image forces or the presence of weak image forces, the deformable model is known to tend to shrink. In addition to this, deformable models only possess generic a-priori knowledge. In order to avoid these, Rueckert and Burger [150] proposed using a Geometric Deformable Template (GDT) for modelling the LV and RV from 4D MR images. In the GDT, the continuity stabilisers are replaced by a stabiliser on the deformation field between an equilibrium model and a deformed model. This attracts the GDT to shapes that are similar to the equilibrium model. In addition to this, specific prior knowledge about the expected object shape is incorporated using a probabilistic framework where the energy minimisation step is formulated using the Bayes theorem. The prior distribution of expected shapes is modelled using a Gibbs distribution.

Shape-constrained deformable surface models

It is common for cardiac structures of interest to exhibit shape variability across different patient subjects. To make deformable models robust to shape changes, it is useful to incorporate prior shape information into the classical model. A statistical shape model encodes shape and can be associated with the internal energy of the deformable surface. This deformable model technique primarily involves two steps: shape extraction and model-fitting. Prior shape information is extracted and learnt from a set of training images. In shape extraction, a primitive shape such as a sphere is placed inside a structure of interest in a training image [182]. The sphere deforms freely into the structure of interest. A mean shape is constructed from these extracted shapes, and can be represented by its vertex co-ordinates or mesh points [178]. A shape model is then constructed using the first m-modes of variation. An internal energy function is formulated which utilises the difference vectors between two neighbouring mesh points on both the shape and deformable models. In the model fitting step, these difference vectors are compared and any deviation from the shape model is penalised.

Kaus et al. [77] use a similar approach to segment the left ventricle in short and long-axis cardiac MRI. They integrate various sources of prior knowledge learned from annotated images into the deformable surface model. These various sources of prior information include inter- and intra-subject shape variability, surface features and spatial relationships between the endoand epi-cardium. Other priors such as intra- and inter-subject variability are modelled using a shape model, following the same technique as described in Weese et al. [178]. In addition to this, surface features are modelled with a K-means clustering scheme. To prevent the two separate surface meshes from intersecting one another due to attraction to false features, the spatial relationship between the epi- and endo-cardium is also modelled. See Fig. 3.4 for model initialisation and adaptation steps.

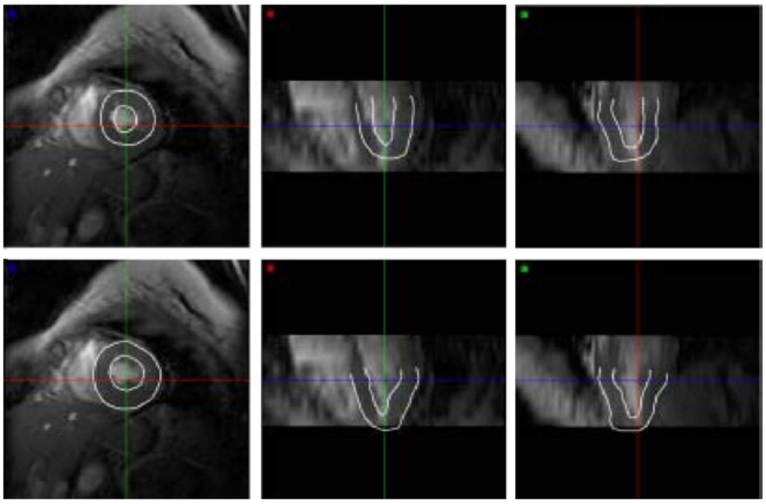

Figure 3.4: Top row: After initialisation of the end-systolic model. Bottom row: After automated adaptation. Image adopted from [77].

Lorenz and Berg [95] proposed using such shape-constrained deformable surface models for modelling all the four chambers of the heart, including the coronary arteries. The external energy functional is similar to that in Weese et al. [178], where triangular surface mesh barycenters move towards image features. The internal energy is again constrained with a shape model. The important difference here is the use of primitive shapes in the shape model training phase: spheres for ventricles/atria and cylindrical tubes for vessels. The method does not particularly address the anatomic variability of the left atrium. The anatomic configuration of the mean surface model of the left atrium depends entirely upon the first training set sample, as it is used in initialising the multi-surface model. This restricts the model to fit to any other anatomic configuration. See Fig. 3.5 for an illustration of the four-chamber model and an example of model adaptation to a CT image.

The shape-constrained deformable surface model has been applied to the problem of left atrium

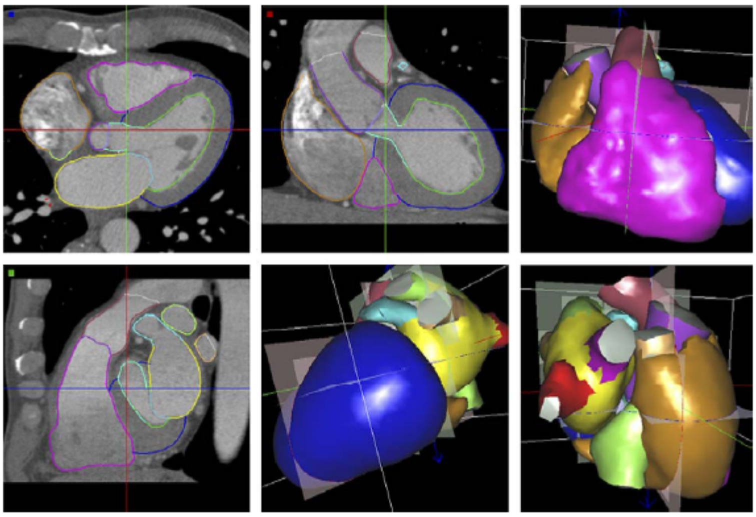

Figure 3.5: The four-chamber model adapted to a multi-slice CT image. The image shows three orthogonal cut planes and three renderings of the surface model from different perspectives. Image adopted from [95].

segmentation. Berg and Lorenz [94] use this technique to segment the left atrium in CT images. Mean model building and model-fitting steps are similar to the one described in Lorenz and Berg [95]. The authors address the problem of anatomical variants of the left atrium, but only validate it on a single anomalous case. The most interesting anatomical differences occur to the right side [109]. Meyer et al. [115] use a similar method for segmenting the left atrium from rotational X-ray angiography images. Using shape models for segmenting the left atrium encounters the inevitable problem of finding enough rarely occurring variants for training the shape model. A second major drawback of using these approaches is that they require good initialisations.

3.3.2 Level set methods

Most deformable models are not designed to deal with topological changes. To handle topological changes as contours deform, Osher and Sethian [129] introduced level set techniques. They rely on a radical shift in how evolving curves or surfaces are modelled.

The level set of a real-valued function ϕ of n variables is a set of the form (c is a constant):

$$\{(x_1, \ldots, x_n) \mid \phi(x_1, \ldots, x_n) = c\} \tag{3.2}$$

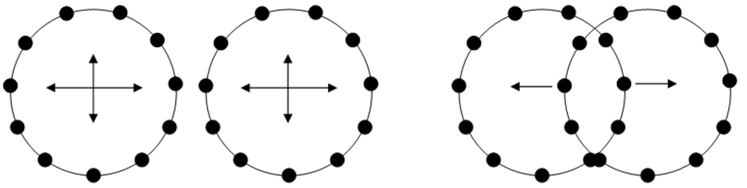

Figure 3.6: Tracking the merging of two closed curves in the 2D case. The curves are discretised using marker points as indicated by black circles. Tracking these points through time becomes difficult when the curves merge as indicated in the second figure. The arrows indicate direction of curve evolution

Instead of following the surface itself, the level set approach takes the original surface and adds an extra dimension of time t to it. The new higher dimensional function is a *hypersurface* which is allowed to move along its gradient field at a certain speed. At any time instant, the zero level set of the hypersurface defines the evolving surface. Consider a closed surface C, which can be implicitly defined as the zero level set of a higher dimensional function $\phi(x, y, z)$:

$$C = \{(x, y, z) \mid \phi(x, y, z) = 0\} \tag{3.3}$$

The initial surface $\phi(x(0), y(0), 0) = 0$ is usually defined manually by the user. The higher dimensional function $\phi(x, y, z)$ can then be constructed by representing it as a signed distance function to the surface:

$$\phi(x, y, z) = \pm d(x, y, z) \tag{3.4}$$

where $d(x, y, z)$ is the Euclidean distance from the point (x, y, z) to the surface C. Hence, for points on the surface, $\phi(x, y, z) = 0$. For points inside and outside, the sign is assigned accordingly: negative sign (-) for points outside the surface and positive sign (+) for points inside.

Once the hypersurface $\phi(x, y, z)$ is determined, equations for its motion can be formulated. We begin by assuming that the surface C moves in an outward or inward normal direction $\vec{n}$. The normal to the surface can be conveniently derived from $\phi(x, y, z)$. It can be shown that [129]:

$$\vec{n} = -\frac{\nabla\phi}{|\nabla\phi|}, \; \textit{where} \; |\nabla\phi| = \sqrt{(\phi_x^2 + \phi_y^2 + \phi_z^2))} \tag{3.5}$$

Assume also, that the surface evolves under a speed function F. Using Eq. 3.5, the motion of the function $\phi(x, y, z)$ can be derived [129]:

$$\frac{\partial \phi}{\partial t} = -F|\nabla \phi\,| \tag{3.6}$$

The computational schemes involve using a discrete grid in $x - y - z$ domain and substituting finite difference approximations for the spatial and temporal derivatives. As an illustration, a uniform mesh of spacing h can be used for C. Assume grid nodes coordinates on this mesh to be (i, j, k). Using the notation ϕ^n_{ijk} to be the solution to $\phi(ih, jh, kh, n\triangle t)$ where $\triangle t$ is the time step, an approximation scheme for Eq. 3.6 can be given as:

$$\frac{\phi^{n+1}_{ijk} - \phi^n_{ijk}}{\triangle t} + F|\nabla_{ijk}\phi^n_{ijk}| = 0 \tag{3.7}$$

Here, a forward difference in computing the derivatives has been used. The above proposition includes the assumption that the surface stays smooth through time. In all but the simplest flows, this smoothness is soon lost. Sharp corners can develop in an evolving front and the derivatives at these points cease to exist. By adding a modified speed function, these sharp corners can be prevented. The modified speed function is of the form:

$$F = 1 - \epsilon\kappa \tag{3.8}$$

where κ is the curvature of the front defined as $\kappa = \operatorname{div}\vec{n}$ and ϵ is the *viscosity* term. It can be shown that for $\epsilon > 0$ the moving front stays C^∞-continuous, as desired [160]; thus preventing singularities and sharp corners. In addition to this regularisation term, it may be desirable to halt the evolution at the object boundaries. the speed function is then multiplied by the term:

$$g_I(x, y, z) = \frac{1}{1 + |\,\nabla\,(G_\sigma * I(x, y, z))|} \tag{3.9}$$

where the expression $G_\sigma * I$ denotes the convolution of the image with a Gaussian filter. The $|\nabla\,(G_\sigma * I(x, y, z))|$ term is close to zero in homogeneous regions, and has a high value at edge locations due to high image gradient. Incorporating the speed function $F = 1 - \epsilon\kappa$ into Eq.

3.6 turns it into a special case of the well-known *Hamilton-Jacobi* equation [13]. The solution to these equations were introduced by Crandall and Lions [35] and guarantees smoothness. Efficient numerical schemes such as the narrow band method have been proposed [161].

A technique fundamentally different from the level set method discussed so far, yet in some ways similar is the *fast marching* method [162]. It is a fast numerical algorithm available as an alternative to level set methods for fronts which always move in the same direction and also does not involve a change in topology. The idea is to discretise the space and compute the distance function by successive updates at each mesh point. Consider the evolving front C drawn on a mesh of grid points. A boundary value formulation of the evolving front can be derived by considering the crossing time function $T(x, y, z)$ at each grid point. The crossing time gives the arrival time of the front at each of the grid points. Using the fact that $distance = rate \times time$, it can be shown that:

$$|\nabla T|F = 1, \qquad T = 0 \text{ on } C \tag{3.10}$$

This is the *Eikonal* equation, and the front motion is characterised as the solution to this boundary value problem. Numerical schemes for solving this can be found in [162].

Level set methods have been applied to medical image segmentation problems and are sometimes preferred for their ease of implementation and topology-change handling capabilities. Improvements have been made to the classical level set approach. Much of these improvements involve enriching the speed term. A combination of the fast marching and narrow band methods can be used [103]. The fast marching method can be used to accelerate the initial front from the seed structure to the near boundary. The narrow band approach is then used to get more accurate results. The method is validated on liver CT images.

Although the implementations of level set methods and active contours are significantly different, their fundamental goal is to model the evolving surface. This has made possible the use of some variations of the energy functional developed solely for active contours. One such example is [24] where an active contour technique which does not rely on edge gradients is proposed. The constraints imposed are region-based (i.e. intensity averages) to prevent mis-segmentation due to spurious edges. Chenoune et al. [27] take this idea to their level set technique for segmenting the left-ventricular cavity in cine-MRI scans. The goal is to assess myocardial deformations. The speed term of the level set is modified to include the region-based constraint. The other classical contour constraints remain the same. The results indicate a substantial improvement in border detection of left ventricular cavity.

Caiani et al. [22] uses a simple edge-based speed term for detecting the endocardial and epicardial borders of the left ventricle. More recent works have involved incorporating *a priori* shape information. Leventon et al. [89] evolves the higher dimensional surface based on local (i.e. image gradient) and global (i.e. shape information) priors. In tagged cardiac MR images, due to the high clarity of tagged lines, the propagating front can leak into these tag lines if a simple gradient-based speed reciprocal (Eq. 3.9) is used. Qu et al. [142] modifies the speed term by including a faster halting term than the one in Eq. 3.9. For stopping before tagged lines, a texture feature term for vertical tags is added to the speed function. The algorithm was validated on short-axis left ventricle tagged MR images.

3.3.3 Statistical models

Deformable models (see section 3.3.1) may not incorporate a-priori information about an object's expected shape. See [149] for deformable models with shape priors. Shape priors are powerful constraints and very useful in segmenting medical structures most of which vary in size, shape and appearance. Statistical models capture the variability of a statistic in a training set. Using Principal Components Analysis (PCA) [71], this variability can be decomposed into separate modes. In statistical models capturing shape, the inter-variability between the spatial coordinates of sampled points of an object's contour is analysed. These models are then used to fit to unseen instances of the shape. To exploit the intensity features in an image, this model of shape has been extended to include a statistical model of appearance. Statistical shape and appearance models have found many applications in medical image segmentation.

Active shape models

Active shape models (ASM) incorporate statistical models of a set of training shapes allowing it to fit to unseen instances of the shape. The shape of an object can be represented by a set of n landmark points sampled on its boundary. A statistical shape model can be constructed using landmark points from each example shape. The shape examples are aligned to a common frame using a Generalised Procrustes Analysis [55]. By concatenating the coordinates of the landmark points, a shape vector for each example shape is obtained. Cootes et al. proposed that the set of shape vectors can be modelled using a multivariate Gaussian distribution [32]. The modes of variation, which are the predominant ways in which the points of the shape tend to move together, can be found by applying PCA to the deviations from the mean. See [31] for an elaborated description of ASM.

Establishing point correspondences between members of the training set is an important problem in ASM. Manually landmarking salient features in shapes is a time-consuming and error-prone process. The Iterative Closest Point (ICP) algorithm is a commonly used algorithm for establishing point correspondences [14]. The basic ICP has been extended in [43, 143]. Leventon et al. [89] perform statistical analysis on the signed distance maps of a set of aligned shapes. It relies on an important assumption that corresponding points of two shapes are closest. Frangi et al. [51] use atlas deformation for propagating landmarks. A probabilistic atlas is constructed from training examples, followed by a non-rigid registration of every sample to the atlas. Landmarks are extracted from the atlas using surface triangulation and propagated to each training sample. Other techniques known as statistical deformation models (SDM) proposed by Rueckert et al. [151] utilise the deformation fields obtained by morphing training samples to a reference image using non-rigid registration. The method is applied to structures having a rigid shape such as the brain. It is not clear if the method is feasible for non-rigid structures such as the atrium.

ASMs have been applied to several cardiac segmentation problems. Cootes et al. [30] applied ASM to echocardiographic images for segmenting the cardiac chamber. Part of the right ventricle wall, the entire left ventricle and part of the left atrial wall was segmented. The technique was also applied to MR images of the lower abdomen. Here, the prostate gland was modelled and located. The technique was only tested on healthy patients and normal data. Its performance on abnormal data is unclear.

Lötjönen et al. [97] construct a 3D statistical shape model of the heart (atria, ventricles and epicardium) by combining information from both long and short-axis MR images. The shape variations were modelled in two ways: using PCA and Independent Component Analysis based shape models, and with non-parametric distributions. Non-parametric distributions were proposed to capture the twisting motion of the heart, as opposed to a Gaussian normal distribution. The shape model was evaluated on the basis of how well it segmented an unseen instance. Probabilistic atlases performed better than shape-based models, especially when the training data was relatively small. When the training set is large, and point distribution models have enough degrees of freedom to model all variabilities in the shape, shape-based models may outperform probabilistic atlases. A drawback of this segmentation technique in relation to left atrium segmentation is that it does not model the pulmonary veins.

Active appearance models

ASMs only use shape and sparse image intensity information. They do not utilise the overall texture information and pixel intensities. Moreover, a correlation between the parameters of the shape model and the texture model can exist. Active appearance models (AAM) incorporate statistical models of texture along with shape allowing it to fit to unseen instances of shape and appearance. For an elaborated description of AAM, see [31].

Active shape and appearance models have been applied to a wide variety of cardiac segmentation problems. The original technique has been applied to a hybrid technique which uses both ASM and AAM and was proposed by Mitchell et al. [117]. AAMs fail to produce precise borders in segmentation. This is since AAMs are optimised for global appearance and thus less sensitive to local structures and boundary information. ASM use local intensity information and tend to locate local structures well. The hybrid approach uses both ASM and AAM matching to obtain two different sets of shape and pose parameters. These parameters are then combined using a weighted average for further iterative optimisation until the error between model and image is minimised. The technique was validated on left and right ventricle MR images.

Most AAM techniques segment a single slice at a time. Cootes et al. proposed a coupled view AAM [33] where the frontal and side views of faces are segmented simultaneously by building separate models for each view. A combined model for both views was then constructed. Lelieveldt and other researchers [86, 126] have extended this technique for medical images exploiting shape and appearance correlation between different views (i.e. short-axis, long-axis, perfusion, etc.) of the same object. The multi-view model is constructed by aligning the training shapes for different views separately, and concatenating the aligned shape vectors for each of the view into one vector. PCA is applied on the combined covariance matrix. A similar method is also used for the intensity model.

Until recently, most applications of AAM applied the original concept to 2D segmentation problems. Extensions have been proposed for higher dimensions. In 3D, obtaining corresponding boundary points between landmark points is non-trivial. In 2D, these intermediate points can be trivially obtained by evenly sampling points in between landmarks. To overcome the problem in 3D, Lorenz and Krahnstover [96] construct a 3D template mesh from a sample shape and uses this to deform to other shapes in the training set. The deformed templates are then used to extract landmark and intermediate points. Mitchell et al. [116] use a normalised cylindrical coordinate system to extract intermediate points. Landmark points are mapped to this new coordinate system, and intermediate points are obtained by interpolating points in between. They also solve shape alignment problems in 3D using Besl's algorithm [14] and optimising a seven-element pose vector containing Quaternions, analogous to the Procrustes analysis in 2D. For 4D (3D + Time) images, Lapp et al. [82] use statistical deformation models for extracting landmarks. Medical images in higher dimension also frequently include time sequences. Bosch et al. [18] apply AAM to time-sequences of 2D cardiac Echocardiograms. The idea is to concatenate the shape and appearance vectors from all time frames into one vector and apply the PCA. The technique is validated on the left ventricular cavity.

Despite the success of AAM in medical image segmentation, it has some limitations. AAMs fail to fit to abnormal data when trained on normal patient data. This is evident when fitting to target objects with grey-level appearance significantly changed due to gross local disturbances caused by tumors, artificial implants, tag markers. Recently, some researchers have concentrated on producing more robust forms for both ASM and AAM (See [11, 85, 73]). Most techniques use outlier detection. Beichel et al. [11] analyses the probability density function of the residual difference between model and image to find the inlier and outlier pixels. Only inlier pixels are used to update the model during the fitting process, thereby suppressing the effect of outliers in abnormal data. Lekadir et al. [85] used ratio of inter landmark distances as a discriminant for detecting outliers in ASM. Outliers are expected to produce extreme ratios which are easily detected using statistical tolerance analysis (see [58]). The technique is validated on the cartoid artery and myocardial borders of the left ventricle in MR images.

3.4 Vessel segmentation

Segmentation of vessels is important to our study since the pulmonary veins are important components of the left atrium. Vessel segmentation is of growing interest as it allows the analysis and visualisation of complex vessel networks within the human body, especially in the vicinity of major organs. Once vessels are segmented, they can be quantified and further assessments are made. A 3D pre-filtering step for enhancing vessels is essential before a segmentation method can proceed [4]. We briefly discuss some of the well-known pre-filtering techniques (see [167]).

3.4.1 3D vessel pre-filtering techniques

Non-linear anisotropic filtering

Anisotropic diffusion filtering has been studied extensively in image processing (See [134, 179]). These are edge-preserving smoothing filters. The idea is to encourage smoothing within a region in preference to smoothing across the boundaries. Interestingly, it can be shown that anisotropic diffusion smoothing is analogous to heat diffusion, and can be represented by the simple heat diffusion equation [134]:

$$\frac{\partial I}{\partial t} = c\nabla^2 I \tag{3.11}$$

where c is the conductance coefficient, I is the image and ∇^2 is the Laplacian operator. By selecting a suitable conduction co-efficient, selective diffusion can be achieved. Perona and Malik [134] suggest using a function of the edge magnitude:

$$c = g(\parallel E \parallel) \tag{3.12}$$

For preserving vessel structures, the above approach has been extended by feeding back any extra information about vessels. Orkisz et al. [128] use median filters and local vessel orientation for selectively smoothing vessels. The method performs well on straight vessel segments but not as well in strongly curved vessels. In regions of high vessel curvature, the median filter mask does not adapt itself accordingly but maintains the thin-lined shape. Manniesing et al. [105] introduced a vessel smoothing filter based on the *vesselness* measure due to Frangi et al. [50] (see following section). Selective non-linear smoothing within vessels is achieved by targeting regions of high vesselness.

Filtering with second-order structure

A new generation of vessel enhancing filters exploit second-order information. These filters exploit the amount of intensity variation after the vessel image is smoothed with a Gaussian of appropriate width. As it is common for vessels to vary in width, a multi-scale analysis is necessary, whereby smoothing is performed at various different scales that closely match the vessel widths. These filters have been simultaneously proposed in [153, 50] and earlier in [80].

To extract intensity variation, the second derivative of the Gaussian is required. A convolution of the second derivative of the Gaussian with the image gives intensity variations. This second derivative Gaussian kernel can access the inside and outsides of a vessel and this is illustrated by the shape of its curve (see Fig. 3.7). Applied to a vessel of diameter $d = \sigma$, this convolution with the second-order Gaussian kernel probes the inside and outside contrasts of the vessel.

This is inside and outside the range $(-\sigma, +\sigma)$. As Gaussian convolution and differentiation operations are commutative, computing the second derivative of the image that is convolved with the Gaussian gives the equivalent result. The Hessian matrix $H(\mathbf{x})$ defines the second derivative information at each point in the image $I(\mathbf{x})$:

$$H(\mathbf{x}) = \begin{bmatrix} \frac{\partial^2 I}{\partial x^2} & \frac{\partial^2 I}{\partial x\,\partial y} & \frac{\partial^2 I}{\partial x\,\partial z} \\ \frac{\partial^2 I}{\partial y\,\partial x} & \frac{\partial^2 I}{\partial y^2} & \frac{\partial^2 I}{\partial y\,\partial z} \\ \frac{\partial^2 I}{\partial z\,\partial x} & \frac{\partial^2 I}{\partial z\,\partial y} & \frac{\partial^2 I}{\partial z^2} \end{bmatrix} \tag{3.13}$$

The Hessian matrix can be analysed using a standard eigen decomposition. Assuming an ordering of the eigenvalues of the Hessian as:

$$|\lambda_1| \leq |\lambda_2| \leq |\lambda_3| \tag{3.14}$$

The sizes of the eigenvalues are proportional to the amount of intensity variation and the corresponding eigenvectors $\mathbf{e}_1, \mathbf{e}_2, \mathbf{e}_3$ indicate the directions of these variations. For an ideal bright line on a dark background, maximum intensity variation is expected in the two orthogonal directions $\mathbf{e}_2$ and $\mathbf{e}_3$ and, minimum intensity variation is found in $\mathbf{e}_1$. As vessels are rarely ideal bright lines, authors have proposed similarity measures that attempt to distinguish line-like structures from other possible structures such as plate-like or blob-like. Frangi et al. [50] apply ratios of the eigenvalues for distinguishing line-like structures. An exponential function defined on these ratios yields maximum response at the vessel axis, thereby giving a degree of *vesselness* at each voxel in the image. As the filter is tested at multi-scale resolutions, before a response can be computed, it is necessary to provide the filter with the correct scales. The range of scales must correspond to vessel diameters in the image.

Thus, by exploiting the second-order structure of images convolved with a Gaussian, voxels lying within tubular structures such as vessels can be found. However, this is not sufficient for segmenting tubular structures as these filters only take into account local information. For example, structures that have local tubular-like shapes cannot be distinguished. Nevertheless, it is a powerful pre-filtering step that is useful for segmenting vessels.

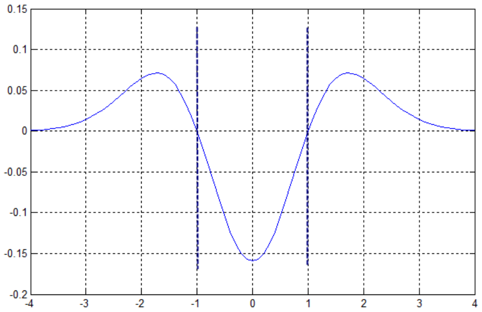

Figure 3.7: The second derivative of the one-dimensional Gaussian kernel of width $\sigma = 1$: $y = \frac{1}{\sqrt{2\pi}}(x^2 e^{-\frac{x^2}{2}} - e^{-\frac{x^2}{2}})$. The shape of the curve shows how convolution with this kernel can achieve a probing behaviour inside/outside the range (-1,1) - analog to the 3D case of a vessel with radius 1.

3.4.2 3D vessel segmentation

The literature for vessel segmentation is rich with various different kinds of approaches. For a survey on vessel segmentation, see [78, 168]. Although there are many ways to classify the different approaches, we use the classification given in Suri et al. [168]. The two main categories are the skeleton and non-skeleton based. The skeleton based techniques first compute the vessel centrelines, and then reconstruct the vessels from these centrelines. The non-skeleton based techniques determine vessel structures in 3D directly. We discuss these techniques in detail.

Non-skeleton based techniques

The simplest of this category of techniques are threshold-based. In many medical images, vessels appear as brighter than other structures, e.g. in contrast-enhanced or time-of-flight (TOF) MR images. Nevertheless, simple thresholding will usually fail to segment the vessels. This is due to the variation of intensities within the vessel. A local adaptive thresholding technique can be more effective. Wilson et al. [183] propose a technique for segmenting vessels from TOF-MRI images. Using the Expectation-Maximisation (EM) algorithm [40], the parameters of the intensity distributions of TOF-MR images are predicted. These parameters are used to classify

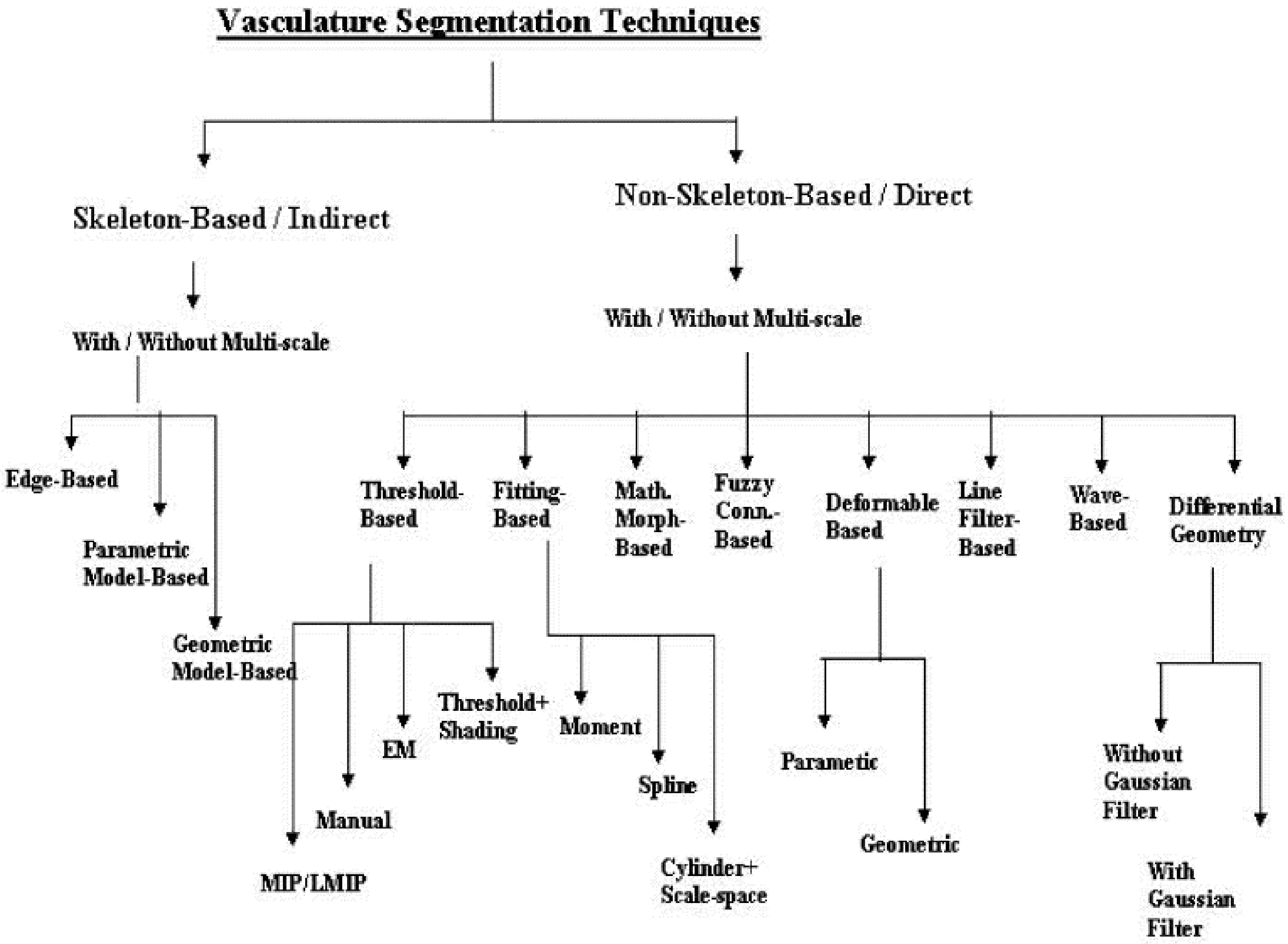

Figure 3.8: A classification of vessel segmentation techniques. Adapted from [168]

the voxels into artery and non-artery voxels. The algorithm is adaptive because the model fitting is performed recursively so that classifications are made on local sub-volumes of data. Major disadvantages of this technique include the relatively high computational expense and absence of validation on non-healthy patients.

Because of the tubular shapes of vessels, they can be modelled using generalised shapes such as cylinders, B-splines and triangulated surfaces. Frangi et al. [48] use a B-spline surface resembling a flexible cylinder to model vessel walls. In the first step, an initial spline curve is used to fit to the vessel centreline. An energy functional is derived based on the vesselness functions (see section 3.4.1) and curve continuity constraints similar to active contours. This energy functional is minimised to obtain the centreline. Using this centreline, the B-spline surface model deforms to fit the vessel walls by minimising a second energy functional. For other model-fitting techniques, see [125, 174].

The frequency domain of images is commonly used in feature search. Bhalerao and Wilson [17] applied fourier transforms at mutli-scale resolutions [184] for estimating 3D local features in images. The method relies on the fact that, after smoothing an image, small neighbourhoods within interesting features such as vessels can be approximated with a 3D Gaussian. The fourier transform of the 3D Gaussian also yields a 3D Gaussian with its spectral energy distribution dependent on the type of feature. This can then be used as a discriminator for locating desirable features. Bhalerao et al. [16] further extended this work for inferring complete vascular structures. An iterative model-fitting technique is employed where the model approximates local structures of vessels using a 3D Gaussian function, similar to that in [17]. The maximum likelihood of the parameters of the Gaussian function is estimated by minimising the residual between model and data. To draw inferences about the global structure of vessels, a Bayesian formalism is employed. The technique was applied to retinal images [16] and the cerebral vasculature [120, 17]. It was successful in identifying both large and small vessels, and detecting aneurysms. A drawback of the approach is the manual selection of appropriate resolution scales.

Udupa and Samarasekera [173] developed the concept of fuzzy connectedness in images by defining a strength of connectedness between every pair of voxels in a 3D image. This is done by considering all possible connecting paths between any two voxels. The strength assigned to a path is defined as the weakest affinity between successive voxels along the path. Affinity is in turn defined as the degree to which voxels hang together locally in the image. Two voxels have high affinity if their intensities are homogeneous and they are spatially close to each other. The notion of scale was also introduced in fuzzy connectedness by Saha et al. [152], making it possible for more accurate segmentation of vascular trees. The technique has been extended for separating artery and veins [84].

More recently, Friman et al. [52] used a multiple hypothesis tracking algorithm for segmenting low contrast liver vessels from CT angiography images. The technique uses 3D vessel templates for finding tubular-like structures. The vessel template is an image patch containing an idealised vessel segment. The template is fitted to an image of a vessel using a least-squares approach. For traversing through bifurcations, a search tree is built to investigate the possible vessel paths.

Skeleton-based methods

A natural way to detect a vessel is to find its medial axis also known as its centreline. Vessel centrelines greatly simplify visualising dense vessel networks such as the cerebral vasculature. They can also be used to obtain symbolic representations of vessels. Vessel trees are one such representation, where segments of vessel centrelines are joined together using a parent-child relationship [20].

Manniseng and Niessen [106] use level set techniques for extracting the medial axes of the carotid arteries. The method uses skeletonisation of the evolved surfaces. Wink et al. uses the second-order filter discussed in chapter 3.4.1 for tracking vessels using a minimum cost path strategy [185]. Starting from a seed point, a minimum cost path algorithm computed the best path through the set of voxels. This essentially produces a path through the highest vesselness voxels, giving the centreline. A major drawback of this approach is it requires the user to select the start and end points of the vessel to be segmented.

A different centreline detection approach is to track *ridges* in images. In these approaches, intensity images are considered to be 3D elevation maps in which intensity ridges approximate the centrelines of tubular objects. Intensity ridges within vessels can be generated using a multi-scale Gaussian blurring of the image. These scales must match the vessel widths. As ridges in a 3D images are local maximum points in at least two directions, they are found using an eigen-decomposition of the Hessian. It is also important to track these ridge points in a sequential fashion such that the order of centreline points is established. Aylward and Bullitt [7] implement ridge search and tracking using a combination of 1D and 2D searches. A 1D line search in the direction of maximum gradient initially takes the tracker to a point that is a 1D maximum. From this point, a plane orthogonal to the underlying ridge is constructed using the eigenvectors of the Hessian. A plane search follows extracting ridge points using the Hessian eigen-decomposition, as the plane moves each step (see Fig. 3.9).

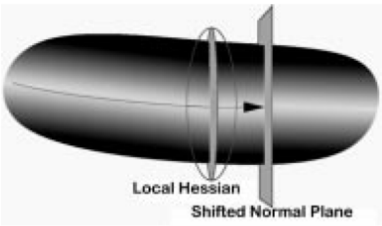

Figure 3.9: An illustration of the ridge tracking process using search planes. Adapted from Aylward and Bullitt [7]

Xue et al. [189] extracted the cerebral vasculature of neonates using a similar approach. They minimise a ridge function $J(x)$ unifying the criteria that finds a ridge in 3D images:

$$J(x) = \mathbf{e}_1.\nabla_x I + \mathbf{e}_2.\nabla_x I \tag{3.15}$$

where $\nabla_x I$ is the gradient of the image I at x. At a point x on the ridge, $J(x)$ attains a minimum. Starting from the seed, a Quasi-Newton minimisation is used to find the minima. Once on the ridge, subsequent ridge points are found by moving small distances along the ridge direction (i.e. $\mathbf{e}_3$) and re-minimising $J(x)$ from that new point.

3.5 Summary

This chapter has presented a review of segmentation techniques which have been previously applied to cardiac segmentation and vessel segmentation. Table 3.1 lists the important cardiac segmentation techniques discussed, the modalities they use, the degree of automation and the structures they segment. They are listed in chronological order.

The popularity of model-based methods in cardiac image segmentation is apparent. They incorporate *a priori* knowledge of the object to be segmented and this is a useful and important feature of these methods. Deformable models provide smoothness constraints and statistical shape models provide shape information. Both have limitations; deformable models are limited by the smoothness constraints on the variability of the object it can segment, shape models are biased to initialisations. In vessel segmentation, there is a growing interest in extracting vessel centrelines. This is primarily to analyse dense cerebral vasculature networks. Most techniques exploit the second order structure of images. A drawback of these approaches is the use of multi-scale analysis which requires prior knowledge of the range of vessel diameters in the image. For obtaining good results, the chosen scales are required to match the diameter of the vessels.

Advances and improvements in cardiac imaging have made it possible to acquire images with increasing spatial and temporal resolution. With the increasing capacity of computer memory and advances in cluster computing, it has now become easier to store and process larger volumes of imaging data. Cardiac segmentation is an essential step prior to further image analysis. Moreover, with the increasing use of minimally invasive cardiac procedures, it has attracted growing interest within the research community. In the near future, automated cardiac image segmentation is expected to play a greater role in image diagnostics and cardiac research.

Authors	Modality	Dim	Automation	Structure(s)
Classical approaches (e.g. thresolding, edge-detection, watershed)				
Weng et al. [181]	MR/CT	2D	Learning-based	LV
Waiter et al. [175]	MR	2D	semi-auto	LV, M
Cristoforetti et al. [36]	CT	3D	semi-auto	LA
Model-based				
Cootes et al. [30]	US	2D	semi-auto	LV, RV
Rueckert and Burger [150]	MR	4D	automatic	LV, RV
Mitchell et al. [117]	MR	3D	semi-auto	LV, RV
Bosch et al. [18]	US	2D	semi-auto	LV
Lelieveldt [86, 126]	MR	3D	semi-auto	LV, RV, LA, RA
Qu et al. [142]	MR	3D	automatic	LV
Lapp et al. [82]	MR	4D	automatic	LV,RV,M
Berg and Lorenz [94]	CT	3D	semi-auto	LA
Chenoune et al. [27]	MR	3D	semi-auto	LV
Lorenz and Berg [95]	CT	3D	semi-auto	LV, RV, LA, RA
Lekadir et al. [85]	MR	3D	semi-auto	M
Meyer et al. [115]	X-ray angio	3D	semi-auto	LA
Zheng et al. [191]	CT	3D	semi-auto	LV, RV, LA, RA
John and Rahn [69]	MR/CT	3D	automatic	LA

Table 3.1: A summary of important cardiac segmentation techniques. Abbreviations: US-echocardiogram, LV-left ventricle, RV-right ventricle, LA-left atrium, RA-right atrium, M-myocardium

Chapter 4

Left atrium segmentation

Traditional techniques used in electrophysiology can accurately map electrical activity in the atrial chambers [101], but cannot resolve the underlying left atrial anatomy. Three dimensional imaging of the left atrium has now become a standard method for visualising its anatomy for RFCA procedures (see section 2.3.3). In addition to visualising anatomy, robotic ablation procedures demand a segmentation of the atrium prior to the procedure. The conventional way of obtaining this segmentation is using manual or semi-automated techniques such as interactive region-growing. Segmentation of left atrium can be difficult because its anatomy is highly complex. There is also significant inter-subject variability of its anatomy [109].

In this chapter, we present a semi-automatic method for segmenting the left atrium from MRA images. Our work is based on [69], which has many limitations. The chapter extends and improves the method in [69] by adding the following components in the algorithm.

1. An anisotropic diffusion step is used for retaining important geometrical information. It also makes the algorithm robust against noisy MRA acquisitions.
2. A region growing step based on automatic threshold selection for segmenting the blood pool is used. This greatly improves the quality of results.
3. A ventricle exclusion step using a bounding-box also helps to separate the atrium from the ventricle. This is important as the ventricle and atrium share a common blood pool.

4. A cell-exclusion step is included and this corrects for over and under-segmentations using very little user-interaction.

5. There are also important differences from [69], such as the use of the complete voxel 26-neighbourhood in all computations. A second difference is the calculation of sizes of connecting surfaces between adjacent cells. The size is equivalent to the point on the surface with the maximum Euclidean distance value, giving the true diameter of the separating surface.

The combination of these improvements and differences makes the algorithm more robust for MRA datasets.

4.1 Introduction

The images that were acquired for the algorithm development were pre- and post-contrast MRA images. The method is based on a combination of techniques. Following a subtraction of the pre- and post-contrast MRA image, region growing using automatic thresholding is used to extract the largest blood pool. This pool comprises of the contrast-enhanced blood in the aorta, pulmonary artery, pulmonary veins, left atrium and ventricle. In contrast-enhanced MRA images, the left atrial blood pool frequently appears connected to blood pools of neighbouring structures such as the pulmonary artery, aorta and the left ventricle. The connections to pulmonary artery and aorta are due to the partial volume effect. The connection to the ventricle is inevitable as they share the same blood pool. These connections can either be narrow or non-narrow. The segmentation method handles narrow and non-narrow connections separately. This is performed in two separate steps:

1. Region-split-and-merge: The binary blood pool region splits based on the Voronoi tessellation of the Euclidean distance transform (DT) space. Each split region is a Voronoi *cell*. Only cell pairs with non-narrow connections are merged. A seed cell is chosen by

selecting a voxel inside the atrium. The set of merged cells containing the seed cell is the segmented left atrium.

2. Cell exclusion: The left ventricle has non-narrow connections with the left atrium because of the common blood pool. Non-narrow connections are also often created between the pulmonary veins and arteries. Unwanted cells pertaining to these structures are excluded in a post-segmentation step.

The complete list of steps involved in the segmentation algorithm is given in Fig. 4.1.

4.2 MRA image acquisition

In order to assess the proposed techniques presented in this thesis, left atrium MR angiography images were acquired of 35 patients who visited the Royal Brompton Hospital in London, UK. Informed written consent was obtained from all patients prior to the study. These are images acquired using a Siemens Avanto 1.5T scanner. The image size ranges between $250 \times 250 \times 30$ to $380 \times 380 \times 100$ voxels. The slice thickness ranges between 1.0-3.0 mm. Gadovist was used as the contrasting agent. The acquisition time for the studies is typically 20 seconds although preparatory scans are necessary making the total time for MRA alone approximately 10 minutes. However, patients often require other evaluations as well such as assessment of ventricular function and assessment for myocardial fibrosis. The total scanning time in these scenarios is approximately 45 minutes. There was a significant amount of inter-subject variability of the atrial anatomy. However, some rarely occurring variants such as R4 and R5 could not be found (see Fig. 2.4 and 2.5). Table 4.1 provides a summary of the image datasets. The table also lists the datasets that were randomly selected for algorithm development. See Fig. 2.10 on page 35 for examples of images from these datasets.

Subjects	**Image size** (voxels)	**Voxel size** (mm)
Subject No. 1	384×384×67	1.09×1.09×1.30
Subject No. 2	384×384×62	0.99×0.99×1.30
Subject No. 3	320×384×100	1.04×1.04×1.30
Subject No. 4	420×420×124	1.00×1.00×1.00
Subject No. 5	384×384×96	1.04×1.04×1.20
Subject No. 6	352×384×91	1.04×1.04×1.30
Subject No. 7	384×384×100	1.04×1.04×1.30
Subject No. 8	352×384×96	1.04×1.04×1.30
Subject No. 9	352×384×80	0.99×0.99×1.30
Subject No. 10	384×240×84	0.91×0.91×1.30
Subject No. 11	256×384×120	1.04×1.04×1.30
Subject No. 12	256×384×120	1.04×1.04×1.30
Subject No. 13	384×384×96	1.04×1.04×1.30
Subject No. 14	384×384×92	0.99×0.99×1.26
Subject No. 15	384×384×88	1.04×1.04×1.30
Subject No. 16	384×384×96	0.99×0.99×1.30
Subject No. 17	384×384×95	1.04×1.04×1.30
Subject No. 18	352×384×87	1.04×1.04×1.20
Subject No. 19	384×384×88	1.04×1.04×1.20
Subject No. 20	384×512×80	0.78×0.78×1.50
Subject No. 21	448×512×80	0.78×0.78×1.50
Subject No. 22	256×256×32	1.56×1.56×3.00
Subject No. 23	448×512×60	0.78×0.78×1.50
Subject No. 24	240×256×32	1.56×1.56×3.00
Subject No. 25	240×256×32	1.56×1.56×3.00
Subject No. 26	320×384×80	1.04×1.04×1.30
Subject No. 27 †	320×384×80	0.99×0.99×1.20
Subject No. 28	384×384×80	1.04×1.04×1.30
Subject No. 29 †	320×384×96	1.04×1.04×1.30
Subject No. 30	384×384×96	1.04×1.04×1.30
Subject No. 31	352×384×96	1.04×1.04×1.30
Subject No. 32	384×384×96	0.98×0.98×1.30
Subject No. 33	384×240×96	0.91×0.91×1.30
Subject No. 34	320×384×80	1.04×1.04×1.30
Subject No. 35	384×384×96	1.04×1.04×1.30

Table 4.1: Summary of the patient MRA datasets acquired for our studies. † - Used in algorithm development.

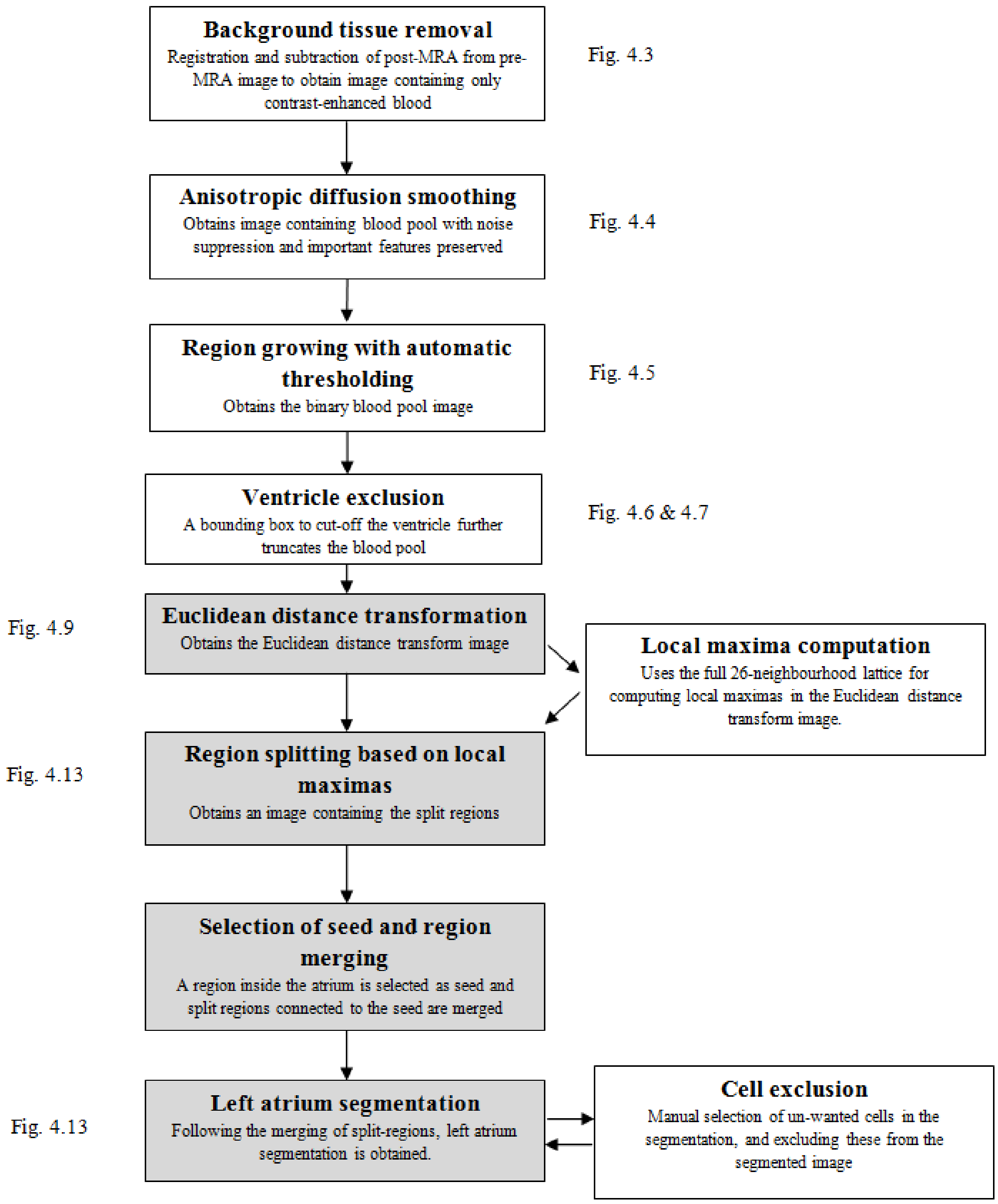

Figure 4.1: A flow diagram showing the steps involved in the left atrium segmentation algorithm. The steps marked in grey are adopted from the algorithm described in [69]. References to figures show images obtained after each step.

4.3 Pre-processing steps

4.3.1 Removal of background tissues

In angiograpic imaging studies blood is enhanced with a contrasting agent, causing unwanted tissues such as bone, lungs and fat to remain un-enhanced. Often these tissues remain despite the non-enhancement and it is desirable to remove them completely, leaving only soft tissues that carry the contrasting agent. This can be achieved using simple image subtraction. An MR acquisition prior to injecting the contrasting agent is taken; this is called the *pre*-contrast MRA image. Following contrast injection, the *post*-contrast MRA image is acquired. Since the patient may have moved between the two acquisitions, for instance due to breathing, it is important that these two images are correctly aligned prior to computing the subtraction. A rigid registration technique can be used to align the two images [164]. This technique uses voxel similarity measures. Once alignment is complete, a voxel-wise subtraction can be computed on the pre- and post-contrast MRA images. See Fig. 4.2 for results of subtraction. The resulting image will primarily contain enhanced blood carrying the contrasting agent. It is difficult to image the veins and arteries separately, as acquisition times are generally long enough to allow the perfusion of the contrast agent into both. Thus, the ascending aorta, pulmonary artery, pulmonary veins, left atrium and left ventricle will all be visible in the subtraction image. Collectively, they form the largest blood pool in the image.

Figure 4.2: A slice taken through pre-contrast MRA (left), post-contrast MRA (middle) and their voxel-wise subtraction (right). Abbreviation: LA - left atrium.

4.3.2 Anisotropic diffusion

MRA images may often contain noise arising from the image acquisition process. Isotropic smoothing using a Gaussian kernel can remove some of the noise but frequently smoothes the image in such a way that narrow connections between neighbouring structures are widened. The preservation of narrow connections is important as it forms the basis of the segmentation algorithm. It is thus desirable to preserve these features while smoothing the image at the same time. This is possible using a technique known as anisotropic diffusion where the amount of smoothing or diffusion can be selectively controlled. Diffusion is anisotropic and thus not the same in every direction. A diffusion *tensor* dictates the amount of diffusion in each direction. Anisotropic diffusion, like isotropic diffusion, can be derived from scale-space theory.

In scale-space theory (see Lindeberg [91]), the image $I(\mathbf{x})$ is embedded in a higher dimensional function of derived images I_σ generated by evolving the image according to the diffusion equation:

$$I_\sigma = div(\mathcal{E}\nabla I) = \mathcal{E}\Delta I + \nabla\mathcal{E} \cdot \nabla I \tag{4.1}$$

where div, ∇ and Δ are the divergence, gradient and Laplace operators respectively. Here, σ is the scale size and $\mathcal{E}$ is the diffusion tensor. The original image $I = I_0$ is used as the initial condition. The diffusion tensor $\mathcal{E}$ allows selective smoothing of features and varies the strength of diffusion anisotropically. This is transformed to the heat-flow equation $I_\sigma = \mathcal{E}\Delta I$, when the tensor $\mathcal{E}$ is replaced with an identity matrix. This shows that the process simulates heat diffusion. Such anisotropic smoothing was first proposed by Perona and Malik [134]. To preserve narrowing connection between structures it is sufficient to preserve edges in the image as pixels within these regions lie close to an edge. To achieve selective smoothing of non-edges, the diffusion tensor $\mathcal{E}$ is replaced by the scalar of the gradient magnitude of the image:

$$\mathcal{E} = e^{-(\frac{|\nabla I|}{\varkappa})^2} \tag{4.2}$$

where $\varkappa$ is a tuning parameter determining the weighting of this gradient. An anisotropic diffusion filtering step is thus applied to images degraded by acquisition noise.

4.4 Blood-pool extraction

The left atrium is frequently part of the largest blood pool in the image and it becomes important to extract this blood pool. The blood pool is a well-connected region containing voxels that have some degree of uniformity in their intensities. Region growing is a well-known segmen-

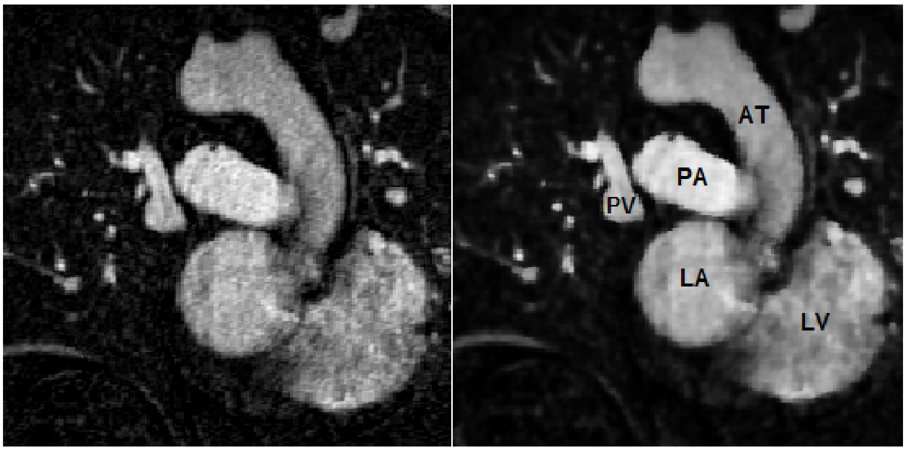

Figure 4.3: A slice through an MRA before (left) and after (right) applying the anisotropic diffusion filter smoothing with edge preservation. The different structures have been labelled: LA - left atrium, PV - pulmonary vein, PA - pulmonary artery, AT - aorta, LV - left ventricle.

tation technique (see section 3.2), where such connected regions can be extracted. It requires a uniformity criterion to be defined. For blood pool segmentation, intensity homogeneity is a feature that can be exploited for this purpose. An automatic threshold selection process computes the intensity range for blood. Fig. 4.4 illustrates the images that are used in this step along with a surface reconstruction of the obtained blood pool.

4.4.1 Automatic threshold selection

With a good contrast between background and soft tissues in MRA images, an intensity range for segmenting the blood pool via region growing can be found automatically. To determine the range, we propose using the Otsu method [130] for thresholding, as it is fast and automatic. Assuming that there are two classes (i.e. background and soft tissue) in the image, the Otsu method finds the optimal threshold value T_{opt} that maximises the *between-class* variance - a statistic that represents the amount of intensity variability between two classes. The between-class variance can be derived as follows: Assume that the image has n pixels and intensities ranging from 1 to l. The probability of pixels having a intensity i where $1 \leq i \leq l$ can be denoted as:

$$P(i) = \frac{\mathcal{F}_i}{n} \tag{4.3}$$

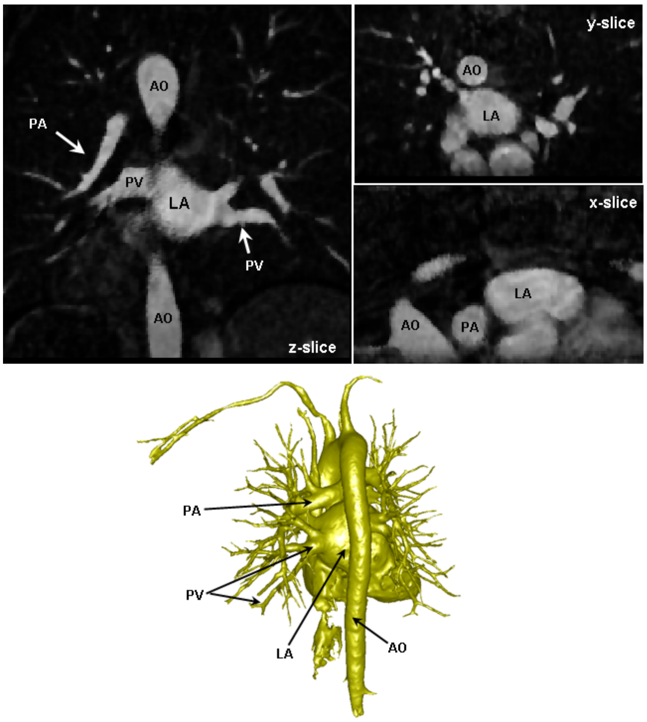

Figure 4.4: The three orthogonal planes of the image resulting from the subtraction of pre- and post-contrast MRA (Top). A surface reconstruction of the largest blood pool extracted from the MRA image on top (Bottom). Abbreviations: LA - left atrium, AO - aorta, PA - pulmonary artery, PV - pulmonary vein.

where $\mathcal{F}_i$ is the number of pixels with intensity i. Assume, that the image is partitioned into two arbitrary classes C_1 and C_2 where $C_1 = [1, \ldots, k]$ and $C_2 = [k+1, \ldots, l]$ respectively. The class probabilities χ_1 and χ_2 can be approximated as:

$$\chi_1(k) = \sum_{i=1}^{k} P(i) \text{ and } \chi_2(k) = \sum_{i=k+1}^{l} P(i) \tag{4.4}$$

From these probabilities, the mean for each class μ_1 and μ_2 can be derived:

$$\mu_1 = \sum_{i=1}^{k} \frac{iP(i)}{\chi_1(k)} \text{ and } \mu_2 = \sum_{i=k+1}^{l} \frac{iP(i)}{\chi_2(k)} \tag{4.5}$$

The mean intensity μ_T of the entire image can also be calculated:

$$\mu_T = \frac{1}{n} \sum_{i=1}^{k} i\mathcal{F}_i \tag{4.6}$$

It can be shown that:

$$\chi_1(k)\mu_1 + \chi_2(k)\mu_2 = \mu_T \tag{4.7}$$

where $\chi_1(k) + \chi_2(k) = 1$. Using this relationship in Equation 4.7, the between-class variance σ_B^2 can now be derived:

$$\sigma_B^2(k) = \chi_1(k)(\mu_1 - \mu_T)^2 + \chi_2(t)(\mu_2 - \mu_T)^2 \tag{4.8}$$

The optimal threshold value k^* is the one which maximises the between-class variance:

$$k^* = \arg \max_{1 \leq k \leq l} \{\sigma_B^2(k)\} \tag{4.9}$$

Given that two classes (i.e. soft tissues and background) are present in the image, the Otsu threshold can be computed in fairly quick time on most modern day PCs. The region growing algorithm uses the intensity range:

$$k^* \leq k \leq l \tag{4.10}$$

4.4.2 Region of interest

Image sizes can be large depending on their spatial resolutions. It is useful to crop the image using a bounding box and exclude everything outside a selected region of interest. This is important for two reasons:

- Ventricle exclusion: Separates the atrium and the ventricle. Due to the faint visibility of the mitral valve in MRA, a manually-defined plane that separates the ventricle from the atrium is defined using a face of the bounding box.
- Computational load: The size of the cropped image is smaller thereby increasing the performance of subsequent steps such as the region-splitting process.

Based on the operator's visual assessment, the box is placed, preferably centred on the atrium. The box size can be interactively adjusted, with handles provided on each face of the box for easy user interaction. Fig. 4.5 shows a bounding box placed to select a region of interest using a set of orthogonal views of the MRA dataset.

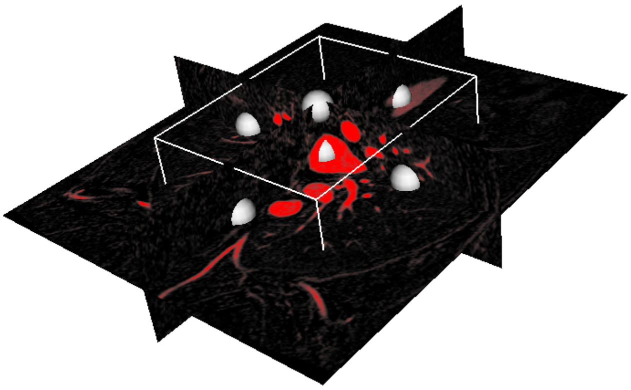

Figure 4.5: Orthogonal slices through the dataset with a user-interactive bounding box restricting the region growing process. The bounding box also defines the plane that separates the atrium from the ventricle and is thus useful for excluding the ventricle.

4.4.3 Region growing

A 3D region growing segmentation is used with a single seed point. The seed point is the voxel location with the maximum Euclidean distance value. This is also the centre of the largest blood pool containing the atrium. Starting from the seed point, a 26-connected neighbourhood is used where adjacent voxels of the seed points are examined. Voxels connected to the seed point and also satisfying the criteria given in Eq. 4.10 are included in the growing region.

To generate visualisations for the extracted region, a marching cubes algorithm [93] is used. The algorithm extracts a polygonal mesh of an iso-surface from the image. The polygonal mesh is iteratively smoothed using the Laplacian smoothing technique [47] and this generates a smooth surface mesh. Fig. 4.6 shows 3D surface renderings of the result of the region growing step, with and without the bounding box constraint.

Sections of the ascending aorta, pulmonary arteries and left ventricle are frequently part of the extracted region resulting from the region growing process. It can be difficult to ignore these structures as these lie very close to the atrium, and also appear to have direct connections between them. These connections can primarily be attributed to the partial volume effect (see section 2.7.4). Any voxels remaining from the left ventricle can be easily removed using region growing *subtraction*: the region grown is subtracted from the original image, with the bounding box placed interactively around the ventricle. However, the position of the interface between the left ventricle and the atrium, also known as the mitral valve must be defined. Because of its lack of visibility in MRA images, it is not possible to identify the mitral valve plane automatically and we will therefore assume that this plane is manually defined.

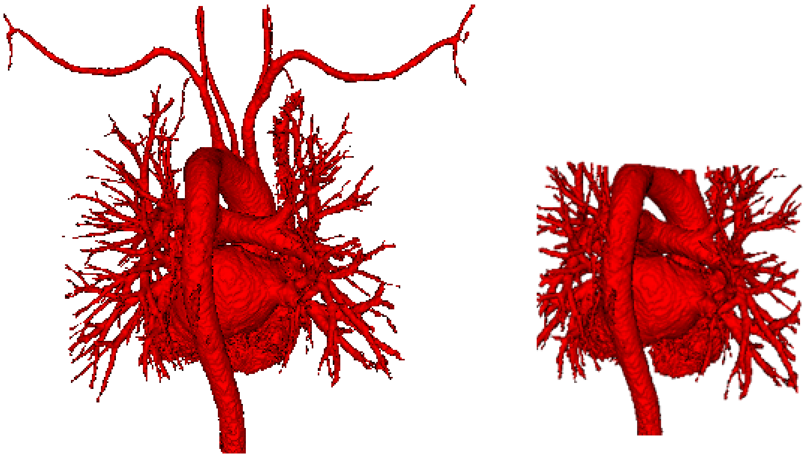

Figure 4.6: Surface reconstructions of result of region growing process, with (right) and without (left) the bounding box constraint.

The direct connections between the atrium and surrounding structures just discussed, are mostly narrow, owing to the fact that they are caused by the partial volume effect. It is clear that these are not anatomical connections, for example the pulmonary artery cannot be connected directly to the pulmonary vein due to the nature of the blood they transport. Fig 4.7 shows these connections between the two vascular systems: arteries and veins, the latter carrying de-oxygenated and the former carrying oxygenated blood. In the next section, we discuss how distance transformations can be used to detach structures at these narrow junctions. This will form the basis of our left atrium segmentation algorithm.

4.5 Distance transformations

The DT of an image I assigns to each pixel p the distance to the closest feature pixel in I. As illustrated in Fig. 4.8, it is the distance between point $\mathbf{p}$ and the nearest point on the object,

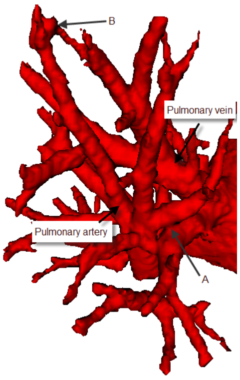

Figure 4.7: A and B are regions affected by the partial volume effect. The pulmonary arteries and veins are spatially close to each other in many subjects.

i.e. point $\mathbf{q}$. Assume that image I is segmented into object O and background O', the distance transform ξ for a pixel $\mathbf{p}$ can be defined as:

$$\xi(\mathbf{p}) = \begin{cases} 0, & \text{if } \mathbf{p} \in O' \\ \parallel \mathbf{p}, \mathbf{q} \parallel_{\mathcal{L}}, & \text{if } \mathbf{p} \in O \end{cases} \tag{4.11}$$

where $\parallel \cdot \parallel_{\mathcal{L}}$ is the distance between points based on a pre-defined metric $\mathcal{L}$. DT algorithms compute distance maps for the entire image and store the DT value at every pixel. These distance maps (see Fig. 4.8) are useful for making fast lookups without the need to compute distances on the fly.

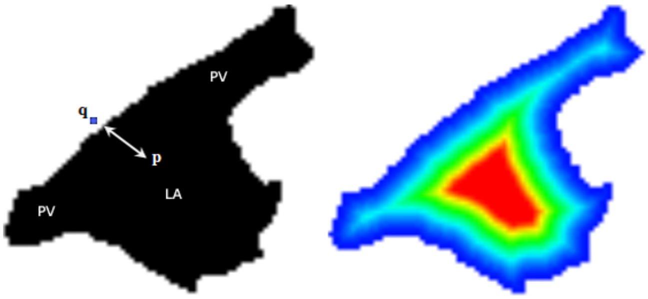

Figure 4.8: A typical distance computed in distance transformations (left) with labelled structures (LA - left atrium, PV - pulmonary vein). A distance rainbow map generated for fast distance transformation lookup (right). The colour gradient from blue to red map distances from low to high respectively.

The distances computed in a DT can be based on some pre-defined metric $\mathcal{L}$:

$$\| \mathbf{p}, \mathbf{q} \|_{\mathcal{L}} = \left(\sum_{i=1}^{k} |p_i - q_i|^{\mathcal{L}} \right)^{1/\mathcal{L}} \tag{4.12}$$

where $\mathbf{p}$ and $\mathbf{q}$ are k-tuples. p_i and q_i are the ith coordinates of $\mathbf{p}$ and $\mathbf{q}$. Some commonly used distance metrics are the city block ($\mathcal{L} = 1$), Euclidean ($\mathcal{L} = 2$) and chess-board distances. The Euclidean distance metric is the most useful as it corresponds to the way distances between any two points are measured in the real world. A drawback of using the Euclidean metric in DT is that it is more costly to compute. Previously, most DT algorithms have used other metrics as approximations to the Euclidean distance and these are relatively fast to compute.

The most commonly known algorithm to approximate the Euclidean metric is the Chamfer DT [19].

Recently, efficient algorithms for computing the exact Euclidean distance have been proposed [111, 8, 38]. These mostly run in time $O(n)$, where n is the image size. This is a significant improvement over earlier techniques. We use the feature transform algorithm proposed in [111]. The Euclidean distance transform is a trivial modification of this algorithm. The feature transform algorithm assigns to every voxel the closest feature voxel. This is accomplished using a Voronoi diagram, which is constructed with feature voxels as Voronoi centres. However, the complete Voronoi diagram is not constructed: the basic idea is to construct a partial Voronoi diagram at each dimension level, starting at the 1D level. The algorithm runs in $O(n)$ steps, with n being the number of pixels in the image.

For our binary blood pool image I from the region growing process, containing the blood pool O and background O', we compute the distance transform using the $\mathcal{L}_2$ norm:

$$\xi(\mathbf{p}) = \begin{cases} 0, & \text{if } \mathbf{p} \in O' \\ \| \mathbf{p}, \mathbf{q} \|_{\mathcal{L}_2}, & \text{if } \mathbf{p} \in O \end{cases} \tag{4.13}$$

where, pixel $\mathbf{q}$ is the closest feature pixel to $\mathbf{p}$. The closest feature pixel in our case are the background pixels, i.e. $\mathbf{p} \in O'$. This DT gives voxels in the blood pool a distance value of

$\xi > 0$. At narrowings, due to the proximity of background pixels, these distance values are small compared to non-narrow regions.

4.6 Region-split-and-merge process

We are interested in splitting the binary blood pool based on its Euclidean DT image. The algorithm is similar to the one described in [69]. Consider a local maximum point in the Euclidean DT image. For points in the neighbourhood of this local maximum, if the direction of gradient ascent is followed, all paths will lead to the local maximum. Using this notion, points in neighbourhoods of local maximums form *Voronoi cells* with the local maximum as the Voronoi centre. In this way, the binary blood pool is split and subdivided into a group of disjoint Voronoi cells. As the binary blood pool image is discretised, each Voronoi cell is a collection or group of voxels. Fig. 4.9 shows region-splitting in a phantom model, and Fig. 4.12 shows region-splitting of a segmented blood pool.

With the binary blood pool split into disjoint cells, the aim of the region merging process is to merge adjacent cells that are not connected by a narrowing. This goes back to the notion of separating the left atrium from neighbouring structures by making cuts at narrowings [69]. A measure of size is thus ascribed to each Voronoi cell and surfaces between adjacent Voronoi cells. The size of a Voronoi cell is equivalent to the largest Euclidean DT value of its voxels. Similarly, the size of the surface between adjacent Voronoi cells is equivalent to the largest Euclidean DT value of voxels within the surface. With these measures of size available for Voronoi cells and separating surfaces, it is possible to determine if a connection between adjacent Voronoi cells are narrow or non-narrow using the difference $\Delta D_{i,j}$:

$$\Delta D_{i,j} = \min\{D(\mathcal{C}_i)\ , D(\mathcal{C}_j)\} - D(\mathcal{Y}) \tag{4.14}$$

where $\mathcal{C}_i$ and $\mathcal{C}_j$ are adjacent cells, $\mathcal{Y}$ is the separating surface between the cells and $D(\cdot)$ is the size function. For narrow connections, ΔD should be relatively large compared to non-narrow connections (See Fig. 4.10). In region merging, starting from a seed Voronoi cell, adjacent cells are merged only if ΔD is larger than a user-specified threshold. Once two cells are merged, they form a single unit, with its new size equivalent to the larger of the cell sizes. The seed Voronoi cell is selected by the operator, by picking a voxel inside the atrium. Region merging terminates once there are no cells left to merge, and the merged-region containing the seed cell is the segmented left atrium. The process guarantees that the merged-region contains the atrium, as the seed cell lies within the atrium and only cells that are connected to the seed are traversed when merging.

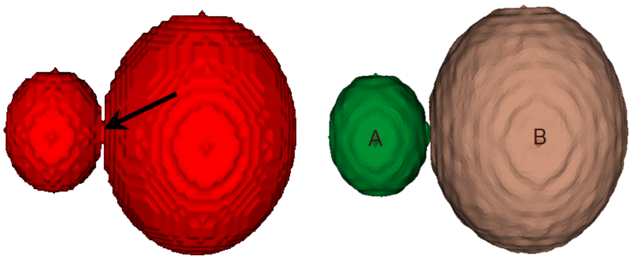

Figure 4.9: A phantom model of two structures joined by a narrowing, as marked by the arrow (left). The Voronoi cells (A and B) after region splitting, marked in different shades (right)

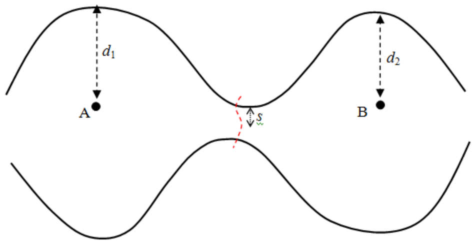

Figure 4.10: An example with two adjacent Voronoi cells A and B with a connecting surface of diameter s. Narrow connections become evident when the distance $\min\{d_1, d_2\} - s$ is compared. With the right threshold, these cells should *not* be merged.

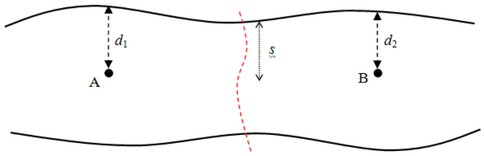

Figure 4.11: An example of two adjacent Voronoi cells A and B with a connecting surface with diameter comparable to that of the cells. There is no narrow connection and $\min\{d_1, d_2\} - s$ is small. With the correct threshold, these cells are merged.

Figure 4.12: Surface reconstruction of the extracted blood pool (left), blood pool with region-splitting where each colour represents a separate Voronoi cell (middle), left atrium segmentation after region-merging (right).

4.7 Cell exclusion

The degree of partial volume effect can be high in low-resolution MR images. In these images the algorithm's assumption that connections are narrow between structures does not always hold true. Often the result of this is that there are more voxels or Voronoi cells from unwanted structures in the segmented image. These voxels are generally part of a neighbouring pulmonary artery. A mechanism to remove these voxels in a post-processing step is possible with some user intervention. Instead of selecting on a voxel-by-voxel basis, the user can select entire Voronoi cells or a group of cells for exclusion from the segmented image. This process is assisted by visual feedback from an image displaying Voronoi cell regions superimposed on the left atrium segmented image. For easy reference, each Voronoi cell is also colour-coded (see Fig. 4.12).

For quicker removal of structures, it is also possible to select an entire structure. The entire merging process discussed in section 4.6 can now be applied for selecting a group of cells that are *not* connected by a narrowing, i.e. cells within a structure. The only change required in this case is to lower the threshold on the size criterion in Eq. 4.14. Once a structure is selected it can be excluded using simple voxel subtraction.

In MRA, the interface between the atrium and the ventricle is hardly visible. This is the mitral valve that opens and closes in a beating heart. In 3D images, locating the valve thus becomes difficult because it is motile and poorly visible. The ventricle is removed manually using surface visualisation images of the segmented left atrium. The user places a resizable rectangular box to define a region of interest around the ventricle. All voxels within the region of interest are removed. The ventricle is thus cut off from the atrium at a user-defined plane.

4.8 Performance evaluation

The segmentation algorithm presented in this chapter improves on an existing approach [69] by adding additional processes. These processes are outlined in Fig. 4.1. In this section, results from an experiment are presented which compares the existing approach described in [69] with the improved segmentation algorithm. For the rest of the section, we denote the existing algorithm in [69] as algorithm A, and the proposed improved algorithm described in this chapter as algorithm B.

In this study, twenty different images were selected as a good representative subset of our images. Algorithm A was implemented and its performance on segmentations were compared with that of algorithm B. The quality of segmentations of the algorithms are quantitatively compared against manual segmentations. These manual segmentations were performed by a clinician. For a particular image sequence, five slices through the dataset were selected at equally spaced intervals. These slices were selected from the most interesting areas of the image, i.e. in and around the atrial body chamber. Each slice is manually delineated by the clinician and compared against their computer-delineated counterparts. For a particular image, the segmentation overlap O_s between computer segmentation and manual segmentation is given by:

$$O_s = \frac{\mathrm{Area}(\mathcal{M} \bigcap \mathcal{C})}{\mathrm{Area}(\mathcal{M})} \tag{4.15}$$

Where $\mathcal{M}$ is the set of points on the manually segmented atrium's outline and $\mathcal{C}$ is the set of points on the computer-segmented atrium's outline.

The overlap results are given in Table B.1 (Appendix B) for 20 patient datasets. Overlaps are given for each of the five slices that were manually delineated. The mean overlap over all five slices is also stated. Fig. 4.13 illustrates mean overlaps across all 20 images used in the study. In at least one case (image 10), algorithm A was unable to generate a plausible segmentation. Algorithm B was successful in segmenting all datasets and had an overall mean overlap of

0.83 compared to A with a mean of 0.62. The results obtained clearly indicate that algorithm B, proposed as an improvement to algorithm A, is more robust and has greater accuracy in segmenting the left atrium.

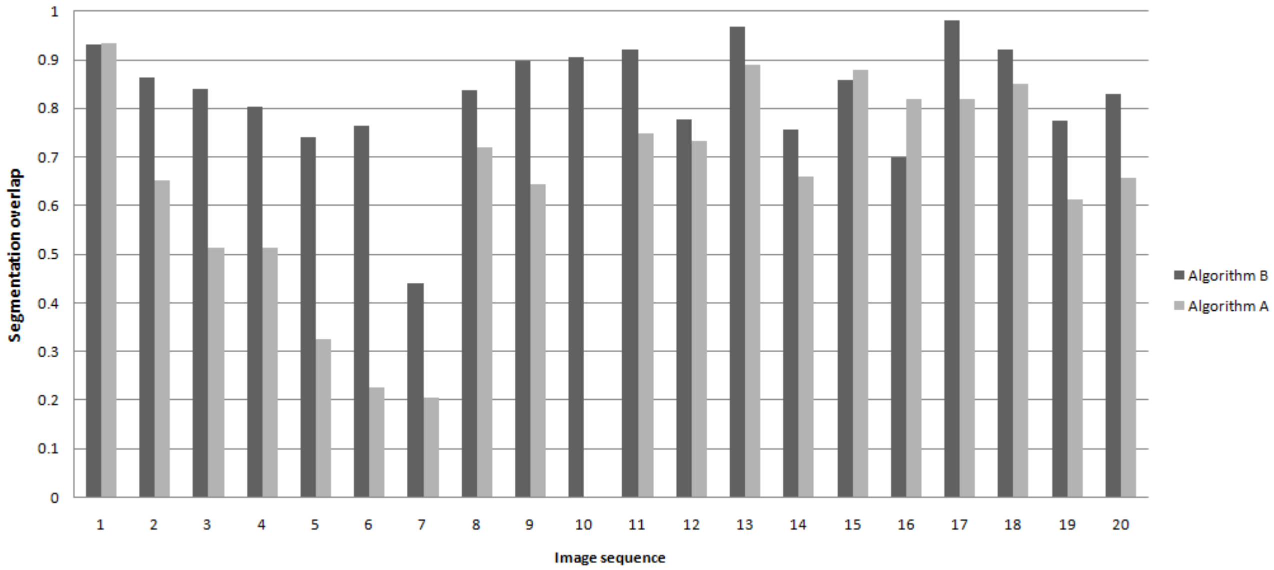

Figure 4.13: The segmentation overlap (between computer and manual-delineated) results of the 20 image sequences from which the left atrium was segmented using both algorithm A (John and Rahn [69]) and our proposed algorithm B.

4.9 Discussion

The structures of most interest in RFCA procedures are the atrial body and pulmonary veins, both of which are retained in this segmentation method. This is due to the following reasons:

1. The seed Voronoi cell in the region merging step is normally within of the atrial body, as it selected manually by the operator.
2. Unless there is extreme stenosis in pulmonary veins, it is *not* common to find narrow connections within pulmonary veins. As a result, an entire length of a pulmonary vein is included without difficulty.

For an evaluation of the proposed method, see section 7.2. Results show that 87% of the datasets in a study were segmented with a single step. Furthermore, the comparative study on performance with the existing approach given in section 4.8 provides evidence on the improvements in segmentations obtained with this approach. The occurrence of non-narrow connections between structures is most prevalent in images with low spatial resolution. This emphasises the importance of the cell-exclusion step for low-to-medium resolution images. Moreover, in images with low signal-to-noise ratio, important anatomical information such as narrow connections between structures are perturbed by noise. These are sometimes not recoverable, even with the anisotropic diffusion step. In such images the cell-exclusion step is also useful. However, Voronoi cells containing voxels that may belong to two separate structures such as the pulmonary artery and pulmonary vein cannot be excluded. Thus, small segments of unwanted structures may still remain in the segmented image.

The method described is fast and can extract the left atrium from medium-sized images (e.g. 250×250 to 380×380 and 30-100 slices) in less than 5 minutes on a modern PC. The most time consuming are the anisotropic diffusion smoothing and region-splitting steps.

4.10 Summary

A method for segmenting the left atrium from MRA images is proposed. The method exploits narrow connections between the atrium and neighbouring structures. It uses a combination of several image processing techniques such as region-growing and region-merge-and-split.

The algorithm proposed is an improvement over John and Rahn [69] which was tested primarily on CT-angiography images. Anisotropic diffusion to preserve critical features such as narrow connections is proposed. Furthermore, a region-growing approach for extracting the blood pool using automatic threshold selection is also proposed. A bounding box is used in region-growing allowing the ventricle to be excluded and separated at a user-defined plane (i.e. the mitral valve). Finally, a post-processing cell exclusion step allows the user to remove un-wanted segments of the pulmonary arteries or other structure. A comparative study on the performance of the proposed approach confirms its suitability for use on left atrium MRA images.

Left atrium segmentation obtained with this method can be used for further analysis. The segmentation of the left atrium is an important process in pre-procedural treatment planning of RFCA. Left atrium segmentation images provide a unique non-obstructed view of the atrium. These also simplify the computation of several procedural parameters.

Chapter 5

Segmentation of Pulmonary Veins

Total electrical isolation of the pulmonary veins is an effective way of correcting atrial fibrillation (see section 2.3.3). The complex anatomy of the left atrium is primarily described by the number and branching configurations of the pulmonary veins draining into it. The size of the ostium also plays an important role for post-ablation stenosis (see section 2.3.4). The first step towards automating the computation of these parameters is the segmentation of pulmonary veins. Skeleton or centreline extraction is a common segmentation technique for vessels. Centrelines are a simplified and compact representation of vessels.

This chapter presents a method for extracting the centrelines of pulmonary veins from segmented left atrium MRA images. The proposed method is based on computing medial axes of tubular structures. The method assumes that a segmentation of the left atrium is available, as computed in chapter 4. The main contribution of this chapter is a method that can extract centrelines of left atrium pulmonary veins. A method for segmenting the central atrial body is also presented. The segmentation of sub-atrial structures is an important step towards automating the computation of several of left atrial features such as anatomy, ostial diameters and atrial volume. The accuracy to which these features can be computed prior to an ablation procedure can play an important role in its success.

5.1 Introduction

Left atrium segmentation algorithm as presented in the previous chapter will segment the atrium, which includes its pulmonary veins and atrial body (see section 2.4.1 for left atrial anatomy). It does not distinguish between the two sub-atrial structures: Atrial body and pulmonary veins. A simple set theoretic definition can be given for the segmented atrium L:

$$L = B \cup P \cup R \tag{5.1}$$

where B and P are voxels contained within the atrial body and pulmonary veins respectively. R are residual voxels belonging to structures such as the pulmonary artery and aorta. These voxels are not removable using techniques presented in the previous chapter and may occur if a single Voronoi cell contains voxels that belong to two separate structures, one of which is not part of the left atrium. An illustration of the sub-atrial structures is given in Fig. 5.1. In the context of an RFCA procedure, the classes of most interest are the B and P classes. The algorithms presented in this chapter will search for these classes from the segmented atrium image obtained from the algorithm described in the previous chapter. See Fig. 5.2 for a flow diagram of the proposed algorithm.

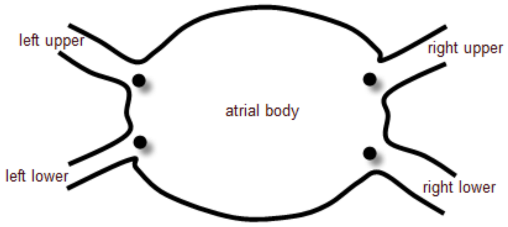

Figure 5.1: An illustration of a common configuration of the left atrium, showing four pulmonary veins draining into the atrial body. The dark circles indicate the locations of venoatrial junctions that are also called pulmonary vein drainage.

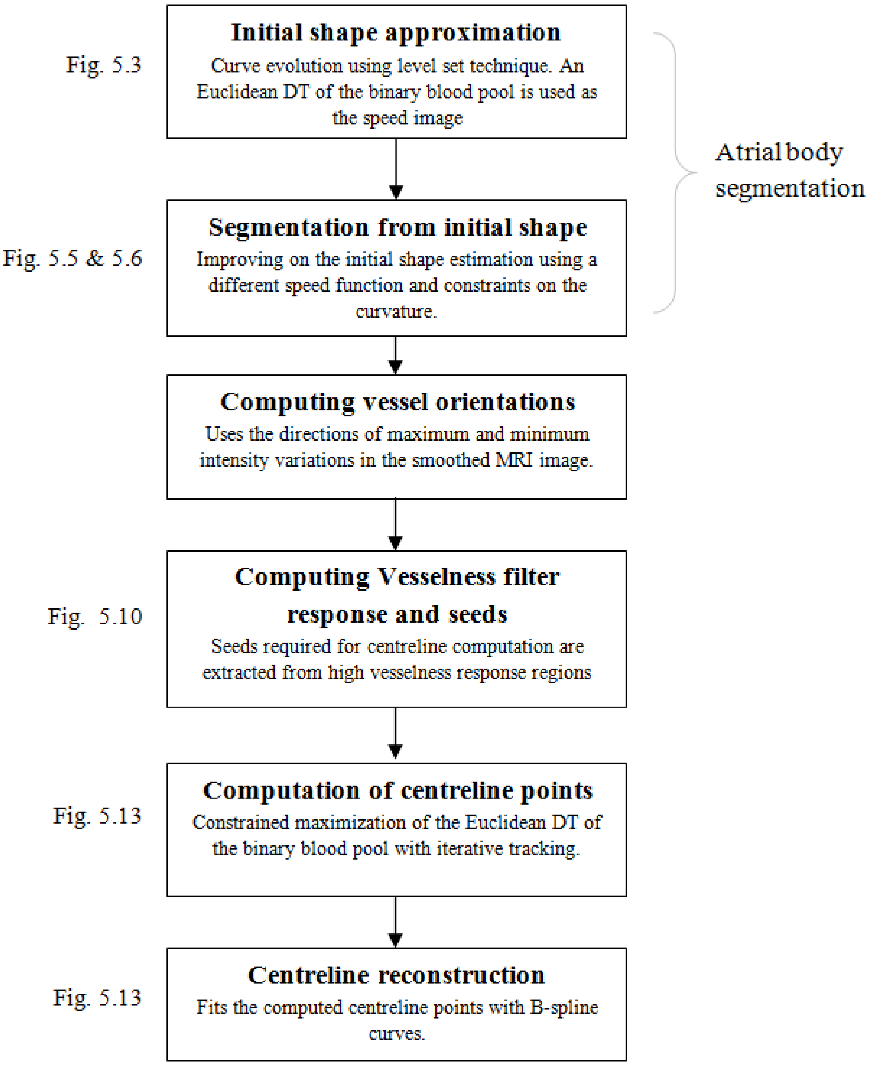

Figure 5.2: A flow diagram showing the major steps involved in the proposed algorithm for segmenting pulmonary veins. References to figures show examples of images obtained after each step.

5.2 Segmentation of the atrial body

The atrial body is a variably shaped closed structure which normally has three or more pulmonary veins draining into it. The segmentation of the atrial body is an important step towards further analysis of the left atrium. The benefits of segmenting the atrial body for pulmonary vein segmentation are twofold:

1. It simplifies the pulmonary vein centreline extraction process. Subtracting the atrial body from the left atrium segmented image leaves out pulmonary vein voxels. This simple

process is illustrated using the set-theoretic description in Eq. 5.1:

$$P \cup R = L \setminus B \tag{5.2}$$

where $L \setminus B = \{x \in L | x \notin B\}$ is the set-theoretic difference. The pulmonary vein centreline extraction process discussed in the following sections (see section 5.3) utilise this atrial body subtracted image, i.e. $L \setminus B$.

2. The location of the atrial body serves as a landmark for stopping the pulmonary vein centreline extraction process. Moreover, since the pulmonary vein drainages are incident upon the atrial body, determining its boundary facilitates the detection of drainages and subsequently left atrial anatomy. (see section 6.1.1). Drainage areas serve as important ablation sites.

Segmentation techniques for the atrial body have been proposed previously by some authors. Lötjönen et al. [97] proposed a four-chamber shape model of the heart from MRI images. This requires *a-priori* knowledge of the atrium's shape; a mean model is constructed from several manually segmented images. Zheng et al. [191] also proposed a four-chamber shape model from CT images. However, the interface between atria and ventricles (e.g. the mitral valve) is less faint in CT than MRI images. The visibility of this interface gives a distinct basal area for the left atrium allowing a shape model to be constructed.

In the previous chapter due to the lack of visibility of the mitral valve, the left atrium was separated from the ventricle using a manually defined plane (see section 4.4.3). The basal area of the left atrium in the segmented images is thus arbitrarily defined. Statistical shape models are not appropriate in such cases making it difficult to construct the true mean shape. For the segmenting atrial body, a level set segmentation technique is proposed. The method is based on deformable contours using a level set implementation framework. There are two advantages of using level set methods:

- Incorporates shape information using constraints on the curvature of the evolving shape.

- A convenient framework for implementing deformable contours.

It is inevitable for most techniques based on evolving fronts to leak through venoatrial junctions, unless constraints are imposed. With well-defined speed functions, level set methods can be used to achieve this segmentation.

5.2.1 The level set framework for segmentation

Level set methods [129] provide the mathematical and numerical mechanisms for computing surface deformations as time-varying iso-values of a higher dimensional function ϕ by solving a partial differential equation on the 3D grid. Level set methods are well documented in the literature [129] and have been applied to medical image analysis [104, 102]. They are discussed in detail in section 3.3.2. Starting from seed points inside the atrial body, the aim is to evolve these seed points into the atrial body. Let us denote the surface of this time-dependent evolving front as $\gamma(t)$, where $\gamma(0) = \gamma_0$ is the initial surface (i.e. ball). We assume that $\gamma(t)$ is an $(n-1)$-dimensional hyper-surface that evolves in the normal direction:

$$\frac{\partial \gamma}{\partial t} = F.\vec{N} \tag{5.3}$$

where F denotes the force field, and $\vec{N}$ is the normal vector to the hyper-surface. Instead of following the evolving surface $\gamma(t)$ explicitly, an n-dimensional function $\phi(x,t)$ is defined such that its zero level-set always corresponds to $\gamma(t)$:

$$\gamma(t) = \{\phi(x,t) = 0\} \tag{5.4}$$

It has been shown that if $\gamma(t)$ evolves according to Eq. 5.3, then the corresponding evolution of $\phi(x,t)$ is given by:

$$\frac{\partial \phi}{\partial t} + F|\nabla \phi(x,t)| = 0 \tag{5.5}$$

where F is a speed term that specifies the way in which ϕ should evolve. Thus, we have an implicit representation of the evolving surface $\gamma(t)$ using the level set of $\phi(x,t)$. The approach has the added advantage that topological changes in $\gamma(t)$ are naturally accounted for. For example, during evolution such changes may be encountered at isolated spots of image noise; the front propagates around these points, breaks into two and the ring around the isolated spot closes back in on itself and then disappears. On the contrary, such robustness is difficult to achieve with the active contour framework.

The choice of the speed term F in Eq. 5.5 is crucial for the segmentation as it influences the convergence and accuracy of the boundary positions for the evolving surface. The speed term F can depend on external forces derived from the image, and intrinsic geometric properties of the evolving front, e.g. its curvature. Since an evolving surface initialised at the centre of the atrial body is bound to leak into pulmonary veins (see Fig. 5.1), the speed function must be appropriately chosen to prevent this. The idea is to construct a speed function that generates high speed values inside the atrial body and low speed values close to its edge. Additionally, it must also generate low speed values at the pulmonary vein drainage locations. We are able to segment the atrial body in two distinct level set evolutions each one with a different speed function.

It is difficult to achieve segmentation with the use of a single speed function as there will eventually be a trade-off between evolution leakage through venoatrial junctions and under-segmentation. The use of two speed functions avoids this trade-off. The first speed function produces an under-segmentation, but, helps to acquire an approximation of the atrial body's shape. The second speed function utilises this approximation to drive the evolution to obtain the correct segmentation. Leakage is avoided in the second step as evolution is constrained to the obtained shape.

5.2.2 Approximation of atrial shape

In the first step, an approximation of the atrial body's shape is found. A Euclidean distance transform (DT) of the binary left atrium segmented image can be used as a speed function to stop leakage through the pulmonary vein drainages. It is the relative sizes of the atrial body and pulmonary vein drainages that make the Euclidean DT suitable. The Euclidean DT of a binary image of an object O computes for each pixel in O its distance to the closest pixel not in O (see section 4.5). At pulmonary vein drainages, due to the presence of edge pixels in the vicinity, low Euclidean DT values are expected. Conversely, at the atrial body centre, due to the absence of background pixels in the neighbourhood, high Euclidean DT values are found. A threshold-based level set evolution is used. The evolution stops in regions where speed values fall below a certain threshold. These speed values are mapped directly from the Euclidean DT ξ, thus stopping the evolution process in places where ξ is small. A threshold value τ_ξ specifies the lower bound on $\xi(L)$. We use a fixed value of $\tau_\xi = 2.0$ for our studies and this has shown to work well. The speed function F_1 can be given simply as:

$$F_1 = \xi(L) \tag{5.6}$$

where $\xi(L)$ is the Euclidean DT of the left atrium segmented image L.

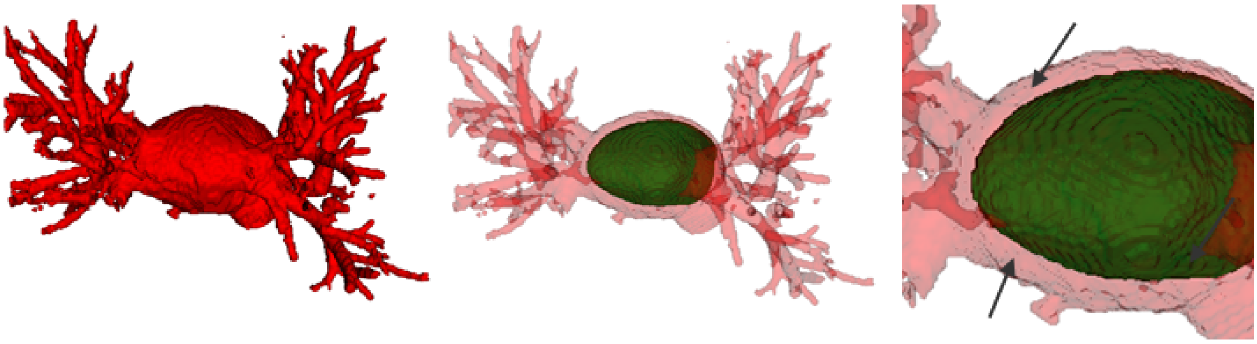

Figure 5.3: Level set evolution of a surface using the Euclidean distance transform of the binary left atrium as a speed function. The surface obtained from evolution (right) is an approximation of the atrial body's shape and thus an *under* segmentation. The evolved surface is over-laid and shown through a transparent surface of the segmented left atrium. Arrows mark parts of the atrial body not segmented correctly.

Evolution under the speed function F_1 will cause the surface to stop propagating before it approaches the atrial body border. This happens due to a combination of two effects:

1. The Euclidean DT value and thus the speed, is close to zero near the atrial body border.
2. The surface evolution is implemented to stop when the root mean square (R.M.S.) change between successive iterations is less than some pre-defined value ϵ. Because of a drop in speed near the atrial body border, the R.M.S. changes is likely to be less than ϵ.

An *under*-segmentation of the atrial body is thus the result. Nevertheless, this evolution step using F_1 is useful as it gives a good first approximation of the atrial body's shape. In addition to this, leaks through the pulmonary vein drainages are unlikely. This is illustrated in Fig. 5.3.

5.2.3 Segmentation from initial shape approximation

With the initial approximation of the atrial body's shape $\gamma_o(t)$ obtained in the previous step, it is possible to improve on this approximation by further evolving $\gamma_o(t)$. However, a different speed function is required. Unlike the previous speed function F_1, the new speed function F_2 must allow the surface to extend as far as the atrial body's border. Furthermore, to constrain the evolving front to its initial shape $\gamma_o(t)$, strict curvature constraints must be imposed. Another advantage of level set methods now becomes apparent: The curvature κ of the moving front can be conveniently computed directly from the level set function $\phi(x,t)$:

$$\kappa = \nabla . \frac{\nabla \phi}{|\nabla \phi|} \tag{5.7}$$

Incorporating this curvature term into the level set equation given in Eq. 5.5, we obtain:

$$\frac{\partial \phi}{\partial t} + F_2(1 - \omega\kappa)|\nabla \phi(x,t)| = 0 \tag{5.8}$$

where F_2 is our new speed function, and ω is the weighting factor for the front's curvature κ. The second speed function is based on the segmented binary left atrium image's gradient information. The gradient image is computed by convolving the left atrium image with the first-order derivative of a Gaussian kernel. The gradient magnitude is mapped to speed values using a sigmoid function. In this function evolution the speed decreases exponentially with increasing gradients, thereby significantly slowing the evolution process at the edges of the left atrium. The second speed function is thus given by:

$$F_2 = \frac{1}{1 + e^{-\frac{\nabla I_\sigma - \beta}{\alpha}}} \tag{5.9}$$

Here, the gradient magnitude of the intensity image: $\nabla I_{\sigma} = \nabla G_{\sigma} * I$, where $*$ denotes a convolution. α and β are scaling parameters for the sigmoid, and we use $\alpha = -1, \beta = 7$. Fig. 5.4 shows F_2 plotted against gradient magnitude values with $\alpha = -1, \beta = 7$.

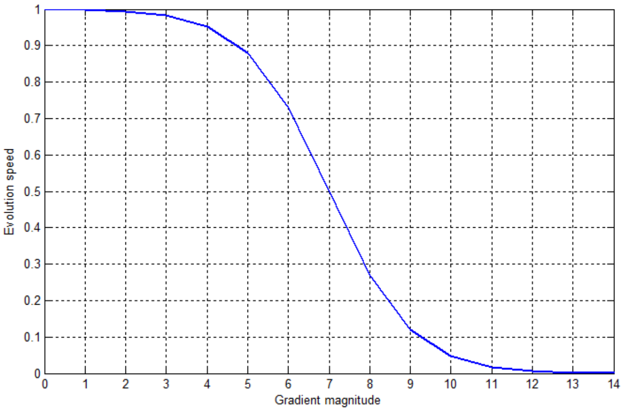

Figure 5.4: The sigmoidal speed function for the second evolution step F_2 stated in Eq. 5.9. This uses the scaling parameters: $\alpha = -1, \beta = 7$.

The speed values are required to decay with increasing gradient magnitude. The values $\alpha = -1$ and $\beta = 7$ allow the sigmoid to model this decay appropriately. $\alpha = -1$, reflects the generic sigmoid (i.e. $1/(1 + e^{-x})$) about the vertical axis allowing decay to take place with increasing gradient magnitude. $\beta = 7$, translates the generic sigmoid appropriately along the horizontal axis, allowing speed values to saturate to 1 at low gradient magnitudes and to 0 at high gradient magnitudes. This saturation plays an important role in segmentation by starting and stopping the evolution process. It is also important to note that the generic sigmoid $1/(1+e^{-x})$ saturates at $x = 7$, which is also why the sigmoid is shifted seven units along the horizontal axis using $\beta = 7$. A sigmoid is more suitable than an ordinary exponential decay function (e.g. e^{-x}) as it is ideally bounded between $[0, 1]$ allowing the speed function to be restricted within these values.

This second evolution step closes the gap between the initial surface $\gamma_o(t)$, obtained in the first step and the border of the atrial body. This is illustrated in Fig. 5.5. With a low curvature constraint and evolution under F_2, leakage through pulmonary vein drainage is likely. Thus high curvature constraints ($\epsilon >> 1.0$) are important prerequisites for obtaining a correct segmentation of the atrial body.

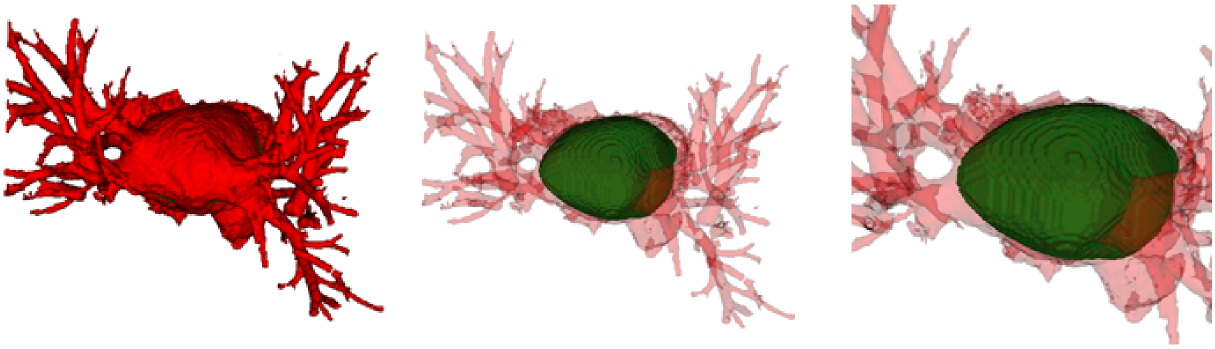

Figure 5.5: Evolving the initial surface obtained from shape approximation step using speed function F_2 given in Eq. 5.9. The surface reconstruction of the segmented atrium (left), with the atrial body seen through the transparent surface (middle) and close-up to show improvement after the final segmentation step (right). Compare with Fig. 5.3.

5.3 Pulmonary vein centrelines

The centrelines or medial axes of veins provide a compact representation of the veins. Moreover, such representations can be stored and processed more efficiently than a voxelwise representation of vessels. There is rich literature on vessel segmentation techniques [78], and vessel skeletonisation processes are not uncommon. Centreline extraction has been applied mostly to the cerebral vasculature [106, 7, 189] (see section 3.4.2). There are several benefits of extracting the pulmonary vein centrelines. It enables us to compute left atrial anatomy, determine ostial locations and their diameters. In addition to this, once each pulmonary vein segment is classified based on a vessel tree-hierarchy system, only pulmonary vein segments that drain into the left atrium can be selectively visualised; these segments are most relevant for ablation procedures.

The pulmonary vein centreline extraction process is based on determining the medial axis of tubular-like structures. The medial axis is found by maximising the Euclidean DT function at each perpendicular cross sectional plane of the vessel. A vessel response filter is used to generate seed points, from which the extraction processes are initiated. The technique is fast and can extract entire pulmonary vessel trees in less than 5 seconds for typical medium-resolution MR images[1].

The centreline extraction algorithm is essentially a tracking process that can be divided into

---

[1] The vessel extraction algorithm has been tested on images with a size of 350 × 350 × 80.

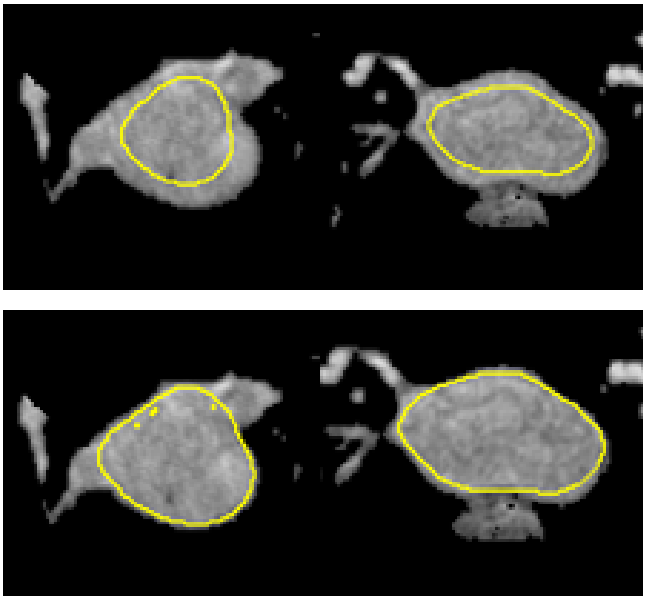

Figure 5.6: Views of the transversal (left) and sagittal (right) planes of a left atrium image, with segmented atrial body contour overlaid. Atrial body contours are obtained from first (top) and second evolution steps (bottom).

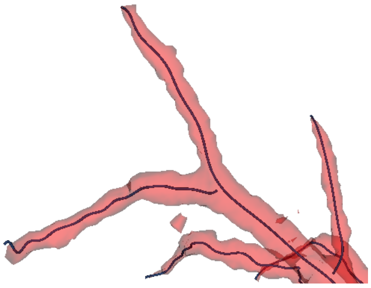

Figure 5.7: Vessel centrelines or medial axes can be efficiently stored and processed. The extraction of pulmonary vein centrelines is crucial for determining drainage locations and subsequently the left atrial anatomy.

two important steps. The first step generates seed points inside the vessel. The second step finds a vessel centreline point for each seed point. Depending on the distribution of seed points, each length of a vessel is traversed as points along its centreline are found. The process begins at a seed point and terminates at the vessel boundaries. The process is repeated for every seed point. There are typically 3000-5000 seed points in an image. These are selected automatically. Prior to the tracking process, several pre-processing steps are required to extract important information necessary while tracking. These are:

- Computing the vessel direction at each voxel.

- Computing the multi-scale vesselness response filter output at each voxel. This is necessary for generating good seed points. It also computes the appropriate scale size for each voxel.

5.3.1 Vessel directions

Vessel centreline extraction is an iterative tracking process, which is initiated at a seed point inside the vessel. At each iterative step, the direction of the vessel being tracked must be followed. Without prior computation of these directions, it is impossible to make progress while tracking. The directions are found by analysing the second-derivative information or Hessian of the vessel 3D image. These techniques have been investigated by several authors [153, 50, 7] (see section 3.4.1). For these techniques it is assumed there is a good contrast between the vessel and the background. This is easily achieved in contrast-enhanced MRA images.

The Hessian is the second derivative information which at each point gives the rates of change of intensity variation in all three directions. Following is the Hessian matrix computed at each point $\mathbf{x}$ of a 3D image f:

$$H(\mathbf{x}) = \begin{bmatrix} \frac{\partial^2 f}{\partial x^2} & \frac{\partial^2 f}{\partial x\,\partial y} & \frac{\partial^2 f}{\partial x\,\partial z} \\ \frac{\partial^2 f}{\partial y\,\partial x} & \frac{\partial^2 f}{\partial y^2} & \frac{\partial^2 f}{\partial y\,\partial z} \\ \frac{\partial^2 f}{\partial z\,\partial x} & \frac{\partial^2 f}{\partial z\,\partial y} & \frac{\partial^2 f}{\partial z^2} \end{bmatrix} \tag{5.10}$$

The underlying idea is that, after smoothing of the image, in the direction of the vessel, there will be minimum intensity variation. Thus, the initial assumption that there is good contrast between vessel and background, is an important one. Maximum intensity variation is expected to be found in the other two directions which are perpendicular to the axis of the vessel. This distinguishes the different directions and using this notion the direction of the vessel at each voxel can be extracted. This is illustrated in Fig. 5.8 and is discussed in section 3.4.1. Prior to

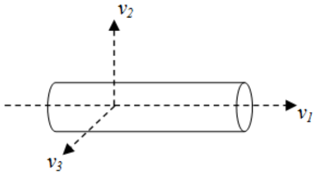

Figure 5.8: The extracted directions that can be determined by analysing the Hessian matrix. The direction of minimum intensity variation is along $\mathbf{v}_1$, which is also the vessel direction. The other two directions along which there is maximum intensity variation are perpendicular to $\mathbf{v}_1$.

computing the Hessian, the image must be smoothed with Gaussian kernels of varying widths $\sigma^{(i)}$. This serves two purposes:

1. It avoids singularities due to image acquisition noise when computing partial derivatives for the Hessian.
2. It enables a multi-scale analysis of the image, allowing for vessels of different widths.
3. It produces 1D maximum convexity height *ridges* which can be characterised by the eigenstructure of the Hessian matrix. Ridges in 3D images are points that are local maxima in at least two directions.

As described in section 3.4.1, an eigen decomposition of the Hessian is necessary to extract the amounts of intensity variations and their directions at each voxel in the image. Assume the eigenvalues of the Hessian $H(\mathbf{x})$ to be:

$$|\lambda_1| \leq |\lambda_2| \leq |\lambda_3| \tag{5.11}$$

As there is minimum intensity variation along the direction of the vessel, we retain the eigenvalue-vector pair: $(\lambda_1, \mathbf{e}_1)$. Here $\mathbf{e}_1$ is the direction of the vessel. We have not yet stated how the widths $\sigma^{(i)}$ of the Gaussian smoothing kernels are chosen. The widths $\sigma^{(i)}$ are determined using a multiscale analysis of a vessel response filter called the *vesselness* filter (refer to Eq. 5.15).

5.3.2 Vesselness filter and seed selection

The *vesselness* filter was proposed by Frangi et al. [50] and its basis is discussed in greater detail in section 3.4.1: Voxels within tubular-like structures give a higher response to this filter than voxels within non-tubular structures. The basic principle is the same as described in section 3.4.1: the contrast inside and outside of a vessel are measured using an eigen decomposition of the Hessian matrix. As vessels can vary in width, the Hessian and thus the filter response are computed at a range of scales, making it a multiscale filter. The vesselness filter $\mathcal{V}(\sigma)$ computed at scale σ is given as:

$$\mathcal{V}(\sigma) = \begin{cases} 0, & \text{if } \lambda_2 > 0 \text{ or } \lambda_3 > 0 \\ (1 - e^{-\frac{\mathcal{R}_A^2}{2\alpha^2}})(1 - e^{-\frac{\mathcal{S}^2}{2c^2}})e^{-\frac{\mathcal{R}_B^2}{2\beta^2}}, & \text{otherwise} \end{cases} \tag{5.12}$$

where $\mathcal{R}_A = |\lambda_2|/|\lambda_3|$, and $\mathcal{R}_B = |\lambda_1|/\sqrt{|\lambda_2\lambda_3|}$. The constants α, β and c control the sensitivity of the filter. For our purposes, we use $\alpha = \beta = c = 0.5$ to increase its sensitivity. These ratios are understood with the second-order ellipsoid spanned by the three eigenvalues: $\lambda_1, \lambda_2, \lambda_3$ (see Fig. 5.9). The ratios maintain what shape the second-order ellipsoid must take for the case of a vessel. Ratio $\mathcal{R}_B$ distinguishes blob-like ellipsoids, and attains a maximum for anything that is blob-like. Ratio $\mathcal{R}_A$ is a ratio of the larger two eigenvalues and corresponds to the largest cross-

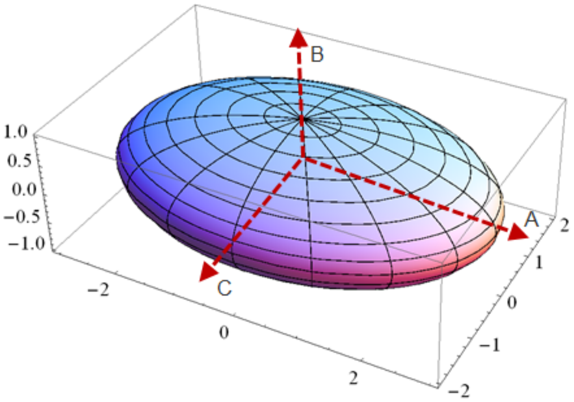

Figure 5.9: The second order ellipsoid constructed from the eigenvalues of the Hessian H. Here, the axes are A $= \mathbf{e}_1$, B $= \mathbf{e}_2$ and C $= \mathbf{e}_3$, and the ellipsoid extends λ_1, λ_2 and λ_3 respectively in those directions. The size of an eigenvalue $|\lambda_k|$ represents the amount of intensity variation in the direction $\mathbf{e}_k$.

sectional area of the ellipsoid. It is thus important for distinguishing between plate-like and line-like structures. The term S in Eq. 5.12 is sensitive to unpredictable responses from noisy background pixels. Although desirable values for the ratios $\mathcal{R}_A$ and $\mathcal{R}_B$ may also be attainable by noisy pixels, the magnitude of their eigenvalues will be small for typical signal-to-noise ratios. This can be tested by S:

$$\mathcal{S} = \sqrt{\lambda_1^2 + \lambda_2^2 + \lambda_3^2} \tag{5.13}$$

Finally, the vesselness filter $\mathcal{V}(\sigma)$ in Eq. 5.12 generates a maximum value when all three conditions $\mathcal{R}_A$, $\mathcal{R}_B$ and $\mathcal{S}$ are met. The response is analysed at different scales and the scale at which the filter response is maximal is retained as an estimate of vesselness:

$$\mathcal{V} = \max_{\sigma_{min} \leq \sigma \leq \sigma_{max}} \mathcal{V}(\sigma) \tag{5.14}$$

Similarly the scales $\sigma^{(i)}$ at which the Hessian is computed for extracting vessel directions is thus:

$$\sigma^{(i)} = \arg\max_{\sigma_{min} \leq \sigma \leq \sigma_{max}} \mathcal{V}(\sigma) \tag{5.15}$$

Vesselness filter responses allow not only to obtain the correct scales for the Hessian in vessel direction computation, but are also useful for generating seed points that lie within tubular-like structures. These seeds are guaranteed to lie within vessels and are thus used as starting points for the centreline tracking process. Voxels that generate a vesselness filter response above a certain user-selected threshold value are used as seed points. Since there may be many voxels with responses above the threshold value, only a certain percentage of these total voxels are randomly chosen as seed points[2] (See Fig. 5.10) .

5.3.3 Centreline tracking

The medial axis or centreline of a vessel is a continuous smooth curve that runs along the middle of the vessel. The vesselness filter proposed by Frangi et al. [50] can help locate voxels that lie

---

[2] Given that the atrial body is removed from the image, isolating 5 -10% of high vesselness response voxels give around 3000-4000 seed points, which is a reasonable amount for extracting the centrelines.

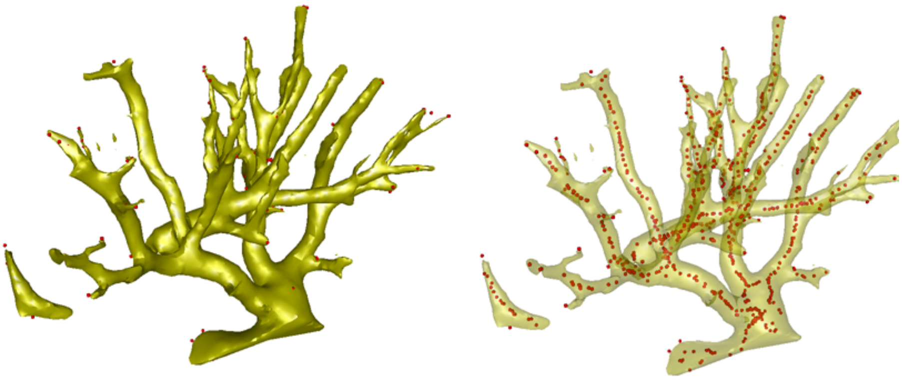

Figure 5.10: Surface reconstruction of a vessel drainage branch (left) with the computed seed points overlaid on a semi-transparent surface (right)

close to the medial axis or centreline of the vessel. However, the filter cannot find centrelines of vessels. Wink et al. [185] extends this approach for vessel centreline reconstruction. However, a major disadvantage of the approach is the user requiring to specify both start and endpoints of each vessel. In this section, an approach to reconstruct the centrelines of pulmonary vessels is proposed. These centrelines are reconstructed starting from seed locations within vessels.

For each pixel inside the left atrium, the Euclidean DT function ξ of the left atrium segmented binary image computes the distance to the nearest edge pixel. For points on the centreline curve, the Euclidean DT value must be a maximum at least along any one plane. This is the basic principle behind the tracking process. The centreline tracking process is iterative and comprised of two main steps:

1. Initial estimation.

2. Maximisation step.

The tracking process initiates at a seed point. At this seed point no initial estimation step is required and the maximisation step computes the first centreline point. From this centreline point, the process continues by making an initial estimation/guess for the next centreline point followed by a maximisation step to improve on this estimate. Fig. 5.11 illustrates the tracking process.

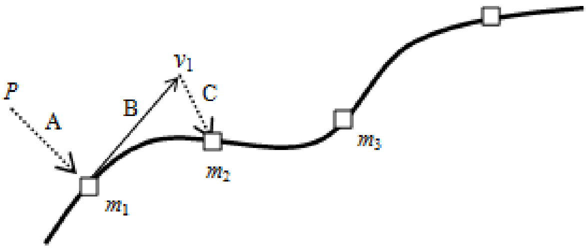

Figure 5.11: An overview of the iterative steps involved in traversing a vessel centreline represented by the curve. **A** - Starting from a seed point P, the ED transform ξ is maximised, bringing us to a centreline point $\mathbf{m}_1$. **B** - A small number of steps is taken in the vessel direction $\mathbf{v}_1$. **C** - The function ξ is maximised again yielding a new centreline $\mathbf{m}_2$.

Initial estimation

In this step, the centreline tracker estimates the location of the next centreline point by interpolating along the vessel direction. This is essentially step B in Fig. 5.11. At each iteration $k > 1$, using the previous tracked centreline point $\mathbf{m}_{k-1}$, the position of the next centreline point $\mathbf{m}_k$ is guessed by interpolating along the vessel direction $\mathbf{v}_{k-1}$ at $\mathbf{m}_{k-1}$. We denote this initial estimation as $\mathbf{s}_k$:

$$\mathbf{s}_k = \mathbf{m}_{k-1} + (-1)^n \delta \mathbf{v}_{k-1} \tag{5.16}$$

where $n = \{0, 1\}$ indicates the two directions in which the tracking can proceed. For any seed point, both forward and reverse directions are explored. The step size $\delta \in \mathbb{R}$ is important and is dependent on vessel width. It is a constant and its value should never exceed that of the radius of the smallest vessel; we use $\delta = 0.5$ mm. A larger step size δ may cause $\mathbf{s}_k$ to fall outside the vessel. At $\mathbf{s}_k$, a perpendicular plane Π_k is constructed, using the vessel direction $\mathbf{v}_{s_k}$ at that point:

$$\Pi_k : \mathbf{v}_{s_k} \cdot (\mathbf{x} - \mathbf{s}_k) = 0 \tag{5.17}$$

It is important to note that this step is not used in the first iteration as the maximisation step is used instead to locate the first centreline point $\mathbf{m}_0$. The seed point itself is considered as an initial estimation of the centerline.

Maximisation step

The estimation $\mathbf{s}_k$ for the centreline point is improved by maximising the 3D Euclidean DT function ξ of the binary left atrium segmented image, but constrained to a 2D plane Π_k. This constraint in the maximisation step is an important one, as maximisation of ξ in 3D space would yield the same local maxima for neighbouring points - making it impossible to make any progress whilst tracking. See Fig. 5.12 for an illustration of the kth iteration step. Maximisation is accomplished using a simple hill-climbing approach. Starting from the initial guess $\mathbf{s}_k$, the direction of maximum ascent is followed by exploring its 8-neighbourhood. To impose the plane constraint, only voxel neighbours that lie on the plane Π_k are traversed. The 8-neighbourhood $N_\pi(\mathbf{p})$ of points $\mathbf{p}$ on the plane can then be given as:

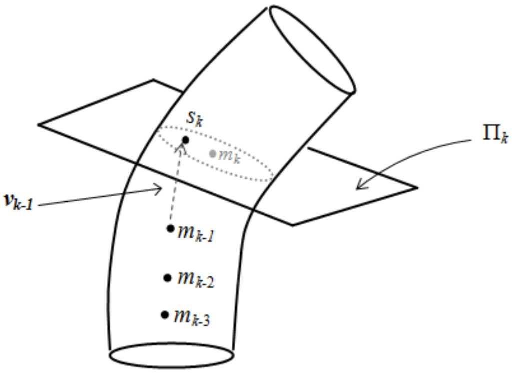

Figure 5.12: Illustration of the kth iteration step of the centreline tracking process. After having tracked centreline points $\mathbf{m}_{k-3}, \mathbf{m}_{k-2}$ and $\mathbf{m}_{k-1}$, an initial guess $\mathbf{s}_k$ is made for the k^{th} centreline point. This guess is improved by maxisiming the Euclidean DT ξ, constrained to the vessel transversal plane Π_k at $\mathbf{s}_k$.

$$N_\pi(\mathbf{p}) = \bigcup_{\substack{o_y=-r,r \\ o_x=-r,r}} \{\mathbf{p} + o_x\mathbf{w}_1 + o_y\mathbf{w}_2\} \tag{5.18}$$

where r is the step-size for the hill-climbing process, and $\mathbf{w}_1$ and $\mathbf{w}_2$ are two vectors of the plane Π_k. A step size of $r = 0.5$ mm gives reasonable precision for finding the maximum point. These fractional step sizes require sub-voxel computations which are made possible by interpolating on a grid. Cubic B-spline interpolation is used to obtain sub-voxel values for the function ξ.

The tracking process must be allowed to stop once it has traversed the entire length of a vessel. There are also situations where the tracking process may enter a region that has already been traversed. These situations are used to formulate a set of termination conditions which determine when tracking should stop:

1. **Crossing vessel boundaries:** When the vessel tracker is outside the vessel, or inside the atrial body, the tracking process is stopped.

2. **Tracking vessels multiple times:** The tracking stops when a visited centreline is encountered. The tracked segment is discarded if it is not significantly large in size[3].

3. **The degree of curvature between consecutive centreline points:** tracking is also stopped if the angle θ_k between two consecutive steps along the centreline becomes too large:
$$\cos\theta_k = \frac{(\mathbf{m}_k - \mathbf{m}_{k-1}).(\mathbf{m}_{k-2} - \mathbf{m}_{k-1})}{|\mathbf{m}_k - \mathbf{m}_{k-1}|\,|\mathbf{m}_{k-2} - \mathbf{m}_{k-1}|} \tag{5.19}$$
The new centreline point is accepted if $\theta_k \leq \theta_\tau$. Furthermore, the eigenvectors of H in eq. 5.10 giving the vessel directions can flip. In such cases this curvature constraint also prevents turns of 180°.

The entire centreline tracking algorithm is given in algorithm 1.

5.3.4 Modelling centreline curves

Vessel centrelines are continuous curves in 3D. The tracking process generates discrete points that approximately lie on the true vessel centreline. It is useful to reconstruct a centreline curve from these discrete set of points. Cubic B-spline curves are used to fit to the tracked centreline points, and thus model each vessel medial axis segment. A parametric B-spline curve with $n+1$

---

[3] A user-defined constant is placed on the allowable minimum vessel segment size. Size is represented as the number of tracked centreline points on a segment. Currently, this is set to 15 centreline points for step sizes of 0.5 mm (see Eq. 5.16).

Algorithm 1 findVesselCenterlines

```
Require: segmented image $I$, vesselness filter response $\mathcal{V}$, step size $\delta = 0.5$, empty set $T$
Ensure: the set $T$ of tuples: $(p_i, M_i)$ contain set of centreline points $M_i$ for each seed point $p_i$
$\mathcal{P} \leftarrow$ get seed points from vesselness filter response. Select 10% of points only
for all seed points $p_i \in \mathcal{P}$ do
    $M_i \leftarrow \varnothing$
    for each direction $d = \{0, 1\}$ do
        $k \leftarrow 0$
        while none of the termination conditions are satisfied do
            if $k = 0$ then
                $v_\pi \leftarrow$ compute direction vector of the vessel at $p_o$
            else
                $v_\pi \leftarrow$ compute direction vector of the vessel at $\mathbf{s}_k$
            end if
            $\Pi_k \leftarrow$ compute equation of plane at $\mathbf{s}_k$ using $v_\pi$
            $\mathbf{m}_k \leftarrow \arg\max_{\Pi_k}\{\xi\}$
            $M_i \leftarrow M_i \cup \mathbf{m}_k$
            $v_k \leftarrow$ compute direction vector of the vessel at $\mathbf{m}_k$
            $\mathbf{s}_{k+1} \leftarrow \mathbf{m}_k + (-1)^d \delta v_k$
            $k \leftarrow k + 1$
        end while
    end for
    $T \leftarrow T \cup \{(p_i, M_i)\}$
    $\mathcal{P} \leftarrow \mathcal{P} - p_i$
end for
```

controlled points $\{\mathbf{Q}_i\}_{i=0}^{n}$ is given by:

$$P(t) = \sum_{i=0}^{n} \zeta_{i,k}(t)\mathbf{Q}_i \tag{5.20}$$

where the basis functions $\zeta_{i,k}(t)$ are:

$$\zeta_{i,0}(t) = \begin{cases} 1, & t_i \leq t < t_{i+1} \\ 0, & \text{otherwise} \end{cases}$$

$$\zeta_{i,k}(t) = \tfrac{t-t_i}{t_{i+k}-t_i}\zeta_{i,k-1}(t) + \tfrac{t_{i+k+1}-t}{t_{i+k+1}-t_{i+1}}\zeta_{i+1,k-1}(t)$$

Let a detected segment of centreline points be denoted by $M = [\mathbf{m}_1\, \mathbf{m}_2 \ldots\, \mathbf{m}_l]^T$. In order to fit a B-spline curve through these points we look to minimise the scalar energy function E:

$$E(Q) = \frac{1}{2} \sum_{i=0}^{l} \left| \sum_{j=0}^{n} \zeta_{j,k}(t_i)\mathbf{Q}_j - \mathbf{m}_i \right|^2 \tag{5.21}$$

where $Q = [\mathbf{Q}_1\, \mathbf{Q}_2 \ldots\, \mathbf{Q}_n]^T$ is a collection of unknown control points for the B-spline curve. By setting the partial derivatives of E to be zero, the set of control points Q that minimise this energy can be found. The number of control points for the fitting spline can be set to be a percentage ($\sim$ 10%) of the number of centreline points being fitted. For small segments, the number of control points is fixed. See Fig. 5.13 for images of reconstructed vessel centrelines of a drainage.

Figure 5.13: Surface reconstruction of drainage vessels (left image) and reconstructed centrelines using B-spline curves (middle image). A closeup of a vessel with its reconstructed centreline spline curve fitted through a series of computed centreline points as marked by the points (right image)

5.4 Discussion

In the method presented for atrial body segmentation, the first step approximates the atrial body shape. It is important for the evolving front in this first step to stop before entering into the pulmonary vein drainages. An important assumption prevents this leakage in most circumstances; the diameters of the drainages are assumed to be smaller than the diameter of the atrial body. This enables the Euclidean DT function of the segmented left atrium binary image to descend rapidly close to the drainage causing the evolution process to gradually stop, thereby preventing the leakage. However, few cases of anomalous enlarged drainages have been found in our MRA acquisitions. The evolving contour usually leaks into the drainage and often stops before reaching the first pulmonary vein bifurcation. This over-segmentation affects the computation of several procedural parameters:

- Ostial diameters: These are the diameters of pulmonary vein drainages. If drainages become part of the atrial body segmentation, it becomes impossible to locate them.
- Atrial anatomy: The anatomy is described in terms of the number of drainages. If drainages become a part of the atrial body, this information is lost.

To overcome front evolution leakage problems in such anomalous cases a simple solution exists: Raising the threshold value τ_ξ on the lower bound of $\xi(L)$ in Eq. 5.6 prevents potential leaks. The consequence of this is usually an under-segmented atrial body. However, the centreline tracking process is robust to such under-segmentations and will generate centrelines.

For the centreline extraction process, computation of the vesselness filter response is an important step as it allows the process to distinguish between tubular and non-tubular structures. Furthermore, seed points to initiate centreline tracking are only generated within regions of high vesselness. This ensures that centrelines of non-tubular structures are not extracted.

5.5 Summary

A method for segmenting the atrial body from binary left atrium segmentation images is presented. The atrial body is segmented using evolving fronts under the level set method framework. Intuitive speed functions are used to avoid leakage through venoatrial junctions. Segmentation of the atrial body is an important pre-processing step required for further analysis of the left atrium. A technique for fast extraction of pulmonary vein centrelines is also presented.

The method finds centrelines by computing local maxima of the Euclidean DT of the binary left atrium segmentation.

The proposed approaches utilises existing techniques such as level set methods [129] and the vesselness filter [50]. Level sets only provide a general framework for implementing deformable models. The approaches described for atrial body segmentation applies this framework using novel speed functions. Furthermore, the vesselness filter is applied to obtain pulmonary vessel centrelines. The vesselness filter, on its own, cannot generate centrelines. It only finds voxels within tubular structures. Extensions to this work have been proposed for centreline extraction [185]. However, this method requires a significant amount of user intervention.

The methods proposed for centreline extraction apply novel techniques which can efficiently track and reconstruct the medial axes of pulmonary vessels. Together the described methods provide us with a compact representation of the left atrium in terms of its two important sub-structures: the atrial body and the pulmonary vessels. Important anatomical information can now be derived from the spatial locations of these structures. Moreover, computation of several procedural parameters such as atrial volume, ostial diameters and bifurcation distances is not possible without a prior segmentation of the atrium's sub-structures.

Chapter 6

Modelling pulmonary vessel trees and quantification of ostia

With a growing interest in investigating the precise anatomy of the heart, a majority of the pre-procedural planning studies for ablation require a good understanding of the atrial anatomy. It is now well established that the anatomical architecture of the left atrium and pulmonary veins play an important role in the genesis and maintenance of atrial fibrillation [59]. Traditional techniques used in electrophysiology can accurately map electrical activity in the atrial chambers [101] but cannot resolve the underlying left atrial anatomy. Automatic extraction, identification and classification of atrial anatomy have both pre- and intra-procedural benefits.

This chapter presents techniques to automatically extract atrial anatomy and identify ostia. Techniques for computation of ostial diameters are also presented. The proposed algorithm identifies the pulmonary vein drainages of the left atrium and constructs vessel trees from pulmonary vein centrelines at each drainage location. This tree representation helps to classify the underlying left atrial anatomy. Once pulmonary vein drainage locations are identified, ostial diameters can be computed using the proposed techniques. Fig. 6.1 shows the main steps involved in the proposed algorithm.

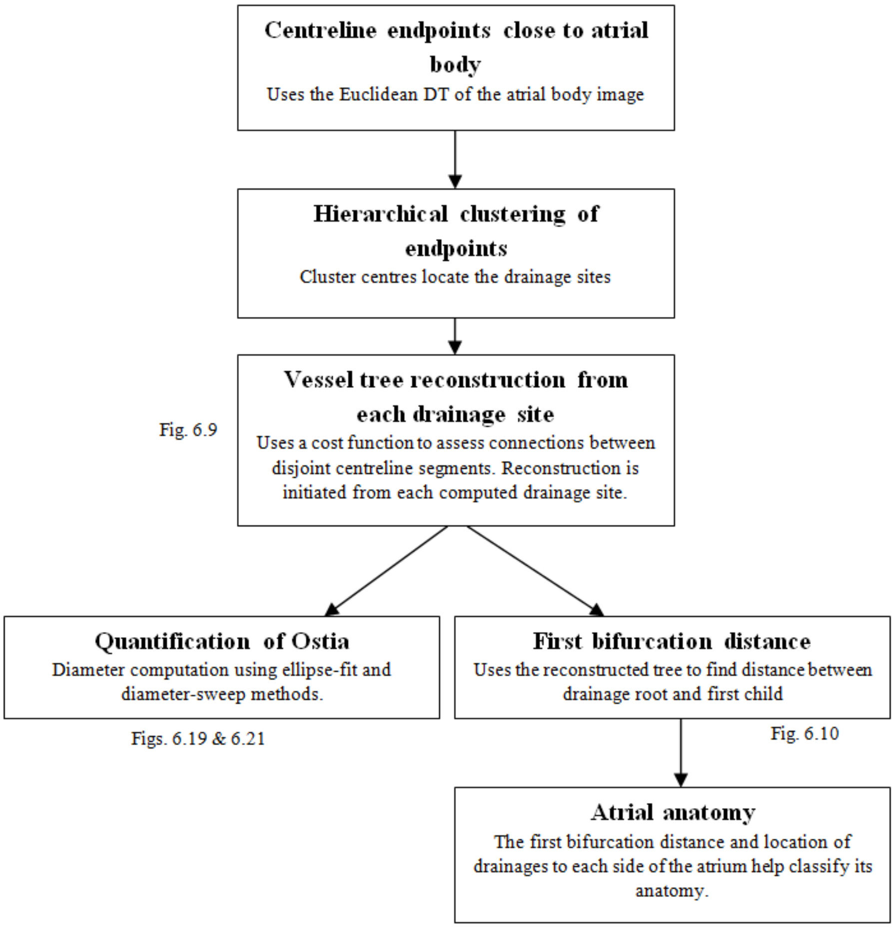

Figure 6.1: A flow diagram showing the main steps involved in the proposed algorithm.

6.1 Modelling pulmonary vessel trees

The principal idea behind extracting atrial anatomy is to generate a symbolic representation of the detailed pulmonary vessel tree at each drainage. This representation can be most naturally retained as an n-ary tree, with vessel centreline segments as nodes in the tree graph. Using graphs to reconstruct vessel networks is not uncommon and is discussed in section 3.4.2 on page 59. Since each pulmonary vessel tree can drain into separate locations on the atrial body, the identification of every drainage to the left atrium is important (see Fig. 5.1 on page 85 for drainage sites in the left atrium). Once these are identified, the pulmonary vessel tree building process can initiate from each pulmonary vein drainage. In this section an algorithm is presented to construct a pulmonary vessel tree from the centrelines as found in Chapter 5.

The pulmonary vein centreline tracking process described in section 5.3.3 will inevitably produce disconnected vessel segments. It is useful to connect these segments in some systematic fashion and construct a tree-like representation of the pulmonary veins. The algorithm for building the vessel tree involves two steps: In the first step, pulmonary vein drainage sites and their root vessels are determined. In the second step vessel segment connections are found and used to build the vessel tree.

6.1.1 Pulmonary vessel drainage sites and root vessels

Assuming that centrelines of pulmonary veins and a segmentation of the atrial body are both available, locating pulmonary vein drainage sites is equivalent to the problem of finding centreline segments that are incident upon the atrial body. Once these segments are found, their endpoints are a good approximation of the drainage location. Recall that one of the termination conditions imposed in centreline tracking in section 5.3.3 on page 98 was intersection with atrial body. With this condition, it is likely for most centreline segments in drainage sites to be incident upon the atrial body. This simplifies the problem of finding drainages. However, the other termination conditions such as the one imposed for sudden increase in curvatures may cause a drainage centreline to stop prematurely, before it reaches the atrial body. We propose a simple and fast technique for automatically detecting the location of pulmonary vein drainage areas using the atrial body and endpoints of centreline segments.

It is reasonable to make the assumption that centrelines in drainage sites lie in close proximity to the atrial body surface. The Euclidean distance between the endpoints of the centrelines and the atrial body surface is a good discriminant for finding vessel segments close to the atrial body. This distance can be found using a simple Euclidean DT transform. Assume two subsets in the image space I: left atrium (L) and atrial body (B) where $B \subset L \subset I$. The complement set B':

$$B' = I \backslash B \tag{6.1}$$

where B' contain all pixels that are not in B, i.e. $x \in B'$, $x \notin B$. Let $\xi(.)$ be the Euclidean DT (see chapter 4.5). We can compute $\xi(B')$ which yields the shortest distance value between each voxel and the atrial body surface. Using this, the distance of each centreline endpoint to the atrial body surface can be determined. Since DT functions are pre-computed for whole images, obtaining distance values for centreline endpoints is fast. Only centreline segments that have a distance value less than d_τ and a certain length are selected. The length is the total sum of the distance between its detected centreline points. We use d_τ =50 mm for our purposes. This technique of selecting centrelines will capture not only segments that are incident upon the atrial body, but also those that terminate prematurely before reaching the atrial body (see Fig. 6.2(a)).

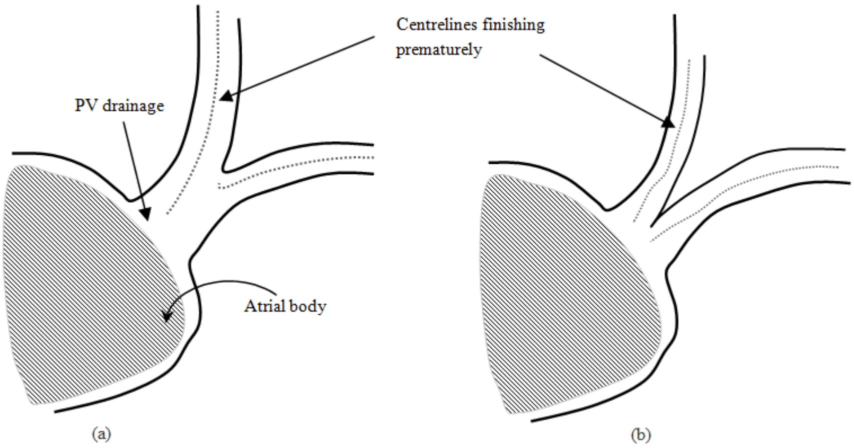

Figure 6.2: The two cases where the centrelines finish prematurely and are not incident upon the atrial body. The Euclidean distance transform can be applied to find centrelines close to the atrial body in these cases.

It is reasonable to assume that a pulmonary vein drainage with bifurcations at distances less than d_τ from the atrial body, will yield more than one centreline segment with the above atrial body distance threshold technique, i.e. at least one for each branch. This case is illustrated in the double branch bifurcation example in Fig. 6.2(b), where both segments are reasonably close to the atrial body, but not incident upon it. Thus one or more centreline segments can be expected to be found for each drainage. The centreline endpoints, with atrial distance less than d_τ, are clusters of points spatially distributed near or on the atrial body surface (see Fig. 6.3). To resolve the number and location of drainages, a clustering algorithm can be applied on the centreline endpoints. Recall that these endpoints are position vectors in image space. Endpoints are *clustered* using a technique known as *Hierarchical clustering* that gives optimal spatial separation between them. Once the optimal cluster set is found, the drainage locations are revealed.

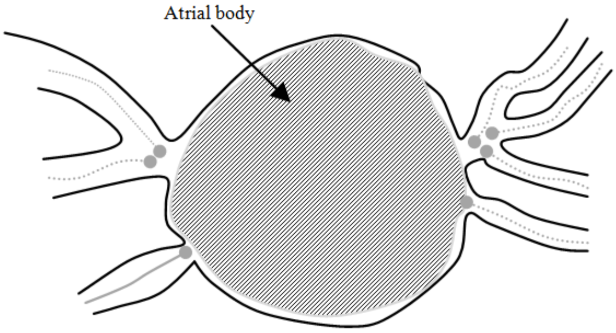

Figure 6.3: An illustration showing how centreline endpoints (marked by shaded dots) of selected segments form point clusters. A clustering algorithm can detect the separate clusters. Cluster centres can be used as approximate locations for the pulmonary vein drainages.

Hierarchical clustering [70] is a well-known clustering algorithm. Other clustering algorithms such as K-means have been applied to a wide variety of machine learning problems [62]. In hierarchical clustering, a hierarchy of clusters are constructed starting from the individual elements at one end and a single cluster containing every element at the other. One of the ways of representing this hierarchy is using a tree representation called a *dendogram* (see Fig. 6.4). Clusters at each level are formed using a distance similarity measure. We use the *single-linkage* variant, where the distance between two clusters is assumed to be the distance between the two closest elements in the two clusters. At each level of the tree, the closest clusters are merged. The output of the algorithm is thus only the hierarchy tree. An advantage of using this technique is that it requires no information about the number of clusters present, which is unlike the more commonly used K-means algorithm. However, it requires the use of a parameter (see Eq. 6.6) which specifies the desirable cluster separation distance.

We are interested in finding the level of the tree at which the cluster groupings are optimal based on intra-cluster distances. Let the tree contain a hierarchy level h where there are w clusters. Assume that the kth cluster R_k contains n centreline endpoints:

$$R_k = \{\mathbf{p}_0, \mathbf{p}_1, \mathbf{p}_2, \ldots, \mathbf{p}_{n-1}\} \qquad 0 < k \leq w \tag{6.2}$$

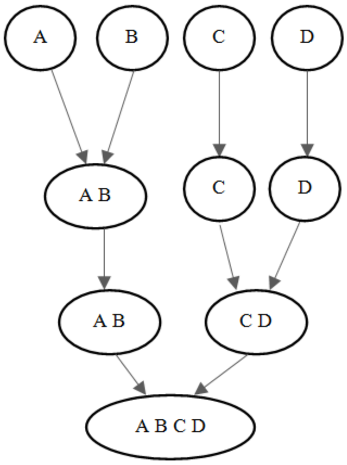

Figure 6.4: A tree representation of the hierarchy of clusters starting from individual elements $A.B, C, D$ and E. Clusters are formed at each level using a pre-defined similarity measure. Representations like these are constructed in the Hierarchical clustering algorithm.

The mean of intra-cluster distances μ_k for the kth cluster in this hierarchy is given by:

$$\mu_k = \frac{1}{n}\left[\sum_{0 \leq i < j < n} d(\mathbf{p}_i, \mathbf{p}_j)\right] \tag{6.3}$$

where $d(\mathbf{p}_i, \mathbf{p}_j)$ is the Euclidean distance between two points. Similarly, a measure of variance on the intra-cluster distance for the kth cluster can be given as:

$$\sigma_k^2 = \frac{1}{n}\left[\sum_{0 \leq i < n} (\mathbf{p}_i - \mu_k)^2\right] \tag{6.4}$$

Thus, the total mean and variance for all w clusters at this hth level of hierarchy is:

$$\mu_h = \sum_{i=1}^{w} \mu_i \qquad \text{and,} \qquad \sigma_h^2 = \sum_{i=1}^{w} \sigma_i^2 \tag{6.5}$$

The variance measure σ_h^2 at each level of the hierarchy explains how sparsely or densely distributed the points are within each cluster at that level. Because there is some spatial separation between drainages on the atrium, the variance is expected to rise sharply when two drainages are joined into one cluster. Since clusters are merged at each level of the tree, the tree must be traversed from top to bottom. The variance difference measured between levels reveals the level containing the optimal cluster set h^*, and is controlled by the *variance-differential* parameter

s_τ:

$$|\sigma_h^2 - \sigma_{h+1}^2| > s_\tau \tag{6.6}$$

The variance-differential is an important parameter, mostly useful for finding dense drainage neighbourhoods in rarely occurring anatomical variants of the left atrium (see section 7.5.4 for further details).

Recall that clusters represent drainages and it is reasonable to assume that the distances between pulmonary vein drainages are relatively larger than the distances between points (i.e. centreline endpoints) within a drainage. Starting from the lowest level, $h = 0$, where every element is a cluster on its own, the total variance is zero. As we move from top to bottom, the first *significant* increase in variance is found. The threshold value s_τ in Eq. 6.6 defines what can be appropriately classified as a significant increase. If this increase is found as we move from level $h = i$ to $h = i + 1$, then the optimal cluster set level $h^* = h$. Once the optimal cluster grouping is found, each cluster correctly represents a pulmonary vein drainage location. Pulmonary vein vessel tree model building starts from each drainage and requires a root vessel to which other vessels are subsequently connected. The vessel with the largest size in each cluster is selected as the root. The vessel length is estimated using:

$$v_{length} = \sum_{i=0}^{\eta} |\mathbf{c}_i - \mathbf{c}_{i+1}| \tag{6.7}$$

where η is the total number of centreline line points $\mathbf{c}_i$ in vessel segment v.

6.1.2 Vessel segment connections

With a root vessel selected for each pulmonary vein drainage, the vessel tree at the drainage is constructed by progressively attaching child nodes to the connected base (see Fig. 6.5). The attachments are drawn using a straight line that connects the child to the parent. Before connecting vessels, possible connection paths between them are evaluated using a cost function. The cost function weighs the following:

1. **Distance:** The distance of the line connecting the vessels, which is referred to as the *spatial proximity*.
2. **Vesselness:** A similarity measure based on the vessel response filter described in sections 3.4.1 (page 54) and 5.3.2 (page 97). Recall that the vessel response filter gives high responses within segments inside vessels and low responses otherwise. The mean vesselness response along the proposed connection is used as the discriminant. This is referred to as the *vesselness measure*.

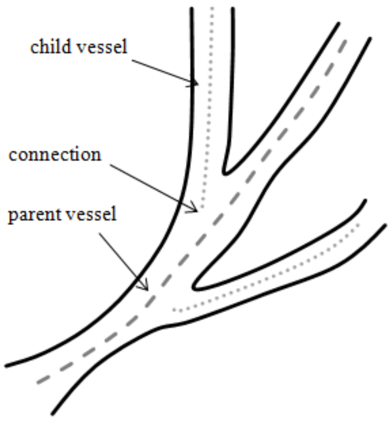

Figure 6.5: Parent vessels are selected after cluster computation; child nodes are progressively attached to the parent base. The cost function favours spatial proximity and high vesselness.

A low distance value coupled with a high vesselness response is strong evidence for a connection. The cost function $\varphi : \mathbb{R} \rightarrow [-1, 1]$ evaluates these criteria for evidence of a connection using:

$$\varphi = \omega\mathcal{V} + (1 - \omega)\mathcal{D} \tag{6.8}$$

where $\omega \in [0, 1]$, trades off penalty function for vesselness measure $\mathcal{V}$ and for the spatial proximity $\mathcal{D}$. A positive cost favours connection and a negative cost otherwise.

The range of values of vesselness response and spatial proximity can vary between different images. It is necessary to map these values to the same range as that of the cost function. The mapping functions are derived from a sigmoid function. The penalty term for spatial proximity is straightforward: Any parent-child connection distance is penalised according to their separation distance d:

$$\mathcal{D} = 1 - \frac{2}{1 + e^{-(d - \epsilon_d)}} \tag{6.9}$$

where any distance greater than ϵ_d acquires negative penalty. A threshold value of $\epsilon_d = 6$ has empirically shown to work well. The separation distance d is the Euclidean distance between a child's endpoint and the closest centreline point on the parent it is being connected to. Fig. 6.6 illustrates this penalty term.

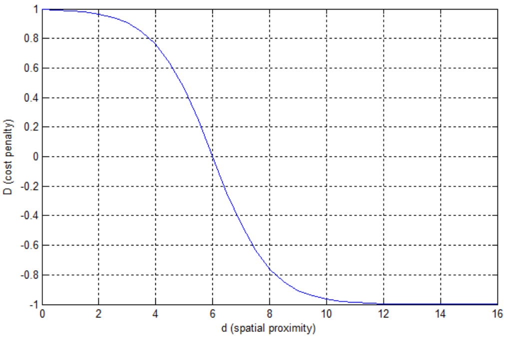

Figure 6.6: The sigmoid penalty term for spatial proximity of child and parent vessels. A positive value (vertical axis) favours connection, while a negative value inhibits connections.

Unlike the spatial proximity penalty term, it is difficult to select a threshold for the vesselness penalty function as the range of filter response is known to vary between different images. To overcome this, the penalty function for vesselness $\mathcal{V}$ in Eq. 6.8 along the proposed connection is based on the observed distribution of vesselness filter responses over all detected centreline segments. Any deviation from the mean of the observed distribution is penalised. Empirically, it can be shown that vesselness responses at centreline points are normally distributed (See Fig. 6.7). This is since vesselness responses do not vary with vessel width for the following reasons:

- The vesselness filter is defined in terms of eigenvalue ratios (see Eq. 5.12) which are invariant to the vessel width.
- The vesselness is computed using a multiscale filter and hence the response is analysed across all scales.

Normal distribution for vesselness responses along detected centrelines has mean μ and variance σ: $\mathcal{N}(\mu, \sigma)$. For a proposed connection between parent and child, the mean vesselness measure

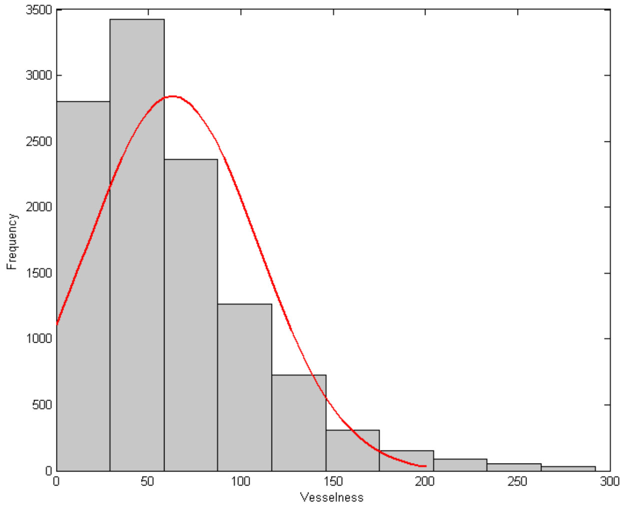

Figure 6.7: A histogram of vesselness response from computed centreline points of a patient dataset. A gaussian using the computed mean and variance approximates the distribution.

μ_o is determined by sampling points on the straight line connecting them. The standard score or z-score of the observed quantity μ_o, with respect to the distribution $\mathcal{N}(\mu, \sigma)$, indicates how many standard deviations μ_o is above or below μ. It is given by:

$$z = \frac{\mu_o - \mu}{\sigma} \tag{6.10}$$

The penalty term for vesselness determines the amount of penalisation based on the z-score. The mapping from z-score to accrued cost is derived from a sigmoid function:

$$\mathcal{V} = \frac{2}{1 + e^{-(z+\epsilon_v)}} - 1 \tag{6.11}$$

where ϵ_v is a constant. A value of $\epsilon_v = 2$ has empirically shown to work well. See Fig. 6.8 for the vesselness penalty function with $\epsilon_v = 2$. Recall that positive penalty favours connection. Since high vesselness is a strong indicator of a vessel connection, a positive penalty is awarded not only when $\mu_0 \geq -\epsilon_v \sigma$, but also when $\mu_0 > +\epsilon_v \sigma$. For $\mu_0 > \epsilon_v \sigma$, the penalty value saturates to +1. This explains the positive penalty $\mathcal{V} > 0$ for $z > -2$, and penalty saturation beyond $z > +2$ in Fig. 6.8.

The cost function is evaluated for every vessel segment pair. For each vessel pair (v_i, v_j), it is computed at every pair of their centreline points. The maximum attainable cost for each

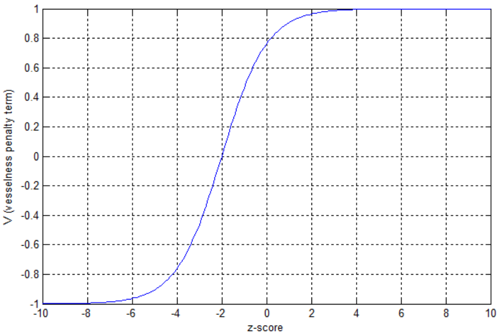

Figure 6.8: The vesselness penalty function for measure of child and parent vessels

vessel pair is retained. See Algorithm 2 for computation of cost functions for vessel segment pairs. Given that the number of vessel segments is typically in the order of hundreds, the cost function for all vessels can be computed in less than a minute. However, there is room for optimising the algorithm. To this end, instead of computing the cost for every pair of centreline points of a vessel pair (v_i, v_j), it can be computed for every 3rd or 4th pair, giving considerable improvement in speeds.

Algorithm 2 The getVesselConnectivityMatrix routine

```
Require: all vessel segments $\Omega = \{v_0, \ldots, v_n\}$
Ensure: a matrix $\psi(i,j)$ which stores a triple $(B, c_a, c_b)$. $B$ is a boolean which is TRUE if
    vessel segments $v_i$ and $v_j$ can be connected. $c_a$ and $c_b$ are endpoints of the connecting line
    between $v_i$ and $v_j$ .
for i=0 to n do
    for j=i+1 to n do
        for all pairs of centreline points $(p_k^{(i)}, p_l^{(j)})$ of vessels $v_i$ and $v_j$ do
            $s(k,l) \leftarrow$ Evaluate cost function $\varphi = \omega\mathcal{V} + (1-\omega)\mathcal{D}$
        end for
        if $\max\{s(k,l)\} \geq 0$ then
            $\psi(i,j) \leftarrow (TRUE, \mathbf{p}_k^{(i)}, \mathbf{p}_l^{(j)})$
        else
            $\psi(i,j) \leftarrow (FALSE, \varnothing, \varnothing)$
        end if
    end for
end for
```

6.1.3 Vessel tree building

The left atrial anatomy is determined by constructing vessel trees at each drainage. A connectivity matrix is computed for all vessel segments which stores a triple: $(\mathcal{B}, c_a, c_b)$. $\mathcal{B}$ is a boolean which is set to true if there is a connection between the vessel segment pair. c_a and c_b are the centreline points on the two vessel segments as endpoints of this connection. This matrix is computed in Algorithm 2. With the connectivity matrix pre-computed, tree building at each drainage then becomes a simple process. With a root vessel selected, child nodes that are connectable as indicated by the connectivity matrix, are appended to the root. The process is essentially recursive, as illustrated in Algorithm 3. The entire algorithm for finding atrial anatomy is outlined in Algorithm 4. Vessel trees can be retained and processed now as n-ary tree data structure. This is a powerful and natural representation of left atrial vessel trees, as it allows further post-processing such as atrial anatomy.

Algorithm 3 The buildTree routine

Require: root vessel $R^{(i)}$, a vessel tree T, ψ a vessel connectivity matrix.
Ensure: vessel tree T with appended child nodes.

```
for all $j$ where $\psi(i,j) = TRUE$ and $i \neq j$ do
    $T \leftarrow T \oplus v_j$ {$\oplus$ - append as child to tree}
    buildTree($v_j, T$)
end for
```

Algorithm 4 The getAtrialAnatomy routine

Require: all vessel segments $\Omega = \{v_0, \ldots, v_n\}$
Ensure: set of vessel trees γ

```
$\mathcal{C} \leftarrow$ getOptimalClusterGrouping($\Omega$)
$\psi \leftarrow$ getVesselConnectivityMatrix($\Omega$)
for all drainage $c_i \in \mathcal{C}$ do
    $R^{(i)} \leftarrow$ select a root vessel from cluster $c_i$ such that it is the longest vessel
    buildTree($R^{(i)}, T^{(i)}, \psi$)
    $\gamma = \gamma \cup T^{(i)}$
end for
return $\gamma$
```

6.2 Atrial anatomy

With the vessel trees symbolically represented and retained, they can now be reported and displayed to the clinician. These are displayed as a tree data structure (see Fig.6.11). Vessel segments are annotated and numbered (see Fig. 6.9) for quick and easy reference. It is sometimes desirable to view only veins that are incident on the atrial body, as these are frequently sites of ablation [133]. Removing peripheral vessels to gain an unobstructed view of the atrial body's incident veins is difficult using a manual approach, as each peripheral vessel has to be removed individually. With the symbolic tree representation of pulmonary veins, obtaining these unobstructed views become simple. Since the tree data structure has a height component, the vessel trees can simply be truncated at any desirable height without any additional computational overhead. See Fig. 6.12 for a truncated tree view of an atrium. These truncated models are a typical requirement for most robotic catheter ablation systems. The Sensei robotic navigation system developed by Hansen Medical Inc. is one such example where surface models of segmented and truncated atria are displayed on its workstation.

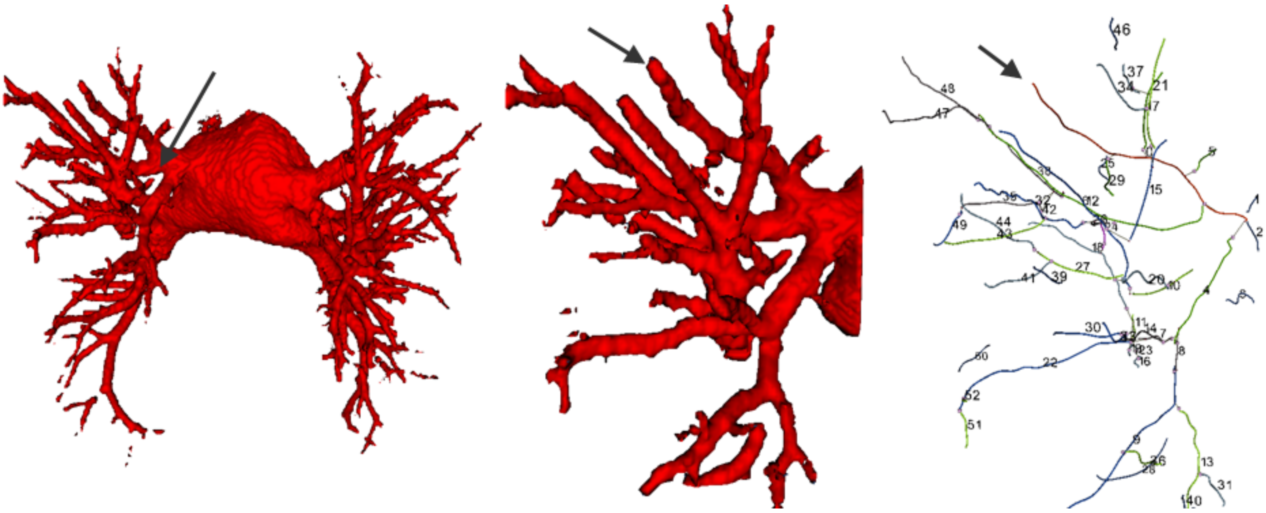

Figure 6.9: A left atrium with a drainage marked by an arrow (left). Close-up of the marked pulmonary vein drainage; the arrow indicates the root vessel used to build the tree (middle). The detected and annotated centrelines; vessels are annotated using numbers by the system for easy reference; the root node vessel is indicated by the arrow (right).

6.2.1 First bifurcation distances

An important indicator and parameter for distinguishing atrial anatomy is the FD (see Fig. 1.2 on page 7). Each pulmonary vein drainage is expected to have bifurcations at certain distances along the drainage. The FD is measured from the atrial body. It was used in [109] for classifying major variations in left atrial anatomy on a 200-patient study (see Fig. 2.4 and 2.5). For example, both to the right and left sides of the left atrium, the anatomy can be differentiated based on whether the FD is less or greater than 10 mm. In Fig. 2.4, the classes

R2a/b, R3b/c, L1a/b all have FD less than 10 mm. The rest have FD greater than 10 mm. We refer to these classes in the remaining of this thesis as the ones with an early (< 10 mm) or late branching.

Recall that vessel centrelines are modelled with cubic B-spline curves (see chapter 5.3.4). The B-spline curve is composed of piece-wise cubic polynomials joined at locations called knots. An important constraint imposed on the cubic B-spline is on its smoothness allowing it to maintain a C^2-continuity throughout its length. It is thus twice-differentiable within and across knots. Length of the centreline B-spline and thus a vessel segment $[a, b]$ can then be computed using:

$$\mathcal{T}_v = \int_b^a \parallel P'(t) \parallel dt \tag{6.12}$$

where $P(t)$ is the B-spline curve in Eq. 5.20 with parameter t. The length of the segment of the vessel drainage prior to the first bifurcation is measured to give the FD. With vessel trees computed for each pulmonary vein drainage, this equates to finding the distance to the *first* child of a root vessel - the first child from the atrial body. As vessels can twist and turn in 3D space, a simple Euclidean distance between the child and root nodes does not suffice. The geodesic distance between them is required and is well approximated by the spline segment of the root vessel centreline connecting these nodes. This segment begins from the root vessel endpoint that is closest to the atrial body and ends where the first child connects to the root (see Fig. 6.5). The length of this segment approximates the FD. Assume that this segment is $[a, b]$. The integral in Eq. 6.12 can be approximated by sampling the spline segment $P(t)$ at intervals $a = l_0 \leq \ldots \leq l_n = b$:

$$\mathcal{T}_v \approx \sum_{i=0}^{n} |P(l_i) - P(l_{i+1})| \tag{6.13}$$

For each computed pulmonary vein drainage tree, the FD is computed automatically and reported. See Fig. 6.10 for an illustration.

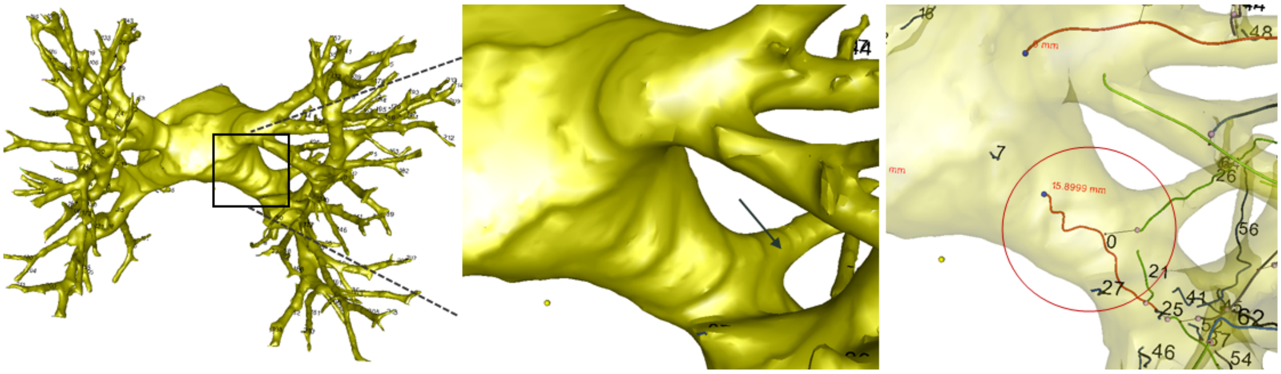

Figure 6.10: Left image: Surface reconstruction of a segmented left atrium. Middle image: Close-up of a drainage with its first bifurcation marked by an arrow. Right image: The computed first bifurcation distance (15.889 mm) measured using reconstructed vessel trees as marked by a circle.

6.2.2 Classification of anatomy

To our knowledge, the only documented anatomical classification of the left atrium is due to Marom et al. [109]. The classification is based on two distinct classes for the left and right sides. The proposed naming system is a three letter acronym that can be represented by the following *regular expression*: $(R|L)n(a|b|c)$ (see Fig. 2.4 and 2.5). For instance, an anatomy with three pulmonary vein drainages to the right side with an early branching can be an R3b class. It is clear that the number of drainages together with the FD distance describe left atrial anatomy to any one side. All three parameters are computed from the vessel trees. Recall that optimal clustering of centreline endpoints incident upon the atrial body gives the number of drainages to the left atrium (see chapter 6.1.1), giving the first parameter in the naming. FD distance values are overlaid on surface visualisations of the left atrium and displayed alongside each drainage tree, making it immediately clear whether trees have an early or late branching. The third parameter represents specific pulmonary vessel tree branching configurations. Most configurations are essentially bifurcations except for R1 which has an early trifurcation. The FD distances are again used to assess if certain branching configurations are noteworthy, especially the b and c classes.

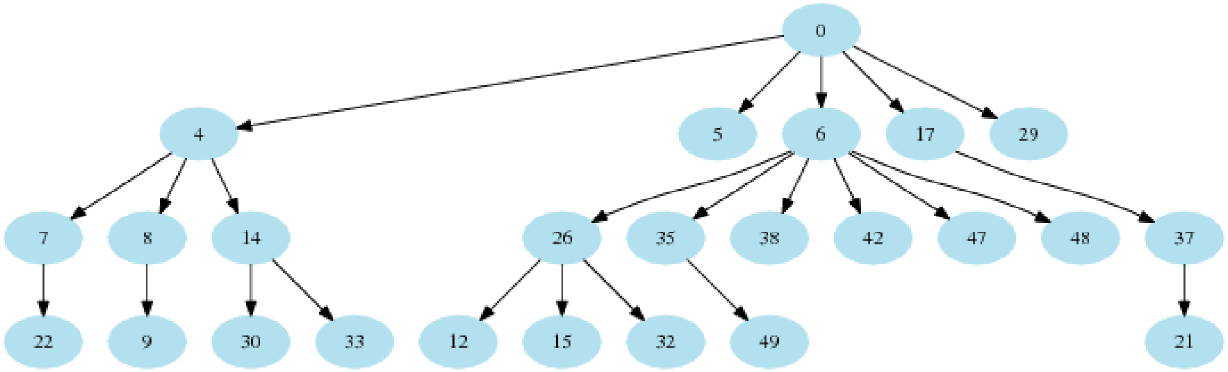

Figure 6.11: The vessel tree of the drainage in Fig. 6.9. Vessel trees are displayed to the end-user in these graphical formats.

6.3 Measuring ostial diameters

Familiarity with the normal range of ostial diameters is important for pre-operative management of patients (for ostium see Fig. 1.2 on page 7). Post-procedural complications in RF ablation commonly include vessel stenosis (see section 2.3.3) and thus ostial diameters assist in the early detection of such conditions [99]. Most institutions will adhere to a set of protocols for RF ablation procedures, and some institutions may not include ostial measurements as part of their protocol. However, studies continue to indicate that the occurrence and progression of pulmonary vein stenosis is a potentially significant complication for ablation procedures [42]. Its early onset can be identified by measuring the ostium.

There is little literature which discusses how ostial diameters are conventionally measured. Scharf et al. [155] report on measuring diameters with digital callipers from surface reconstruction images. In that study, the maximum distance between two ostial points (i.e. boundary points) in the same plane and in at least two orthogonal projections was measured to give the diameter (see Fig. 6.14). Although this specification of the ostial diameter may give a reasonable approximation of the diameter, locating ostial points separated by the *maximum* distance may not always be straightforward. Moreover, this method only regards two orthogonal projections leaving out the rest.

Assuming that pulmonary vein centrelines and drainage locations are available, ostial diameters

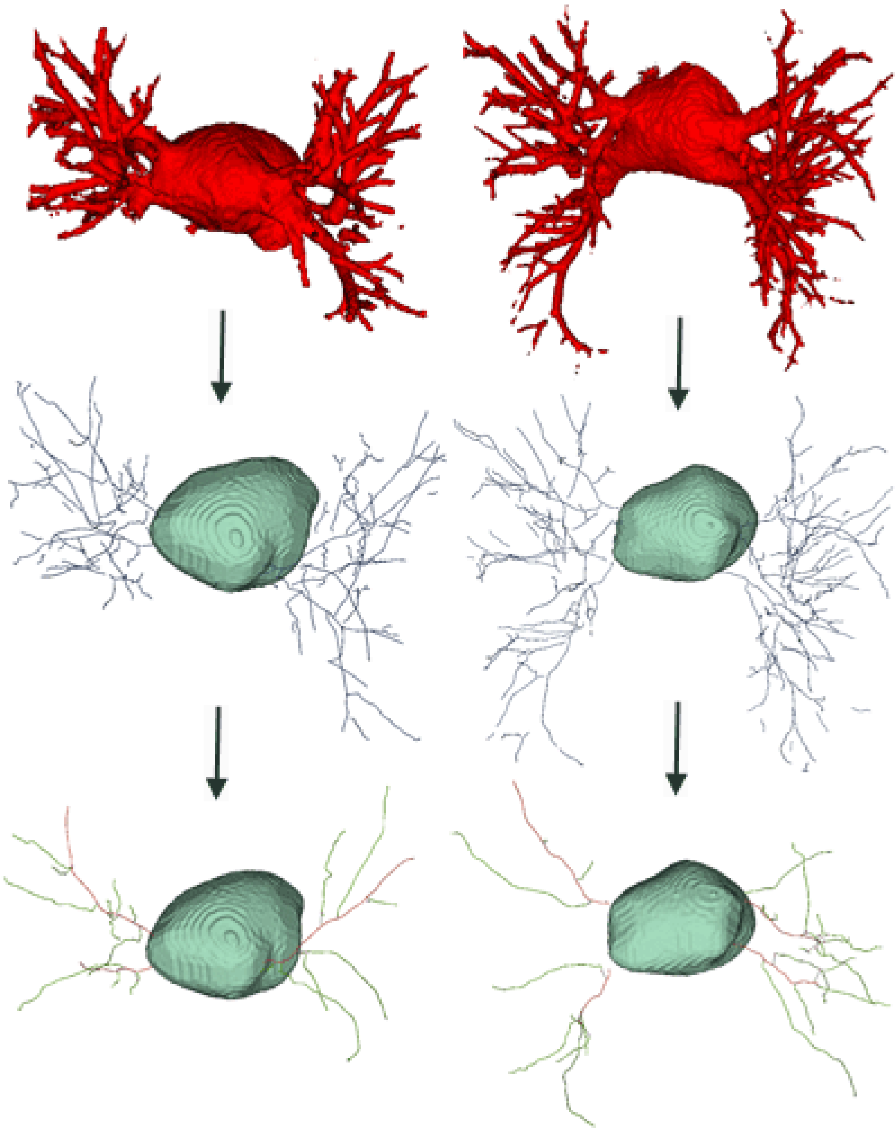

Figure 6.12: Two segmented left atria (top row). Extracted vessel centrelines are shown along with segmented central atria (middle row). The truncated vessel view with peripheral vessels removed (bottom row). Vessels at a depth of $h \geq 2$ have been removed.

can be computed using a semi-automatic approach. The ostium is located at each drainage giving positions from which diameters can be computed. The root vessel of a pulmonary vein drainage is used as a reference point for measuring these diameters. The algorithm to measure ostial diameters comprises the following steps:

1. Computation of the diameter plane at a point on the root vessel.
2. Locating the ostial boundary on this diameter plane and sampling points on this boundary.
3. Fitting an ellipse to the sampled set of points or finding the mean of distances to the

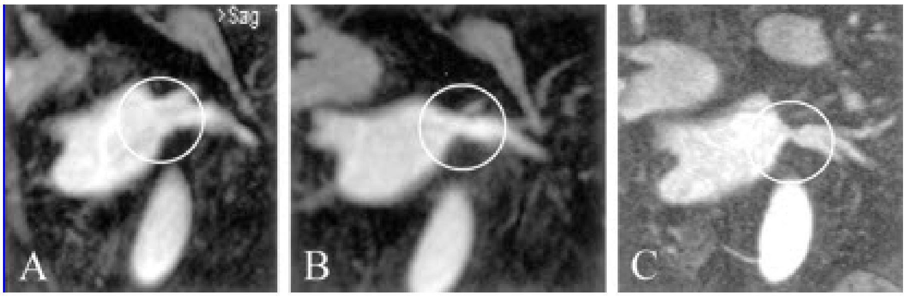

Figure 6.13: Progressive ostial diameter reduction (circled) in lower left pulmonary vein. A: Before RF Ablation; B: 1 day after RF ablation; C: 3 months after RF ablation. Image adopted from [42].

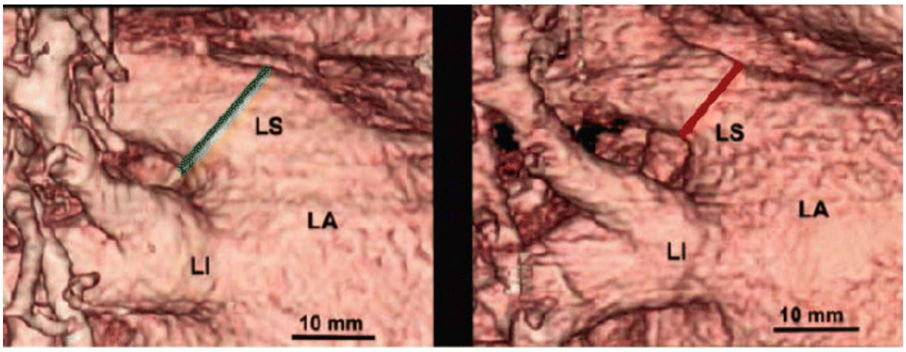

Figure 6.14: The image shows lines drawn to mark the ostial diameter. More precisely, it is the maximum distance between two ostial points in the same plane and in at least two orthogonal projections. This is the technique used by Scharf et al. [155]. Image adopted from [155].

sampled points by *sweeping* the diameters radially.

The above steps are discussed in greater detail in the following sections.

6.3.1 Computation of the diameter plane

The diameter plane is the plane on which the ostial diameters are measured. This plane cuts the pulmonary vein at a right angle and the intersecting region is a pulmonary vein cross-section. The boundary of this cross-section is the ostial boundary if the plane is placed correctly at the ostium. The root vessels identified for reporting of atrial anatomy in section 6.2 clearly form the best possible candidate for finding the ostium and thus measuring ostial diameters. However, it may not be immediately clear as to how far along the vessel centreline these measurements should be made. If measurements are made too close to the atrial body, allowing for small differences between actual and segmented atrial body boundaries, the diameter measured may be influenced by the atrial body rather than the ostium. This is illustrated in Fig. 6.15. To overcome this problem, a series of diameter measurements can be made. Recall that vessels are modelled with a B-spline curve (see chapter 5.3.4). Starting from a point $\mathbf{c}'_0$ on the root vessel spline, at a distance ϵ_d from the atrial body, diameters are measured successively at $\mathbf{c}'_0, \mathbf{c}'_1, \mathbf{c}'_2, \ldots$ and so on until the diameter value stabilises along a certain range of centreline points. It is at this *stabilisation range* that ostial diameter can be reliably and sensibly measured.

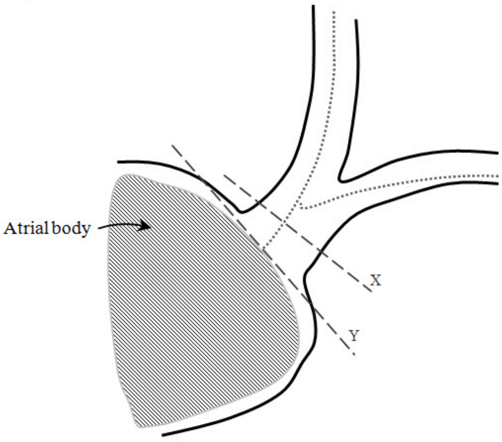

Figure 6.15: A plane is used to cut the pulmonary vein across. Placing this plane too close to the atrial body (Y) may give incorrect ostial diameters as it cuts a larger section of the atrium. The plane must be positioned correctly, as shown, for reliable measurements to be made (X).

The diameter plane is computed at each spline point $\mathbf{c}'_k$, and it must be orthogonal to the vessel axis. This is illustrated in Fig. 6.16(a). With the medial axis approximated by a B-spline curve, computing this plane becomes simple. Assume that sampled points on the spline are: $\{\mathbf{c}'_0, \ldots \mathbf{c}'_n\}$. The diameter plane Π normal to the vessel at $\mathbf{c}'_k$ is given as:

$$\Pi : (\mathbf{c}'_{k+1} - \mathbf{c}'_k) \cdot (\mathbf{x} - \mathbf{c}'_k) = 0 \tag{6.14}$$

The plane is thus oriented in the direction of the vector between consecutive spline points: $(\mathbf{c}'_{k+1} - \mathbf{c}'_k)$.

6.3.2 Point sampling on intersection boundary

The boundary of the ostium from the result of the intersection between the diameter plane and pulmonary vein is required to approximate its diameter. To circumvent the problem of obtaining the continuous boundary, in the discrete space, the idea is to sample points on the boundary. This is illustrated in Fig. 6.16(a). These points are then used for fitting an ellipse.

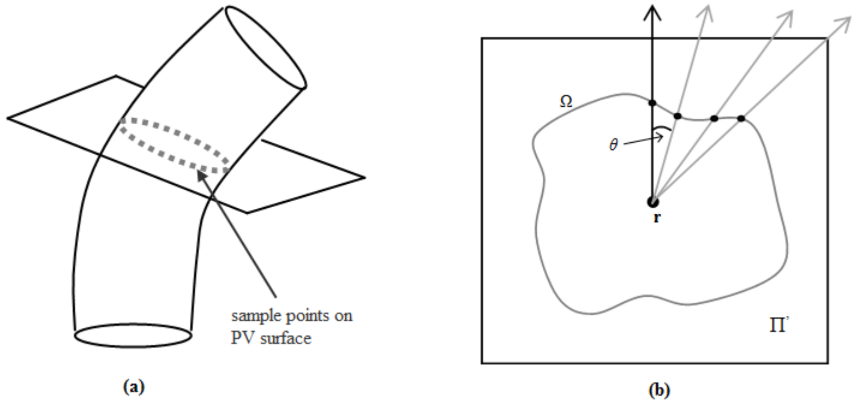

Figure 6.16: (a) An illustration of points sampled on the pulmonary vein boundary with the cutting plane shown. PV - pulmonary vein (b) Points are sampled on the ostial boundary Ω using a ray-casting technique. Rays are cast from the plane centre $\mathbf{r}$ at θ degree intervals. The edge gradient along the ray determines where it intersects the ostial boundary.

A simple process can generate infinitely many sampled points on the intersection boundary Ω. With the plane Π computed in Eq. 6.14, a finite plane Π' is contained within Π where $\Pi' \subset \Pi$ is placed by the operator. Although the orientations and position of the plane are pre-computed, the user only ensures that the plane Π' adequately encloses the pulmonary vein. For example, in Fig. 6.16 the plane Π' adequately covers the pulmonary vein. Since Π' is a finite plane, it has well-defined corners and a centre. Rays are cast from the centre of the plane to the ostial boundary. These rays are cast at θ degree intervals (see Fig. 6.16). The edge gradient along each ray determines where the ray intersects the ostial boundary Ω. In this fashion points can be sampled on the ostial boundary using a pulmonary cross-section. The resulting points are used to fit an ellipse for obtaining an approximation of the diameter.

6.3.3 Outlier detection

The ellipse-fitting method using a least-squares approach can be very sensitive to outliers present in the set of sampled points on the boundary Ω. To make the ellipse-fitting more robust, the set of sampled points is checked for any outliers that may arise due to the elongation of the pulmonary vein cross section boundary. This elongation is due to the continuity of the atrial structure on the cutting plane Π'. Figure 6.17 illustrates this phenomenon. Depending on the orientation of the plane, the plane may cut through a larger section of the atrium generating the elongated cross-section or ideally cut through only the pulmonary vein ostium. Sampling points with the ray-casting technique will give outliers. It is desirable to remove outliers from the sampled point set ρ prior to ellipse-fitting.

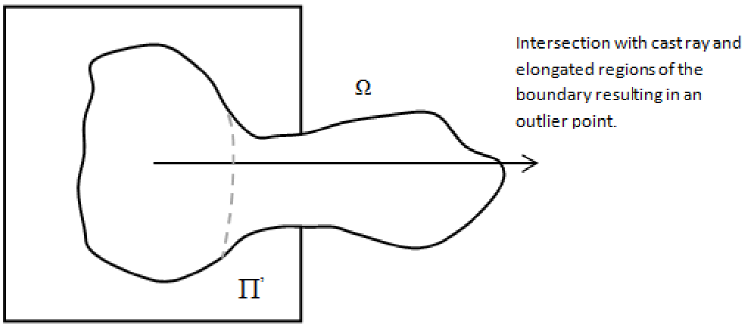

Intersection with cast ray and elongated regions of the boundary resulting in an outlier point.

Figure 6.17: Figure illustrates an instance where the pulmonary vein cross section boundary may not be circular as depicted in Fig. 6.16. Depending on orientation of the cutting plane, the cross section projected on the plane can have elongated boundaries as shown above. The missing segment of the pulmonary vein boundary, not visible on this projection plane, is drawn in grey. Outliers can result from rays cast into elongated regions of the boundary.

To detect outliers in the set ρ, we define a statistic on the distances of each point $\rho = \{\rho_i\}_{i=1}^{m}$ in the set to the finite plane's Π' centre $\mathbf{r}$. The set of these distances ρ^r is given by:

$$\rho^r = \bigcup_{i=1}^{m} |\mathbf{r} - \rho_i| \tag{6.15}$$

Empirically, it can be shown that distances ρ^r are distributed normally (see Fig. 6.18) with mean μ and variance σ^2:

$$\rho^r \sim N(\mu, \sigma) \tag{6.16}$$

Using Grubb's test for outliers [57], the ratio $\varkappa$ can reveal if ρ_i is an outlier:

$$\varkappa = \frac{|\rho_i^r - \mu|}{\sigma} \tag{6.17}$$

where ρ_i^r is the ith distance in ρ^r. Critical values of this ratio are given in [57] and are dependent on population size. However, since most ostia have nearly circular cross-sections, we can derive a value for this ratio from a Monte-Carlo simulation for ellipses of varying size. Given an ellipse centred at the origin, points are randomly selected on the ellipse. The mean and variance of the distances of these points from the origin are computed. Table 6.1 shows variance measures for typical ellipses. Since the ostium is nearly circular, a low *eccentricity* can be assumed. Eccentricity is defined as $\sqrt{1 - (b^2/a^2)}$, where a and b are the semi-lengths of the major and minor axes respectively. For our purposes, we use $\varkappa = 1.2$.

Minor axis	Major axis	std. deviation
2	2	0
2	3	0.3052
2	4	0.6173
2	5	0.9292
2	6	1.2404
2	8	1.8590
2	15	3.988

Table 6.1: Values from a Monte-Carlo simulation of 10^5 points selected randomly from an ellipse centred at the origin. The variance of the underlying distribution for the distance of these points to the origin is reported. This simulation is performed on ellipses of increasing eccentricity.

6.3.4 Diameter estimation

We propose the use of two methods for diameter estimation: Ellipse-fitting and diameter-sweep methods. Consider the sampled points on boundary Ω to be $\{\rho_i\}_{i=1}^m$. These points all lie on an arbitrary plane Π in 3D space. Before an ellipse can be fitted through these points, they are transformed to the XY-plane. This simplifies the ellipse-fitting process by constraining it to the XY-plane. An ellipse-fitting subroutine is employed [157], which minimises the sum of least-square distances between the ellipse and point cloud. The major and minor-axes of the

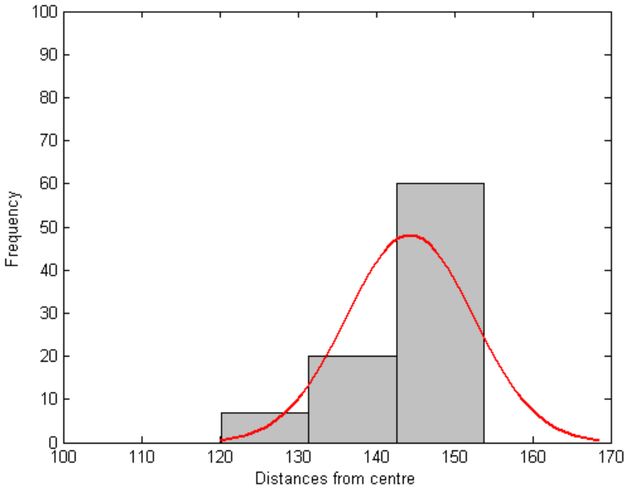

Figure 6.18: A histogram of distance-to-centre values for ostial points and a gaussian fit to show that these ostial points are distributed normally.

ellipse give a good estimate of the ostial diameter. Fig. 6.19 shows how an ellipse might fit to an ostium.

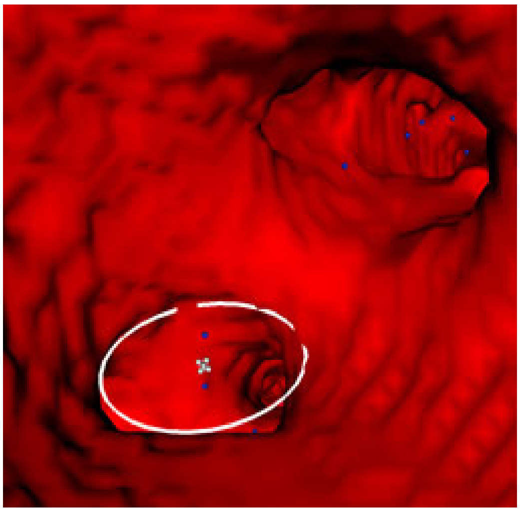

Figure 6.19: An endoscopic view of two ostia, with the best-ellipse fit (for measuring diameters) which can be seen drawn in the figure.

A second approach is to sweep the diameters radially to obtain an estimate for the ostium (see Fig. 6.20). The rays cast in Fig. 6.16 at θ degree intervals, each give a radius that can be averaged to obtain the mean diameter:

$$\frac{2}{m}\sum_{i=1}^{m}|\mathbf{r}-\rho_i| \tag{6.18}$$

where $\mathbf{r}$ is the diameter plane centre (see Fig. 6.19) and m is the sampling rate of boundary

Ω.

In order to improve on these estimates of the diameter, several measurements can be made along the B-spline, moving a small number of steps forward and backward each time along the vessel medial axis spline (see Fig. 6.21). The average over the set of all diameters gives a better estimate of the ostial diameter.

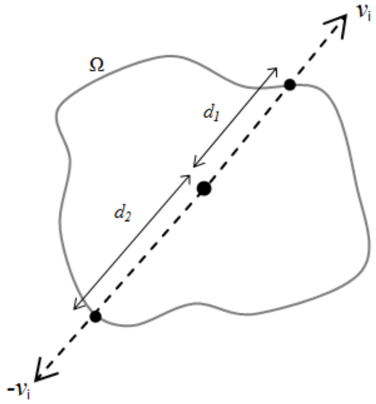

Figure 6.20: In the diameter-sweep method, points are sampled radially on the ostial boundary using ray tracing in both directions v_i and $-v_i$. The diameter is then given by $d_1 + d_2$. The mean over these diameters is reported.

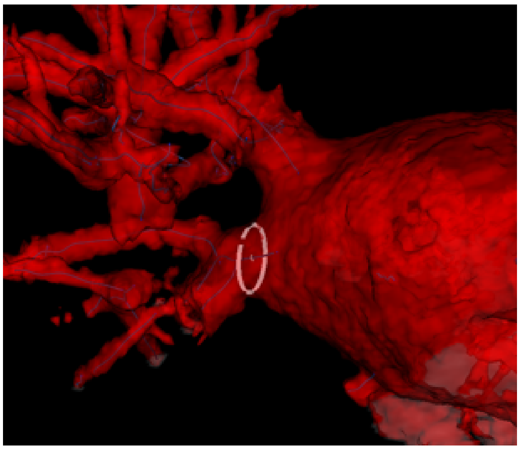

Figure 6.21: An iso-surface rendering of the segmented left atrium with a low opacity value to allow to see through. An ellipse fits to the pulmonary vein to measure its diameter automatically.

6.4 Discussion

Finding drainage locations to the atrium is a first step towards modelling pulmonary vessel trees. Recall that vessel segment endpoints that are close to the atrial body and of a certain size are used in the hierarchical clustering algorithm. The threshold value used for size is 50 mm. This makes an important assumption that at least one vessel of this size can be found near a genuine drainage to the atrial body. Otherwise, a drainage can go undetected. Occasionally, vessels that are otherwise larger than the threshold size can have smaller detected segments. Making the threshold size too small makes it difficult to distinguish genuine vessel segments from segments that result from noise. Generally, a lower bound set at 15 mm on the threshold size has shown to work well.

False vessel segments also can occasionally arise from acquisition artefacts or noise. These segments will rarely be greater than the threshold size of 50 mm. In cases where they are found to be greater, a second constraint helps distinguish false segments: they will not have elaborated vessel trees as genuine drainage vessels. Thus, segment endpoints that are considered in the clustering algorithm for identifying drainage locations must have elaborated vessel trees that are at least two levels deep.

In evaluating vessel segment connections for building vessel trees, the cost function evaluates the spatial distances between vessel endpoints in its spatial proximity term (see Eq. 6.9). A threshold value of $\epsilon_d = 6$ is used which assigns a negative value for penalty for distances greater than 6 mm. Vessel segments that have genuine connections but with a minimum separation of 6 mm or more between their endpoints are not connected unless their vesselness penalty term can compensate the accrued penalty for spatial distance. Most often this offset is possible if there is strong vesselness response along the proposed connection. Moreover, the bounds on the cost function (i.e. $[-1, +1]$) make most segment connections recoverable even if they are separated by large distances. Recall that the penalty for large separation distances $d > \epsilon_d$, saturates to -1 (see Fig. 6.6) requiring only a +1 to compensate for the offset.

The computation of ostial diameters is robust. There can be perturbations in the vector computed between consecutive spline points for ostial diameters (see Eq. 6.14) causing the diameter plane to be not perfectly orthogonal. Nevertheless, the diameter plane is adjustable with handles provided to change its orientation and size. A small adjustment by the operator can easily rectify the computed plane. Also, as ostia are normally elliptical with low eccentricity, this *a priori* knowledge is incorporated in the ratio $\varkappa$ in Eq. 6.17 making the fitting process more robust.

6.5 Summary

In this chapter, we proposed techniques to extract important left atrial characteristics that are of interest in RFCA for atrial fibrillation. It is assumed that a segmentation of the left atrium and sub-atrial structures namely the atrial body and pulmonary veins are available. These are obtained from techniques presented in chapters 4 and 5 respectively. The chapter proposes two important methods. Drainages to the atrium are located using a clustering algorithm followed by model construction of each drainage tree using graph structures. The computation of drainages and their trees enable the classification of atrial anatomy. Furthermore, a method to compute ostial diameters is proposed. Manual computation of diameters is often prone to inter- and intra-observer variabilities. Locations of ostia are found from the computed trees, followed by methods for approximating the diameter.

The presented methods are fast requiring less than 30 seconds on a modern PC. This assumes pre-computed segmentations of left atrium and pulmonary veins. Also, the generation of vessel tree graphs, first bifurcation distances and ostial diameters are almost instantly obtained on modern PCs. A model of vessel drainage trees provides a framework on which further computations and analysis are possible. Ostial diameters and first bifurcation distances are just some important examples of computations possible. Further computation and analysis can be performed using this framework. It is envisaged that these proposed techniques will add important value and increase the accuracy of ablation procedures.

Chapter 7

Results

The motivation of this thesis is primarily to develop techniques that can assist and add value in pre-planning atrial fibrillation procedures. The proposed techniques in chapters 4, 5 and 6 are evaluated by considering its clinical applications to be an important aspect of the evaluation process. Attention is given to features of the atrium that have relevance in RFCA.

7.1 Data acquisition

The details of the acquisition process can be found in section 4.2 on page 65. A summary of the image datasets acquired for these studies is also given. See Fig. 2.10 on page 35 for examples of images from these datasets.

7.2 Left atrium segmentation

Since circumferential ablation has now become a preferred way of correcting atrial fibrillation, most institutions target the ostial regions of pulmonary veins for ablation [60, 133] (see also section 2.3.3 on page 19). The collaborators in our study at the St. Mary's Hospital in London also prefer circumferential ablation for many of their patients [135]. In this technique each pulmonary vein drainage is electrically isolated by circumferentially ablating around them. The location of these lesions are more towards the atrial body than towards the vein as ablating venous regions poses a high risk of triggering vessel stenosis. In RFCA, the only regions in the left atrium that have clinical importance are the atrial body and the segments of the pulmonary veins as far as the first bifurcation. Pulmonary veins beyond the first bifurcation are of little importance. This puts an important constraint on the evaluation strategy for left atrium segmentation. An atrium segmentation needs only to consist of the atrial body and every possible pulmonary vein drainage as far as the first bifurcation. Segmentation is evaluated on this very basis; it evaluates features that have clinical relevance. Both a qualitative and quantitative assessment of the segmentation results have been presented. The quantitative evaluation study is presented in section 4.8 on page 80.

7.2.1 Experimental details

Digital subtraction MR angiography studies were used for patients with pre- and post-angio images already well aligned. For patient data requiring registration, the pre- and post-angio images were registered to a common frame using a rigid registration technique [164] followed by a voxel-wise subtraction (see section 4.3.1 on page 67). An anisotropic diffusion filtering step was used to remove noise and preserve edges in the images. A time-step of 0.05 is used along with a conductance rate of 3.0. The time-step corresponds to the Δt in the finite difference update equations for Eq. 4.2 on page 69. The conductance rate specifies the extent to which the features (i.e. high gradient) should be preserved; a low conductance favours strong preservation. These values are critical for 3D MRA images and have shown to work well in all our images. For example, the time-step should be at or below $1/2^N$ where N is the dimensionality of the image. Also, the conductance rate should be below 3.0.

The atrial blood pool in the image is obtained using threshold-based region growing with a region of interest selected manually by the operator. A seed is placed close to the centre of the atrium. The intensity value k^* that optimally separates the blood and non-blood tissue classes is computed automatically (see section 4.4.1 on page 70). The range $[k^*, l]$ is used, where l is the maximum intensity in the image. Visualisations of the extracted blood are generated with an iso-surface marching cubes algorithm. The iso value used is the obtained optimal threshold value k^*. The Euclidean DT of the extracted blood pool is pre-computed. Also pre-computed is the region-split image that stores voxel memberships for each split region (see section 4.6 on page 77). Before regions are merged to produce the segmented atrium, the operator selects a point inside the atrium along with a merging threshold. These threshold values normally range between 15-25 mm.

A perfect left atrium segmentation may not always be possible in one single step. One or more semi-automatic steps to remove non-atrial regions may be necessary (see section 4.7 on page 79). These regions are part of a neighbouring structure such as the aorta and pulmonary artery. Recall that these non-atrial regions are removed in the cell exclusion step. This can occur in medium to low resolution images where frequently connections between structures are not particularly narrow; low resolution images tend to have more partial volume effect. The experiments thus involve a first step followed possibly by several semi-automatic steps in which the operator chooses a different non-atrial seed point and modifies the threshold value. Depending on the number of steps required to get an ideal segmentation, the segmentation is evaluated, in the worst-case, four different times. Beyond the fifth attempt, segmentation is generally considered as difficult to achieve, but nevertheless evaluated with the best possible achievable segmentation. The experiments were carried out on a 2.0 GHz Pentium machine with 3GB of RAM.

7.2.2 Segmentation evaluation

The segmentation results for the left atrium are qualitatively evaluated by a clinician. Each segmentation result is visualised with an iso-surface rendering. This gives a good three dimensional view of the segmentation. Based on how good or bad a segmentation is, it is classified into one of the following distinct classes:

- C_1: Atrial body with one or more missing pulmonary vein drainage (see Fig. 7.1).

- C_2: Atrial body with every pulmonary vein drainage present but one or more drainage having its pulmonary vessel tree truncated (see Fig. 7.2).

- C_3: Atrial body with every pulmonary vein drainage present. The pulmonary vessel tree of each drainage, at least up to the first bifurcation, is also present (see Fig. 7.2).

- C_4: Atrial body with every pulmonary vein drainage present including their pulmonary vessel trees, but containing a significant portion of the pulmonary artery (see Fig. 7.3).

- C_5: Atrial body with every pulmonary vein drainage present including their pulmonary vessel trees, but containing a significant portion of the aorta.

- C_6: Contains the atrial body, pulmonary veins and significant portion of the pulmonary artery and aorta (see Fig. 7.4).

The classes are listed in a particular order where at the two extreme end classes C_1 and C_6 are considered to be poor segmentations. Class C_1 is the worst-possible under-segmentation whereas C_6 is the worst-possible over-segmentation. In between are classes that are acceptable segmentations with classes C_2 and C_3 being most desirable. Class C_3 is considered to be the most ideal segmentation output.

The justification of using these classes and ordering them in such manner are two-fold. Firstly, classes deemed acceptable are only so because they include every structure of clinical relevance in RFCA. Classes C_2 and C_3 are ideal since they *only* contain structures of clinical importance and exclude the rest. Secondly, the ordering of the classes reflects to a degree the level of obstruction in the field of view caused by an unwanted structure. For example, C_5 follows C_4 in the list as the obstructions created by the ascending aorta in the left atrium visualisation are normally worse than the obstructions created by the pulmonary artery. Compare obstructions in Figs. 7.3 and 7.4.

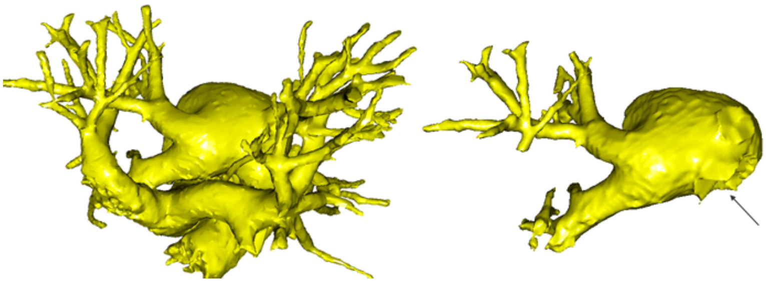

Figure 7.1: An example of left atrium segmentation classified as C_1 due to the missing pulmonary vein drainage in the location marked by the arrow (right). The neighbouring atrial structures for this atrium (left).

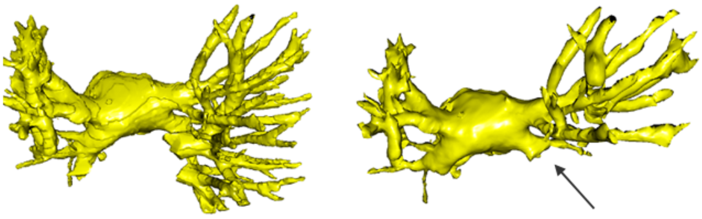

Figure 7.2: An example of left atrium segmentation classified as C_2 due to the missing pulmonary vessel tree in the drainage marked by the arrow (right). A segmentation of the same atrium that can be classified as C_3 (left).

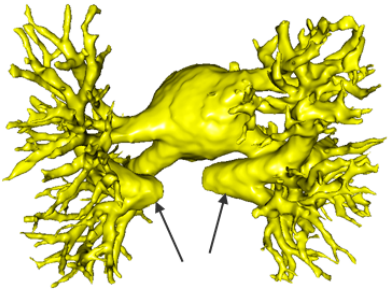

Figure 7.3: An example of left atrium segmentation classified as C_4 since it retains a significant portion of the pulmonary artery marked by the arrows.

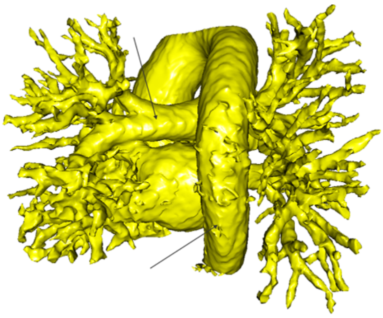

Figure 7.4: An example of left atrium segmentation classified as C_6 since it contains both the pulmonary artery and the ascending aorta (indicated by arrows). This can be regarded as a severe case of over-segmentation since it includes most neighbouring structures.

7.2.3 Results

The iso-surface rendering of the left atrium segmentations for the 35 datasets are given in Figs. 7.5, 7.6 and 7.7. The results are analysed based on the number of segmentation steps required to successfully extract the left atrium. The first step requires the user to place a seed inside the atrium and select a threshold value (i.e. the merging threshold). Until the segmentation can be placed in the C_3 class further segmentation steps involving cell inclusion or exclusion are attempted, however, this time requiring more user interaction. For example, the user needs to place a seed inside an un-wanted/wanted region and re-adjust the merging threshold.

The total number of segmentations in each class C_i are found at pre-defined intervals of segmentation steps. These intervals are: 1) the first step, 2) 1-3 steps, 3) 3-5 steps and 4) more than 5 steps. The results are given in table 7.1. In the first step, 31 out of the 35 datasets were segmented and classified as acceptable segmentations by clinicians (classes C_2, C_3 and C_4) . This represents 87% of the total datasets segmented successfully in one single step and typically requiring less than a minute. Taking a more conservative stance, after the first step, more than half of the total datasets ($\sim$ 55%) were classified as either C_2 or C_3. These percentages are illustrated in Fig. 7.8.

Segmentation correction using the cell inclusion and exclusion processes were effective in correcting most segmentations. This is also illustrated in table 7.1 and Fig. 7.8. In 5 steps, 32 out of the 35 datasets were classified as acceptable segmentations (classes C_2, C_3 and C_4) and this represented 94% of the total datasets. However, there is no noticeable improvement in segmentation after applying 3 steps (see Fig. 7.8). For the segmentation correction process to be effective, at least 5 or more steps were typically required. It was impossible to segment one of the patient datasets. The contrast-enhanced blood had appeared to penetrate both ventricles when the acquisition was taken. This made it impossible to differentiate the left atrial body from the adjacent ventricles (see last row in Fig. 7.7).

	segmentation classes					
steps	C_1	C_2	C_3	C_4	C_5	C_6
1^{st} step	1	5	14	12	0	3
1-3 steps	1	6	16	9	2	1
3-5 steps	0	9	18	6	1	1
>5 steps	0	4	26	3	1	1

Table 7.1: The total number of segmentation results classified into one of the 6 classes after: the first step, 1-3 steps, 3-5 steps, and more than 5 steps.

7.2.4 Discussion

In the segmentation evaluation study, the proposed left atrium segmentation algorithm in chapter 4 was used to segment the left atrium from 35 MRA patient datasets. In a quantitative evaluation of its segmentations, it was shown to perform better than the algorithm it improves upon (see section 4.8 on page 80). In this study, the segmentation was successful in all but one case. Most images were degraded by noise, and this was the most important contributing factor in mis-segmentations. Important image information can be lost due to noise degradation and in the worst cases this is very difficult to recover with anisotropic or isotropic blurring. With noise degradation, the proposed segmentation method was able to segment atria in one single automatic step for 84% of the cases. All the C_2, C_3 or C_4 segmentations were approved by a clinician and regarded as good segmentations.

The segmentation correction steps with cell inclusion/exclusion following the first segmentation step are important for obtaining near-perfect segmentations. These steps require minimal user interaction with the user placing a seed on a non-atrial voxel before selecting a merging threshold. The time required for each segmentation step is less than 2 seconds and an entire atrium can be segmented typically in under 2 minutes on a 2.0 GHz machine, and this excludes the pre-processing steps. The time taken in pre-processing images depends on the size of MRA data. For a typical image of size 380 × 380 × 90 it could take up to 1-3 minutes. The segmentations can be performed by a non-expert user with little training and knowledge of atrial anatomy.

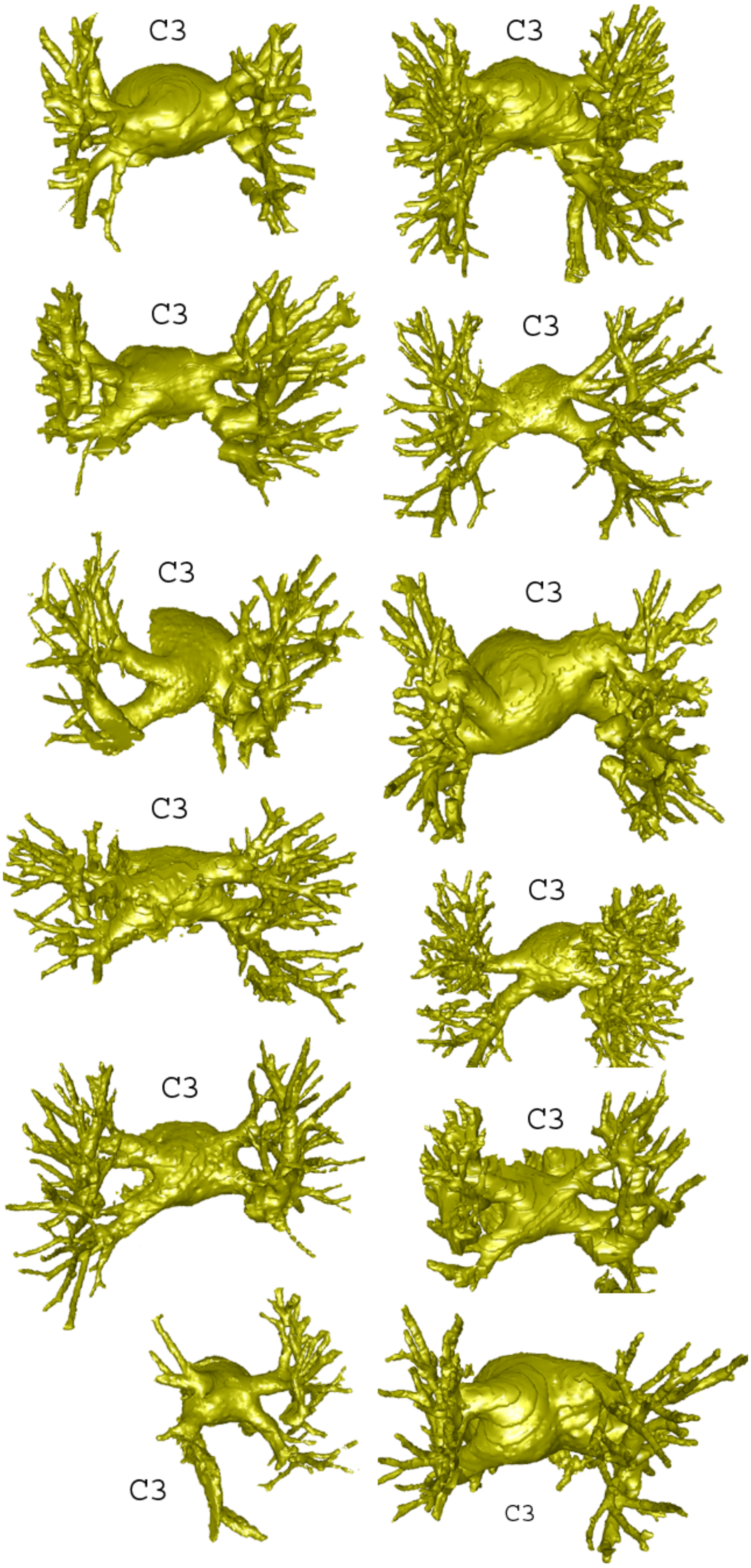

Figure 7.5: Iso-surface renderings with marching cubes followed by Laplacian mesh relaxation of the first twelve segmented datasets that were classified as C_3. The remaining datasets can be found in Fig. 7.6 and Fig. 7.7.

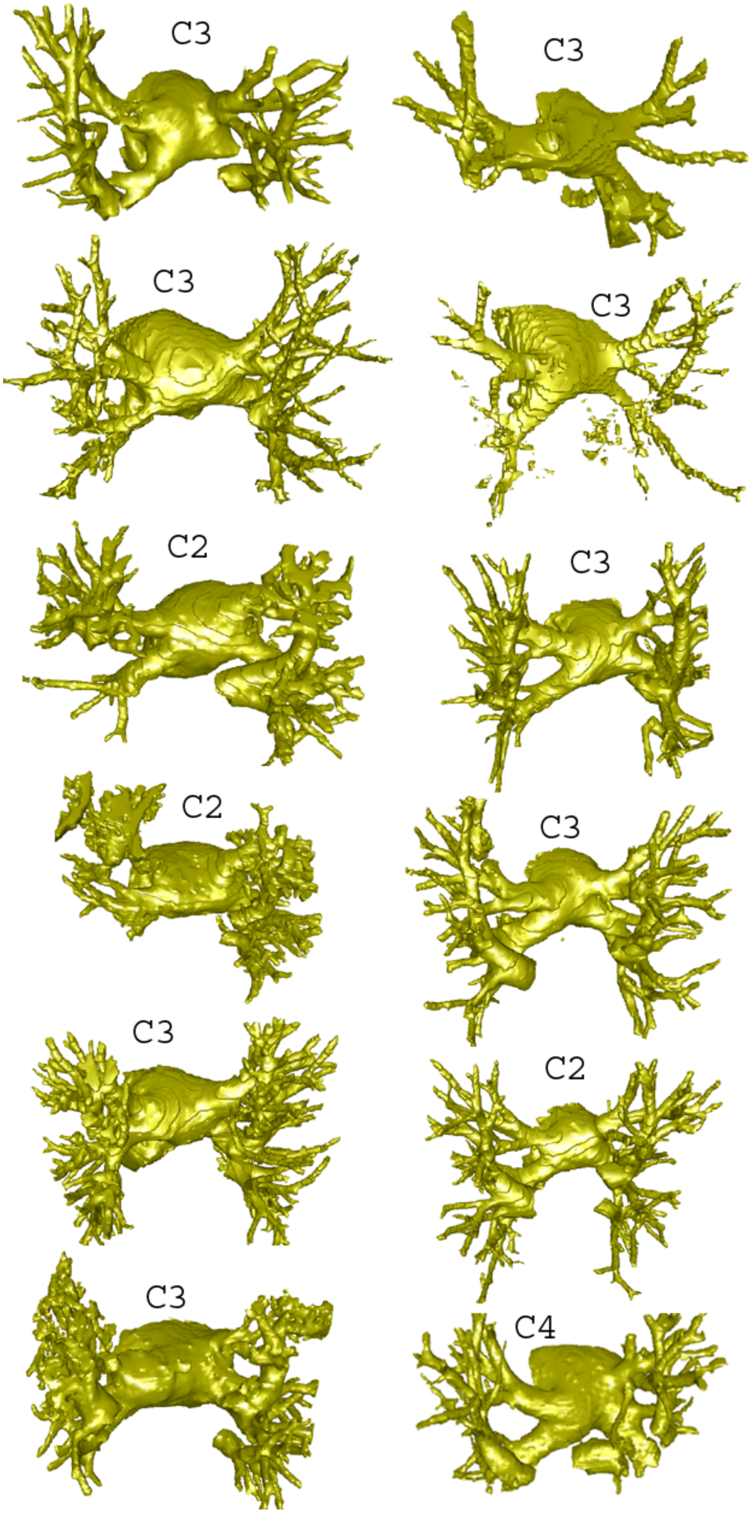

Figure 7.6: Iso-surface renderings with marching cubes followed by Laplacian mesh relaxation of the next twelve segmented datasets classified either as C_2, C_3 or C_4. The remaining datasets can be found in Fig. 7.5 and Fig. 7.7.

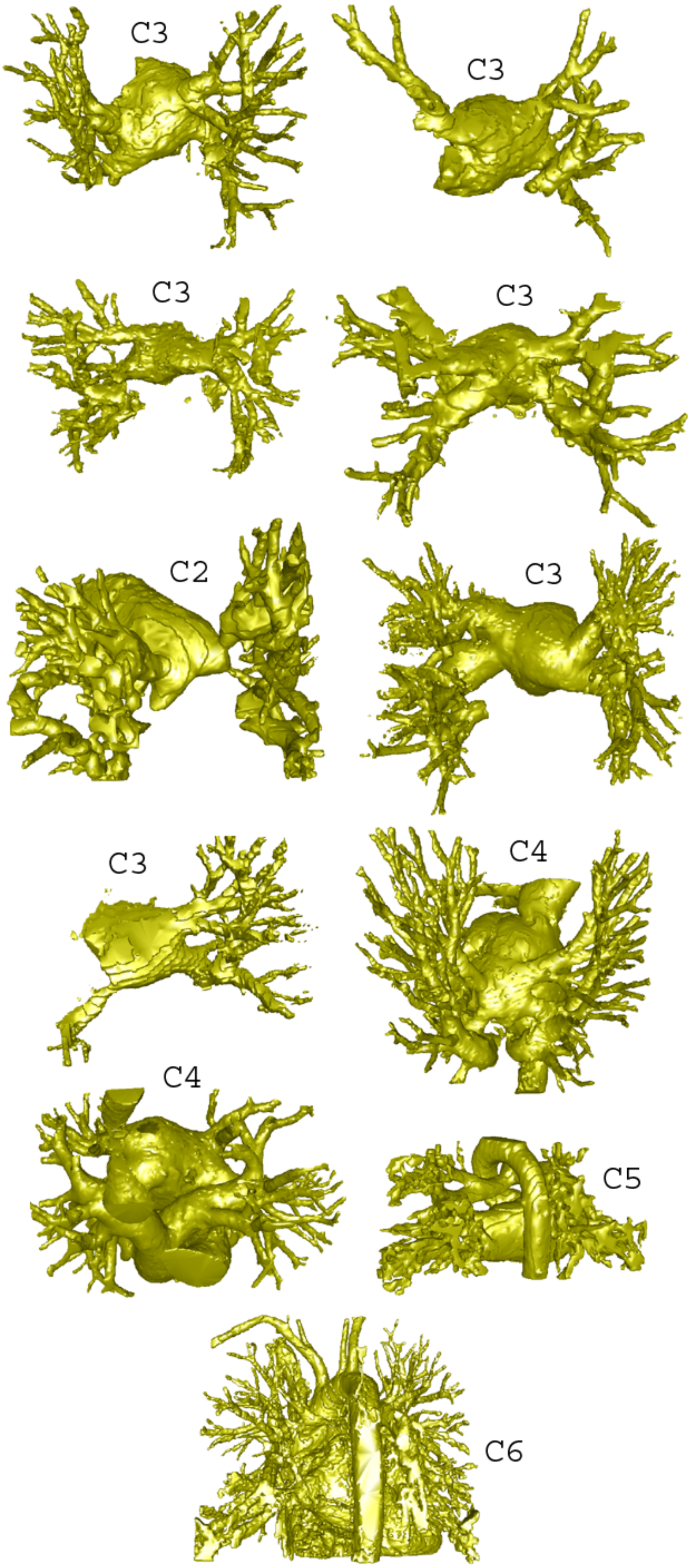

Figure 7.7: Iso-surface renderings with marching cubes followed by Laplacian mesh relaxation of the remaining eleven segmented datasets.

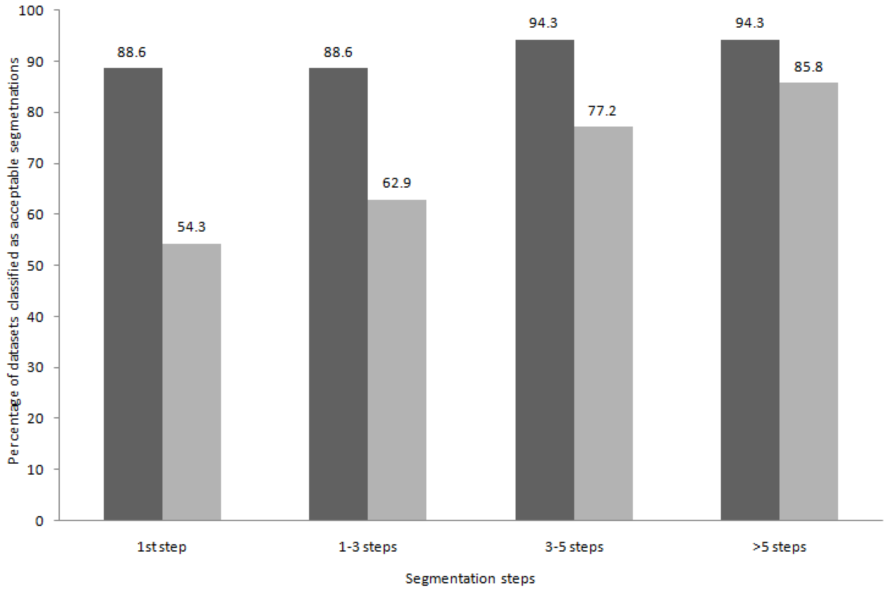

Figure 7.8: The number of segmentations considered *good* as a percentage of the total number of datasets. The dark grey bars correspond to percentages if classes considered good are C_2, C_3 and C_4 and the lighter grey bars if only C_2 and C_3 are considered to be good segmentations.

7.3 Pulmonary vein centrelines

In chapter 5, following the detection of left atrial body, pulmonary vein centreline points were tracked by gradient ascent in the Euclidean distance transform space. These are later fitted with a distance-minimizing B-spline curve. To evaluate the detected pulmonary vein centrelines, we take into consideration some important clinical outcomes of determining pulmonary vein centrelines:

- Centrelines help annotate pulmonary vein locations in a left atrium segmented image.
- Centrelines are required for building symbolic representations of drainage trees for reporting atrial anatomy (see section 6.1.2).
- Centrelines provide ideal locations for placing the centres of best-fit ellipses when computing ostial diameters (see section 6.3.1).

The exact location of the true pulmonary vein centreline at voxel-level precision is of little clinical importance in RFCA. Consequently, validation using voxel-wise differences between the detected centreline and ground truth holds little relevance. Moreover, in ostial diameter computations, an approximate location of the centreline is sufficient. We present centreline evaluation strategies which ensure that detected centrelines are effective in fulfilling the aforementioned clinical outcomes. Ostial diameter evaluation is presented separately in a later section (see section 7.4.1). In RFCA, segmentation of the left atrium up to and including the first bifurcation in the pulmonary vessel drainage tree is a pre-requisite. The ostia are targeted for ablation, making vessels before the first bifurcation susceptible to stenosis. We restrict our evaluation as far as the second bifurcation of the pulmonary vessel drainage tree, which is sufficient for most practical purposes.

7.3.1 Experimental details

The left atrium segmentation images are pre-computed using the techniques presented in chapter 4. The atrial body is segmented from these images using level-set methods (see section 5.2). In the first evolution step, the evolution speed function is the Euclidean DT of the left atrium segmented image, which is pre-computed. The operator selects a seed point close to the centre of the atrium and picks threshold values for the Euclidean distance. Values are typically low (~ 2.0) for the lower bound and infinity for the upper bound. For the second evolution step, the speed function is defined by the left atrium segmented image's edge potential map (see Eq. 5.9). Using the evolved surface obtained from the first step as the initial shape, the surface is further evolved with $\alpha = -1.0$ and $\beta = 7.0$ (see Eq. 5.9) and a high curvature scaling value (~ 2.0) to maintain a smoother resulting contour (see Eq. 5.7).

The multiscale vesselness filter responses are computed on the left atrium segmented image at 10 different scale intervals between $\sigma_{min} = 1.0$ to $\sigma_{max} = 5.0$. The step size δ between intervals is given by:

$$\delta = \frac{\ln(\sigma_{max}) - \ln(\sigma_{min})}{n_\sigma} \tag{7.1}$$

where $n_\sigma = 10$ is total number of intervals. The scale σ_i at the ith interval is given by:

$$\sigma_i = e^{\ln(\sigma_{min})+i\delta} \quad , 1 \le i \le n_\sigma \tag{7.2}$$

These scales σ_i are also used to compute the vessel directions at each voxel location in the left atrium segmented image (see section 5.3.1). Both the vesselness filter response and vessel direction computation step is automatic and require no user interaction. With these images pre-computed, the pulmonary vein centrelines are automatically computed for the entire left atrium segmented image in less than 5 seconds on a 2.0 GHz machine. The computed centrelines are overlaid on a transparent iso-surface rendering of the segmentation (see Fig. 7.9). Each pulmonary vein drainage tree is analysed and the first, second and third *splits* are found along with the number of vessels with/without centrelines before each split. Split denotes the branching of vessels into two or more vessels; a bifurcation is an example of a split.

Figure 7.9: Centrelines overlaid on an iso-surface rendering of a pulmonary vein drainage tree branch. Images such as these are used to evaluate if certain pulmonary veins are tracked and found.

7.3.2 Centreline evaluation

The centrelines of pulmonary veins are qualitatively evaluated. They are visualised by overlaying them on the left atrium segmented image. For each pulmonary vessel drainage tree, vessels are counted into one of the categories: 1) Before the first split, 2) Before the second split, and 3) Before the third split. Vessel split or bifurcations are important landmarks within pulmonary vessel trees. Moreover, they are important in RFCA as they are used as reference markers for first bifurcation distances. In addition to this, most institutions will truncate segments of vessel trees beyond the first or second split, as ectopic (i.e. abnormal) regions are known to occur mostly within the first or second splits.

The number of vessels with centrelines are counted into one of the above categories and are

Pulmonary vessel tree	Before 1st split		Before 2nd split		Before 3rd split	
	Detected	Actual	Detected	Actual	Detected	Actual
Tree No. 1	1	1	2	2	8	9
Tree No. 2	0	1	1	2	6	6
Tree No. 3	1	1	0	0	0	0
Tree No. 4	1	1	3	3	6	9
Tree No. 5	0	1	4	5	6	6

Table 7.2: Centreline results presented for five sampled drainage trees.

not cumulative - vessels counted into the first category are excluded in the second category. Vessels are normally marked as detected if a centreline is found along their entire length. Table 7.2 lists the actual number of vessels against the number of vessels for which centrelines were found successfully from five drainage trees. See Fig. 7.10 for an illustration of how vessels are counted.

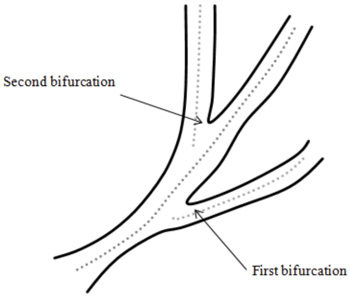

Figure 7.10: Illustration of how vessels are counted when evaluating their detection using centrelines. In this case there is one vessel before the first bifurcation and two vessels before the second.

7.3.3 Results

In the centreline evaluation study, a total of 53 pulmonary vein drainage trees were selected randomly from the 35 left atrium segmentations. The centrelines of vessels in the drainage trees were found by the system and each drainage tree was analysed. The centreline extraction had a high success rate, especially for vessels before the first and second splits. The vessels before the first split are primarily the drainage trunks which drain into the atrium. For a pulmonary vein drainage tree there can only be one drainage trunk before the first split (see Table 7.3). In all but three cases the drainage trunks were successfully tracked, and this represents a 94% success rate. In the three cases in which the centrelines could not be found, it was merely due to the atrial body contour leaking entirely into the trunk. The trunk is not completely disregarded as it now becomes part of the atrial body. This can be common if the trunk is short and has a large diameter. There is also some ambuguity as to whether such short trunks should be regarded as a single or multiple drainages. Fig. 7.13 illustrates this. For vessels beyond the first split, the centreline extraction process was also very successful. All except four vessels were extracted successfully before the second split. There were 135 vessels in total before the second split and for 131 vessels the centrelines could be extracted. The success rate was 97%. This result is illustrated in Fig. 7.11 where the actual number of vessels are plotted against the number of vessels with centrelines for each of the 53 drainages. Note the close agreement for most drainages. For vessels before the third split, there were a total of 263 vessels across the 53 drainages. The centrelines could be extracted for 250 of these vessels and this represented a success rate of 95%. This result is illustrated in Fig. 7.12.

	Drainage trees
Centreline found	50
Not found	3

Table 7.3: Vessel centreline extraction results before the first bifurcation. There is a maximum of one vessel for each drainage tree before the first bifurcation.

7.3.4 Discussion

From the centreline extraction results, the proposed centreline extraction process was shown to be successful with an average success rate of 95%. Vessels were classified according to where they can be found, i.e. before or after the nth split. The results can be interpreted in terms of vessel width as vessels normally tend to diminish in width as they branch out from a split. The centrelines of vessels of smaller widths are harder to detect than the centrelines of larger vessels. Thus, the drop in success rate from 97% to 95% can be explained: it is harder to find centrelines of smaller vessels as we move from the 2nd split to the 3rd split. On the contrary, the relatively lower success rate ($\sim$ 94%) for vessels before the first split is primarily due to the leaking of atrial body contour. Usually leaks can be avoided if the parameter value τ_ξ in

Eq. 5.6 is raised to a higher value (~ 50.0) (see section 5.2.2). At higher values there is usually a trade-off between less leakage and under-approximation of the atrial body shape. In many occasions the under-segmented atrial body obtained in the first evolution step has shown to work well and the segmentation obtained from the second evolution step may not be necessary - the primary reason being drainage leaks.

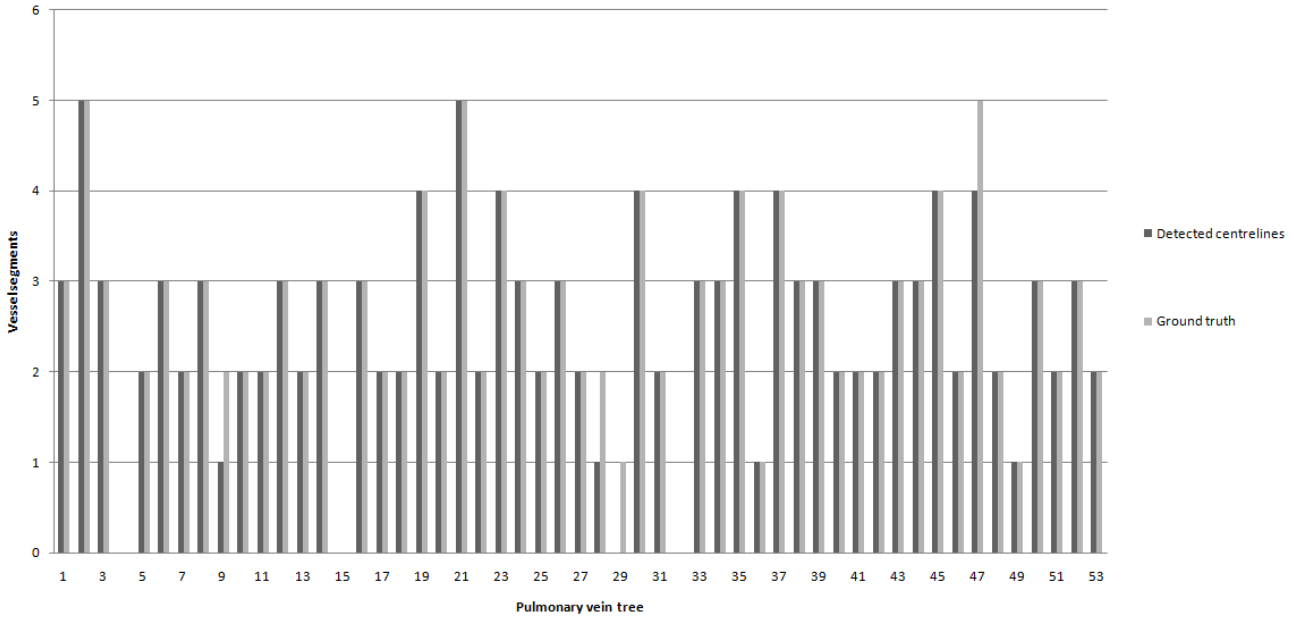

Figure 7.11: Comparison of centreline extraction results before the second split in each of the 53 drainages studied.

7.4 Estimation of the ostial diameters

7.4.1 Diameter evaluation

In section 6.3 (page 122), semi-automatic techniques to measure ostial diameters were presented. Diameters are measured on a fixed plane called the *diameter plane* that is orthogonal to the vessel axis vector. These measurements are taken along root vessels of each pulmonary vein drainage to the left atrium, where the diameter plane can be moved along sampled points on the B-spline approximating the vessel axis (see section 5.3.4 on page 102). At a new point on the spline, the plane and diameter are re-computed. The locations of root vessels are identified using the symbolic tree representation of the pulmonary vein drainage (see section 6.1 on page

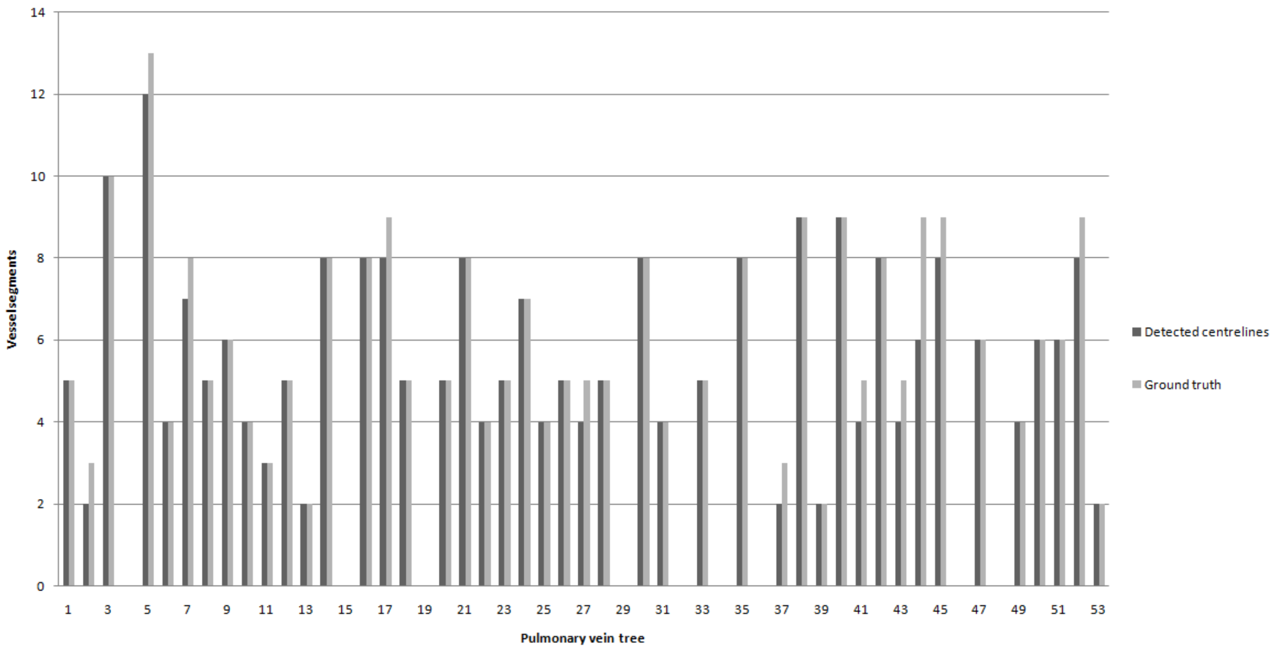

Figure 7.12: Comparison of centreline extraction results before the third split in each of the 53 drainages studied.

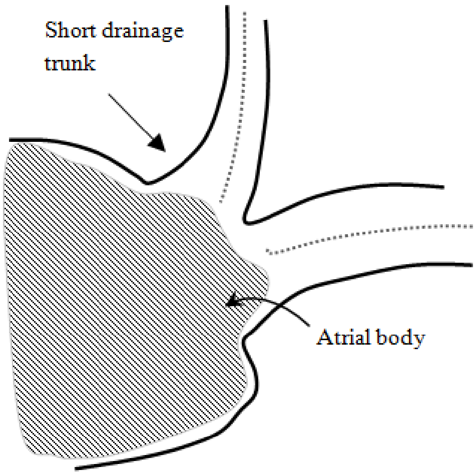

Figure 7.13: Figure illustrates how the atrial body contour can leak into pulmonary vein drainage trunks that are short in length and have a large diameter.

108). Protocols for measuring ostia can vary between institutions. Scharf et al. [155] reports on a manual approach where the maximum distance between two ostial points in the same plane and in at least two orthogonal projections of a surface reconstruction of the ostium is measured to give the diameter (see Fig. 6.14 on page 124). We use the same approach for obtaining ostial diameters with a manual technique. This is considered as the gold standard and the benchmark against which our proposed automated methods are compared.

For ostial diameters, measurements depend greatly on both the location and orientation of the diameter plane. The use of only two orthogonal planes can restrict the diameter planes and give inaccurate diameter values. It is more common for diameter planes to be oriented arbitrarily in space than being parallel to one of the X, Y and Z planes. Thus, finding this arbitrary plane can be difficult. Our system finds this plane to reasonable accuracy using vessel axis vectors. Moreover, the plane can be adjusted by the operator, if necessary. Diameter values from the two methods, ellipse-fitting and diameter-sweep, are compared against manual measurements.

7.4.2 Experimental details

With a left atrium segmentation available, the pulmonary vein centrelines are extracted as described in section 5.3 on page 93. Tree representations for each pulmonary vein drainage are also extracted as described in section 6.1 on page 108. The root vessels for each drainage tree can be obtained from these trees. The endpoints of root vessels (endpoint closest to the atrial body) become locations for placing the ostial diameter plane. In our system, the operator clicks on the ostium of interest and the system automatically places the diameter plane at the root vessel endpoint. The major and minor axes of the best-ellipse fit are also reported instantly with the ellipse drawn and overlaid on the surface reconstruction of left atrium segmentations (see Fig. 6.20). To get the diameter values from the ellipse-fitting process, only the length of the major axis of the ellipse is recorded. The diameter-sweep method also reports its mean diameter alongside and this is noted (see Fig. 6.20) on page 130.

Points are sampled on the centreline B-spline curve of the vessel to allow the diameter plane to be moved along these points (see Fig. 7.14). The operator moves the plane forward or backward along this curve and the plane and ellipse are re-computed. The plane is moved until the diameter stabilises (see section 6.3.1 on page 124). This is usually obtained in less than five clicks.

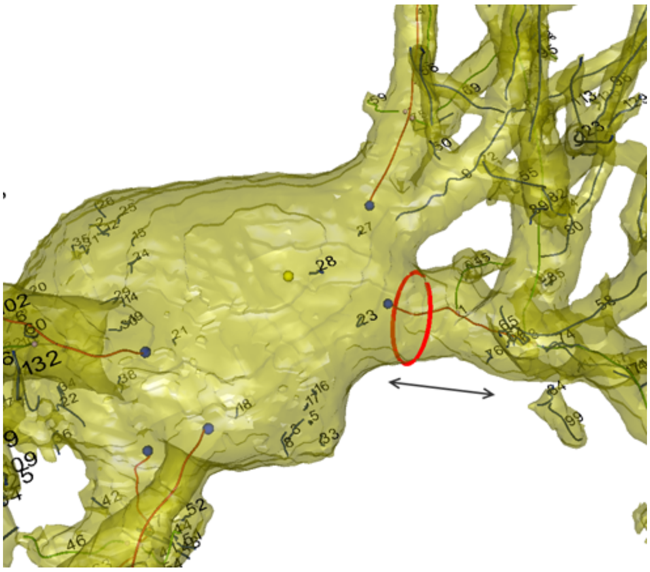

Figure 7.14: The system allows the diameter plane to be moved along the centreline B-spline curve (marked with arrow). At each new plane location, the ellipse is re-calculated and drawn on a transparent left atrium segmentation image showing vessel centrelines.

For obtaining diameters manually, points are selected on two of the three orthogonal planes (X, Y and Z) of the left atrium segmented MRI image as carried out in the clinical setting [155]. For any single plane, two points on the ostial border with the maximum possible separation distance are selected. These points are selected based on the operator's visual judgment.

7.4.3 Results

In the ostial diameter study, a total of 62 different ostia were measured. The diameter measures from the ellipse-fitting and diameter-sweep studies are compared against the manual measurement. The percentage difference between the manual measurements and the two techniques for each ostium measurement was found. The percentage difference is given as:

$$\text{Percentage difference} = \frac{d_s - d_m}{d_m} \tag{7.3}$$

where d_s is the diameter measured for example in the ellipse-fitting study and d_m is the manual measurement. All diameters values are reported in millimetres (see Table B.2 in Appendix B).

Fig. 7.15 shows the fractional differences where a value of 1 represents complete agreement with the manual measurement and a value of 0 represents a percentage difference of 100%. In the comparison studies, 43 out of the 62 ostia measured in the ellipse-fitting study had a percentage difference of less than 5% when compared with the manual measurement (see Table 7.4). Comparing this to the diameter-sweep method, only 24 out of the 62 ostia measured had less than 5% difference. The average percentage difference with the manual measurement in the ellipse-fitting study was 4.7%. Comparing this with the diameter-sweep study, it was 10%.

7.4.4 Discussion

Results indicate that the ellipse-fitting technique was more accurate than the diameter-sweep technique for measuring ostial diameters. As the mean percentage difference between ellipse-fit and gold standard measurements is less than 5%, it makes the method suitable for measuring diameters. The diameter-sweep technique was found to be less accurate. However, the high inter- and intra-operator variability in the manual measurements for ostial diameters must be taken into consideration when interpreting these results. A severe drawback in manual measurements is its use of two orthogonal planes and thus only a mere four points for measuring the diameter. With such low sampling the values obtained cannot be relied upon to give an accurate figure for the diameter. Moreover, the orientation and location of the diameter plane is completely in the discretion of the operator's visual judgment. Nevertheless, it remains arguably the gold standard.

7.5 Pulmonary vein tree composition for atrial anatomy

In chapter 6, techniques to automatically extract the underlying left atrial anatomy were presented. This was obtained using a symbolic representation of each pulmonary vein drainage

	Ostia measurements	
Percentage difference	Ellipse-fitting	Diameter-sweep
$0-5\%$	43	24
$5-10\%$	15	14
$> 10\%$	4	24

Table 7.4: A summary of the percentage differences (with the manual ostia measurements) in the diameters measured using the ellipse-fitting and diameter-sweep methods over all 62 ostia measured.

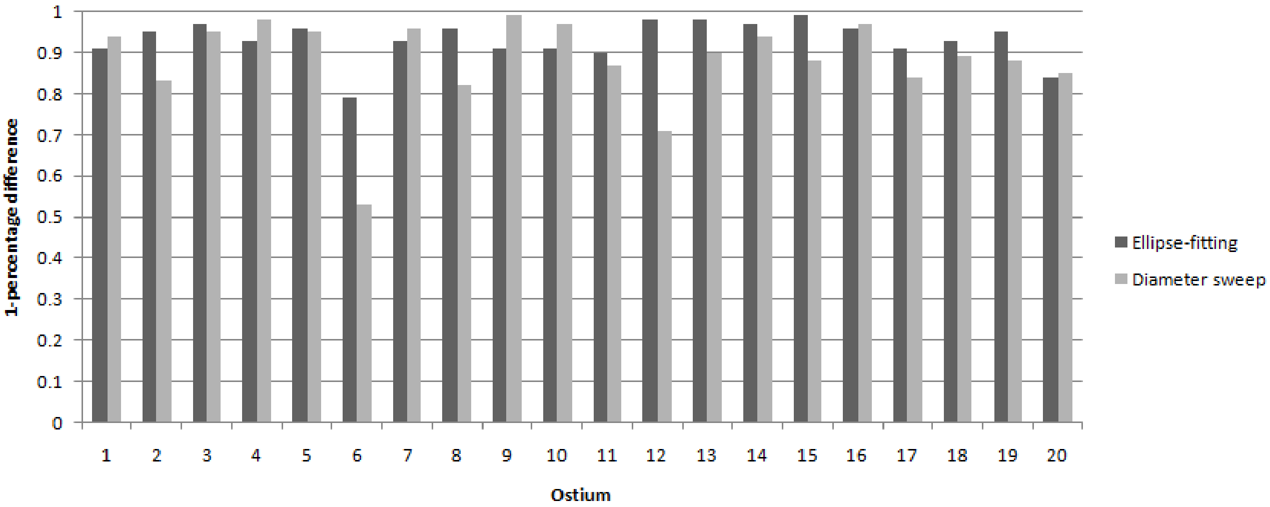

Figure 7.15: Comparison of the difference of manual measurements (i.e. gold standard) of twenty randomly selected ostial diameters with the diameters computed using ellipse-fit and diameter-sweep techniques. The vertical axis shows (1−fractional difference) values, where a value of 1 represents complete agreement with the gold standard. Note that only twenty ostia are shown here for brevity.

tree. The representation was retained in a tree data structure, constructed from vessel centrelines. Recall also that each drainage to the atrium was found using a cluster analysis of centreline endpoints incident on the atrial body (see section 6.1.1). The clinical applications of computing pulmonary vessel trees are the following:

- Locating the first bifurcation in each pulmonary vessel tree to assess an early or late branching - an important determinant for classifying left atrial anatomy (see section 6.2.1).
- Locating root vessels that become landmarks for computing ostial diameters.
- Cropping the tree beyond the nth branching to exclude unwanted details of peripheral vessels.

In RFCA, locating and annotating drainage vessels at least as far as the first bifurcation is essential and useful. This is because ablating the drainage before the first bifurcation can prevent any channel of ectopic beats from passing into the atrial body. For classifying the left atrium, the naming system in [109] is used; the classification is based on distances to the first bifurcation. To constrain validation for trees to the first bifurcation, the n-ary trees are restricted to a maximum *depth* of 1, where depth of a tree is defined as the length of the path from the root node. A depth of 1 does not necessarily guarantee vessels as far as the first bifurcation. This can be seen in Fig. 6.5 on page 114, where the vessel tree has depth 1 but also includes a second bifurcation.

7.5.1 Experimental details

In this study, a total of 116 pulmonary vein drainage trees were analysed from 30 patients. The left atrium segmentation, atrial body and vessel centrelines are all pre-computed. The location and number of drainages to each side are found using cluster analysis. Vessel trees can then be computed. It requires the occasional tuning of some parameters. These parameters control distinctive features of root vessels, allowing to distinguish them from other vessels:

- τ: The search range for root vessels as a function of the distance from the atrial body surface (i.e. atrial distance).
- $|v|^r_{\min}$: The minimum size required to become a candidate for a root vessel. This is the total sum of the distances between its detected centreline points.

Recall that centreline-tracked vessel segments that satisfy both τ and $|v|^r_{\min}$ become candidates for root vessels (see section 6.1.1 on page page 109). The value of τ ranges between 35-40 mm and the value of $|v|^r_{\min}$ for most parts of the study is 50 mm. A large value for $|v|^r_{\min}$ is desirable as this allows small insignificant centrelines (mostly caused due to noise) to be excluded. In addition to this, it is advantageous having a large root segment as its larger size allows it to span across most parts of the tree.

The computed trees are overlaid on a see-through surface reconstruction of the segmented left atrium (see Fig. 6.9 on page 119 and Fig. 7.9). Each tree node (i.e. vessel centreline segment) is numbered and annotated. The connections between nodes are displayed using straight lines. The root and child vessels are also colour-coded for distinctiveness. With vessel trees computed, the first bifurcation distance (FD) is found automatically. The FD values are displayed at each pulmonary vein drainage for easy reference. The operator selects two points on the atrial surface and the Euclidean distance between these gives an estimate for the FD . This is considered as the gold standard for FD distance. Graphical representations of vessel trees generated in the *GraphViz* format (see Fig. 6.11) are also assessed alongside.

7.5.2 Evaluation of trees and anatomy

Vessel trees are evaluated qualitatively and are based on the classification due to Marom et al. [109] (see Fig. 2.4 and 2.5 on page 24). Recall important aspects of the classification such as classes R2a/b/c and R3b/c to the right side and L1a, L2b to the left all have a bifurcation. Class R1 is the only trifurcation. The remaining classes have no bifurcations, although beyond the 10mm mark it is likely that vessels will branch. To evaluate the computed trees, the numbers of vessels in the first bifurcation are noted for each pulmonary vein drainage of the 30 patients

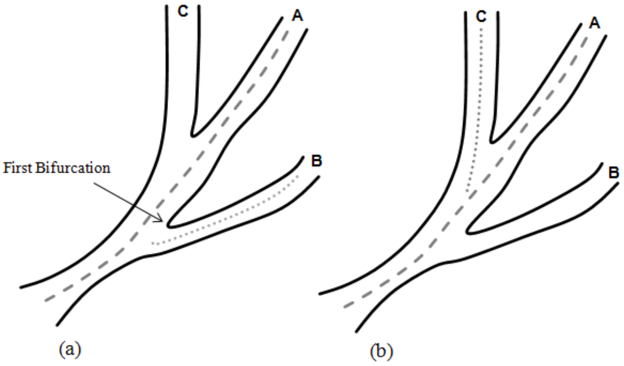

Figure 7.16: (a) The representation of this tree is correct if the system builds a tree (root → child): $A \rightarrow B$. (b) The representation of this tree is incorrect if the system misses B and builds a tree $A \rightarrow C$, although B's centreline was found prior. The FD in this case will also be incorrect. In the tree validation study, two vessels A and B are counted to be in the first bifurcation. In (a) both vessels are part of the constructed tree. In (b) only A is part of the constructed tree.

in the study. These vessels are easily counted in iso-surface visualisations of the left atrium. An illustration of how vessels are counted is given in Fig. 7.16. The ground truth is compared against the number found in the computed trees.

For evaluating atrial anatomy, two important determinants of anatomy are quantitatively evaluated against the gold standard. These are the FD values and number of drainages to the right and left sides. It can be difficult to find an accurate value for the FD. Normally, in a clinical setting, a radiologist will measure the distance from the end of the drainage (i.e. where it drains into the left atrium) to the first bifurcation using digital callipers. When a surface visualisation is not available, these distances are measured on orthogonal planes of the MRI data. In the evaluation study, with iso-surface renderings available, the operator can pick points on the surface of the left atrium to get a reasonable estimate for the FD distance. The ground truth for the location and number of drainages can also easily be obtained with an iso-surface rendering of left atrium segmentation.

7.5.3 Results

The results for vessel tree evaluation is illustrated in Fig. 7.19 for the first 50 drainages and Fig. 7.20 for the remaining 56 drainages. Results showed that 71% of the all drainages evaluated in this study had correctly computed trees. A further 23% had trees which were partially correct, mostly with one or two branches not included. The computed trees were incorrect for 6% of the drainages studied. Thus, a high success rate is found giving correct or partially correct trees in 94% of drainages evaluated in the study.

For the FD study, signed differences between the computed and gold standard manual measurements are reported. These differences expressed as a percentage of the manual measurement are illustrated in Fig. 7.21. The percentage differences show that approximately 80% of the drainages measured had a difference of less than 30%. The location and number of drainage locations are illustrated in Fig. 7.22 and Fig. 7.23 for the left and right sides respectively. A high success rate of 87% and 93% can be seen for the left and right sides respectively. The technique of finding drainages using cluster analysis (see section 6.1.1 on page 109) is shown to be robust.

7.5.4 Discussion

A technique for extracting vessel drainage trees and representing them using a graph structure was presented in chapter 6. This was useful for determining the underlying atrial anatomy using a set of predictors such as distances to the first bifurcation and the number of drainages to the right and left sides. Moreover, building vessel trees helps to exclude and filter noisy centreline segments. The computed trees, as far as the first bifurcation, were evaluated against ground truth. Results show that the technique was successful for extracting trees in 116 drainages studied.

Manual measurement of FD as is done in the clinical setting, can only give rough estimates of actual FD values. This is since these measurements are only made on the surface (i.e. of the blood pool). However, it remains the gold standard for FD. In the computer method, geodesic distances are computed within the volume. Recall that the FD obtained, with the computer method, is a fraction of the spline length (see Eq. 6.13 on page 120). The geodesic distance between the endpoint of the drainage to the first bifurcation provides a more rational approximation for the FD distance. As distances obtained with the two methods differ in such way, their values are also expected to differ to a certain degree. These explain the relatively higher discrepancies between manual and computer-obtained measurements, as illustrated in Fig. 7.21.

Although a high success rate was found in the drainage location study, most of the data available contained the commonly occurring anatomical variants of the left atrium - two drainages to the right and left respectively. For rarely occurring variants with 3 or more drainages to a side, occasional tuning of the variance-differential parameter s_τ may be required (see Eq. 6.6 on page 113). This controls how close or far apart drainages are expected to lie. The rarely occurring variants to the right side R4a, R4b and R5 exhibit such dense drainage neighbourhoods containing the extra one or two right middle drainages. Most clinicians are in the lookout for these anomalies during RFCA procedures as missing them can lead to reconnection of pulmonary vein ectopic regions. It has been generally found that lowering the variance-differential s_τ can reveal such anomalies.

7.6 Sensitivity analysis of user-adjustable parameters

7.6.1 Left atrium segmentation

The proposed left atrium segmentation algorithm (chapter 4) requires user-adjustable parameters such as the selection of a seed point within the atrium and a merging threshold level. These parameters are critical to the quality of segmentation generated by the algorithm. To assess sensitivity of the parameters and hence reproducibility of the obtained results, a comparison of segmentations obtained with four different runs of the algorithm is studied. In each run, a different set of seed points and merging threshold level is used. Similar to the manner in which segmentations are quantitatively assessed in section 4.8 on page 80, each segmentation obtained is compared against its manually-delineated counterpart. The mean segmentation overlap is found from five slices chosen at equally spaced intervals. Ten different images were selected for this study, ensuring that they were a good representative subset of our images.

The results obtained in this study are illustrated in Fig. 7.17. A comparison of the segmentation overlaps obtained in each run is shown. To obtain a measure of how far apart segmentations were in each run, the maximum percentage difference of overlap for each image was found. Table 7.5 lists these percentage differences along with the mean. In image subject 6, a difference of 9.10% was noted and in image subject 10 there was no difference in segmentations generated between the runs. The differences in segmentations in the remaining subjects ranged between these values. A mean difference of 4.27% was found. These results indicate that the segmentations obtained are reproducible and the algorithm's sensitivity to parameter settings is reasonably low.

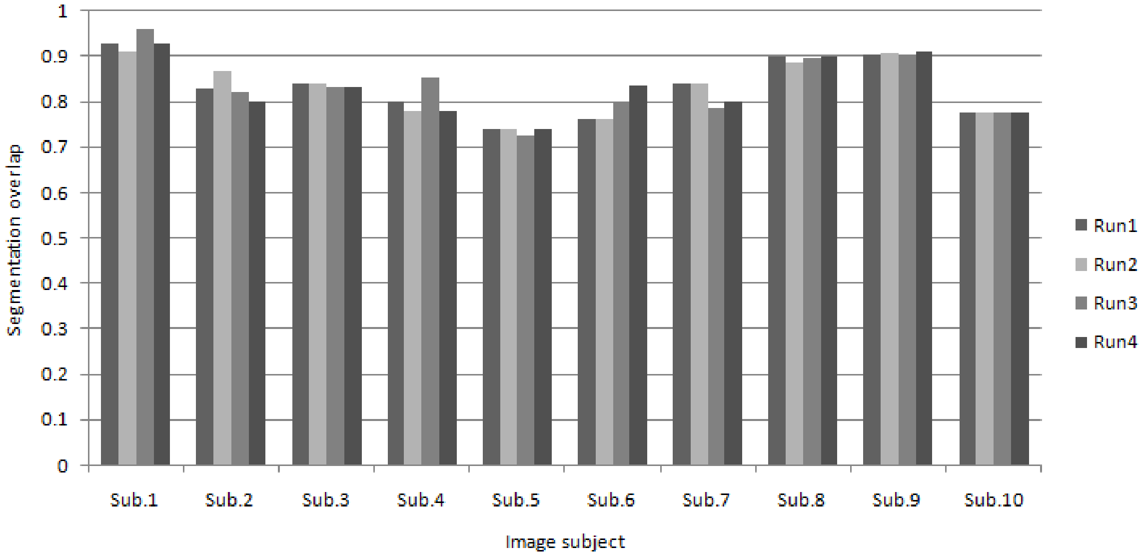

Figure 7.17: A comparison of mean segmentation overlaps obtained between four different runs of the left atrium segmentation algorithm. As a representative subset, ten MRA images were selected. The overlaps are computed against manual segmentations and an overlap of 1 represents complete agreement (see Eq. 4.15 on page 80). Each run uses a different set of seed points and user-adjustable merging threshold value.

7.6.2 Vessel tree composition for anatomy

Methods for computing and classifying atrial anatomy were presented in section 6.2 on page 118. Recall that atrial anatomy was classified based on the FD distance and the number of drainages to each side. In order to have the correct value for FD distance, it is important to have correctly computed drainage trees. In section 7.5, computed trees were evaluated against ground truth.

Image	Max. % difference
Sub. 1	5.20
Sub. 2	7.70
Sub. 3	1.00
Sub. 4	8.90
Sub. 5	1.90
Sub. 6	9.10
Sub. 7	6.40
Sub. 8	1.80
Sub. 9	0.70
Sub. 10	0.00
Mean	4.27

Table 7.5: The maximum percentage difference (i.e. between the best and worst segmentations) in segmentation overlaps across all four runs by each image subject.

Vessel tree composition and re-construction requires three user-adjustable parameters. Two of these parameters are listed in section 7.5.1 on page 154. These are namely the search range τ and the minimum root vessel size $|v|^r_{\text{min}}$ parameters. The third is the variance-differential parameter s_τ described in section 6.1.1 on page 109. In this study, we assess the sensitivity of these parameters in relation to obtaining correctly computed trees and drainage.

Four different runs of the tree composition algorithm were taken using a different set of parameters for each run. Ten different images were selected for this study, ensuring that they were a good representative subset of our images. From these ten images, forty different pulmonary drainages were studied separately for their computed trees. To evaluate the correctness of computed trees, vessels in the first bifurcation of the computed tree are compared against the ground truth. This is similar to the manner in which computed trees were evaluated in section 7.5.2 and illustrated in Fig. 7.16.

The results from this study are illustrated in Tables 7.6 and 7.7. Table 7.6 show a comparison of the computed drainages obtained in each run including the ground truth. For 7 out of the 10 images, the number of drainages computed in all four runs of the algorithm were exactly the same. One of the seven images can be seen in Table 7.6 (image 4), where three drainages were found in each run, however, this value differed from the ground truth. Table 7.7 show a comparison of the computed trees obtained in each different run by reporting the number

	Images			
	1	2	3	4
Run1	4	4	3	3
Run2	4	4	3	3
Run3	4	4	5	3
Run4	3	3	5	3
Ground truth	4	3	4	4

Table 7.6: A comparison of the drainages computed in each different run of the pulmonary vein tree composition algorithm. Each run used a different set of user-adjustable parameters. Ten left atrium images were studied and the table only shows the four images for which the computed drainages differed between runs or from the ground truth. For the remaining six images, there was complete agreement between each run and ground truth.

of vessels in the first bifurcation. For 36 out of the 40 drainages studied, there was complete agreement between the number of vessels found (in the first bifurcation) for all four runs of the algorithm. Four drainages for which there was disagreement in values are given in Table 7.7 (see image 6,7,8 and 10). However, for images 6 and 10, there was agreement in the first three runs of the algorithm with only the fourth run generating a different result. These results indicate that the output obtained from the algorithm are reproducible and the sensitivity of the parameters on drainage and tree computation are relatively low.

7.6.3 Ostial diameters

Diameters are measured along root vessels of each computed drainage. Recall that the diameter plane is moved along the root vessel spline (see section 5.3.4 on page 102). The user stops this diameter plane at a position from which the ostium can be correctly measured. The position of the plane is an important user-adjustable parameter that affects the outcome of ostium measurements. Furthermore, computation of drainage trees and root vessels also play an important role. In this study, the sensitivity of the diameter-plane position parameter along with the search range τ, minimum root vessel size $|v|^r_{\min}$ and variance-differential s_τ parameters on ostium measurements are investigated. Four separate runs of the ostium ellipse-fitting process are taken, with a new set of parameters for each run.

	Experimental runs and ground truth				
Drainages	Run1	Run2	Run3	Run4	Ground truth
1	1	1	1	1	2
2	1	1	1	1	2
3	1	1	1	1	2
4	1	1	1	1	2
5	3	3	3	3	3
6	2	2	2	1	2
7	2	2	1	1	3
8	2	2	2	0	2
9	1	1	1	1	2
10	3	3	3	0	3
11	1	1	1	1	2
12	1	1	1	1	2
13	1	1	1	1	2
14	1	1	1	1	2

Table 7.7: A comparison of the computed trees obtained in each different run of the pulmonary vein tree composition algorithm. The correctness of computed trees is evaluated by counting the number of vessels in the first bifurcation as shown here. Forty pulmonary vein drainages were selected in this study and the table lists only drainages for which computed values differed between runs or from the ground truth. For the remaining 26 drainages, there was complete agreement between each run and the ground truth.

Ostium	Max. % difference
1	4.60
2	3.90
3	1.20
4	0.20
5	9.90
6	1.40
7	3.70
8	1.40
9	2.64
10	2.90
11	1.40
12	3.90
13	9.20
14	4.60
15	1.30
Mean	3.50

Table 7.8: Maximum percentage differences across all four runs by each ostium.

A comparisons of the results in this study are illustrated in Fig. 7.18. Fifteen ostia were measured. Diameters computed using the ellipse-fit from each run are compared. Table 7.8 lists the maximum percentage difference (between measurements) recorded for each run. 12 out of the 15 ostia measured had a percentage difference of less than 5%. A mean of 3.5% indicate a low amount of discrepancy in measurements between different runs. Results from this study thus show that ostium measurements are reproducible and sensitivity of its parameters are relatively low.

7.7 Summary

An evaluation of the proposed techniques of chapters 4, 5 and 6 was presented in this chapter. The features of the atrium that are of clinical interest and relevance are evaluated. We summarise the obtained results. The left atrium segmentation method was able to segment 87% of the datasets with a single automatic step. Further semi-automatic correction steps were required for the remaining patients. For evaluating the pulmonary vessel centreline extraction

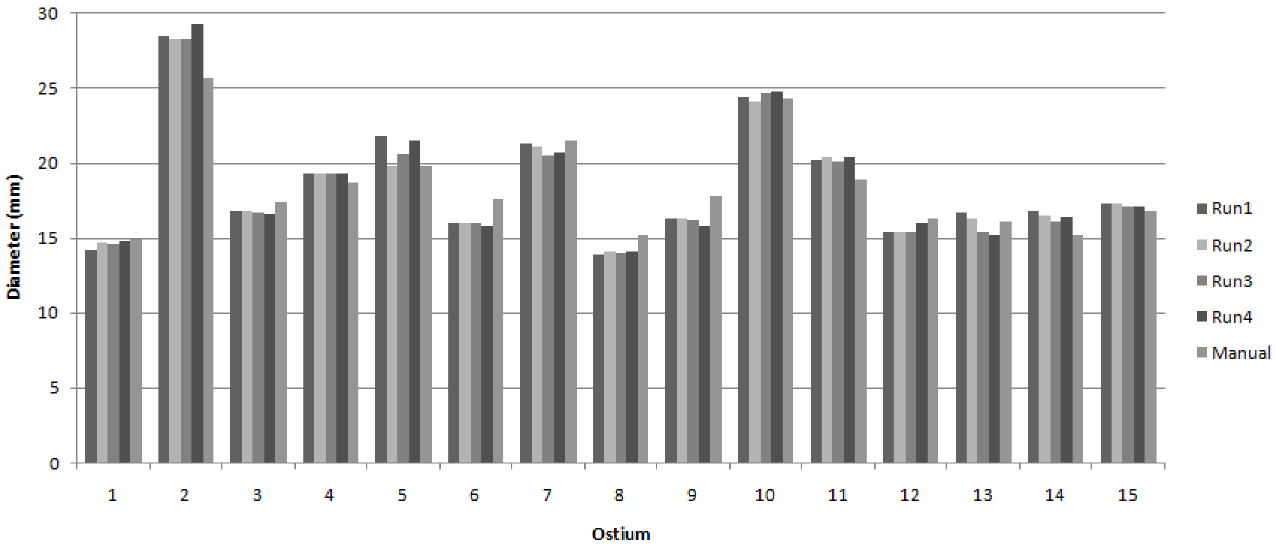

Figure 7.18: Comparison of the computed trees obtained in each different run of the pulmonary vein tree composition algorithm for the remaining twenty drainages. See Fig. 7.7 for the first twenty drainages. Abbrevation: PV - pulmonary vein.

process, vessels were classified as first, second or third generation vessels depending on whether they were found before the first, second or third splits respectively. Results showed 94%, 97% and 95% success rates for the first, second and third generation vessels respectively.

The ostial diameter ellipse-fitting and diameter-sweep methods were evaluated against a manual approach for measuring diameters which is considered as the gold standard. When compared against gold-standard measurements, the ellipse-fit method approximated the diameter better than the diameter-sweep technique, with a mean percentage difference of 4.7% with the gold-standard..

In the atrial anatomy study, first bifurcation distances were evaluated in addition to the number of drainages to the right and left sides of the atrium. The percentage differences for bifurcation distances showed high discrepancy with approximately 80% of measurements taken having an error of less than 30%. Manual measurements were taken on the left atrium surface and this only gives approximate values for the distance. This is also how they are measured in a clinical setting. Bifurcation distances are also prone to inter- and intra-observer variabilities. There is some ambiguity on where the actual atrial body boundary lies - distances are measured between the boundary and bifurcation. In comparison, there was a higher success rate for finding drainages with 87% and 93% for the left and right sides of the atrium respectively.

The results indicate that the proposed methods for segmentation of the atrium and pulmonary veins, including the methods proposed for extracting important left atrial characteristics and classifying anatomy, are robust. The MRA data on which these methods were evaluated included images of different resolution and quality. Furthermore, anatomies of both the commonly and rarely occurring variants could be classified.

The sensitivity of user-adjustable parameters and reproducibility of obtained results are investigated in a series of studies. A good representative subset of our images is used. The effect of critical parameters in algorithms for left atrium segmentation, pulmonary vessel modelling and ostial diameter computation is assessed. The studies consistently confirm the reproducibility of obtaining correct results together with a relatively low response to parameter adjustments. Nevertheless, it is important to have parameters to allow the user make adjustments as and when felt necessary. As the atrium exhibits variable anatomy, parameter adjustments in some instances can give better results as shown in the reproducibility studies.

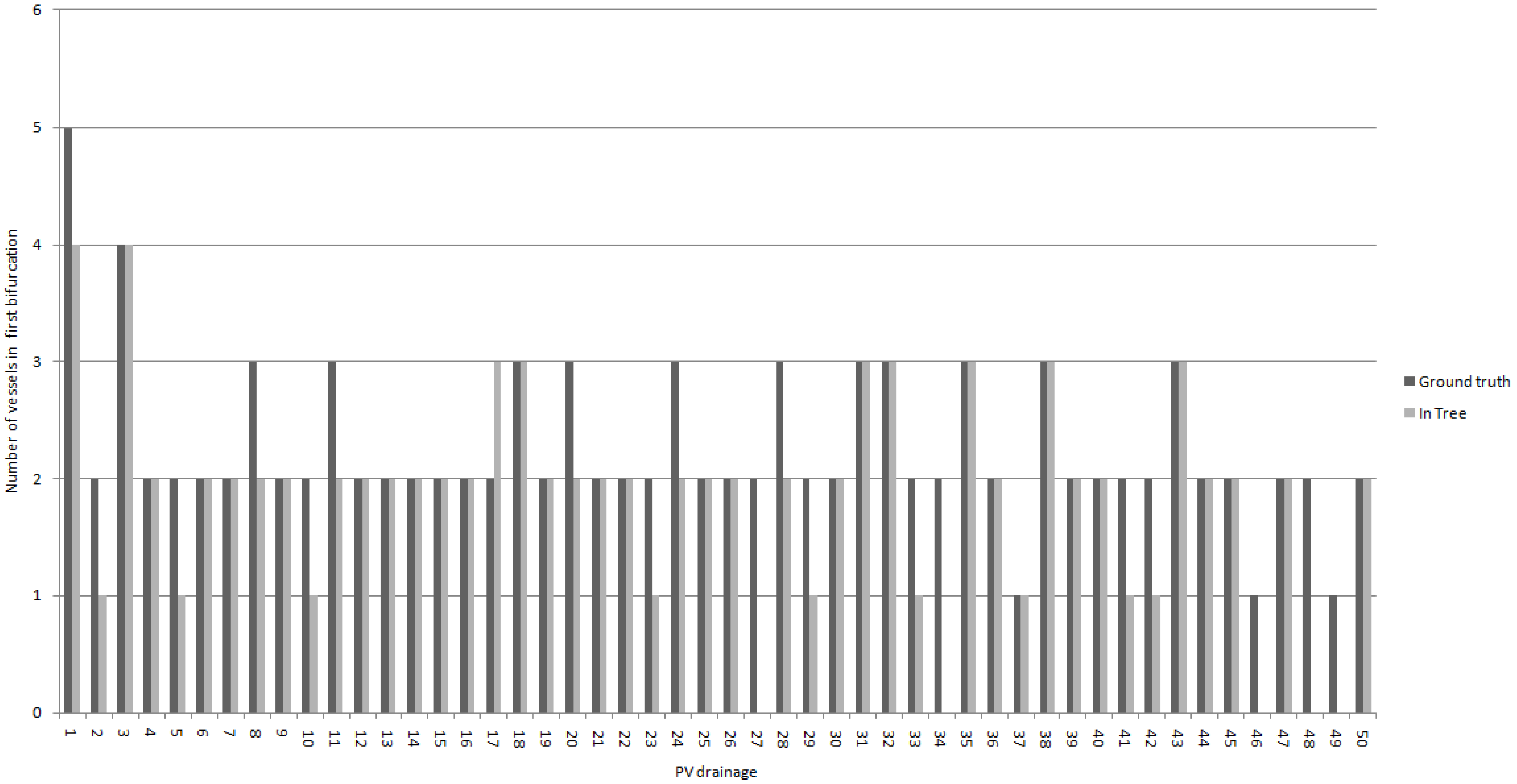

Figure 7.19: Comparisons of the number of vessels in the first bifurcation/trifurcation obtained from the study of 50 out of 116 total drainage trees. The results for the remaining 56 can be found in Fig. 7.20. Abbreviation: PV - pulmonary vein

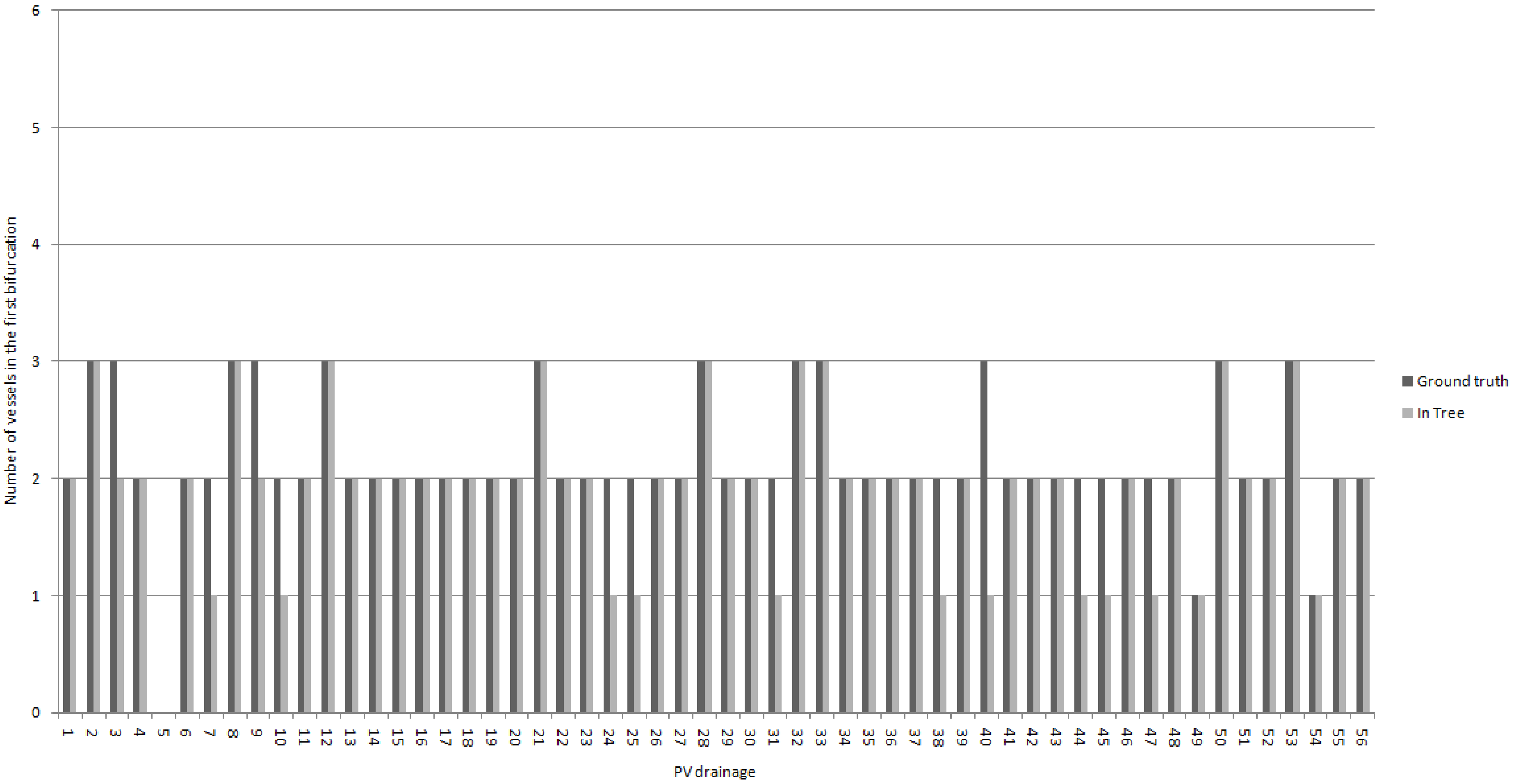

Figure 7.20: Comparisons of the number of vessels in the first bifurcation/trifurcation obtained in the remaining 56 pulmonary vein drainage trees studied. The results for the first 50 trees studied can be found in Fig. 7.19. Abbreviation: PV - pulmonary vein

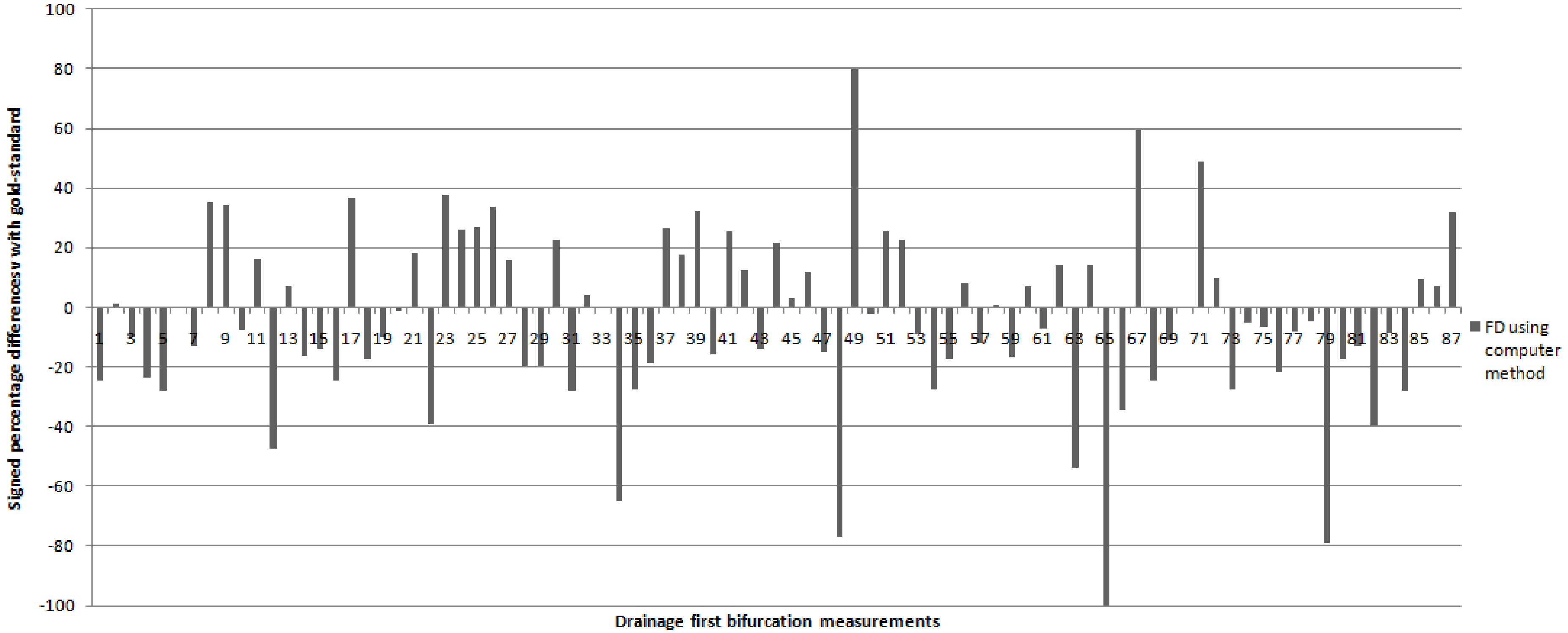

Figure 7.21: The signed differences in FD values measured using manual (i.e. gold standard) and computer methods. The differences are expressed as a percentage of the manual measurement. A positive difference represent over-estimation.

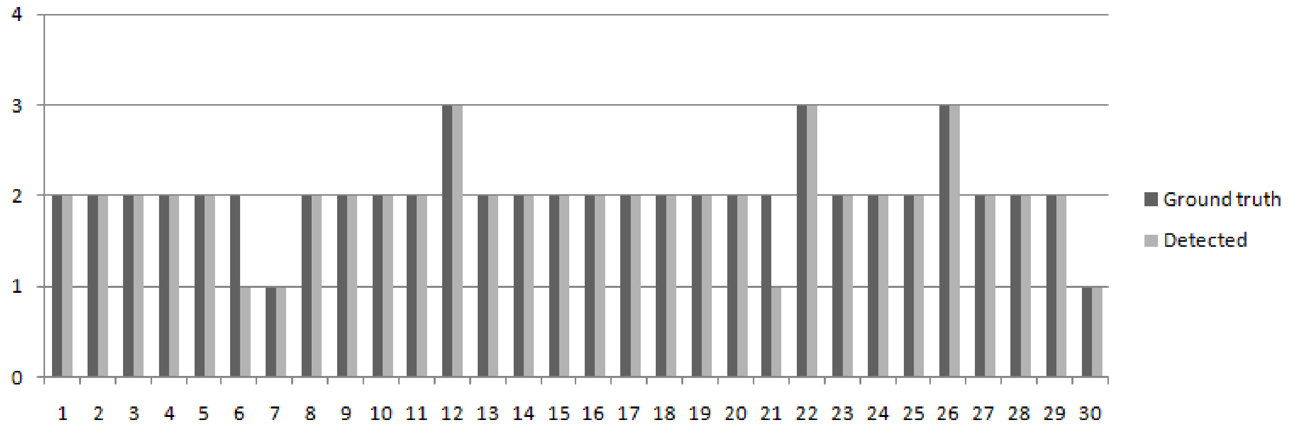

Figure 7.22: Comparisons of the number of drainages to the left side of the 30 patient LAs studied. Note that most anatomies are the commonly occurring variants L2a and L2b.

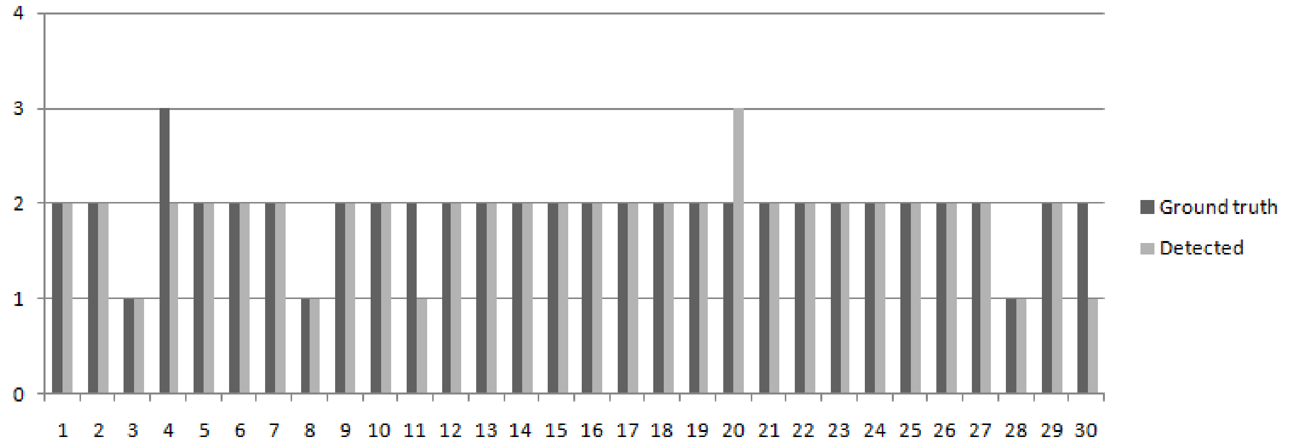

Figure 7.23: Comparisons of the number of drainages to the right side of the 30 patient LAs studied. Note that most anatomies are the commonly occurring variants R2a, R2b and R2c.

Chapter 8

Conclusion

The thesis has aimed to provide techniques that overcome current problems in analysing atrial MRA data for RFCA. It has proposed several algorithms for solving these problems. Techniques for segmenting the atrium, segmenting sub-atrial structures and obtaining important procedural parameters have been presented. In this chapter, the main contributions are outlined. The general limitations of each presented technique and future research areas are also discussed.

8.1 Contributions

In **chapter 4**, a method for segmenting the left atrium from contrast-enhanced MRA images was presented. The method can segment atria by exploiting narrow connections. Results show that 84% of the datasets in our study could be segmented successfully. To achieve correct segmentations in the remaining datasets, a post-segmentation correction step was found to be necessary. To this end, a semi-automatic segmentation method capable of obtaining better segmentations was also proposed. Results have shown that the post-segmentation correction steps improved the segmentations. To compensate for low signal-to-noise ratio and preserve narrow connections, an anisotropic diffusion filtering step is proposed. An algorithm for extracting the largest blood pool in the image using automatic thresholding selection is also presented. The chapter presented an algorithm which is an improvement over [69]. A comparative study showed that the proposed algorithm produced better segmentations than the existing technique.

Chapter 5 has proposed techniques for segmenting central atrial body and pulmonary veins of the left atrium. Further in the chapter, a novel method for extracting centrelines of pulmonary veins is proposed. Centrelines provide a minimal and meaningful representation of pulmonary veins that can be conveniently retained and used for further analysis. Although the centreline extraction process was developed specifically for pulmonary veins, it can also be used for vessels in general. The method was evaluated on 451 vessels consisting of first, second and third generation vessels of pulmonary vein drainage trees. High success rates of 94%, 97% and 95% were found for the first, second and third generation vessels, respectively. Results show that the proposed methods are robust and applicable for left atrial pulmonary veins.

Chapter 6 has proposed techniques for quantifying atrial anatomy. The atrial drainage networks are represented using graph structures. Anatomy is quantified using the number of drainages, the tree configuration at each drainage and first bifurcation distances. Results show that 94% of all drainages studied had correct or partially correct computed trees. Results also show that 80% of drainages studied had a percentage difference of less than 30% in their computed first bifurcation distance. Furthermore, success rates of 87% and 93% were found for determining the number of drainages to the left and right sides of the atrium respectively. The chapter also proposed a technique for quantifying ostial diameters from computed drainage trees. Ostia are modelled in 2D using ellipses. Results showed that 93% of all ostial diameters computed had a percentage difference of 10% or less when compared to the standard manual approach. Evaluation of the proposed methods show that they are applicable for quantifying important atrial characteristics that are frequently needed in RFCA procedures.

Together the techniques presented in this thesis provide essential segmentation and measurement tools for pre-planning atrial fibrillation procedures. Commercial systems currently available only provide only generic tools that demand a substantial amount of the operator's time in segmenting and analysing left atria. The proposed system adds value by utilising novel computational algorithms to provide for semi-automatic segmentation and quantification. Moreover, it opens way for computer-guided interventions involving the atrium. A list of key features

	Systems		
Features	Sensei™	CARTO™	Proposed
LA segmentation module	×	×	√
LA reconstruction for visualisation	√	√	√
PV segmentation	×	×	√
Computation of atrial anatomy	×	×	√
Computation of ostial size	×	×	√
Surgical catheter navigation	√	√	×
Electroanatomical mapping	√	√	×

Table 8.1: A comparison of the key features relevant to atrial fibrillation procedures present in commercial and the proposed systems. Abbreviations: LA - left atrium, PV - pulmonary veins.

found in two popular commercial systems are given in Table 8.1.

8.2 General limitations

The approaches presented in this dissertation have some limitations:

8.2.1 Manual user interaction

As some of the proposed techniques are not completely automatic, manual user interaction is necessary in some instances. Most take the form of a selection of a seed point or threshold value. The following is a list of all the manual interaction steps that are necessary and their impact on the usability of the approach involved:

- **Blood pool extraction**: As described in section 4.4 (page 69), the user is required to select a seed voxel within the blood pool. Defining a region-of-interest using a bounding box control is optional (see Fig. 4.5), but, significantly improves the performance of the algorithm by truncating the dataset.

- **Region-split-and-merge process** : As described in section 4.6 (page 77), the user is required to select a merging threshold interactively based on the segmentation result. Selection of the right threshold is necessary for acquiring good segmentations.

- **Cell exclusion**: To correct for mis-segmentations, exclusion and inclusion of cells may be necessary with the user selecting wanted or un-wanted cells. This step is shown to improve the segmentation results by about 6%. (see Fig. 7.8).

- **Atrial body segmentation**: The user is required to select a seed point within the atrial body in the level set segmentation technique proposed (section 5.2.3 on page 91). It is important for the seed point to lie within the atrial chamber as it initiates the front evolution, starting from a sphere centred at that point.

- **Computation of vessel medial-axis**: Prior to computing centrelines, the system computes seed points based on a user-defined threshold for the vesselness response (see section 5.3.3 on page 98). A threshold value of 2-5 has known to work well in all our images. The higher this threshold is set to, the more difficult it becomes for small vessels to satisfy the threshold requirement. Selecting a low threshold value has the advantage of ensuring that small vessels are included. In addition to this, seed points resulting from low vesselness and lying near the boundaries of vessels, have no impact on the computation of medial axes.

- **Modelling pulmonary vessel trees**: In the vessel drainage tree reconstruction technique proposed in section 6.1.1 on page 109, the user is required to select a threshold value for the variance-differential parameter. This parameter dictates the degree of separation between each drainage site. Selecting the right threshold value is important as it determines the correct computation of location for the drainages.

8.2.2 Imaging artefacts

In left atrium segmentation, the underlying assumption that the atrium is connected to neighbouring structures via narrow connections may not always hold true. In images with low spatial resolution, there is a high possibility of more pronounced partial volume effect. As vessels are smaller relative to the voxel size, the partial volume effect within vascular structures creates connections that are not essentially narrow. Consequently, regions are merged in places where they should split. This is most common between pulmonary arteries and veins. The result of this is the inclusion of pulmonary artery voxels in the segmented atrium. A second limitation in left atrium segmentation is the image signal degradation due to noise. The anisotropic diffusion filtering step is useful for alleviating image noise and preserving edge boundaries. However, boundary information can be lost in images with low signal-to-noise ratios, especially within regions of small structures such as vessels.

In the segmentation technique for left atrial body, leaks through the drainage are undesirable. Such leaks will cause the drainage vessel to become part of the atrial body structure, causing it to be excluded from the resulting vessel tree graphs. The curvature constraint on the level-set evolution equations (see Eq. 5.7 on page 91) will restrict extensive leaks through narrow drainages but cannot prevent leaks through drainages that are relatively large in size compared to the atrial body. One such example was illustrated in Fig. 7.13. The parameter τ_ξ in eq. 5.6 should be increased to avoid leaks in the initial evolution step. However, increasing it to a value that is too high can severely under-segment the atrial body, making the second evolution step unable to recover the atrial shape to the full extent. Thus, there is a trade-off between avoiding leaks and under-segmentation. Nevertheless, an under-segmentation of the atrial body is adequate for it to be used in finding drainages and building vessel trees.

The pulmonary vein centreline extraction technique can be sensitive to noise and partial volume effect. Recall that the centreline extraction process maximises the Euclidean DT function at each step. Noise pixels cause perturbations in the Euclidean DT image. The initial assumption made about centrelines of vessels being ridges of Euclidean DT function becomes a loose one. The partial volume effect within pulmonary arteries and veins cause connections between the two vascular structures. There is no explicit modelling of these connections that can help the centreline extraction process distinguish it from a vessel that branches. The seed generation process (see section 5.3.2 on page 97) and cost function (see section 6.8 on page 114) for tree building help to some extent in preventing the centreline tracker from drawing a centreline through the connection and connecting a vein to an artery. However, for vessels of small diameter breaches of such nature are unavoidable.

8.2.3 Observer errors

There are some limitations in our study for obtaining the gold standards for ostial diameters and first bifurcation distances (see sections 7.4 and 7.5). Observer errors have to be put into consideration when assessing computed values against the available gold standard. For ostial diameters, it is often not entirely trivial to visually look for two points on the ostial circumference that will correctly give the diameter. Scharf et al. [155] proposed selecting points on at least two orthogonal planes and it is this method which is used in the present study for reporting ostial diameters. For manually obtaining first bifurcation distances, an observer selects points on the atrial surface. This only gives an approximate value. The true first bifurcation distance is measured within the atrial volume, from the atrial body surface to the first bifurcation.

8.3 Future research

The pulmonary arterial and venal trees frequently appear intertwined together in a dense vessel mesh. As outlined earlier, partial volume effects within these regions are common in most images and more pronounced in low spatial resolution images. This creates non-narrow connections between the two trees causing the left atrium segmentation method to often include segments of the arterial tree. Future research directions in left atrium segmentation will look into developing a mechanism for identifying and excluding the arterial tree. It is envisaged that this is possible if the centreline detection process can distinguish between two types of vessel branching: 1) Appears to be a branch, but is a connection to another tree due to partial volume effect, 2) A genuine branching of the vessel. Separate and disjoint tree graphs can be constructed for each vessel tree. Exclusion of the arterial tree provides ideal segmentations of the left atrium. Moreover, with drainage tree graphs available, segmentation as far as the nth bifurcation can be queried and obtained.

It is non-trivial to determine the basal area of the left atrium. Future research will also look into ways of modelling the mitral valve interface separating the left atrium from the ventricle.

Zheng et al. [191] have modelled the mitral valve from CT images. Tracking the mitral valve becomes difficult in contrast-enhanced MRA as it is faintly visible. In addition to this, the mitral valve also exhibits significant translational movement during the cardiac cycle. As the valve opens up to allow the flow of blood, its boundaries become less visible as they merge with the contrast-enhanced blood. Incorporating tissue information from other image sources such as late-gadolinium-enhancement MR images can reveal its anatomy. This will help build a more accurate model for the basal area of the atrium.

Appendix A

A.1 Implementation details

The software developed to test the proposed algorithms was written in Visual C++ under the Microsoft Windows environment. The list below gives an outline of the implementations used in each module.

- **Visualisation tools**: Most visualisation techniques employed to enhance the visualisation of the MRI data use library functions found in the Visualisation toolkit (VTK) [158]. Some examples include surface reconstruction using marching-cubes, volume renderings, etc.

- **Image registration**: A rigid registration technique is applied to pre- and post-MRA scans, as described in section 4.3.1 on page 67. We use an implementation from the Image registration toolkit (IRTK) [63]. The algorithm used can be found in [164].

- **Anisotropic diffusion filter**: The pre-processing steps involving anisotropic diffusion described in section 4.3 on page 67 uses an implementation from the Insight toolkit (ITK) [67]. The ITK library function implements the algorithm proposed in [134].

- **Region-growing with automatic thresholding**: The blood pool extraction process using region-growing as described in section 4.4 on page 69 uses our own implementation of region-growing. For automatic thresholding, our implementation of [130] is used. Fig. A.1 shows a snapshot of the graphical user interface (GUI).

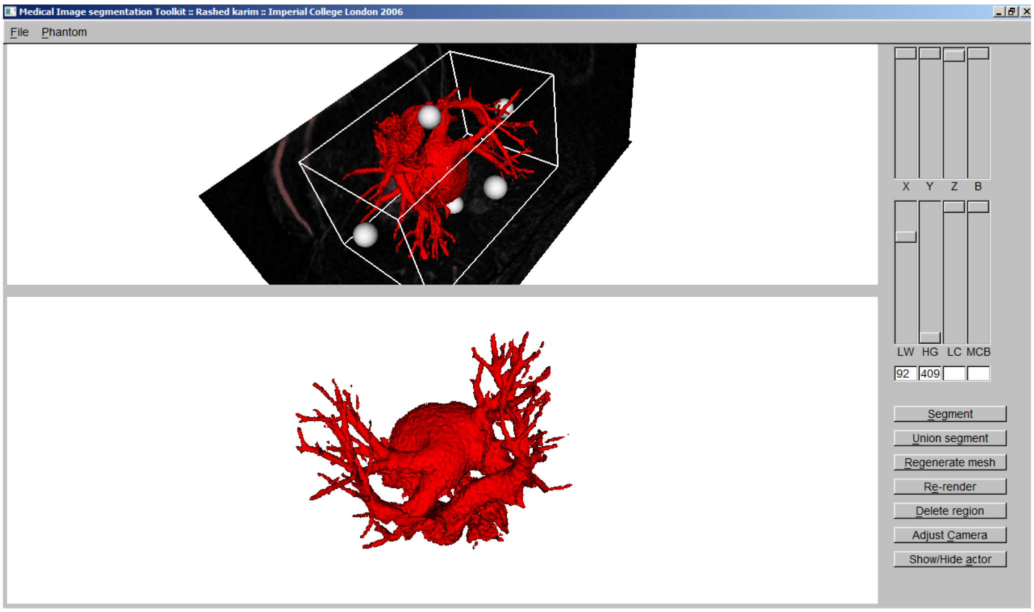

Figure A.1: Snapshot of the GUI used for blood pool extraction using region-growing. The sliders are used for threshold selection and these are automatically set when the MRI data is loaded.

- **Distance transformation**: The distance transformation filter described in section 4.5 on page 74 uses an implementation found in the IRTK [63]. The library functions implements the algorithm set out in [111].

- **Region-split-and-merge**: The left atrium segmentation region-split-and-merge process described in section 4.6 on page 77 uses our own implementation and improvement of the algorithm in [69]. Fig. A.2 shows a snapshot of the GUI used.

- **Atrial body segmentation**: Level set method implementations are used in atrial body segmentation as described in section 5.2 on page 86. The implementations used are the ones found in the library functions of ITK [67]. Fig. A.3 shows a snapshot of the GUI with atrial body overlaid on the surface rendering of segmented left atrium.

- **Pulmonary vein centreline computation**: The centreline computation outlined in section 5.3 on page 93 uses our own implementation. The vesselness filter (section 5.3.2 on page 97) used for finding seed points uses the implementations found in ITK's library functions.

- **Modelling of centreline curves using B-splines**: Computed centreline points are

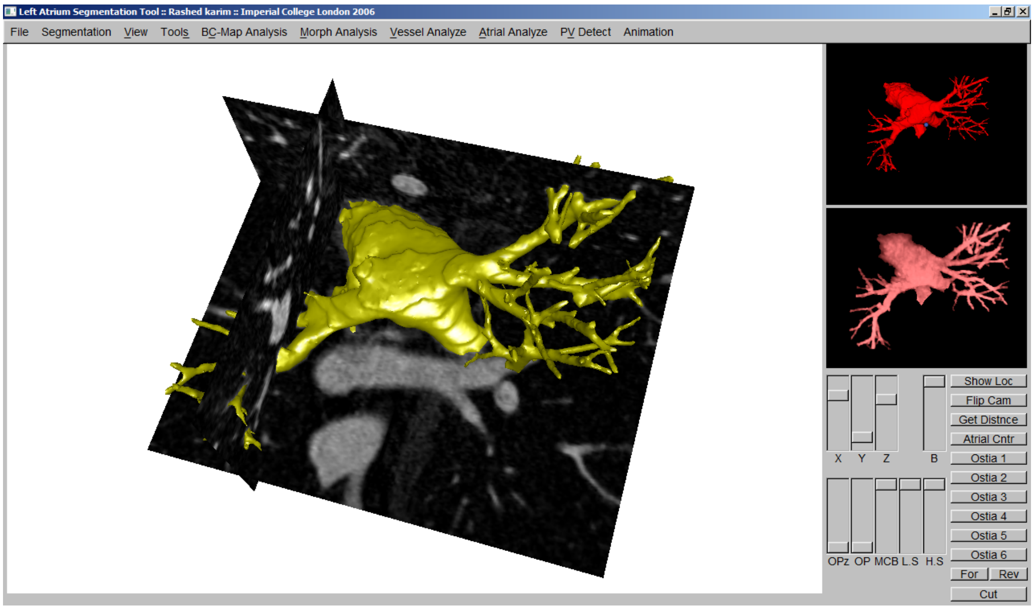

Figure A.2: Snapshot of the GUI used for region-split-and-merge process and left atrium segmentation.

modelled using a least-square B-spline fit (section 5.3.4 on page 102). We use the implementatons found in the library functions of the Geometric tools toolkit [157].

- **Modelling of pulmonary vessel trees**: All of the techniques outlined in chapter 6 pertaining to modelling of pulmonary vessel trees use own implementations. Some of these include hierarchical clustering, vessel drainage tree reconstruction, atrial anatomy, etc.

- **Ostial diameter computation**: Library functions found in the Geometric tools toolkit [157] are used for the ellipse-fitting procedure. The diameter-sweep method uses our implementation. See Fig. A.5 for a snapshot.

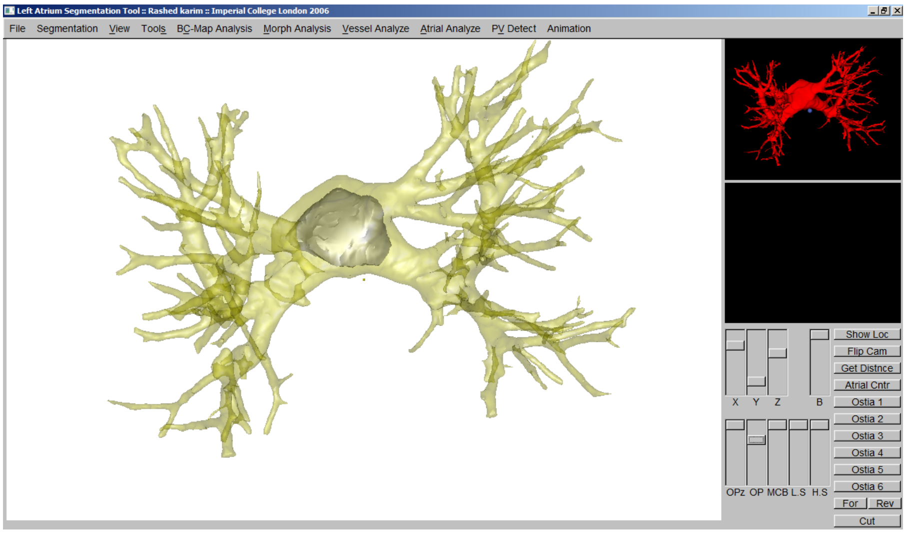

Figure A.3: Snapshot of the GUI used for region-split-and-merge process and left atrium segmentation.

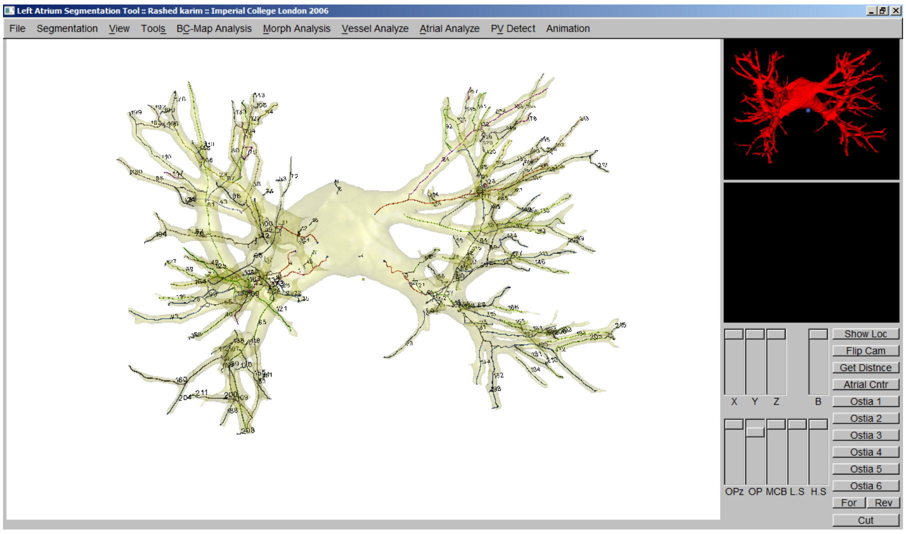

Figure A.4: GUI showing a rendering of the computed centrelines overlaid on a transparent surface rendering of the segmented left atrium.

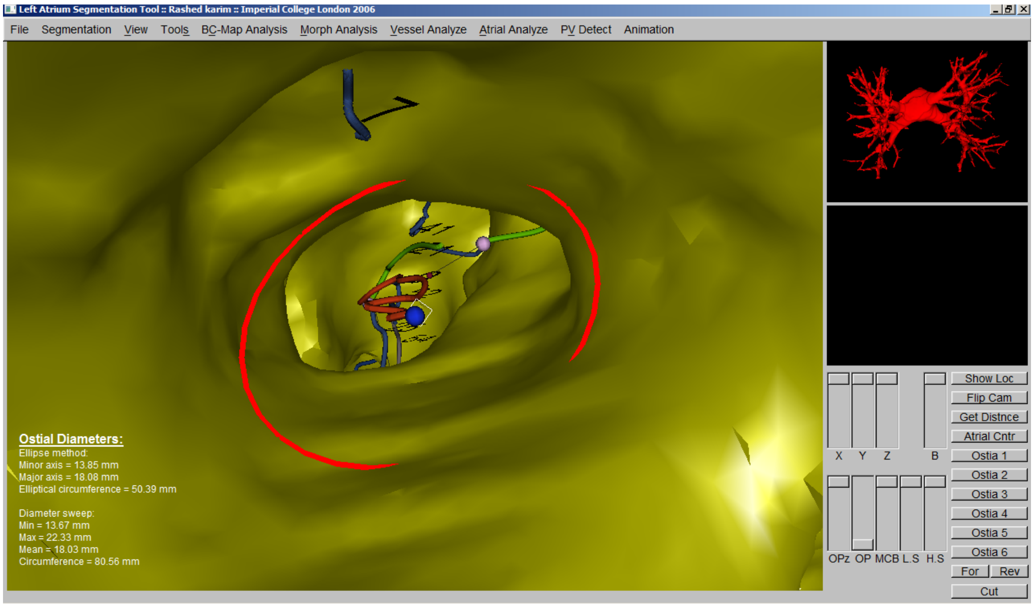

```
Ostial Diameters:
Ellipse method:
Minor axis = 13.85 mm
Major axis = 18.08 mm
Elliptical circumference = 50.39 mm

Diameter sweep:
Min = 13.67 mm
Max = 22.33 mm
Mean = 18.03 mm
Circumference = 80.56 mm
```

Figure A.5: A snapshot of ostial diameter computation using the two computer methods - ellipse-fitting and diameter-sweep.

Appendix B

Table B.1: Segmentation overlaps between manual and computer-delineated outlines. For each image sequence the first and second rows show overlaps from algorithms A [69] and our proposed algorithm B respectively in each of the five slices selected. The mean overlaps are also shown.

Segmentation overlap (Algorithm A and B)							
Image sequence	Algo.	Slice 1	Slice 2	Slice 3	Slice 4	Slice 5	Mean
Image 1	A	0.90	0.94	0.89	0.94	0.99	0.93
	B	0.94	0.92	0.88	0.95	0.97	0.93
Image 2	A	0.45	0.56	0.45	0.95	0.85	0.65
	B	0.86	0.79	0.87	0.95	0.85	0.86
Image 3	A	0.41	0.54	0.37	0.48	0.77	0.51
	B	0.82	0.88	0.78	0.83	0.89	0.84
Image 4	A	0.66	0.37	0.38	0.53	0.63	0.51
	B	0.71	0.69	0.69	0.93	0.98	0.80
Image 5	A	0.25	0.35	0.36	0.24	0.44	0.32
	B	0.73	0.86	0.86	0.81	0.44	0.73
Image 6	A	0.23	0.22	0.17	0.45	0.06	0.22

Continued on Next Page…

Image sequence	Algo.	Slice 1	Slice 2	Slice 3	Slice 4	Slice 5	Mean
Image 6	B	0.74	0.69	0.59	0.83	0.96	0.76
Image 7	A	0.24	0.14	0.09	0.13	0.42	0.20
	B	0.43	0.39	0.29	0.31	0.78	0.44
Image 8	A	0.87	0.63	0.51	0.76	0.82	0.72
	B	0.87	0.79	0.88	0.82	0.83	0.84
Image 9	A	0.59	0.62	0.57	0.57	0.87	0.65
	B	0.91	0.91	0.81	0.90	0.96	0.90
Image 10	A	0.00	0.00	0.00	0.00	0.00	0.00
	B	0.94	0.81	0.95	0.99	0.83	0.90
Image 11	A	0.7	0.82	0.82	0.61	0.79	0.75
	B	0.99	0.97	0.91	0.82	0.92	0.92
Image 12	A	0.58	0.72	0.56	0.86	0.95	0.73
	B	0.81	0.69	0.7	0.93	0.76	0.78
Image 13	A	0.83	0.85	0.87	0.92	0.98	0.89
	B	0.94	0.96	0.99	0.97	0.98	0.97
Image 14	A	0.78	0.61	0.57	0.65	0.69	0.66
	B	0.88	0.69	0.63	0.72	0.86	0.76
Image 15	A	0.98	0.84	0.87	0.84	0.87	0.88
	B	0.93	0.71	0.88	0.96	0.80	0.86
Image 16	A	0.76	0.69	0.77	0.94	0.93	0.81
	B	0.41	0.65	0.69	0.81	0.93	0.70
Image 17	A	0.70	0.81	0.85	0.90	0.83	0.82
	B	0.99	0.99	0.98	0.99	0.95	0.98
Image 18	A	0.8	0.75	0.91	0.92	0.87	0.85
	B	0.87	0.92	0.98	0.91	0.93	0.92
Image 19	A	0.43	0.38	0.71	0.82	0.72	0.61
	B	0.71	0.81	0.81	0.75	0.79	0.77

Continued on Next Page…

Image sequence	Algo.	Slice 1	Slice 2	Slice 3	Slice 4	Slice 5	Mean
Image 20	A	0.65	0.59	0.64	0.67	0.73	0.66
	B	0.8	0.75	0.81	0.88	0.90	0.83

Table B.2: Ostial diameter values for all 62 ostia measured using manual, ellipse-fit and diameter-sweep methods. The final two columns show the percentage difference between the manual and computer-methods. Symbols: ‡Worst and best-cases for the ellipse-fitting method, †Worst and best-cases for the diameter sweep method.

Ostium	**Manual (mm)**	**Ellipse-fit (mm)**	**Diameter-sweep (mm)**	**% difference in ellipse-fit and manual**	**% difference in diameter-sweep and manual**
1	21.60	23.61	20.31	9.31	5.97
2	16.93	17.83	19.65	5.32	16.07
3	19.68	19.06	18.71	3.15	4.93
4	15.28	16.49	15.54	7.92	1.70
5	16.25	17.03	15.58	4.80	4.12
6	8.65	10.48	12.66	21.16‡	46.36
7	16.02	17.16	16.55	7.12	3.31
8	18.15	17.41	14.97	4.08	17.52
9	16.62	15.03	16.46	9.57	0.96†
10	17.09	18.75	17.48	9.71	2.28
11	18.38	20.34	16.01	10.66	12.89
12	11.93	11.63	15.30	2.51	28.25
13	16.39	16.81	14.89	2.56	9.15
14	13.60	14.11	12.80	3.75	5.88
15	17.30	17.07	19.37	1.33	11.97
16	21.38	22.29	21.97	4.26	2.76
17	9.75	10.65	11.22	9.23	15.08
18	18.28	19.65	20.25	7.49	10.78
19	18.27	19.33	20.46	5.80	11.99
20	14.83	17.32	16.98	16.79	14.50
21	14.83	15.53	15.76	4.72	6.27
22	12.88	11.38	12.23	11.65	5.05
23	15.95	16.30	13.03	2.19	18.31

Continued on Next Page...

Ostium	**Manual (mm)**	**Ellipse-fit (mm)**	**Diameter-sweep (mm)**	**% difference in ellipse-fit and manual**	**% difference in diameter-sweep and manual**
24	18.09	19.70	18.85	8.93	4.20
25	12.79	12.12	11.15	5.24	12.82
26	10.01	10.01	9.08	0.00‡	9.29
27	12.93	13.08	13.76	1.16	6.42
28	8.83	9.60	10.00	8.72	13.25
29	18.42	19.46	21.37	5.65	16.02
30	23.94	22.53	19.36	5.89	19.13
31	21.51	22.26	23.49	3.49	9.21
32	15.15	15.13	15.71	0.13	3.70
33	21.75	22.52	22.30	3.54	2.53
34	18.65	18.49	14.90	0.86	20.11
35	28.00	30.37	32.46	8.46	15.93
36	16.16	19.22	24.19	18.94	49.69†
37	20.69	18.76	18.04	9.33	12.81
38	18.08	18.12	18.89	0.22	4.48
39	17.97	16.92	16.38	5.84	8.85
40	21.39	22.02	23.71	2.95	10.85
41	21.60	22.34	23.85	3.43	10.42
42	12.23	12.16	12.36	0.57	1.06
43	17.97	17.98	18.57	0.06	3.34
44	17.37	16.95	18.01	2.42	3.68
45	8.11	8.88	8.91	9.49	9.86
46	18.98	19.20	18.50	1.16	2.53
47	17.65	17.50	19.50	0.85	10.48
48	8.83	8.26	9.06	6.46	2.60
49	16.50	16.26	15.61	1.45	5.39
50	17.53	17.58	18.11	0.29	3.31
51	17.41	18.02	16.70	3.50	4.08
52	18.85	17.14	16.73	9.07	11.25
53	20.62	21.84	21.56	5.92	4.56
54	19.38	18.62	20.24	3.92	4.44
55	17.30	17.86	17.53	3.24	1.33
56	28.03	28.37	28.32	1.21	1.03
57	15.96	16.17	16.92	1.32	6.02
58	24.49	25.05	25.12	2.29	2.57
59	18.47	18.69	18.89	1.19	2.27
60	18.72	19.51	20.39	4.22	8.92
61	20.40	21.15	21.99	3.68	7.79
62	11.20	11.83	12.48	5.63	11.43
Average percentage differences				5.25	9.57

Bibliography

[1] W.P. Abhayaratna, J.B. Seward, C.P. Appleton, P.S. Douglas, J.K. Oh, A.J. Tajik, and T.S.M. Tsang. Left Atrial Size: Physiologic Determinants and Clinical Applications. *Journal of the American College of Cardiology*, 47(12):2357, 2006.

[2] R. Adams and L. Bischof. Seeded region growing. *IEEE Transactions on Pattern Analysis and Machine Intelligence*, 16(6):641–647, 1994.

[3] A.S. Agatston, W.R. Janowitz, F.J. Hildner, N.R. Zusmer, M. Viamonte, and R. Detrano. Quantification of coronary artery calcium using ultrafast computed tomography. *Journal of the American College of Cardiology*, 15(4):827–832, 1990.

[4] C.M. Anderson, D. Saloner, J.S. Tsuruda, L.G. Shapeero, and R.E. Lee. Artifacts in maximum-intensity-projection display of MR angiograms. *American Journal of Roentgenology*, 154(3):623–9, 1990.

[5] C. Aschwanden, A. Sherstyuk, L. Burgess, and K. Montgomery. A Surgical and Fine-Motor Skills Trainer for Everyone? Touch and Force-Feedback in a Virtual Reality Environment for Surgical Training. *Studies in health technology and informatics*, 119:19, 2005.

[6] N. Ayache, P. Cinquin, I. Cohen, L. Cohen, F. Leitner, and O. Monga. Segmentation of Complex Three-Dimensional Medical Objects: A Challenge and a Requirement for Computer Assisted Surgery Planning and Performance. *In B. Taylor, Lavallee, G.C. Burdea and R. Mosges, editors, Computer Integrated Surgery: Technology and Clinical Applications*, pages 59–74, 1996.

[7] S.R. Aylward and E. Bullitt. Initialization, noise, singularities, and scale in height ridge traversal for tubular object centerline extraction. *IEEE Transactions on Medical Imaging*, 21(2):61–75, 2002.

[8] D.G. Bailey. An Efficient Euclidean Distance Transform. *10th International Workshop on Combinatorial Image Analysis*, 2004.

[9] I.N. Bankman. *Handbook of medical imaging.* Academic Press, Inc. Orlando, FL, USA, 2000.

[10] I.N. Bankman, T. Nizialek, I. Simon, O.B. Gatewood, I.N. Weinberg, and W.R. Brody. Segmentation algorithms for detecting microcalcifications in mammograms. *IEEE Transactions on Information Technology in Biomedicine*, 1(2):141–149, 1997.

[11] R. Beichel, H. Bischof, F. Leberl, and M. Sonka. Robust active appearance models and their application to medical image analysis. *IEEE Transactions on Medical Imaging*, 24(9):1151–1169, 2005.

[12] E.J. Benjamin, P.A. Wolf, R.B. D'Agostino, H. Silbershatz, W.B. Kannel, and D. Levy. Impact of atrial fibrillation on the risk of death the Framingham Heart Study. *Circulation*, 98(10):946–952, 1998.

[13] S.H. Benton. *The Hamilton-Jacobi equation: a global approach.* Academic Press, New York, 1977.

[14] P.J. Besl and N.D. McKay. A method for registration of 3-D shapes. *IEEE Transactions on Pattern Analysis and Machine Intelligence*, 14(2):239–256, 1992.

[15] J.C. Bezdek, L.O. Hall, and L.P. Clarke. Review of MR image segmentation techniques using pattern recognition. *Medical Physics*, 20:1033, 1993.

[16] A. Bhalerao, E. Thonnes, W. Kendall, and R. Wilson. Inferring Vascular Structure from 2D and 3D Imagery. In *Proceedings of the 4th International conference on Medical Image Computing and Computer-Assisted Intervention*, 2001.

[17] A. Bhalerao, R. Wilson, and UK Coventry. A Fourier approach to 3D local feature estimation from volume data. In *Proceedings of the British Machine Vision conference*, 2001.

[18] J.G. Bosch, S.C. Mitchell, B.P.F. Lelieveldt, F. Nijland, O. Kamp, M. Sonka, and J.H.C. Reiber. Automatic segmentation of echocardiographic sequences by active appearance motion models. *IEEE Transactions on Medical Imaging*, 21(11):1374–1383, 2002.

[19] A.C. Bovik. *Handbook of Image and Video Processing (Communications, Networking and Multimedia)*. Academic Press, Inc. Orlando, FL, USA, 2005.

[20] E. Bullitt, S. Aylward, K. Smith, S. Mukherji, M. Jiroutek, and K. Muller. Symbolic description of intracerebral vessels segmented from magnetic resonance angiograms and evaluation by comparison with X-ray angiograms. *Medical Image Analysis*, 5(2):157–169, 2001.

[21] C. Burgstahler, T. Trabold, A. Kuettner, A.F. Kopp, C. Mewis, V. Kuehlkamp, C.D. Claussen, and S. Schroeder. Visualisation of pulmonary vein stenosis after radio frequency ablation using multi-slice computed tomography: initial clinical experience in 33 patients. *International Journal of Cardiology*, 102(2):287–291, 2005.

[22] E.G. Caiani, C. Corsi, L. Sugeng, P. MacEneaney, L. Weinert, V. Mor-Avi, and R.M. Lang. Improved quantification of left ventricular mass based on endocardial and epicardial surface detection with real time three dimensional echocardiography. *British Medical Journal*, 92(2):213, 2006.

[23] K.R. Castleman. *Digital image processing.* Prentice Hall Press Upper Saddle River, NJ, USA, 1996.

[24] T.F. Chan and L.A. Vese. Active contours without edges. *IEEE Transactions on Image Processing*, 10(2):266–277, 2001.

[25] E.L. Chaney and S.M. Pizer. Defining Anatomical Structures from Medical Images. *Seminars in Radiation Oncology*, 2(4):215–225, 1992.

[26] S.A. Chen, M.H. Hsieh, C.T. Tai, C.F. Tsai, V.S. Prakash, W.C. Yu, T.L. Hsu, Y.A. Ding, and M.S. Chang. Initiation of Atrial Fibrillation by Ectopic Beats Originating From the Pulmonary Veins Electrophysiological Characteristics, Pharmacological Responses, and Effects of Radiofrequency Ablation. *Circulation*, 100(18):1879–1886, 1999.

[27] Y. Chenoune, E. Deléchelle, E. Petit, T. Goissen, J. Garot, and A. Rahmouni. Segmentation of cardiac cine-MR images and myocardial deformation assessment using level set methods. *Computerized Medical Imaging and Graphics*, 29(8):607–616, 2005.

[28] S.I. Choi, J.B. Seo, S.H. Choi, S.H. Lee, K.H. Do, S.M. Ko, J.S. Lee, J.W. Song, K.S. Song, K.J. Choi, et al. Variation of the size of pulmonary venous ostia during the cardiac cycle: optimal reconstruction window at ECG-gated multi-detector row CT. *European Radiology*, 15(7):1441–1445, 2005.

[29] L.P. Clarke, R.P. Velthuizen, M.A. Camacho, J.J. Heine, M. Vaidyanathan, L.O. Hall, R.W. Thatcher, and M.L. Silbiger. MRI segmentation: methods and applications. *Magnetic Resonance Imaging*, 13(3):343–68, 1995.

[30] T.F. Cootes, A. Hill, C.J. Taylor, and J. Haslam. Use of active shape models for locating structures in medical images. *Image and Vision Computing*, 12(6):355–365, 1994.

[31] T.F. Cootes and C.J. Taylor. Statistical models of appearance for computer vision. *World Wide Web Publication, February*, 2001.

[32] T.F. Cootes, C.J. Taylor, DH Cooper, and J. Graham. Training models of shape from sets of examples. *Proceedings of the British Machine Vision conference*, 1992.

[33] T.F. Cootes, G.V. Wheeler, K.N. Walker, and C.J. Taylor. View-based active appearance models. *Image and Vision Computing*, 20(9-10):657–664, 2002.

[34] J.L. Cox. The surgical treatment of atrial fibrillation. II. Intraoperative electrophysiologic mapping and description of the electrophysiologic basis of atrial flutter and atrial fibrillation. *The Journal of Thoracic and Cardiovascular Surgery*, 101(3):406–426, 1991.

[35] M.G. Crandall and P.L. Lions. Viscosity solutions of Hamilton-Jacobi equations. *Transactions of the American Mathematical Society*, 277(1):1–42, 1983.

[36] A. Cristoforetti, L. Faes, F. Ravelli, M. Centonze, M. Del Greco, R. Antolini, and G. Nollo. Isolation of the left atrial surface from cardiac multi-detector CT images based on marker controlled watershed segmentation. *Medical Engineering and Physics*, 30(1):48–58, 2008.

[37] P. Cronin, M.B. Sneider, E.A. Kazerooni, A.M. Kelly, C. Scharf, H. Oral, and F. Morady. MDCT of the Left Atrium and Pulmonary Veins in Planning Radiofrequency Ablation for Atrial Fibrillation: A How-To Guide. *American Journal of Roentgenology*, 183(3):767–778, 2004.

[38] O. Cuisenaire and B. Macq. Fast Euclidean distance transformation by propagation using multiple neighborhoods. *Computer Vision and Image Understanding*, 76(2):163–172, 1999.

[39] J.T. Dell'Orfano, J.C. Luck, D.L. Wolbrette, H. Patel, and G.V. Naccarelli. Drugs for Conversion of Atrial Fibrillation. *American Family Physician*, 58:471–480, 1998.

[40] A.P. Dempster, N.M. Laird, D.B. Rubin, et al. Maximum likelihood from incomplete data via the EM algorithm. *Journal of the Royal Statistical Society*, 39(1):1–38, 1977.

[41] T. Dickfeld, H. Calkins, M. Zviman, R. Kato, G. Meininger, L. Lickfett, R. Berger, H. Halperin, and S.B. Solomon. Anatomic Stereotactic Catheter Ablation on Three-Dimensional Magnetic Resonance Images in Real Time. *Circulation*, 108(19):2407–2413, 2003.

[42] T. Dill, T. Neumann, O. Ekinci, C. Breidenbach, A. John, A. Erdogan, G. Bachmann, C.W. Hamm, and H.F. Pitschner. Pulmonary Vein Diameter Reduction After Radiofrequency Catheter Ablation for Paroxysmal Atrial Fibrillation Evaluated by Contrast-Enhanced Three-Dimensional Magnetic Resonance Imaging. *Circulation*, 107(6):845–850, 2003.

[43] N. Duta, A.K. Jain, and M.P. Dubuisson-Jolly. Automatic Construction of 2D Shape Models. *IEEE Transactions on Pattern Analysis and Machine Intelligence*, pages 433–446, 2001.

[44] S. Ernst, T. Broemel, U. Krumsdorf, H. Hachiya, F. Ouyang, C. Linder, P. Falk, D. Bansch, A. Schaumann, K.H. Kuck, et al. Three-dimensional reconstruction of pulmonary veins and left atrium. Implications for catheter ablation of atrial fibrillation. *Herz*, 28(7):559–65, 2003.

[45] S. Ernst, H. Hachiya, J.K.R. Chun, and F. Ouyang. Remote Catheter Ablation of Parahisian Accessory Pathways Using a Novel Magnetic Navigation System-A Report of Two Cases. *Journal of Cardiovascular Electrophysiology*, 16(6):659–662, 2005.

[46] G.M.X. Fernando and D.M. Monro. Variable Thresholding Applied to Angiography. *Proceedings of the IEEE Computer Society International Symposium on Medical Imaging and Image Interpretation*, 1982.

[47] D.A. Field. Laplacian smoothing and Delaunay triangulations. *Communications in Applied Numerical Methods*, 4(6), 1988.

[48] A.F. Frangi, W.J. Niessen, R.M. Hoogeveen, T. van Walsum, and M.A. Viergever. Model-based quantitation of 3-D magnetic resonance angiographic images. *IEEE Transactions on Medical Imaging*, 18(10):946–956, 1999.

[49] A.F. Frangi, W.J. Niessen, and M.A. Viergever. Three-dimensional modeling for functional analysis of cardiac images, a review. *IEEE Transactions on Medical Imaging*, 20(1):2–5, 2001.

[50] A.F. Frangi, W.J. Niessen, K.L. Vincken, and M.A. Viergever. Multiscale Vessel Enhancement Filtering. *Proceedings of the Medical Image Computing and Computer-Assisted Intervention*, 1998.

[51] A.F. Frangi, D. Rueckert, J.A. Schnabel, and W.J. Niessen. Automatic construction of multiple-object three-dimensional statistical shape models: application to cardiac modeling. *IEEE Transactions on Medical Imaging*, 21(9):1151–1166, 2002.

[52] O. Friman, M. Hindennach, and H.O. Peitgen. Template-based multiple hypotheses tracking of small vessels. In *Proceedings of the IEEE International Symposium on Biomedical Imaging: From Nano to Macro*, 2008.

[53] B. Ghaye, D. Szapiro, J.N. Dacher, L.M. Rodriguez, C. Timmermans, D. Devillers, and R.F. Dondelinger. Percutaneous ablation for atrial fibrillation: the role of cross-sectional imaging. *Radiographics*, 23(90001):19–33, 2003.

[54] T. Giesler, U. Baum, D. Ropers, S. Ulzheimer, E. Wenkel, M. Mennicke, W. Bautz, W.A. Kalender, W.G. Daniel, and S. Achenbach. Noninvasive Visualisation of Coronary Arteries Using Contrast-Enhanced Multidetector CT: Influence of Heart Rate on Image Quality and Stenosis Detection. *American Journal of Roentgenology*, 179(4):911–916, 2002.

[55] J.C. Gower. Generalized Procrustes analysis. *Psychometrika*, 40:33–51, 1975.

[56] V. Grau, A.U.J. Mewes, M. Alcaniz, R. Kikinis, and S.K. Warfield. Improved watershed transform for medical image segmentation using prior information. *IEEE Transactions on Medical Imaging*, 23(4):447–458, 2004.

[57] F.E. Grubbs. Procedures for detecting outlying observations in samples. *Technometrics*, pages 1–21, 1969.

[58] I. Guttman. *Statistical Tolerance Regions: Classical and Bayesian.* Griffin London, 1970.

[59] M. Haissaguerre, P. Jais, D.C. Shah, A. Takahashi, M. Hocini, G. Quiniou, S. Garrigue, A. Le Mouroux, P. Le Metayer, and J. Clementy. Spontaneous Initiation of Atrial Fibrillation by Ectopic Beats Originating in the Pulmonary Veins. *New England Journal of Medicine*, 339(10):659–666, 1998.

[60] M. Haissaguerre, D.C. Shah, P. Jais, M. Hocini, T. Yamane, I. Deisenhofer, M. Chauvin, S. Garrigue, and J. Clementy. Electrophysiological breakthroughs from the left atrium to the pulmonary veins. *Circulation*, 102(20):2463–2465, 2000.

[61] R.M. Haralick and L.G. Shapiro. Image segmentation techniques. *Computer Vision, Graphics, and Image Processing*, 29:100–132, 1985.

[62] JA Hartigan and MA Wong. Algorithm AS 136: A K-means clustering algorithm. *Applied Statistics*, pages 100–108, 1979.

[63] T. Hartkens, D. Rueckert, J.A. Schnabel, D.J. Hawkes, and D.L.G. Hill. VTK CISG registration toolkit: An open source software package for affine and non-rigid registration of single-and multimodal 3d images. *Bildverarbeitung für die Medizin*, pages 409–12, 2002.

[64] W.E. Higgins and E.J. Ojard. Interactive morphological watershed analysis for 3D medical images. *Computerized Medical Imaging and Graphics*, 17(4-5):387–95, 1993.

[65] S.Y. Ho, J.A. Cabrera, V.H. Tran, J. Farre, R.H. Anderson, and D. Sanchez-Quintana. Architecture of the pulmonary veins: relevance to radiofrequency ablation. *Heart*, 86(3):265–270, 2001.

[66] Y.L. Huang and D.R. Chen. Watershed segmentation for breast tumor in 2-D sonography. *Ultrasound in Medicine & Biology*, 30(5):625–632, 2004.

[67] L. Ibanez, W. Schroeder, L. Ng, and J. Cates. The ITK software guide: the insight segmentation and registration toolkit. *Kitware Inc*, 5, 2003.

[68] P. Jais, M. Haissaguerre, D.C. Shah, S. Chouairi, L. Gencel, M. Hocini, and J. Clementy. A Focal Source of Atrial Fibrillation Treated by Discrete Radiofrequency Ablation. *Circulation*, 95(3):572–576, 1997.

[69] M. John and N. Rahn. Automatic Left Atrium Segmentation by Cutting the Blood Pool at Narrowings. *Proceedings of the Medical Image Computing and Computer-assisted Intervention*, 2005.

[70] S.C. Johnson. Hierarchical clustering schemes. *Psychometrika*, 32(3):241–254, 1967.

[71] I.T. Jolliffe. *Principal component analysis*. Springer New York, 2002.

[72] M.R.M. Jongbloed, M.J. Schalij, R.E. Poelmann, N.A. Blom, M.L. Fekkes, Z. Wang, G.I. Fishman, and A.C. Gittenberger-De Groot. A Spatial Correlation with Adult Arrhythmogenic Areas. *Journal of Cardiovascular Electrophysiology*, 15(3):349–355, 2004.

[73] A.N. Julien, M.P. Jolly, and Guang-Zhong Yang. Robust Active Shape Models. In *Proceedings of the Medical Image Understanding and Analysis conference*, pages 115–118, July 2005.

[74] W.A. Kalender, B. Schmidt, M. Zankl, and M. Schmidt. A PC program for estimating organ dose and effective dose values in computed tomography. *European Radiology*, 9(3):555–562, 1999.

[75] P. Kanagaratnam, M. Koa-Wing, D.T. Wallace, A.S. Goldenberg, N.S. Peters, and D.W. Davies. Experience of robotic catheter ablation in humans using a novel remotely steerable catheter sheath. *Journal of Interventional Cardiac Electrophysiology*, 21(1):19–26, 2008.

[76] M. Kass, A. Witkin, and D. Terzopoulos. Snakes: Active contour models. *International Journal of Computer Vision*, 1(4):321–331, 1988.

[77] M.R. Kaus, J. Berg, J. Weese, W. Niessen, and V. Pekar. Automated segmentation of the left ventricle in cardiac MRI. *Medical Image Analysis*, 8(3):245–254, 2004.

[78] C. Kirbas and F. Quek. A review of vessel extraction techniques and algorithms. *ACM Computing Surveys*, 36(2):81–121, 2004.

[79] P.M. Kistler, M.J. Earley, S. Harris, D. Abrams, S. Ellis, S.C. Sporton, and R.J. Schilling. Validation of Three-Dimensional Cardiac Image Integration: Use of Integrated CT Image into Electroanatomic Mapping System to Perform Catheter Ablation of Atrial Fibrillation. *Journal of Cardiovascular Electrophysiology*, 17(4):341–348, 2006.

[80] T.M. Koller, G. Gerig, G. Szekely, and D. Dettwiler. Multiscale detection of curvilinear structures in 2-D and 3-D image data. *Fifth International conference on Computer Vision*, pages 864–869, 1995.

[81] J.M. Lacomis, W. Wigginton, C. Fuhrman, D. Schwartzman, D.R. Armfield, and K.M. Pealer. Multi-Detector Row CT of the Left Atrium and Pulmonary Veins before Radiofrequency Catheter Ablation for Atrial Fibrillation 1. *RadioGraphics*, 23(90001):35–48, 2003.

[82] M. Lapp, L. Lorenzo-Valdes, and D. Rueckert. 3D/4D Cardiac Segmentation Using Active Appearance Models, Non-rigid Registration, and the Insight Toolkit. *In Proceedings of the Medical Image Computing and Computer-Assisted Interventation conference*, 2004.

[83] V.S. Lee and M. Helmers. *Cardiovascular MRI: Physical Principles to Practical Protocols.* Lippincott Williams & Wilkins, 2006.

[84] T. Lei, J.K. Udupa, P.K. Saha, and D. Odhner. Artery-vein separation via MRA-An image processing approach. *IEEE Transactions of Medical Imaging*, 20(8):689–703, 2001.

[85] K. Lekadir, R. Merrifield, and Guang-Zhong Yang. Outlier Detection and Handling for Robust 3-D Active Shape Models Search. *IEEE Transactions on Medical Imaging*, 26(2):212–222, 2006.

[86] B.P.F. Lelieveldt, M. Üzümcü, R.J. van der Geest, J.H.C. Reiber, and M. Sonka. Multi-view active appearance models for consistent segmentation of multiple standard views: application to long-and short-axis cardiac MR images. *International Congress Series*, 1256:1141–1146, 2003.

[87] K. Lemola, M. Sneider, B. Desjardins, I. Case, J. Han, E. Good, K. Tamirisa, A. Tsemo, A. Chugh, F. Bogun, et al. Computed Tomographic Analysis of the Anatomy of the Left Atrium and the Esophagus Implications for Left Atrial Catheter Ablation. *Circulation*, 110(24):3655–3660, 2004.

[88] M.D. Lesh, G.F. Van Hare, L.M. Epstein, A.P. Fitzpatrick, M.M. Scheinman, R.J. Lee, M.A. Kwasman, H.R. Grogin, and J.C. Griffin. Radiofrequency catheter ablation of atrial arrhythmias. Results and mechanisms. *Circulation*, 89(3):1074–1089, 1994.

[89] M.E. Leventon, W.E.L. Grimson, and O. Faugeras. Statistical shape influence in geodesic active contours. *Proceedings of the IEEE conference on Computer Vision and Pattern Recognition*, 1, 2000.

[90] L. Lickfett, R. Kato, H. Tandri, V. Jayam, CR Vasamreddy, T. Dickfeld, T. Lewalter, B. Luderitz, R. Berger, H. Halperin, et al. Characterization of a new pulmonary vein variant using magnetic resonance angiography: incidence, imaging, and interventional implications of the" right top pulmonary vein". *Journal of Cardiovascular Electrophysiology*, 2004.

[91] T. Lindeberg. *Scale-Space Theory in Computer Vision.* Kluwer Academic Print on Demand, 1994.

[92] G.Y.H. Lip, P. Kakar, and T. Watson. Atrial fibrillation: the growing epidemic. *British Medical Journal*, 93(5):542–543, 2007.

[93] W.E. Lorensen and H.E. Cline. Marching cubes: A high resolution 3D surface construction algorithm. In *Proceedings of the 14th annual conference on Computer graphics and interactive techniques.* ACM New York, NY, USA, 1987.

[94] C. Lorenz and J. Berg. Accurate left atrium segmentation in multislice CT images using a shape model. *Proceedings of the Society of the Photo-Optical Instrumentation Engineers (SPIE)*, 2005.

[95] C. Lorenz and J. Berg. A comprehensive shape model of the heart. *Medical Image Analysis*, 10(4):657–670, 2006.

[96] C. Lorenz and N. Krahnstover. 3D statistical shape models for medical image segmentation. *Proceedings of the Second International conference on 3-D Digital Imaging and Modeling*, 1999.

[97] J. Lötjönen, S. Kivistö, J. Koikkalainen, D. Smutek, and K. Lauerma. Statistical shape model of atria, ventricles and epicardium from short-and long-axis MR images. *Medical Image Analysis*, 8(3):371–386, 2004.

[98] C.A. Mack, F. Milla, W. Ko, L.N. Girardi, L.Y. Lee, A.J. Tortolani, J. Mascitelli, K.H. Krieger, and O.W. Isom. Surgical treatment of atrial fibrillation using argon-based cryoablation during concomitant cardiac procedures. *Circulation*, 112(90090):1–6, 2005.

[99] R. Maksimović, T. Dill, A.D. Ristić, and P.M. Seferović. Imaging in percutaneous ablation for atrial fibrillation. *European Radiology*, 16(11):2491–2504, 2006.

[100] Z.J. Malchano, P. Neuzil, R.C. Cury, G. Holmvang, J. Weichet, E.J. Schmidt, J.N. Ruskin, and V.Y. Reddy. Integration of Cardiac CT/MR Imaging with Three-Dimensional Electroanatomical Mapping to Guide Catheter Manipulation in the Left Atrium: Implications for Catheter Ablation of Atrial Fibrillation. *Journal of Cardiovascular Electrophysiology*, 17(11):1221–1229, 2006.

[101] R.A. Malkin, N. Kramer, B. Schnitz, M. Gopalakrishnan, and A.L. Curry. Advances in electrical and mechanical cardiac mapping. *Physiological Measurement*, 26(1):R1–14, 2005.

[102] R. Malladi, R. Kimmel, D. Adalsteinsson, G. Sapiro, V. Caselles, and J.A. Sethian. A geometric approach to segmentation and analysis of 3D medicalimages. *Proceedings of the Workshop on Mathematical Methods in Biomedical Image Analysis*, 1996.

[103] R. Malladi and J.A. Sethian. A unified approach to noise removal, image enhancement, and shape recovery. *IEEE Transactions on Image Processing*, 5(11):1554–1568, 1996.

[104] R. Malladi, J.A. Sethian, and B.C. Vemuri. Shape Modeling with Front Propagation: A Level Set Approach. *IEEE Transactions on Pattern Analysis and Machine Intelligence*, pages 158–175, 1995.

[105] R. Manniesing and W. Niessen. Multiscale vessel enhancing diffusion in CT angiography noise filtering. *Information Processing in Medical Imaging*, 19:138–49, 2005.

[106] R. Manniesing and W. Niessen. Shape constrained vessel centerline extraction by integrating surface evolution and topology analysis. In *3rd IEEE International Symposium on Biomedical Imaging: Macro to Nano*, pages 165–168, 2006.

[107] E. Marbán. Cardiac channelopathies. *Nature*, 415:213–218, 2002.

[108] F.E. Marchlinski, D. Callans, S. Dixit, E.P. Gersrenfeld, R. Rho, J.F. Ren, and E. Zado. Efficacy and Safety of Targeted Focal Ablation Versus PV Isolation Assisted by Magnetic Electroanatomic Mapping. *Journal of Cardiovascular Electrophysiology*, 14(4):358–365, 2003.

[109] E.M. Marom, J.E. Herndon, Y.H. Kim, and H.P. McAdams. Variations in Pulmonary Venous Drainage to the Left Atrium: Implications for Radiofrequency Ablation. *Radiology*, pages 824–829, 2004.

[110] Y. Masutani, T. Schiemann, and K.H. Hohne. Vascular Shape Segmentation and Structure Extraction Using a Shape-Based Region-Growing Model. *Proceedings of Medical Image Computing and Computer-Assisted Interventation*, 1998.

[111] C.R. Maurer Jr, R. Qi, and V. Raghavan. A Linear Time Algorithm for Computing Exact Euclidean Distance Transforms of Binary Images in Arbitrary Dimensions. *IEEE Transactions on Pattern Analysis and Machine Intelligence*, pages 265–270, 2003.

[112] T. McInerney and D. Terzopoulos. Deformable models in medical image analysis: a survey. *Medical Image Analysis*, 1(2):91–108, 1996.

[113] D.W. McRobbie, E.A. Moore, and M.J. Graves. *MRI from Picture to Proton*. Cambridge University Press, 2006.

[114] Writing Committee Members. ACC/AHA/ESC 2006 guidelines for the management of patients with atrial fibrillation. *Europace*, 8(9):651–745, 2006.

[115] C. Meyer, R. Manzke, J. Peters, O. Ecabert, R. Kneser, V.Y. Reddy, R.C. Chan, and J. Weese. Automatic Intra-operative Generation of Geometric Left Atrium/Pulmonary Vein Models from Rotational X-Ray Angiography. In *Proceedings of the 11th International conference on Medical Image Computing and Computer-Assisted Intervention, Part II*, 2008.

[116] S.C. Mitchell, J.G. Bosch, B.P.F. Lelieveldt, R.J. van der Geest, J.H.C. Reiber, and M. Sonka. 3-D active appearance models: segmentation of cardiac MR and ultrasound images. *IEEE Transactions on Medical Imaging*, 21(9):1167–1178, 2002.

[117] S.C. Mitchell, B.P.F. Lelieveldt, R.J. van der Geest, H.G. Bosch, J.H.C. Reiver, and M. Sonka. Multistage hybrid active appearance model matching: segmentation of left and right ventricles in cardiac MR images. *IEEE Transactions on Medical Imaging*, 20(5):415–423, 2001.

[118] Y. Miyasaka, M.E. Barnes, B.J. Gersh, S.S. Cha, K.R. Bailey, W.P. Abhayaratna, J.B. Seward, and T.S.M. Tsang. Secular trends in incidence of atrial fibrillation in Olmsted County, Minnesota, 1980 to 2000, and implications on the projections for future prevalence. *Circulation*, 114(2):119, 2006.

[119] G.K. Moe, W.C. Rheinboldt, and J.A. Abildskov. A computer model of atrial fibrillation. *American Heart Journal*, 67:200–20, 1964.

[120] S. Nakajima, H. Atsumi, A.H. Bhalerao, F.A. Jolesz, R. Kikinis, T. Yoshimine, T.M. Moriarty, and P.E. Stieg. Computer-assisted surgical planning for cerebrovascular neurosurgery. *Neurosurgery*, 41(2):403, 1997.

[121] H. Nakashima, K. Kumagai, H. Noguchi, H. Tojo, T. Yasuda, and K. Saku. Evaluation of the recurrence of atrial fibrillation after pulmonary venous ablation. *Journal of Cardiology*, 40(3):87–94, 2002.

[122] A. Natale. Lessons Learned and Techniques Altered Following Early Experience of the Hansen Robotic System During Catheter Ablation of Atrial Fibrillation. *Heart Rhythm*, 2008.

[123] A. Natale, A. Raviele, T. Arentz, H. Calkins, S.A.N.N. Chen, M. Haissaguerre, G. Hindricks, Yen Ho, K.H. Kuck, F. Marchlinski, et al. Venice Chart International Consensus Document on Atrial Fibrillation Ablation. *Journal of Cardiovascular Electrophysiology*, 18(5):560–580, 2007.

[124] S. Nattel et al. New ideas about atrial fibrillation 50 years on. *Nature*, 415(6868):219–226, 2002.

[125] T. O'Donnell, A. Gupta, and T. Boult. A New Model for the Recovery of Cylindrical Structures from Medical Image Data. *Proceedings of the First Joint conference Computer Vision, Virtual Reality and Robotics in Medicine and Medical Robotics and Computer-Assisted Surgery, Grenoble, France*, 1997.

[126] C.R. Oost, B.P. Lelieveldt, M. Uzumcu, H. Lamb, J.H. Reiber, and M. Sonka. Multi-View Active Appearance Models: application to X-ray LV angiography and cardiac MRI. *Proceedings of Information Processing in Medical Imaging*, 2003.

[127] H. Oral, B.P. Knight, M. Ozaydin, A. Chugh, S.W.K. Lai, C. Scharf, S. Hassan, R. Greenstein, J.D. Han, F. Pelosi, et al. Segmental Ostial Ablation to Isolate the Pulmonary Veins During Atrial Fibrillation: Feasibility and Mechanistic Insights. *Circulation*, 106(10):1256–1262, 2002.

[128] M.M. Orkisz, C. Bresson, I.E. Magnin, O. Champin, and P.C. Douek. Improved vessel visualisation in MR angiography by nonlinear anisotropic filtering. *Magnetic Resonance in Medicine*, 37(6):914–9, 1997.

[129] S.J. Osher and J.A. Sethian. Fronts propagation with curvature dependent speed: Algorithms based on Hamilton-Jacobi formulations. *Journal of Computational Physics*, 79(1):12–49, 1988.

[130] N. Otsu. A threshold selection method from gray-level histogram. *IEEE Transactions on Systems, Man and Cybernetics*, 9(1):62–66, 1979.

[131] N.R. Pal and S.K. Pal. A review on image segmentation techniques. *Pattern Recognition*, 26(9):1277–1294, 1993.

[132] C. Pappone, G. Oreto, S. Rosanio, G. Vicedomini, M. Tocchi, F. Gugliotta, A. Salvati, C. Dicandia, M.P. Calabro, P. Mazzone, et al. Atrial Electroanatomic Remodeling After

Circumferential Radiofrequency Pulmonary Vein Ablation Efficacy of an Anatomic Approach in a Large Cohort of Patients With Atrial Fibrillation. *Circulation*, 104(21):2539–2544, 2001.

[133] C. Pappone, S. Rosanio, G. Oreto, M. Tocchi, F. Gugliotta, G. Vicedomini, A. Salvati, C. Dicandia, P. Mazzone, V. Santinelli, et al. Circumferential Radiofrequency Ablation of Pulmonary Vein Ostia A New Anatomic Approach for Curing Atrial Fibrillation. *Circulation*, 102(21):2619–2628, 2000.

[134] P. Perona and J. Malik. Scale-space and edge detection using anisotropic diffusion. *IEEE Transactions on Pattern Analysis and Machine Intelligence*, 12(7):629–639, 1990.

[135] N.S. Peters, R.J. Schilling, P. Kanagaratnam, and V. Markides. Atrial fibrillation: strategies to control, combat, and cure. *The Lancet*, 359(9306):593–603, 2002.

[136] D.L. Pham, C. Xu, and J.L. Prince. A survey of current methods in medical image segmentation. *Annual Review of Biomedical Engineering*, 2:315–337, 2000.

[137] C. Pluempitiwiriyawej, J.M.F. Moura, Y.J.L. Wu, and C. Ho. STACS: New Active Contour Scheme for Cardiac MR Image Segmentation. *IEEE Transactions on Medical Imaging*, 24(5):593, 2005.

[138] S.M. Prasad, H.S. Maniar, C.J. Camillo, R.B. Schuessler, J.P. Boineau, T.M. Sundt, J.L. Cox, and R.J. Damiano. The Cox maze III procedure for atrial fibrillation: long-term efficacy in patients undergoing lone versus concomitant procedures. *The Journal of Thoracic and Cardiovascular Surgery*, 126(6):1822–1827, 2003.

[139] J.M.S. Prewitt and M.L. Mendelsohn. The Analysis of Cell Images. *Annals of the New York Academy of Sciences*, 128(3):1035–1053, 1965.

[140] A.M. Pritchett, S.J. Jacobsen, D.W. Mahoney, R.J. Rodeheffer, K.R. Bailey, and M.M. Redfield. Left atrial volume as an index ofleft atrial size: a population-based study. *Journal of the American College of Cardiology*, 41(6):1036–1043, 2003.

[141] H. Pürerfellner, J. Aichinger, M. Martinek, H.J. Nesser, R. Cihal, M. Gschwendtner, and J. Dierneder. Incidence, management, and outcome in significant pulmonary vein stenosis complicating ablation for atrial fibrillation. *The American Journal of Cardiology*, 93(11):1428–1431, 2004.

[142] Y. Qu, Q. Chen, P.A. Heng, and T.T. Wong. Segmentation of left ventricle via level set method based on enriched speed term. *Proceedings of Medical Image Computing and Computer-Assisted Interventation*, 2004.

[143] A. Rangarajan, H. Chui, and F.L. Bookstein. The soft assign Procrustes Matching Algorithm. *Information processing in Medical Imaging (IPMI)*, pages 29–42, 1997.

[144] K.S. Reddy. Cardiovascular diseases in the developing countries: dimensions, determinants, dynamics and directions for public health action. *Public Health Nutrition*, 5(1a):231–237, 2006.

[145] V.Y. Reddy, P. Neuzil, Z.J. Malchano, R. Vijaykumar, R. Cury, S. Abbara, J. Weichet, C.D. McPherson, and J.N. Ruskin. View-Synchronized Robotic Image-Guided Therapy for Atrial Fibrillation Ablation: Experimental Validation and Clinical Feasibility. *Circulation*, 115(21):2705, 2007.

[146] Image repository of the scientific electronic library online of Brazil. `http://www.scielo.br/img/revistas/abc/v85n4/en_a14fig02.gif`.

[147] J.B.T.M. Roerdink and A. Meijster. The Watershed Transform: Definitions, Algorithms and Parallelization Strategies. *Mathematical Morphology*, 41:187–S28, 2000.

[148] J. Rogowska. Overview and fundamentals of medical image segmentation. *Handbook of Medical Imaging*, pages 69–85, 2000.

[149] M. Rousson and N. Paragios. Shape priors for level set representations. *Proceedings of the 7th European conference on Computer Vision - Part II*, 2002.

[150] D. Rueckert and P. Burger. Geometrically deformable templates for shape-based segmentation and tracking in cardiac MR images. *Proceedings of the First International*

Workshop on Energy Minimization Methods in Computer Vision and Pattern Recognition, 1997.

[151] D. Rueckert, A.F. Frangi, and J.A. Schnabel. Automatic construction of 3-D statistical deformation models of the brain using nonrigid registration. *IEEE Transactions on Medical Imaging*, 22(8):1014–1025, 2003.

[152] P.K. Saha, J.K. Udupa, and D. Odhner. Scale-Based Fuzzy Connected Image Segmentation: Theory, Algorithms, and Validation. *Computer Vision and Image Understanding*, 77(2):145–174, 2000.

[153] Y. Sato, S. Nakajima, N. Shiraga, H. Atsumi, S. Yoshida, T. Koller, G. Gerig, and R. Kikinis. 3D Multi-Scale Line Filter for Segmentation and visualization of curvilinear structures in medical images. *Medical Image Analysis*, 2(2):143–168, 1998.

[154] H.V. Schaff, J.A. Dearani, R.C. Daly, T.A. Orszulak, and G.K. Danielson. Cox-Maze procedure for atrial fibrillation: Mayo Clinic experience. *Seminars in Thoracic and Cardiovascular Surgery*, 12(1):30–7, 2000.

[155] C. Scharf, M. Sneider, Ian Case, A. Chugh, S.W.K. Lai, F. Pelosi, B.P. Knight, E. Kazerooni, F. Morady, and H. Oral. Anatomy of the Pulmonary Veins in Patients with Atrial Fibrillation and Effects of Segmental Ostial Ablation Analyzed by Computed Tomography. *Journal of Cardiovascular Electrophysiology*, 14(2):150–155, 2003.

[156] D. Scherf, AI Schaffer, and S. Blumenfeld. Mechanism of flutter and fibrillation. *Archives of Internal Medicine*, 91(3):333, 1953.

[157] P.J. Schneider and D.H. Eberly. *Geometric tools for computer graphics*. Morgan Kaufmann, 2003.

[158] W.J. Schroeder, K.M. Martin, and W.E. Lorensen. The design and implementation of an object-oriented toolkit for 3D graphics and visualisation. In *Proceedings of the 7th conference on Visualisation*, 1996.

[159] D. Schwartzman, J. Lacomis, and W.G. Wigginton. Characterization of left atrium and distal pulmonary vein morphology using multidimensional computed tomography. *Journal of the American College of Cardiology*, 41(8):1349–1357, 2003.

[160] J.A. Sethian. Curvature and the evolution of fronts. *Communications in Mathematical Physics*, 101(4):487–499, 1985.

[161] J.A. Sethian. A fast marching level set method for monotonically advancing fronts. *Proceedings of the National Academy of Sciences of the United States of America*, 1996.

[162] J.A. Sethian et al. *Level set methods and fast marching methods.* Cambridge University Press Cambridge, 1999.

[163] J. Sra, D. Krum, A. Malloy, M. Vass, B. Belanger, E. Soubelet, R. Vaillant, and M. Akhtar. Registration of Three-Dimensional Left Atrial Computed Tomographic Images With Projection Images Obtained Using Fluoroscopy. *Circulation*, 112(24):3763–3768, 2005.

[164] C. Studholme, DLG Hill, and DJ Hawkes. An overlap invariant entropy measure of 3D medical image alignment. *Pattern Recognition*, 32(1):71–86, 1999.

[165] P. Suetens. *Fundamentals of Medical Imaging.* Cambridge University Press, 2002.

[166] P. Suetens, E. Bellon, D. Vandermeulen, M. Smet, G. Marchal, J. Nuyts, and L. Mortelmans. Image segmentation: methods and applications in diagnostic radiology and nuclear medicine. *European Journal Radiology*, 17(1):14–21, 1993.

[167] J.S. Suri, K. Liu, L. Reden, and S. Laxminarayan. A review on MR vascular image processing algorithms: acquisition and pre-filtering: part I. *IEEE Transactions on Information Technology in Biomedicine*, 6(4):324–337, 2002.

[168] J.S. Suri, K. Liu, L. Reden, and S. Laxminarayan. A review on MR vascular image processing: skeleton versus non-skeleton approaches: part II. *IEEE Transactions on Information Technology in Biomedicine*, 6(4):338–350, 2002.

[169] H. Tanaka, K.D. Monahan, and D.R. Seals. Age-predicted maximal heart rate revisited. *Journal of the American College of Cardiology*, 37(1):153–156, 2001.

[170] D. Terzopoulos and D. Metaxas. Dynamic 3 D models with local and global deformations: deformable superquadrics. *IEEE Transactions on Pattern Analysis and Machine Intelligence*, 13(7):703–714, 1991.

[171] V. Torre and T. Poggio. On edge detection. *IEEE Transactions on Pattern Analysis and Machine Intelligence*, 8(2):147–163, 1986.

[172] D. Traub, J.P. Daubert, S. McNitt, W. Zareba, and B. Hall. Catheter ablation of atrial fibrillation in the elderly: Where do we stand? *Cardiology*, 16(2):113–120, 2009.

[173] J.K. Udupa and S. Samarasekera. Fuzzy Connectedness and Object Definition: Theory, Algorithms, and Applications in Image Segmentation. *Graphical Models and Image Processing*, 58(3):246–261, 1996.

[174] B. Verdonck, L. Bloch, H. Maitre, D. Vandermeulen, P. Suetens, and G. Marchal. Accurate segmentation of blood vessels from 3D medical images. *Proceedings of the International conference on Image Processing*, 1996.

[175] G.D. Waiter, F.I. McKiddie, T.W. Redpath, S.I. Semple, and R.J. Trent. Determination of normal regional left ventricular function from cine-MR images using a semi-automated edge detection method. *Magnetic Resonance Imaging*, 17(1):99–107, 1999.

[176] O.M. Wazni, H.M. Tsao, S.A. Chen, H.H. Chuang, W. Saliba, A. Natale, and A.L. Klein. Cardiovascular imaging in the management of atrial fibrillation. *Journal of the American College of Cardiology*, 48(10):2077–2084, 2006.

[177] S. Webb. *The Physics of Medical Imaging.* Taylor and Francis, 1988.

[178] J. Weese, M. Kaus, C. Lorenz, S. Lobregt, R. Truyen, and V. Pekar. Shape constrained deformable models for 3D medical image segmentation. *Proceedings of Information Processing in Medical Imaging*, pages 380–387, 2001.

[179] J. Weickert. Coherence-Enhancing Diffusion Filtering. *International Journal of Computer Vision*, 31(2/3):111–127, 1999.

[180] H.J.J. Wellens. Pulmonary Vein Ablation in Atrial Fibrillation Hype or Hope? *Circulation*, 102(21):2562–2564, 2000.

[181] J. Weng, A. Singh, and MY Chiu. Learning-based ventricle detection from cardiac MR and CT images. *IEEE Transactions on Medical Imaging*, 16(4):378–391, 1997.

[182] R.T. Whitaker. Volumetric deformable models: active blobs. *Proceedings of the Society of the Photo-Optical Instrumentation Engineers (SPIE)*, 1994.

[183] D.L. Wilson, J.A. Noble, and N.R. CSIRO. An adaptive segmentation algorithm for time-of-flight MRA data. *IEEE Transactions on Medical Imaging*, 18(10):938–945, 1999.

[184] R. Wilson, AD Calway, and ERS Pearson. A generalized wavelet transform for fourier analysis: themultiresolution fourier transform and its application to image and audiosignal analysis. *IEEE Transactions on Information Theory*, 38(2 Part 2):674–690, 1992.

[185] O. Wink, W.J. Niessen, and M.A. Viergever. Multiscale vessel tracking. *IEEE Transactions on Medical Imaging*, 23(1):130–133, 2004.

[186] F.H.M. Wittkampf, E.J. Vonken, R. Derksen, P. Loh, B. Velthuis, E.F.D. Wever, L.V.A. Boersma, B.J. Rensing, and M.J. Cramer. Pulmonary Vein Ostium Geometry Analysis by Magnetic Resonance Angiography. *Circulation*, 107(1):21–23, 2003.

[187] M.A. Wood, M. Wittkamp, D. Henry, R. Martin, JV Nixon, R.K. Shepard, and K.A. Ellenbogen. A comparison of pulmonary vein ostial anatomy by computerized tomography, echocardiography, and venography in patients with atrial fibrillation having radiofrequency catheter ablation. *The American Journal of Cardiology*, 93(1):49–53, 2004.

[188] C.C. Wu, C.T.A.I. Tai, Y.K.U.O. Lin, H.M. Tsao, W.E.N.C. Yu, and S.A.N.N. Chen. Pulmonary Vein Dissection During Mapping of Atrial Fibrillation. *Journal of Cardiovascular Electrophysiology*, 12(4):505–505, 2001.

[189] H. Xue, L. Srinivasan, S. Jiang, M. Rutherford, A.D. Edwards, D. Rueckert, and J.V. Hajnal. Automatic segmentation and reconstruction of the cortex from neonatal MRI. *Neuroimage*, 38(3):461–477, 2007.

[190] M. Yang, H. Akbari, G.P. Reddy, and C.B. Higgins. Identification of Pulmonary Vein Stenosis After Radiofrequency Ablation for Atrial Fibrillation Using MRI. *Journal of Computer Assisted Tomography*, 25(1):34, 2001.

[191] Y. Zheng, A. Barbu, B. Georgescu, M. Scheuering, and D. Comaniciu. Four-Chamber Heart Modeling and Automatic Segmentation 3D Cardiac CT Volume Using Marginal Space Learning and Steerable Features. *IEEE Transactions on Medical Imaging*, 27(11):1668, 2008.

[192] H. Zhong, T. Kanade, and D. Schwartzman. Sensor Guided Ablation Procedure of Left Atrial Endocardium. *Proceedings of Medical Image Computing and Computer-assisted Intervention*, 2005.